Vanadium oxides based composites for energy storage applications

by

Ndeye Maty Ndiaye

A thesis submitted in partial fulfilment of the requirements for the degree of

DOCTOR OF PHILOSOPHY (PhD.) IN PHYSICS

Faculty of Natural and Agricultural Sciences

University of Pretoria

Hatfield Pretoria

July 2019

Supervisor/promoter: **Prof. N. I. Manyala**

Co-Supervisor/promoter: **Prof. B. D. Ngom**

Declaration

I, **Ndeye Maty Ndiaye** declare that the thesis entitled "Vanadium oxides based composites for energy storage applications" which I hereby submit for the degree Doctor of Philosophy (PhD), is the result of investigation carried out by me under the supervisor of Prof N. I. Manyala and co-supervisor Prof B. D. Ngom, in the physics Department at the University of Pretoria, South Africa and has not been previously submitted by me for a degree at this or any other tertiary institution.

Signature:............................   Date:...

Dedication

With everlasting love: ELhadji Alioune Fall

My parents: Pape Ndiaye, Fallou Fall,

Fambaye Mane and Amy Cisse

My Co-supervisor: Prof Balla Diop Ngom

They are the reason of what I have become today.

Acknowledgments

I don't have the words to thank you enough. I also acknowledge my friend and brother Samba Sarr. You both made my life interesting and wonderful while studying in Pretoria.

I would like to give my endless gratitude to my both adorable family and friends for their constant prayers and encouragement throughout my life.

I will specially like to mention my life, my heart, my energy, my other half, my source of happiness, my dear husband, Elhadji Alioune Fall. I can only say Thank You for your endless love, patience, prayers and support through thick and thin.

Abstract

In this thesis, different vanadium-based materials and vanadium/carbon composites were synthesized and explored as active electrode materials for supercapacitor application.

The major goal of this study was to incorporate carbon-based materials such as graphene foam and activated expanded graphite into the vanadium-based (oxides and oxynitride) materials to explore their outstanding properties. The as-synthesized vanadium-based materials exhibited high charge storage capacities due to the large stable oxidation states and their layered structures while carbon-based materials presented the much needed specific surface area and good electronic conductivity. The combination of these materials led to the modification of the surface and physical properties of the constituent materials as well as the enhancement of the electrochemical performance for supercapacitor applications.

For example, a novel web-like carbon-vanadium oxynitride (C-V_2NO) material exhibiting the most unique textural and morphological features generated using the facile synthesis route.

The diversity in the structural, morphological, porosity and compositional properties for the vanadium-based materials and vanadium/carbon composites were evaluated by using X-ray powder diffraction (XRD), Raman spectroscopy, field-emission scanning electron microscopy (FE-SEM), transmission electron microscopy (TEM), Brunauer-Emmett-Teller (BET) analysis and X-ray photoelectron spectroscopy (XPS).

The electrochemical properties were evaluated through cyclic voltammetry (CV), galvanostatic charge-discharge (GCD), electrochemical impedance spectroscopy (EIS) and stability (cycling and floating) tests in both three (3) - and two (2) electrode configurations using an aqueous electrolyte.

The composite electrode materials containing carbon incorporated into the pristine vanadium-based material portrayed superior electrochemical properties. Specifically, the asymmetric device of VO$_2$/AEG//C-V$_2$NO where the composite electrode has been adopted as a positive electrode and C-V$_2$NO as a negative electrode, demonstrated a 41.6 Wh kg^{-1} specific energy and specific power of 904 W kg^{-1} at a specific current of 1 A g^{-1}. This was the highest device metrics recorded in this study for all vanadium-based devices tested.

Thus, the results obtained from this study have clearly established the capability of carefully tuning the synthesis conditions for obtaining electrochemically active nanostructured electrode materials such as web-like carbon-vanadium oxynitride (C-V$_2$NO) materials as promising candidates for supercapacitor applications.

Table of contents

List of figures

List of Table

List of equations

<div align="right">

Chapter 1

</div>

_____

1.0 Introduction

1.1 Background and General Motivation

The rapid economic development, the increasing world population and an ever-increasing human reliance on energy-consuming appliances have led to the increased need for access to robust and reliable energy. Globally, energy is crucial to any economy's growth, societal activities and general way of life. Thus, energy has become a primary focus of the entire scientific community and has prompted numerous initiatives into examining the future of global energy in relation to the increasing world population and continued economic growth. Researchers have estimated that in the year 2020, the world will need 50% more energy than is required today [1]. This explosive demand for energy has resulted in an increasing mining cost and exhaustion of the limited fossil fuel resources. In addition, the rising heavy emission of greenhouse gas on the global scale, poses serious health risks (lung cancer) and environmental degradation (global warming, air and soil pollution) which is detrimental to the survival of humankind. Therefore, it is of paramount importance to find alternative sources of energy that are renewable (wind, solar, geothermal, hydrothermal, biomass etc.), environmentally friendly and sustainable [2] especially on the African continent and in other less developed countries around the world.

Wind and solar power are currently the leading alternative and renewable energy sources [3]. Renewable energy (also referred to as "green energy"), is easily restored from an unending natural source. Green energy research has grown rapidly due to the clean and safe production of the energy conversion system [4]. In some cases, it can also be used to generate electricity remotely to areas where the infrastructural cost of extending the existing grid is exorbitant [5].

However, the major drawback to the extensive adoption of the renewable energy technologies (particularly wind and solar) is attributed to its intermittent availability over time due to its dependence on climate changes and sunlight. Consequently, this does not provide a sufficient solution to dealing with the increasing demand for global energy [6].

Hence, the development of large-scale energy storage systems is crucially important to store the excess generated energy from these renewable energy sources for use in a specific application when needed. Among the current efficient energy storage devices, batteries and conventional capacitors provide low specific power and low specific energy, respectively. Thus, a necessity to use another energy storage device by associating both properties of batteries and conventional capacitor to yield a system with high performance, environmentally friendly and low cost (as compared to batteries)

Supercapacitor (SCs), Electrochemical capacitors (ECs) or Ultracapacitors (UCs) have drawn wide interest from both the research and industry experts ever since they were initially considered to be a complement and eventually an alternative to batteries in electric energy and conversion systems [7]. Supercapacitors are able to deliver a considerable amount of specific energy in short time (high specific power) coupled with a long cycle life in a wide operating temperature range. SCs provide higher specific power than batteries while their corresponding specific energy is superior to conventional capacitors.

The US Department of Energy (DoE) has regarded SCs as an important as other storage devices like the much commonly used batteries based on the demonstrated potential [8]. These promising properties make them hopeful candidates for various emerging applications such as in smart grid systems, hybrid electric vehicles etc. [9].

Nevertheless, SCs are still plagued with the challenge of low specific energy as compared to batteries and this has delayed its use as a primary power source of energy storage in

applications requiring high energy as well as high power. Enormous efforts are being pooled together by scientists to increase their specific energies in a bid to increase their large-scale industrialization. Supercapacitors can be divided into three types based on the energy storage mechanism namely; (a) Electric double-layer capacitors (EDLCs), (b) Pseudocapacitors (PCs) and (c) Hybrid capacitors (HyCs).

EDLCs are the most common types of SCs which have been extensively studied and are based on the development of a capacitive charge (in the order of 10^6 F) at the electrode/electrolyte interface [10]. Generally, carbon based materials range from three dimensional (3D) carbons to two dimensional (2D) graphene materials, one dimensional (1D) carbon nanotubes (CNTs) and zero dimensional (0D) carbon nano-onions. They are the most common electrode materials used in EDLC due to their unique physical and chemical properties. Carbon-based materials display high conductivity, relatively low cost, good corrosion resistance, high specific surface area and a proper pore size control [11]. Although, some porous carbon based materials have been known to possess a lower conductivity which restrict their application in high power density supercapacitors [12,13].

Graphene has a unique morphology composed of a single-layered 2D lattice structure of carbon atoms. Graphene is revealed as a promising carbon material for designing and fabricating high-performance supercapacitors due to its unique structure and high theoretical specific surface area [14]. Graphene combines its chemical stability, good mechanical strength and high electrical conductivity similar to the CNTs.

In comparison, graphene has been reported to provide a higher electrochemical performance (in terms of the specific energy) than CNTs of up to 85.6 Wh kg^{-1} [14]. Graphene presents a diverse variety based on the different chemical structures and morphologies. 2D carbons also exist as graphite and one way to prepare it is by expansion using microwave to increase its surface area.

For instance, the expanded graphite (EG) synthesized generally by microwave technique have been also examined as a suitable electrode materials for SCs. The activation of the EG leads to the creation of a large fraction of micro - and mesopores which can improve the specific capacitance in aqueous, organic and ionic liquid electrolytes by presenting better and accessible surface area for charge accommodation [15,16].

Faradaic materials are based on redox reactions on the material surface area which governs the nature of charge storage. The Faradaic electrochemical processes arise both on the surface and in the bulk near the surface of the electrode [17]. Thus, Faradaic materials displayed a crucial role in simultaneously delivering high specific capacity and energy which is the setback in energy storage devices [18]. Pseudocapacitors are very much different from EDLCs in their nature of charge storage in that they are governed by a chain of Faradaic reactions [19] and store energy through fast redox reaction [20]. Although the nature of charge storage is seen electrochemically to be similar to pure double layer capacitance which gives it the name "pseudo". The reversible redox reaction at the surface of the electrode contributes more storage charge to supply a higher capacitance than the EDLC materials.

Transition metal oxides, transition metal hydroxides (TMOs/TM-OHs) and conducting polymers are considered as the common examples of faradaic and pseudocapacitive materials. Transition metal oxides have proved to exhibit stable nanostructure, low preparation cost and high theoretical capacity as compared to carbon-based materials [21] due to their ability to exist in variable oxidation states [22].

In comparison with TM-OHs, the transition metal oxide exhibited higher specific capacity than transition hydroxides due to their low specific surface area and their poor electrical conductivity [23]. The transition metal oxides have also a specific capacity superior to conducting polymers [24]. Examples of pseudocapacitive and faradaic are RuO_2 [25], MnO_2 [26], CoO_x [27], NiO [28], V_2O_5 [29], VO_2 [30] among others.

Numerous efforts have been developed to find lower cost metal oxides due to the relatively high cost of ruthenium (RuO_2) [29]. Amongst the numerous transition metal oxides, vanadium oxides have been reported as a potential low cost materials for device electrodes [31]. Vanadium oxide (V_xO_y) has received massive interest among researchers as supercapacitor electrodes due to its multiple oxidation states (from V^{2+} to V^{5+}). Among the various vanadium oxides, vanadium pentoxide (V_2O_5) and vanadium dioxide (VO_2) are mostly adopted in SCs due to their unique physical and chemical properties suitable for energy storage [32–34].

However, these transition metal oxide such as vanadium oxide present a poor conductivity and cycle life [16,23], while carbon based materials still suffer from low specific energy typically 3 - 5 Wh kg^{-1} [20] due to their relatively low specific capacitance as compared to faradaic-type materials. Faradaic type-materials materials on the other hand have low conductivities and poor cyclic stability which limits their application as suitable supercapacitor electrodes. Thus, attempts are made to incorporate different carbon based materials into the faradaic materials to form composite materials in a hybrid capacitor configuration.

Hybrid capacitors (HyCs) are structured by combining two different electrodes materials such as EDLC and faradic materials to function as a better unit. When the faradaic material are generally used as a positive electrode and the EDLC material as a negative electrode, a subclass called an asymmetric device is formed. HCs have been developed to solve the limitations of both EDLCs and Faradaic materials in order to improve the specific energy, extend the cell voltage, cycling stability of the cell among others.

On the other hand, the low specific capacitance of the carbon based materials could affect the device performance for asymmetric capacitors when adopted as a negative electrode material. The investigation of novel and electrochemically enhanced negative materials to design better

performing hybrid supercapacitors has become a recent research hot topic. Some metal oxides such as molybdenum oxide (MoO_{3-x}) and iron oxide (Fe_xO_y) are used as a negative electrode in SCs and are reported to deliver a specific energy higher than carbon based materials, however, their disadvantages such as low conductivities and poor cyclic stability can limit their applications [35].

Vanadium nitrides (VNs) are promising candidates for the negative electrode in SCs due to their unique physico-chemical properties [36]. VN exhibits a good electronic conductivity, chemical stability and a large operating window in the negative potential. However, the use of VN material as a supercapacitor device electrode is limited due to its poor rate performance and cycling life [37,38].

Vanadium oxynitride has been established to solve the issues of VNs to make them suitable for high-performance SC devices. Recently, Shu *et al*. [39] reported the adoption of vanadium oxynitride incorporated with carbon and has been demonstrated to display an even better electrochemical performance than vanadium oxynitride [39].

1.2 Aims and Objectives

The aim of this research study is to synthesize vanadium oxide-based composites with different nanostructures and evaluate their potential applications as supercapacitor electrode materials.

The research objectives are as follows:

- Synthesis of graphene foam (GF) via chemical vapor deposition technique (CVD)
- Preparation of V_2O_5 and V_2O_5/GF composites using hydrothermal and freeze-drying techniques
- Study of the effect of growth time on solvothermal method of VO_2 monoclinic with time-dependent morphological evolution
- Synthesis of carbonized iron-polyaniline (C-FP) via CVD technique
- Evaluation of the VO_2//C-FP device as a high specific energy asymmetric supercapacitor
- Synthesis of porous web-like carbon-vanadium oxynitride (C-V_2NO) using CVD method
- Investigation of the C-V_2NO//C-V_2NO device as a high specific energy symmetric supercapacitor
- Preparation of VO_2 and VO_2/AEG composite via CVD method
- Evaluation of the VO_2/AEG//C-V_2NO for high performance asymmetric supercapacitor

1.3 Structure of the thesis

The thesis is divided into five chapters:

Chapter 1 presents a general background introduction and motivation of this research study, aim and objectives with a brief structural layout of the thesis

Chapter 2 presents a literature review on for electrochemical capacitors.

Chapter 3 describes the details of the synthesis procedures and characterization techniques used in this work.

Chapter 4 presents the research results obtained accompanied with a summary of the conclusion from each results.

4.1 Three dimensional vanadium pentoxide/graphene foam composite as positive electrode for high performance asymmetric electrochemical supercapacitor.

4.2 Effect of growth time on solvothermal synthesis of vanadium dioxide for electrochemical supercapacitor application.

4.3 High-performance asymmetric supercapacitor based on vanadium dioxide and carbonized iron-polyaniline electrodes

4.4 Generation of a mesoporous web-like carbon-vanadium oxynitride as a novel electrode material for symmetric supercapacitors

4.5 High-performance asymmetric supercapacitor based on vanadium dioxide/activated extended graphite composite and carbon-vanadium oxynitride nanostructures.

Chapter 5 presents the general conclusion drawn from the PhD study and the proposed future research work to be performed.

Bibliography

[1]   G. Tegart, Energy and nanotechnologies: Priority areas for Australia's future, Technological Forecasting and Social Change. 76 (2009) 1240–1246.

[2]   X. Chen, R. Paul, L. Dai, Carbon-based supercapacitors for efficient energy storage, National Science Review. 4 (2017) 453–489.

[3]   F. Bonaccorso, L. Colombo, G. Yu, M. Stoller, V. Tozzini, A.C. Ferrari, R.S. Ruoff, V. Pellegrini, Graphene, related two-dimensional crystals, and hybrid systems for energy conversion and storage, Science. 347 (2015) 1246501–1246501.

[4]   Z. Zhu, S. Tang, J. Yuan, X. Qin, Y. Deng, R. Qu, G.M. Haarberg, Effects of Various Binders on Supercapacitor Performances, Int. J. Electrochem. Sci. 11 (2016) 8270–8279.

[5]   U. Bavaskar, A. Khare, M. Scholar, Design Wind Power Generation System Using Supercapacitor for Enlarge Battery Lifetime, © 2018 IJEDR |. 6 (2018).

[6]   H. Kim, K.-Y. Park, J. Hong, K. Kang, All-graphene-battery: bridging the gap between supercapacitors and lithium ion batteries, (2014).

[7]   Y. Huang, S.L. Candelaria, Y. Li, Z. Li, J. Tian, L. Zhang, G. Cao, Sulfurized activated carbon for high energy density supercapacitors, Journal of Power Sources. 252 (2014) 90–97.

[8]   P. Simon, Y. Gogotsi, Materials for electrochemical capacitors, Nat. Mater. 7 (2008) 845–854.

[9]   R.R. Salunkhe, J. Tang, Y. Kamachi, T. Nakato, J. Ho Kim, Y. Yamauchi, Asymmetric Supercapacitors Using 3D Nanoporous Carbon and Cobalt Oxide Electrodes Synthesized from a Single MetalÀOrganic Framework, 17 (2018) 40.

[10] M. Jayalakshmi, K. Balasubramanian, J. Mandapati, N. Materials, T. Development, J. Mandapati, Simple Capacitors to Supercapacitors-An Overview, Int. J. Electrochem. Sci. 3 (2016) 1196–1217.

[11] L.L. Zhang, X.S. Zhao, Carbon-based materials as supercapacitor electrodes, Chemical Society Reviews. 38 (2009) 2520.

[12] Y. Huang, J. Liang, Y. Chen, An Overview of the Applications of Graphene-Based Materials in Supercapacitors, Small. 8 (2012) 1805–1834.

[13] A.G. Pandolfo, A.F. Hollenkamp, Carbon properties and their role in supercapacitors, Journal of Power Sources. 157 (2006) 11–27.

[14] C. Liu, Z. Yu, D. Neff, A. Zhamu, B.Z. Jang, Graphene-Based Supercapacitor with an Ultrahigh Energy Density, (2010).

[15] T. Kim, G. Jung, S. Yoo, K.S. Suh, R.S. Ruoff, Activated Graphene-Based Carbons as Supercapacitor Electrodes with Macro- and Mesopores, ACS Nano. 7 (2013) 6899–6905.

[16] F. Barzegar, A. Bello, D. Momodu, M.J. Madito, J. Dangbegnon, N. Manyala, Preparation and characterization of porous carbon from expanded graphite for high energy density supercapacitor in aqueous electrolyte, Journal of Power Sources. 309 (2016) 245–253.

[17] G. Wang, L. Zhang, J. Zhang, A review of electrode materials for electrochemical supercapacitors, Chem. Soc. Rev. 41 (2012) 797–828.

[18] X. Peng, L. Peng, C. Wu, Y. Xie, Two dimensional nanomaterials for flexible supercapacitors, Chemical Society Reviews. 43 (2014) 3303.

[19] H. Li, B. Wang, X. He, J. Xiao, H. Zhang, Q. Liu, J. Liu, J. Wang, L. Liu, P. Wang,

Composite of hierarchical interpenetrating 3D hollow carbon skeleton from lotus pollen and hexagonal MnO_2 nanosheets for high-performance supercapacitors, J. Mater. Chem. A. 3 (2015) 9754–9762.

[20] C. Xiang, M. Li, M. Zhi, A. Manivannan, N. Wu, A reduced graphene oxide/Co_3O_4 composite for supercapacitor electrode, Journal of Power Sources. 226 (2013) 65–70.

[21] M. Zhi, C. Xiang, J. Li, M. Li, N. Wu, Nanostructured carbon–metal oxide composite electrodes for supercapacitors: a review, Nanoscale. 5 (2013) 72–88.

[22] E. Umeshbabu, G. Ranga Rao, Vanadium pentoxide nanochains for high-performance electrochemical supercapacitors, Journal of Colloid and Interface Science. 472 (2016) 210–219.

[23] J.P. Cheng, J. Zhang, F. Liu, Recent development of metal hydroxides as electrode material of electrochemical capacitors, RSC Adv. 4 (2014) 38893–38917.

[24] C. Peng, S. Zhang, D. Jewell, G.Z. Chen, Carbon nanotube and conducting polymer composites for supercapacitors, Progress in Natural Science. 18 (2008) 777–788.

[25] B. Rong-Rong, W. Xing-Long, C. Fei-Fei, J. Ling-Yan, G. Yu-Guo, Wan Li-Jun, Highly Dispersed RuO_2 Nanoparticles on Carbon Nanotubes: Facile Synthesis and Enhanced Supercapacitance Performance, The Journal of Physical Chemistry C. 114 (2010) 2448–2451.

[26] H. Jiang, C. Li, T. Sun, J. Ma, A green and high energy density asymmetric supercapacitor based on ultrathin MnO_2 nanostructures and functional mesoporous carbon nanotube electrodes, Nanoscale. 4 (2012) 807–812.

[27] J. Zhu, L. Huang, Y. Xiao, L. Shen, Q. Chen, W. Shi, Hydrogenated CoO_x nanowire@$Ni(OH)_2$ nanosheet core–shell nanostructures for high-performance

asymmetric supercapacitors, Nanoscale. 6 (2014) 6772.

[28]   J.-W. Lang, L.-B. Kong, W.-J. Wu, Y.-C. Luo, L. Kang, Facile approach to prepare loose-packed NiO nano-flakes materials for supercapacitors, Chemical Communications. 104 (2008) 4213.

[29]   L.-M.M. Chen, Q.-Y.Y. Lai, Y.-J.J. Hao, Y. Zhao, X.-Y.Y. Ji, Y.Z. Lian-Mei Chen, Qiong-Yu Lai, Yan-Jing Hao, Xiao-YangJi, Investigations on capacitive properties of the AC/V2O5 hybrid supercapacitor in various aqueous electrolytes, Journal of Alloys and Compounds. 467 (2009) 465–471.

[30]   W. Xiao, Asymmetric Capacitor Based on Vanadium Dioxide/Graphene/Nickle and Carbon Nanotube Electrode, University of Akron, 2014.

[31]   C.-C. Hu, C.-M. Huang, K.-H. Chang, Anodic deposition of porous vanadium oxide network with high power characteristics for pseudocapacitors, Journal of Power Sources. 185 (2008) 1594–1597.

[32]   J. Zhu, L. Cao, Y. Wu, Y. Gong, Z. Liu, H.E. Hoster, Y. Zhang, S. Zhang, S. Yang, Q. Yan, P.M. Ajayan, R. Vajtai, Building 3D Structures of Vanadium Pentoxide Nanosheets and Application as Electrodes in Supercapacitors, Nano Letters. 13 (2013) 5408–5413.

[33]   M. Lee, B.-H. Wee, J.-D. Hong, High Performance Flexible Supercapacitor Electrodes Composed of Ultralarge Graphene Sheets and Vanadium Dioxide, Advanced Energy Materials. 5 (2015) 1401890.

[34]   Y. Oka, T. Yao, N. Yamamoto, Powder X-ray crystal structure of $VO_2(A)$, Journal of Solid State Chemistry. 86 (1990) 116–124.

[35]   X. Lu, M. Yu, T. Zhai, G. Wang, S. Xie, T. Liu, C. Liang, Y. Tong, Y. Li, High Energy

Density Asymmetric Quasi-Solid-State Supercapacitor Based on Porous Vanadium Nitride Nanowire Anode, Nano Letters. 13 (2013) 2628–2633.

[36]   R. Wang, X. Yan, J. Lang, Z. Zheng, P. Zhang, A hybrid supercapacitor based on flower-like $Co(OH)_2$ and urchin-like VN electrode materials, J. Mater. Chem. A. 2 (2014) 12724–12732.

[37]   B. Gao, X. Li, X. Guo, X. Zhang, X. Peng, L. Wang, J. Fu, P.K. Chu, K. Huo, Nitrogen-Doped Carbon Encapsulated Mesoporous Vanadium Nitride Nanowires as Self-Supported Electrodes for Flexible All-Solid-State Supercapacitors, Advanced Materials Interfaces. 2 (2015) 1500211.

[38]   S. Ghosh, S.M. Jeong, S.R. Polaki, A review on metal nitrides/oxynitrides as an emerging supercapacitor electrode beyond oxide, Korean Journal of Chemical Engineering. 35 (2018) 1389–1408.

[39]   D. Shu, H. Cheng, C. Lv, M.A. Asi, L. Long, C. He, X. Zou, Z. Kang, Soft-template synthesis of vanadium oxynitride-carbon nanomaterials for supercapacitors, International Journal of Hydrogen Energy. 39 (2014) 16139–16150.

_____

2.0 Literature Review

2.1 Energy Storage Systems

Energy storage systems such as lead–acid batteries, nickel–metal hydride batteries, lithium-ion batteries (LiBs) and supercapacitors (SCs) have attracted global consideration [1].

LiBs and SCs are the most commonly used energy storage systems and are composed of an assembly of two electrodes in contact with an electrolyte solution which allows for ionic conduction [2]. Some fundamental parameters used to determine the performance and relevance of these two energy storage devices for a specific application is the specific energy (E_d), specific power (P_d), charge- and discharge time and cycle life [3].

Lithium-ion batteries are considered the mobile power sources for portable electronic devices, exclusively used in cell phones and laptop computers [4]. They are constructed with a porous material as an anode (source of lithium ions) and a metal oxide as a cathode (sink for the lithium ions) with an electrolyte which provide the internal ionic transport between the electrodes. There are generally two mechanisms for active Li-ion storage: storage of Li ions in the bulk (volume) of the material through intercalation or insertion reactions and storage of Li ions at the intercalated material surface [4–6]. However, LiBs have the potential to store high specific energy and their biggest disadvantage are their low specific power and poor charge-discharge cycles [7,8].

Supercapacitors also called electrochemical supercapacitors (ESs) or electrochemical capacitors (ECs) have the ability to deliver high specific power with a charge-discharge capability ranging up to a millions times [9].

However, ESs provide lower specific energy than LiBs and higher than conventional capacitors [10]. Table 2.1 outlines a comparison of the two energy storage technologies based on vital parameters which define the type of application they can be used for. Supercapacitors have the capability to deliver a higher specific power, fast charge-discharge within seconds and a long lifetime and life span than lithium-ion batteries [11]. SCs also are environmental friendly, low-cost and great operating temperature range as compared to LiBs [12,13].

Table 2. 1: Comparison between supercapacitor and batteries devices [14–18].

Parameters	Supercapacitors	lithium-ion Batteries
Charge time	1 - 30 seconds	1 - 5 hours
Discharging time	1-30 seconds	0.3 hour
Lifetime (charge-discharge cycles)	1 million	1000
Specific energy (Wh kg^{-1})	1-10	10 - 100
Specific power (W kg^{-1})	10 000	< 1000
Safety	Safe	Less safe
Lifespan	10 - 20 years	~ 5 years
Operating temperature range	~ - 40 to + 65 °C	~ 0 to + 40 °C

The merits make supercapacitors garner great potential as a suitable energy storage device. However, the major hurdle of SCs is still related to their lower specific energy values [19].
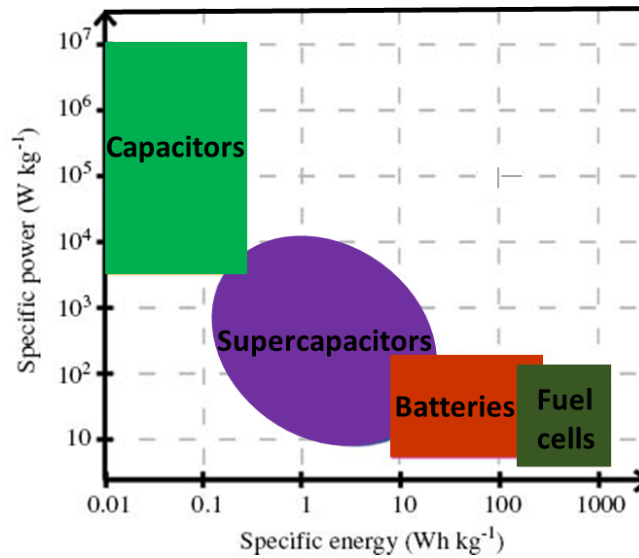
Figure 2.1: Ragone plot for different electrochemical energy storage devices [20].

Figure 2.1 displays the comparison of the specific energy versus the specific power for different energy storage devices in a format called a "Ragone plot". It is clearly evident that capacitors are incapable of delivering a high specific energy due to the electrostatic charge storage mechanism while batteries and fuel cells exhibit a low specific power owing to the chemical/ionic nature of their charge storage mechanisms [21]. Supercapacitors are seen to bridge the gap between conventional capacitors and batteries by incorporating elements of both storage technologies [22]. Thus, recent interests by numerous materials researchers have been focused on improving the energy storage capacity through the re-design of supercapacitors (materials, electrolytes) to simultaneously deliver both a high power and energy [19,23]. Several method or techniques have been used to enhance the specific energy of SCs by focusing on the new electrode design or the electrolyte, and great progress has made in this field [21,24,25]. The capacitor system has been known for many years and was initially developed by Becker in 1957 where the first electrochemical capacitor was fabricated using carbon as an electrode material and a sulphuric acid electrolyte to establish the charge storage [26].

This technology was commercialized in 1969 by the company (known as SOHIO) for manufacturing power saving units in electronics [27]. However, the term "supercapacitors" was coined from the first company which commercialized a SuperCapacitor^{TM} device in 1971. Their most popular success was reported in 1990 with the aid of US government funded programs. The aim of the project was to incorporate SCs into hybrid vehicle systems for delivering a power sufficient for acceleration [28,29]. Studies have shown that the use of supercapacitors can lead to a potential decreased fuel consumption of up to 15% - 20% in automobile applications [14].Recently, the SC-technology has been extensively exploited to meet the ever-increasing demand of modern applications requiring an instant specific power supply [1] and peak power saving [30].

SCs have been successfully integrated into different areas of the manufacturing industry such as in portable electronic devices [31], aviation industry [32], medical industry [33], military applications [34], transport services (for hybrid electric vehicles, trains, buses, light rail systems, trams, aerial lifts, forklifts, and even motor-racing cars) [35–38], energy recovery and renewable energy technologies [39]. The notable and most recent supercapacitor application was reported for the emergency doors on the Airbus A380, highlighting their safe and reliable performance [40]. Other areas include the digital camera [41], UPS [42], robotic [43] and windmill [44] where supercapacitors play also the role to store the energy for braking or to power the starter motor on engine start-up [43,45].

2.2 Evaluating the performance of supercapacitors

The performance of supercapacitors are mainly dependent on various electrochemical parameters such as the specific capacitance (which can be normalized by the mass, area or volume of the active material electrode), the rate capability at high specific current values and the stability of the electrode over cycling or potentiostatic floating tests [46].

The two primordial characteristics of any energy storage device are the specific energy and specific power. The specific energy defines the amount of energy (per unit mass, area or volume) that can be stored while the specific power describes how quickly the device can deliver that specific energy. The specific energy in terms of the mass (E in W h kg^{-1}) and the maximum specific power (P_{max} in W kg^{-1}) in SCs are obtained by using the equations $1 - 2$ as:

$$\mathrm{E} = \frac{1}{2} C_{sp} V^2 \tag{1}$$

$$P_{max} = \frac{V^2}{(4mR)} \tag{2}$$

where C_{sp} (in F g^{-1}) is the total specific capacitance for a constant applied current, V (in V) is the operating device potential, m is the total mass of the two electrodes and R_s (in Ω) is the equivalent series resistance (ESR) of the cell which is the total resistance of the electrode resistance, electrolyte resistance and the resistance of the diffusion of the ion in the electrode pores. To obtain a good electrochemical performance in a supercapacitor, an enhanced specific energy and specific power is required. It is preferable to improve the specific capacitance, maximize the cell voltage and also to control the ESR value to a minimum value possible [47,48].

2.3 Classification of Supercapacitors

Supercapacitors are divided into mainly three types based on their energy storage mechanism namely;

- Electric double-layer capacitors (EDLC) arising from the accumulation of charges at the electrode/electrolyte interface and

- Faradaic capacitors and/or pseudocapacitors which is related to the storage from fast redox reactions

- Hybrid capacitors are the combination of the individual characteristic of both EDLC and faradaic electrodes and can be structured in different architectures to form other subgroups.

The performance of Supercapacitors are largely controlled by the energy storage mechanism, the electrode material used, the electrolyte and device assembly [49,50]. A plot illustrating the types of supercapacitors is shown in Figure 2.2 and will be discussed separately in this section.
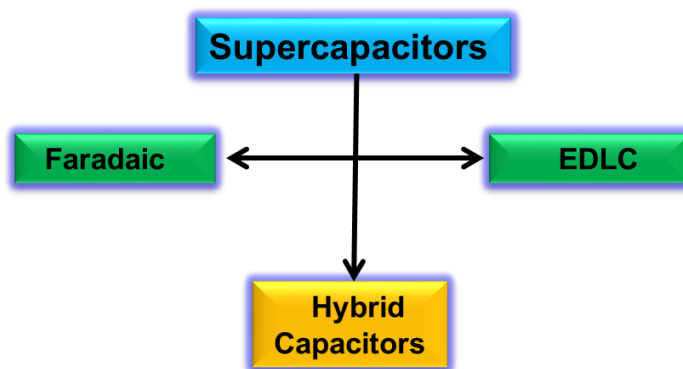
Figure 2.2: Classification of supercapacitors: EDLC, faradaic and their combination to form hybrid capacitors**.**

2.4 Energy storage mechanism of supercapacitor

2.4.1 Electric double-layer capacitance (EDLC)

Electric double-layer (EDL) capacitors usually store their energy by means of an electrical double layer. This electrical phenomenon appears at the interface between a conductive electrode and an adjacent liquid electrolyte if a voltage is applied. For instance in EDLC capacitors, two layers of ions of opposite polarity are aligned at the surface of the electrode in the electrolyte. This dual surface layer of ions is separated by a single layer of solvent molecules that adhere to the surface of the electrode so that a net charge separation can be maintained.

The concept of EDLC was discovered by von Helmholtz in the 19th century and is well-known as the "***Helmholtz double layer***" model [48,51].

The Helmholtz double layer model describes the existence of two layers of opposite charge form which condense at the electrode/electrolyte interface and are separated by an atomic distance as shown in Figure 2.3 (a). This structure is similar to the conventional dielectric capacitors with two planar electrodes separated by a small distance [52]. The capacitance estimation for an EDLC is generally calculated using equation 3;

$$C = \frac{\varepsilon_r \varepsilon_o A}{d} \tag{3}$$

where ε_r is the electrolyte permittivity, ε_o is the dielectric constant or permittivity of vacuum, A is the active material surface area, and d is the distance of the charge separation or effective thickness of the double-layer.

This model was thereafter modified by Gouy and Chapman (in Figure 2.3 (b)) with the consideration of a diffusion layer due to the continuous distribution of electrolyte ion (both cations and anions) in the electrolyte determined by thermal motion [53].
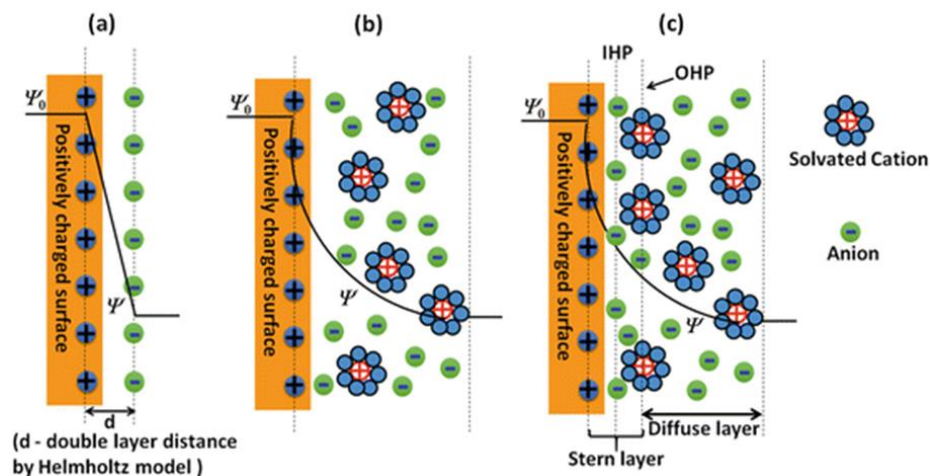
Figure 2.3: Different models of the EDLC at a positively charged surface: (a) the Helmholtz model, (b) the Gouy–Chapman model, and (c) the Stern model [54].

Unfortunately, the Gouy and Chapman model leads to an overestimation of the EDL capacitance and was improved in 1924 with the Stern model which was developed by Otto Stern [55].

The Stern models (in Figure 2.3 (c)) combines the Helmholtz models with the Gouy-Chapman model by distinguishing two regions of ion distribution; the outer region identified as the Gouy-Chapman diffuse layer (OHP) and an inner region (IHP) referred to as the compact layer or Stern layer. The total capacitance in the EDLC (C_S) can be considered as a union of the capacitances from these two regions, the Stern type of compact double layer capacitance (C_H) and the diffusion region capacitance (C_{Diff}) and is expressed as [55];

$$\frac{1}{C_S} = \frac{1}{C_H} + \frac{1}{C_{Diff}}$$

(4)

For example, an EDLC device with two electrodes, A and B. The total capacitance can be evaluated as two capacitors in series with a combined capacitance. The total capacitance C_T of this device is calculated as:

$$\frac{1}{C_T} = \frac{1}{C_A} + \frac{1}{C_B}$$

(5)

where, $C_A = C_S \times A_{i,A}$ and $C_B = C_S \times A_{i,B}$, with A_i, is the surface area of the porous electrodes (A or B)

- $C_A = C_B$, for two identical electrodes and the total capacitance is equal to $C_A/2$.

- $C_A \langle\langle C_B$, hybrid devices with a pseudocapacitive electrode and the total capacitance is given by $C_A = C_T$.

Typical examples of EDLC-type materials are carbon-based materials like carbon spheres carbon nanotubes, carbon aerogels, activated carbons, graphite, carbon nanofibers, etc.

These materials provide large-surface area with good chemical stability and thin electrolytic dielectrics to achieve a reasonable capacitance. The electrochemical performance of EDLC-

type material can be improved by maximizing the total capacitance (C_T) using electrically conducting electrodes and by increasing the working potential (ΔV) of the electrodes [52]. This improvement is greatly influenced by the nature of the active material electrodes and operating electrolytes. Generally, the electrode material and the electrolyte are the key determinants to attain high performance EDL-capacitors.

2.4.2 Faradaic capacitors

Faradaic capacitors have been described as a particularly unique form of energy storage concept. This type of supercapacitor has a special class called pseudocapacitance (PC) by some scholars which is governed by a chain of Faradaic (redox) reactions and their behavior of the charge-discharge curve are near to that of EDLC electrode material surface [56–58]. The charge transfer process is characterized with a fast and reversible redox reaction at the surface of the active materials due to the interaction between the electrode and the electrolyte. They are very much different from the electrostatic type of charge storage in EDL systems. However, the faradaic processes present here has been described by applying the band modes for semiconductors to evaluate the origin of pseudocapacitors [59]. Currently, some transition metals oxides/hydroxides and conducting polymers are known to exhibit pseudocapacitive behaviour [60,61]. In particular, for some transition metal oxides, the advantage of possessing multiple oxidation states aids in increasing the specific capacities [39,62]. Therefore, these materials have the capacity to store a charge of the order of ten to hundred times as compared to carbon-based EDL-capacitors [56].

Charge storage in faradaic capacitors consists of three different mechanisms namely:

(a) underpotential deposition,

(b) redox reactions of transition metal oxides (for instance RuO_2 and Nb_2O_5 electrodes),

(c) intercalation (see Figure 2.4).

a) Underpotential Deposition

As indicated by the name, "underpotential deposition" corresponds to the electrodeposition of adsorbed monolayer(s) from metal ions present in an electrolyte onto the electrode surface of other metals (such as Au, Pt, Ag etc.) that are less electronegative as compared to the metal being deposited. A pictorial illustration is as shown in Figure 2.4 (a).
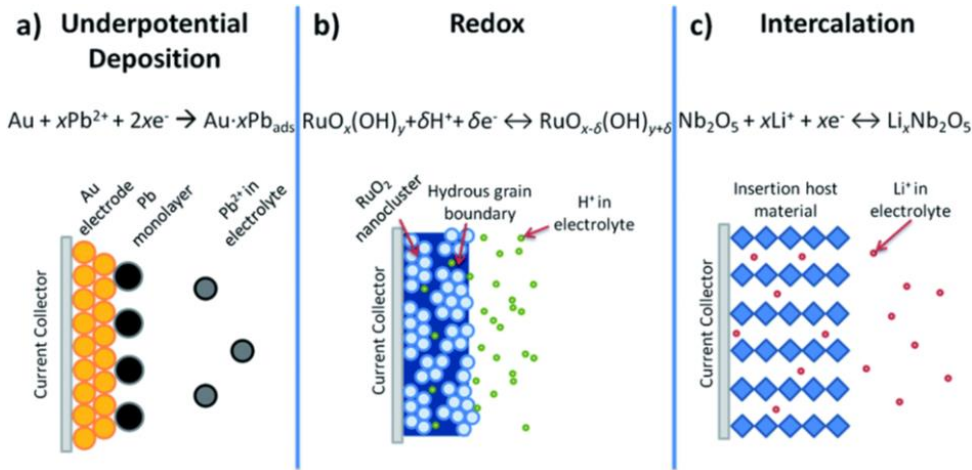
Figure 2. 4: Different types of reversible redox mechanisms in faradaic capacitors [63].

The active relationship adsorbed atom/substrate bonding between these two metals (atoms and substrates) could control the growth behavior and the resulting structures.

Thus, the reaction rates and the study of the surface coverage such as the nature of the metal layer and its electronic properties are crucial in this deposition [58,64].

b) Redox reactions

The charge transfer mechanism in redox reaction results in reduction-oxidation reactions of a faradaic nature. This redox reaction occurs between the electrode and electrolyte changing the oxidation state of the metal. For instance, the redox reaction of RuO_2 is the acceptance (reduction) and release (oxidation) of the protons in the electrolyte.

However, the oxidation reaction modifies the oxidation state of the RuO_2 from +4 to +3 due to the absorption of the ion onto the surface of the material. The low temperature of the synthesis of this material makes the oxidation of the support and possible processes of inter-

diffusion at the solid interface negligible [65,66]. Figure 2.4 (b) shows the illustration of the chemical process and the reaction of the metal oxide.

c) Intercalation

This mechanism is the insertion of an ion into the bulk lattice of the redox active material associated with a faradaic charge transfer as shown in Figure 2.4 (c). To maintain the electrical neutrality of the electrode, a number of electrons should be transferred to the host during insertion. A suitable reducing agent, the presence of Van der Waals gaps (unpopulated spaces), the conservation of the orientation of the elements in the lattice and the existence of the low lying bands in the host facilitate the process of insertion/removal of the intercalation mechanism [66].

2.4.3 Hybrid materials and hybrid capacitors

2.4.3.1 Hybrid materials (HMs)

The electrode materials in supercapacitors play a vital role in determining its performance. The favourable characteristics when using electrochemically active material in the form of a composite design has been considered as a promising solution to provide the desired high specific energy. Hybrid architectures in the form of composite materials have been developed to efficiently merge the two main charge storage mechanisms to coexist as a single unit at the materials level. Most composite materials are comprised of an EDLC and a faradaic nature in a single electrode. HMs have the capacity to offer a broad range of merits for preeminent supercapacitor systems by providing significant improvements in the morphological, textural and electrochemical properties.

In hybrid materials, carbon-based materials have the power to increase the electrical conductivity, thermal conductivity, SSA, pore size distribution and impact strength while the faradaic materials play the role to improve the surface reactivity thereby enhancing the specific capacity of the materials [67−69].

Thus the as-synthesized composite has a synergetic combination of individual properties from the different materials with an increase contact between the electrode and the electrolyte for a good performance in supercapacitors [70]. The carbon-based EDLC materials used for composite electrode are generally carbon nano-onion [71], carbon nanotubes [72], activated carbon [73], graphene [74] and other carbon forms [75]. The composite materials can simultaneously have a high specific energy and high specific power from the faradaic materials and the carbon-based materials respectively [50].

However, an optimized mass ratio of the EDLC materials is required to maximize the performance and the synergistic properties of the nano-carbon/metal oxide composite [76,77].

2.4.3.2 Hybrid capacitors (HCs)

Recently, hybrid capacitor (HCs) are the subject of intense research in energy storage system. HCs have been considered as a novel concept for considering workable configurations which involves combining a faradaic electrode with a non-faradaic material electrode (usually electric double layer type) in the same cell. The research focus on this class of energy storage devices is geared to enhance the electrochemical performance of the supercapacitor by tapping into the merits of both charge storage mechanisms. As a result, the limitations encountered individually in both EDLCs and faradaic materials will be solved leading to high performance supercapacitors [78]. Based on the electrode structure, HCs can be classified into two different types: asymmetric and battery-like hybrids:

a) Asymmetric supercapacitor

The low specific energy in supercapacitors is known to be the drawback limiting its suitability for potential applications in high-energy storage systems. To improve this energy without sacrificing the specific power and cycle life is deeply desirable for device performance. An asymmetric supercapacitor has been demonstrated to be a promising approach to increase the specific energy [79], high specific power and good cycling stability [50]. The configuration of

an asymmetric device comprises of two different types of electrodes: faradaic and EDLC material electrodes. These different electrodes work in the same electrolyte with different electrochemical potential window ranges that could combine the intrinsic properties of each material to extend the device voltage in order to increase the specific energy of the supercapacitors. In asymmetric supercapacitors, EDLC-type (mainly carbon-based) materials are generally used as the negative electrodes and faradaic-type (mainly metal oxides and conducting polymers) materials as the positive electrodes. The EDLC materials are characterized with a high surface area, good electronic conductivity and good chemical/cyclic stability [51,80]. On the other hand, Faradaic materials have fast reversible redox reactions which aids in efficient power delivery [50]. The asymmetric device could provide a large specific energy with a high specific power for stable supercapacitors.

b) Rechargeable battery-type capacitors

This subclass of hybrid capacitors are quite different in operation characteristics from the asymmetric capacitors. The rechargeable battery-type devices entails the incorporation of an EDLC electrode with a battery-type material. The full-cell in this device is comprised of a Li-ion-active material as a positive electrode and an electrochemical double layer capacitance (EDLC) material as a negative electrode. The hybridization of the battery and supercapacitor electrodes leads to the steady redox reaction potential of the battery.

A large surface area, good charge transfer properties associated with a high electrical conductivity and short ion diffusion length is achievable for the hybrid device. The charge and discharge process of the rechargeable battery is governed by faradaic and EDLC mechanisms as a step process. Thus, the amount of the energy stored could be increased with a high rate [81] which requires a good electrode material capacity compatibility [50].

2.5 Electrodes materials for supercapacitor

Among the component of the full supercapacitors system, the electrodes have the main role which can influence the charge storage of the supercapacitor. The electrode material's properties in supercapacitors arise from a combination of chemical and physical properties such as large specific surface area (1 to > 2000 m^2 g^{-1}), high conductivity, high-temperature stability, good corrosion resistance, controlled pore structure, process ability, compatibility as well as low cost are strongly desired [50,82]. The suitable electrodes materials used in supercapacitors are carbon-based materials, conducting polymer and transition metal oxide and metal hydroxide [83,84].

2.5.1 Electrodes materials for electric double layer capacitors

Carbon-based electric double layer capacitor materials continues to be at the forefront of nanoscience and nanotechnology due to their different physical and chemical properties including electrical transport, chemical reactivity, optical and thermal properties depending on their unique structures [85].

Carbon materials have been extensively explored in supercapacitor applications at the laboratory scale and industrially due to their low cost, nontoxicity, and easy availability [86]. The key parameters which govern their adoption in electrochemical energy storage are the pore-size distribution, specific surface area (up to 3000 m^2 g^{-1}), electrical conductivity and surface functionality [87].

Carbon onion, carbon nanotubes, graphene, activated carbons, and expanded graphite are the commonly used EDLC electrode materials in supercapacitors.

a. Carbon nano-onions

Carbon nano-onions (CNOs) are zero-dimensional and belong to the fullerene family, which consist of concentric fullerene-like shells that range from double- and triple-shelled to multi-layered shells forming encapsulated structures [88,89]. Recently carbon nano-onions have

been demonstrated to be a potential material of interest for a variety of applications [90,91] including fuel cells [92], catalysis [93], electro-optical [94], solar cell [95] and energy storage devices [89,96] due to their unusual structure and special physical and chemical properties. In supercapacitors, CNOs are used as promising materials to achieve long cyclic stability and high specific power owing the layered and interconnected shell structure which are easily accessible to electrolyte ions [97]. This unique design of the CNOs however, limits the specific energy. Recently, Gao et al. [71] were successful to overcome this drawback by introducing porosity to the outer shells by chemical activation method. An improved specific energy was achieved by increasing the specific surface area of the carbon nano-onions [71].

b. Carbon nanotubes

Carbon nanotubes (CNTs) are considered as tubular carbon materials [98] with a graphitic structure which have unique features associated with important properties such as electronic, mechanical, optical, and chemical properties [51,98]. CNTs materials are divided into a two-class of materials which are single-walled (SWCNTs) and multi-walled nanotubes (MWCNTs). SWCNTs present a single graphene sheet wrapped into a cylindrical tube while MWCNTs show several arrays of nanotubes which are concentrically nested. They are one-dimensional materials with a mesoporous texture (i.e. the pore size distribution is between 2–50 nm) which promotes an easy ion diffusion when used in electrochemical devices [99].

CNTs can exhibit either a metallic or a semiconductor property depending on the orientation of the two-dimensional sheets of graphene rolled to form the tubular structure which lead to different configurations: armchair, zigzag, and chiral [100] as shown in Figure 2.5. CNTs possess high electrical conductivity, good chemical, and mechanical stability [101,102].

28
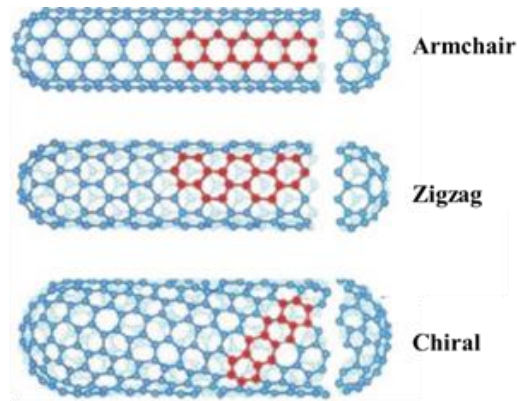
Figure 2.5: SWCNT showing the armchair, zigzag, and chiral configurations [100].

c. Graphene

Graphene is considered an emerging material of interest with fascinating properties relevant to the scientific and technological industry due to their unique physicochemical properties (physical, chemical, and electrochemical properties) [103–106]. Graphene is a single atomic thick two-dimensional (2-D) material composed of sp^2 hybridized carbons bonded in a hexagonal lattice [51,105]. Graphene has a high electrical conductivity combined with a high theoretical specific surface area (SSA) [107,108].

For instance, a monolayer graphene is semi-metallic with a thermal conductivity of ~ 3000 W mK^{-1}, a theoretical SSA of ~ 2600 m^2 g^{-1}, a high intrinsic strength of ~ 130 GPa, a transmittance of ~97.7%, and a high resistance to gas permeation. [103,109–114].
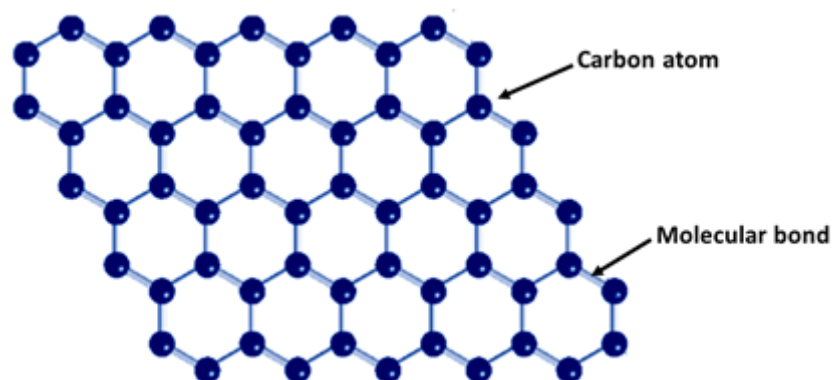
Figure 2.6: Schematic structure of a graphene sheet.

These properties make graphene suitable for many applications including and not limited to supercapacitors [115], batteries [116], fuel cells [117], solar cells [118], sensors [119], photonic devices [120], bioscience/biotechnologies [121,122] and electronics [123]. Several synthesis method of graphene has been largely proposed in the literature [103] with the first method developed by Novoselov *et. al*. [124] in 2004 which involved using a simple mechanical exfoliation technique also known as the scotch-tape method [124]. This preparation method is still widely used in many laboratories to produce few layer(s) of graphene to study their fundamental properties [125]. However, this method lacks the option for large scale [104,125]. Similarly, another synthesis route named the "mild exfoliation method" has also been used to prepare defect-free and high quality graphene [126,127] but also suffer for a low yield of graphene [128]. In order to deal with the yield problem associated with the exfoliation technique, Graphene has also been synthesized by using the chemical vapor deposition (CVD) method using gaseous hydrocarbon sources and a growth template such as ruthenium (Ru), nickel (Ni) and copper (Cu) [129]. Currently, the CVD technique is known to be the most efficient route to grow a large-area of single-layer 30 inch graphene [125].

For instance, Reina *et al*. [130] reported the preparation of large area films ($\sim$cm^2) with 1 to 12 layers using an ambient-pressure chemical vapor deposition (APCVD) method on polycrystalline Ni films. The graphene layer had good electrical and optical properties [130]. Similarly, Qin *et al.* [131] have successfully synthesized a large-area graphene film on Cu-substrates using the CVD growth method. The graphene film growth had a low carbon solubility in copper and a poor carbon saturation in nickel [131]. Kim *et al*. [132] synthesized a large-scale graphene films by using CVD method on Ni substrat. Their graphene film showed a sheet resistance of 280 Ω per square, with $\sim$80 per cent optical transparency [132].

Unfortunately, graphene materials presents two main limitations: the re-stacking of sheets which decreases the available surface for reactions and the low density from the 2-D structure of the material [133,134]. These problems are linked to the $\pi - \pi$ bond interaction between adjacent graphene sheets that reduces the specific surface area of the 2-D material. Consequently, pure graphene used as electrode materials in supercapacitors could display low specific capacitance values [135,136]. To avoid this drawback, other material have been incorporated into the graphene framework or gowned functional groups on the surface of the graphene to form composite materials with EDLC and faradaic materials for improving their surface reactivity in supercapacitor applications [137–140].

Other 2D nanomaterials have been discovered namely "*MXenes*'' which are a novel family of 2D transition metal carbides, nitrides and carbonitrides. MXenes are synthesized by selectively etching the A element layer of the MAX phase materials with $M_{n+1}AX_n$ chemistries, where "M" is an early transition metal, "A" is a group of IIIA and IVA elements, "X" is carbon or nitrogen, and n = 1, 2, or 3 [141]. MXenes have proven to be promising candidates for supercapacitors due to their high volumetric capacitance and good electrical conductivity with tunable transition metal oxide-like surface termination that can undergo redox reactions [142,143]. Similar to graphene, MXenes.nanosheets suffer from aggregation and face-to-face self-restacking during drying and electrode preparation processes owing to the strong van der Waals interaction between adjacent nanosheets.

In order to overcome this drawback, nickel–aluminum-layered double hydroxides, MnO_2 and carbon nanotubes (CNTs) have been introduced to form a hybrid materilas with MXenes [142].

d. Activated carbon

Activated carbons (ACs) are three-dimensional materials with a high specific surface area (SSA) and cost-effective synthesis procedure [144,145]. As such, they are widely applied as suitable electrode materials for EDL capacitors for both research and commercial purposes. Activated carbon can be generated from natural precursors such as wood, coal, plants or agricultural residues or from synthetic precursors such as polymers and phenolic resins. Typically, the high-cost of synthetic precursors make them less adopted with natural precursors more widely used due to their easy availability at a low cost for producing ACs [83,146–148]. Activated carbon can be prepared by either a physical activation (CO_2/steam) or a chemical activation process (KOH, K_2CO_3, H_3PO_4, and $ZnCl_2$ etc.) at different temperatures.

The pores created during the activation process aid in the storage of charges in electrochemical device applications. The evaluation of the pores size have shown that the development of smaller pores relative to the electrolyte ions could yield a poor contribution to the charge storage. Likewise, the large sizes of pores relative to the electrolyte ions can also lead to poor entrapment of electrolyte ions which can also be a limitation to the specific capacitance and the maximum specific power. Therefore, an optimum distribution of varying pore sizes is to provide the necessary pores suitable for efficient charge transport and storage. The large pore size including macropores (> 50 nm) and mesopores (2 - 50 nm) are more suitable for ion buffering and diffusion respectively while the micropores (< 2 nm) contribute to the charge adsorption and storage [149].

The diffusion phenomenon inside the pores of activated carbons could be associated with three diffusion mechanisms: (a) transportation of adsorbate molecules to the external AC surface, (b) diffusion of adsorbate molecules from the macropores to the mesopores and the

micropores and (c) adherence of the adsorbate molecules to the pore surface by weak van der Waals interactions.

The summarized illustration of these processes is presented in Figure 2.7. The diffusion process largely depends on the molecule size and the pore structure of the ACs [150].
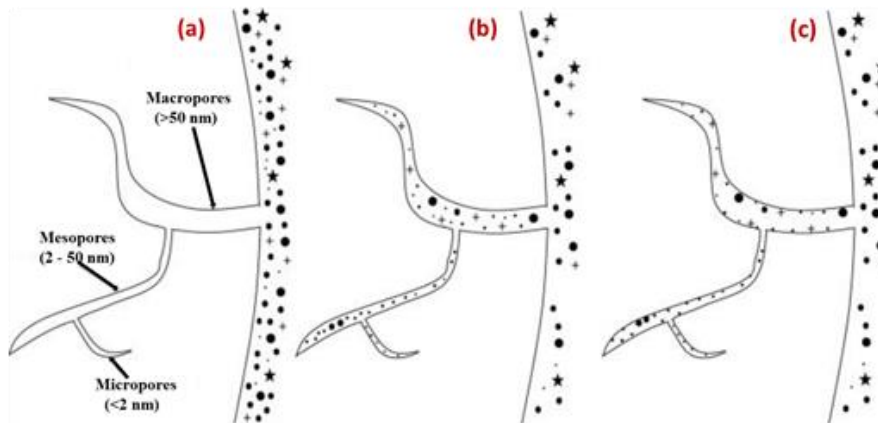
Figure 2.7: An illustration of adsorption in porous activated carbon [150].

e. Expanded graphite

Expanded graphite (EG) has been found to be an appropriate and interesting material for supercapacitors due to its excellent electrical conductivity, high SSA coupled with enhanced porosity and good chemical stability [151]. The expanded graphite are composed of nanosheet- structures which present a large interlayer spacing as compared to the natural graphite flakes [152,153]. These layers display excellent electrical conductivity (~ 290 S cm^{-1}) as well as good thermal and mechanical properties [154,155]. The EG materials have been demonstrated as a high potential candidate to improve the electrochemical performance of metal oxides [156]. For instance, Xu *et al.* [151] prepared a nickel oxide/expanded graphite (NiO/EG) nanocomposites by using chemical deposition of Ni(OH)$_2$ on the EG surface followed by thermal annealing. The NiO/EG composite electrode presented a good electrochemical performance in 6 M KOH as an electrolyte [151].

Recently, expanded graphite sheets were activated to increase its SSA and specific capacitance as suitable supercapacitor material electrodes [156–160].

2.5.2 Materials for Faradaic capacitors

Faradaic materials started to play a crucial role in supercapacitors ever since Brian Evan Conway conducted a large number of experiments using ruthenium oxide (RuO_2) as an electrode materials in 1971 [161,162]. Ruthenium oxide was the first metal oxide to exhibit pseudocapacitive behavior with a high electrochemical performance in water-based electrolyte associated to its change in oxidation state at 1.4 V [63,65,163]. However, the high cost of this metal oxide (currently at $\sim$2000 USD per kg) is an obstacle for large-scale exploration of the material and many efforts have been developed to find other lower cost transition metal oxides [63,163]. Faradaic materials such as transition metal oxides, transition metal hydroxides and conducting polymers are commonly used to achieve similar electrochemical performance.

2.5.2.1 Transition metal oxides/hydroxide

One of the most common family of materials used as supercapacitor electrode materials are the transition metal oxides/hydroxides (TMOs/TM-OHs) which store the charge by a reversible redox reactions [164]. In the design of supercapacitor electrodes, transition metal oxides [165,166], hydroxides [167,168], nitride [169,170], carbides [171,172]and oxynitride [173,174] have received great attention due to the mechanical, structural, and/or electronic properties [175]. These materials have the capability to offer high specific capacities owing to their multiple oxidation states. For example, metal hydroxides have shown high theoretical specific capacity and low cost [175,176]. However, their application suffers a low measured specific capacity and poor cycle stability which can be associated with their low specific surface area and poor electrical conductivity [175].

Transition metal oxides have received great attention as electrode materials and can be categorized into two types: the noble transition metal oxides such as RuO_2 and IrO_2 and the base transition metal oxides including MnO_2, V_2O_3, Co_3O_4, $NiCo_2O_4$, VO_2, V_2O_5, ZnV_2O_4, and so on. [49,177]. The noble metal oxides (specifically RuO_2) show an excellent electrochemical performance associated with a high specific capacity value although are limited by cost [1]. The base transition metal oxides are substantially cheaper and more environmental friendly than noble transition metals and are thus, considered to be the new research hotspot [177].

Amongst the low-cost metal oxides, vanadium oxides have received recent attention in supercapacitor applications as well as other large range of applications in the field of batteries, electronics, memory devices, electro-chromic and thermo-chromic applications and field emission displays [178,179]. Vanadium oxides exhibit higher charge storage capacity than most of the other transition metal oxides due to their earth abundance, the large stable oxidation states (V^{2+}, V^{3+}, V^{4+} and V^{5+}) and their layered structures [115,180]. Unfortunately, vanadium oxides still suffer from poor electrical conductivity and cyclic stability [181] in aqueous electrolytes when used as supercapacitor electrode materials [182]. This drawback is linked to the formation of the soluble species ($H_2VO_4^-$ or HVO_4^{2-}) and the structural degradation induced by repeated ion intercalation/de-intercalation. For example, *Yu et al.* [183] managed to successfully improve the cyclic stability behaviour of the vanadium oxide by tuning the oxidation state of vanadium. They used an electrochemical oxidation method to modify the V_2O_3. After the oxidation process, they obtained a vanadium oxide material with the presence of V^{3+}, V^{4+}, and V^{5+} [183]. With the advancement in research studies, recent reports have demonstrated that the electrochemical performance of the vanadium oxides depend strongly on the synthesis method, its morphology [62] and also the aqueous electrolyte used [184,185].

Vanadium pentoxide (V_2O_5) and vanadium dioxide (VO_2) are also two commonly studied transition metal oxides adopted as electrodes material in SCs. Several synthesis methods have been developed to prepare V_2O_5 or VO_2, such as hydrothermal synthesis [186], melt quenching method [187], solvothermal process [188], sol–gel method [189], pulsed-laser deposition [193], chemical vapor deposition [192].

a) Vanadium pentoxide (V_2O_5)

Vanadium pentoxide (V_2O_5) is the most promising vanadium-oxide based material reported as a supercapacitor electrode material in aqueous and organic electrolyte [82]. This is associated with the unique layered structures which promotes easy access of the ions and its wide operating potential window arising from the mixed oxidation states. The equivalent molecular weight of this vanadium oxide is smaller than ruthenium and also the large difference between the oxidization states (V^{2+}, V^{3+}, V^{4+} and V^{5+}) involves a higher charge storage capability than ruthenium oxides [184].

Consequently, vanadium pentoxide is proposed to have a higher theoretical specific capacitance than ruthenium oxide [193]. In addition, vanadium pentoxide material has the merit of a facile synthesis method and being less toxic [194]. The electrochemical performance of V_2O_5 materials can be enhanced by varying its morphology, designing hybrid materials or capacitors as well as changing the electrolyte used. For instance, Saravanakumar *et al.* [195] reported the synthesis of an interconnected V_2O_5 nanoporous network using a simple capping-agent-assisted precipitation technique at different temperatures. The electrochemical performance of the V_2O_5 in K_2SO_4 aqueous electrolyte showed an increase in the ion diffusion to the electrode material which resulted in a specific capacitance of 316 F g^{-1}. The interconnected nanoporous network of the V_2O_5 material created nanochannels for ion diffusion and enabled the easy accessibility of ions. After 600 charge-discharge cycles, the material presented a capacity retention of 76% [195].

Qu *et al.* [180] synthesized a composite material which comprised of a polypyrrole (PPy) core shell grown on V_2O_5 nanoribbons by using dodecylbenzenesulfonate (DBS$^-$) as a surfactant. They further fabricated an asymmetric device with activated carbon used as a cathode electrode and PPy@V_2O_5 as an anode electrode using 0.5 M K_2SO_4 as the electrolyte in an operating voltage of 1.8 V. The Ppy@V_2O_5//AC supercapacitor displayed a 42 W h kg^{-1} specific energy and a good stability for up to 10,000 cycles. They explained that the asymmetric device performance was due to the benefit of the nanoribbon morphology from the V_2O_5, an improved charge-transfer and polymeric coating effect of Ppy [180]. Similarly, Chen *et al.* [23] fabricated a composite material comprised of CNT and V_2O_5 by hydrothermal method. In their study, they assembled an asymmetric device with a thick-film CNT/V_2O_5 nanowire composite as a positive electrode and a commercial AC-based as a negative evaluated in an organic electrolyte such as 1 M $LiClO_4$ in propylene carbonate (PC) solution. The asymmetric supercapacitor showed a specific energy of 40 W h kg^{-1} with a specific power of 210 W kg^{-1} at 2.7 V. They concluded that the overall energy and power performance is higher than the current electric double-layer capacitors technology [23].

Xu *et al.* [196] prepared a graphene/V_2O_5 xerogels nanocomposites from a commercial graphene using a hydrothermal method. The specific surface areas of the graphene/V_2O_5 xerogels nanocomposites and V_2O_5 xerogels were about 7.65 and 3.99 m^2 g^{-1} respectively showing the effect of incorporating graphene into the main vanadium-based material. The specific capacitance of the nanocomposite (195.4 F g^{-1}) was higher than that of the pristine V_2O_5 xerogels (127.7 F g^{-1}) at 1 A g^{-1} in 0.5 M K_2SO_4 [196].

b) Vanadium dioxide (VO_2)

Very recently, vanadium dioxides have attracted increasing attention as an electrode material in supercapacitors. Vanadium oxide displays a rich polymorphic stable and metastable forms.

Generally, vanadium dioxide (VO_2) has several polymorphs such as VO_2 (A), VO_2 (M), VO_2 (R), VO_2 (B), VO_2 (T) and VO_2 (bcc) [178,197].

However, VO_2 (A), VO_2 (R), VO_2 (M) and VO_2 (B) are the most attractive as they can be easy synthesized and with tuneable properties [178,198]. For instance, Theobald et al. [199] have successfully reported the sequence of the synthesis VO_2(B)→VO_2(A) →VO_2(R) by using hydrothermal method. In addition, VO_2 (M) possesses an exciting phase change from monoclinic (at a temperature about 68 °C) to VO_2 (R) tetragonal structure (at temperatures higher than the 68℃) and can undergo semiconductor-to-metal transition [200] with its resistivity changing by 4 - 5 orders of magnitude [201]. VO_2 exhibits a stable pseudocapacitive behaviour with a high specific capacity and reactivity [202]. Specifically, VO_2 (B) with a metastable monoclinic structure is a potential electrode material for both organic and aqueous electrolyte [203].

Several routes have been investigated to improve the supercapacitor performance by synthesizing a new composite design or using different preparation parameters of the pristine material. For instance, Liang *et al.* [189] presented a coaxial-structured hybrid material composed of vanadium dioxide (VO_2 (B)) and multi-walled carbon nanotubes (MWCNTs) prepared by a facile sol-gel method followed by a freeze-drying process. The composite showed a specific capacity of 250 F g^{-1} at a specific current of 0.5 A g^{-1} and a good cycling stability in 1 M Na_2SO_4. The VO_2 (B)/CNTs composite demonstrated better specific capacitance and superior rate capability than the pristine materials. The improvement of the composite material is governed by the unique coaxial-structure with the CNTs as a core and the VO_2(B) as the shell [189]. Pan *et al.* [204] reported on the reduction of the resistance of VO_2 powder film by ~ 3 orders of magnitude using a H_2 treatment technique. The symmetric device delivered a 300 F g^{-1} specific capacitance with a specific energy of 17 W h kg^{-1} at a

specific current of 1 A g^{-1} tested in 1 M Na$_2$SO$_4$. The cycling stability of the H$_2$-treated VO$_2$ was 4 times higher than the untreated samples [204].

Ma *et al.* [205] reported the first negative electrode material of 3D irregular ellipsoidal VO$_2$ in a CVD system at high temperatures (900 °C) by using a NH$_4$VO$_3$ precursor. In a three-electrode configuration, the VO$_2$ electrode presented a good electrochemical performance at a potential window of −1.0 V to 1.0 V due to the reversible redox response in 1 M Na$_2$SO$_4$ electrolyte. In the two-electrode configuration, the VO$_2$//VO$_2$ symmetric capacitor exhibited a specific capacitance of 60 F g^{-1} at a specific current of 0.25 A g^{-1}. The specific energy and the specific power values of the symmetric device were 21.3 W h kg^{-1} and 207.2 W kg^{-1}, respectively. They concluded that VO$_2$ electrode is suitable for use as both positive or negative electrodes in SCs [205]. Moreover, the performance of the vanadium dioxide can also be enhanced by fabricating a hybrid device. Recently, Xia *et al.* [206] synthesized the hydrogen molybdenum bronze (HMB) electrochemically deposited as a homogeneous shell on VO$_2$ nanoflakes which were grown on graphene foam (GF), forming a GF + VO$_2$/HMB. They fabricated an asymmetric device with the GF + VO$_2$/HMB as the positive electrode and a commercial activated carbon (AC) as the negative electrode tested in a 1 M K$_2$SO$_4$ electrolyte. The asymmetric device delivered a 14.5 W h kg^{-1} specific energy density and an associated specific power of 0.72 kW kg^{-1}. This good performance was linked to the unique composition and integrated conductive architecture [206].

2.5.2.2 Metal nitride/oxynitride
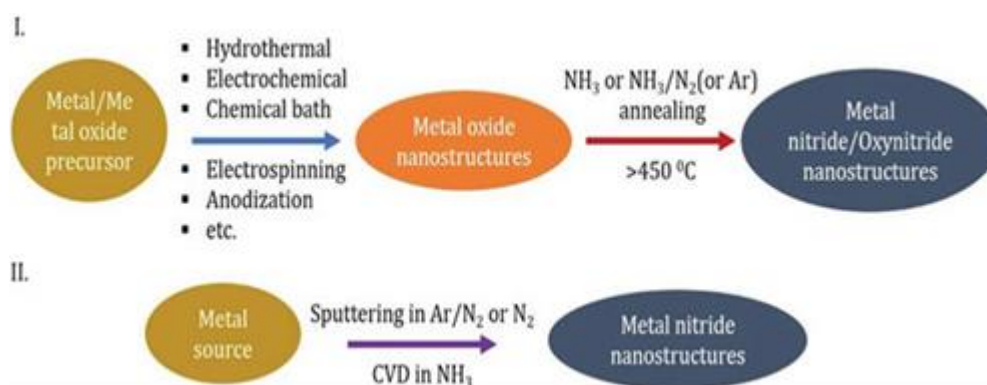
Figure 2.8: Illustration of general techniques to synthesize the metal nitride/oxynitride nanostructures [56].

Metal nitrides/oxynitride have also attracted a recent interest as a hopeful replacement to the less conductive TMOs/TM-OHs due to their unique physico-chemical properties including their metallic conductivity, high temperature strength and corrosion resistance [207–209]. Metal nitrides/oxynitride such as titanium nitride TiN, gallium nitride GaN, vanadium nitride VN, iron nitride Fe_2N, nickel nitride Ni_3N, and molybdenum nitride Mo_xN have been investigated as promising electrode materials in SCs. Generally in the literature, numerous synthesis methods have been adopted in producing metal nitrides/oxynitride nanostructures. The *chemical vapor deposition* method and the routine *metal oxide preparation* coupled with *nitration techniques*, have been most commonly used to successfully synthesize metal nitrides/oxynitride materials. A summary of these techniques with the steps involved for synthesis is shown in Figure 2.8.

Metal nitrides/oxynitride can also be synthesized by using a conventional nitridation or ammonolysis method using an organic precursors (cyanamide, polyvinylpyrrolidone, urea or melamine) as the nitrogen and or carbon sources for converting the metal oxides to metal nitride and /or metal oxynitride at high temperatures [210–213].

However, the NH$_3$ gas used is not as safe as N$_2$ gas, which has the capability to provide a lower conversion percentage of the metal oxide to metal nitride/oxynitride with a better charge storage behavior [56,214].

a) Vanadium nitride

Among the great successes in metal nitride materials, vanadium nitrides (VN) are considered to be excellent candidates because of their environmental safety, low cost [215], excellent chemical stability [174] and large operation range in the negative potential window [216]. This material has also a good bulk electronic conductivity (σ_{bulk} = 1.67 × 10^6 Ω^{-1} m^{-1}) [217] and a high molar density (≈ 6.0 g cm^{-3}) [169].

The VN adopted in supercapacitors, have produced an excellent specific capacitance of up to 1340 F g^{-1} at 2 mV s^{-1} and 554 F g^{-1} at a scan rate of 100 mV s^{-1} in a three-electrode configuration [169]. However, the metal nitride suffers from poor rate performance and cycling life [56] because the VN powder can easily dissolve in the electrolyte [216,218]. Several approaches have been employed to overcome the drawbacks of the metal nitride by controlling the surface composition, dependence on the range of potential window and the gas used during the synthesis.

Other important parameters are the electrolyte used to evaluate the electrode material and the range of the potential window which influence the capacity retention [56]. On the other hand, the electrochemical performance of the vanadium nitrides can be enhanced by oxidizing its active surface [219].

b) Vanadium oxynitride

The existence of an "*oxy*"-functional group on the surface of the VN material could alter its electrochemical performance. Vanadium oxynitride displays a good redox reaction as compared to VN [220] due to the higher wettability of the former electrode material as

compared to the latter [221]. This main advantage (wettability) with a hydrophilic nature is strongly desired and makes this material interesting and attractive as a potential electrode for supercapacitor application [56]. Porto *et al.* [213] reported the growth of vanadium oxynitride VO_xN_y rather than vanadium nitride by a conventional nitridation method using as-prepared VO_2 from the commercial V_2O_5 in a N_2 gas flow. The VO_xN_y electrode displayed a specific capacitance of 80 F g^{-1} in an aqueous 1 M KOH electrolyte. In their report, they concluded that the low specific capacitance obtained with the VO_xN_y electrodes was highly influenced by the low specific surface area of the as-synthesized material ($\sim$29 m^2 g^{-1}) [213].

Several other reports on vanadium nitride and oxynitride materials entail the use of vanadium oxide precursors such as VO_2 or V_2O_5 resulting in the generation of aggregated VN and VO_xN_y particles owing to the low melting point of the vanadium oxides [222]. This consequently limits the electrochemical performance of these agglomerated materials due to their low specific surface areas [213,222].

To overcome this drawback a different synthesis approach of remodelling the vanadium oxynitride materials have been proposed. For example, Shu and co-workers reported on a porous structured VO_xN_y-C nano-material using polyvinylpyrrolidone (PVP) as a template followed by NH_3 reduction of V_2O_5/PVP xerogel by a sol-gel method. They demonstrated that the VO_xN_y-C electrode (specific capacitance of 271 F g^{-1}) exhibited higher electrochemical performance than the VO_xN_y electrode (specific capacitance of 143 F g^{-1}) in 1 M KOH aqueous electrolyte. The good performance of the VO_xN_y-C was ascribed to their superior specific surface area (40.8 m^2 g^{-1}) as compared to the VO_xN_y (28.8 m^2 g^{-1}) which improved the electrochemical capability [174]. The presence of carbon in the vanadium oxynitride matrix can greatly influence the specific surface area, structure and morphology of the VO_xN_y and as a result, improve their electrochemical performance [174].

2.5.2.3 Conducting polymers

The third group of faradaic-type supercapacitor materials is the conducting polymers with a rich presence of π-conjugated polymeric chains [223]. This offers fast charge-discharge kinetics, suitable surface morphology, fast doping and undoping processes which yields unique properties, such as large surface areas and shortened pathways for charge/mass transport etc. [99,224,225]. Their successful adoption in supercapacitors results from their good electrical conductivity, high specific capacity, large pseudo-capacitance [163] and low equivalent series resistance (ESR) [99] that are desirable for efficient electrochemical energy storage.

The commonly used polymeric materials include polyacetylene (PA, with $\sigma = 3$ to 1000 S cm^{-1}), polyaniline (PANI, with $\sigma = 0.01$ to 5 S cm^{-1}), and polypyrrole (PPy, with $\sigma = 0.3$ S cm^{-1} to 100 S cm^{-1}) [226]. However, the main drawback in the use of the conducting polymers as supercapacitor electrodes is the low mechanical stability threshold from the mechanical stress induced from repeated intercalation and depletion of ions during the charging/discharging process [163]. Their combination with other carbon-based material boosts the stability of the conducting polymer electrode [225]. Numerous studies have demonstrated that the inclusion of foreign materials into conducting polymers to produce composite materials can overcome the problem of the low mechanical stability [138,224,227].

Figure 2.9 demonstrates the comparison of the specific capacitance as a function of operating potential in half-cell configurations for material electrodes tested in aqueous electrolytes for porous carbons, conducting polymers and faradaic materials (RuO_2).
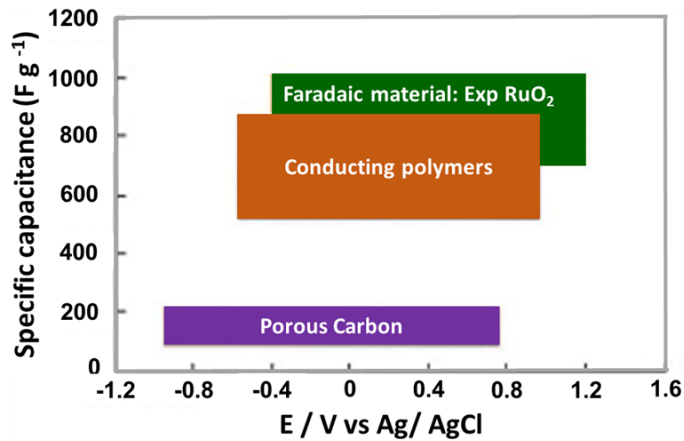
Figure 2.9: The specific capacitance of porous carbon, conducting polymers and faradaic materials (example RuO$_2$) [163].

The conducting polymers display a specific capacitance higher than porous carbons while RuO$_2$ shows the highest value. However, carbons display a relatively larger potential window range as compared to the others. For example, porous carbon electrodes are seen to operate more in the negative potential range with an equally large positive working potential. The combination of carbon as an EDLC electrode with other faradaic material (conducting polymer or metal oxides) in supercapacitors could yield to a synergy of numerous individual merits linked to both materials. This is ideal for scientific and commercial purposes due to the benefit achievable from both materials [163].

2.6 Electrolytes

As discussed in section 2.5, the electrode materials play an important role to reach high capacitance, specific high surface area and good electrical conductivity to yield high-performance supercapacitors. However, the electrolyte is also an equally key determinant of the supercapacitor performance due to dependence on the operating voltage (i.e. Equations 1 & 2). On the other hand, even with the high specific surface area and electrical conductivity of any electrode material, the size of the electrolyte ions could also affect ion dynamics which is directly linked to the performance of the supercapacitor [228,229].

For instance, Chmiola *et al.* [228] successfully evaluated the effective electrolyte pore size required to achieve a good performance in supercapacitor for carbide derived carbon. They concluded that the electrochemical performance of the electrode is higher for pore sizes of less than 1 nm as compared to those greater than 1 nm. This is related to the ability of the ions to adequately access porous sites with higher migration rate [228]. Similarly, in another report, Largeot *et al.* [229] demonstrated that the pore size of the electrode material should be very close to the size of the electrolyte ions for efficient electrochemical performance [229]. Electrolytes used for supercapacitor applications could be gel- type or liquid in nature [230].

In this thesis, we concentrate on liquid electrolytes which are mostly suitable for supercapacitor applications. Liquid electrolytes are generally classified into three subclasses: aqueous electrode, ionic liquids, and organic electrolytes.

2.6.1 Aqueous electrolyte

Acidic, alkaline and neutral electrolytes are water-based electrolytes used in supercapacitors due to their high ionic conductivity which can provide high capacitance. The aqueous electrolytes are greatly used in supercapacitors because of their low viscosity, low cost and easy preparation as compared to ionic liquid/organic electrolytes that need a dry room with a low H_2O content (< 1.0 ppm) [82]. The ionic conductivity of aqueous electrolytes is higher than organic electrolytes and ionic liquid by up one order of magnitude. For instance, Lewandowski and co-workers [231] compared the performance of the activated carbon cloth in three type of electrolytes: aqueous (H_2SO_4 and KOH), organic and ionic liquids. They concluded that the aqueous electrolytes have higher specific conductivity and lower series resistances than the organic electrode and the ionic liquid [231]. Among the aqueous electrolyte, potassium hydroxide (KOH) and sulfuric acid (H_2SO_4) are mostly adopted in supercapacitors due to their high ionic conductivity (up to 1 S cm^{-1}) and low cost [82].

However, the drawback of the aqueous electrolyte is the water electrolysis limitation to 1.23 V. This reduces the working potential and consequently, decreases the specific energy and the specific power [232,233]. With the progress in supercapacitors, hybrid capacitors have been considered to avoid this difficulty in order to add or to combine the potential window of the two different electrodes materials. The combination of the potential windows gain an increase of the cell voltage and high specific capacitance which results in a high specific energy device. Zheng *et al.* [234] reported interpenetrating CNTs with vanadium pentoxide (V_2O_5) nanowires to obtain a nanocomposite synthesized via a simple in-situ hydrothermal process. In the study, they assembled an asymmetric supercapacitor using the V_2O_5/CNTs nanocomposite electrode (with 33 wt% CNTs) as the negative electrode and MnO_2/carbon composite as the positive electrode in 1 M Na_2SO_4.

The asymmetric device based on these nanocomposites delivered a specific energy of 16 W h kg^{-1} with an associated specific power of 75 W kg^{-1} at 0.64 mA cm^{-2} in a 1.6 V cell voltage [234]. Deng *et al.* [235] synthesized graphene/VO_2 (RG/VO_2) hybrid materials by a hydrothermal technique. They fabricated an asymmetric device with the graphene/VO_2 (RG/VO_2) composite as a positive and RG as a negative electrode operated at a cell voltage of 1.7 V in 0.5 M K_2SO_4. The RG/VO_2//RG hybrid device delivered a specific energy of 22.8 W h kg^{-1} and a specific power of 425 W kg^{-1} at 0.25 A g^{-1} [235]. Therefore, the hybrid capacitor have the power to boost the voltage of the aqueous electrolyte.

2.6.2 Ionic liquids

Ionic liquids (ILs) have become an attractive electrolyte for supercapacitor applications due to their unique physicochemical properties such as high thermal stability and negligible vapor pressure [236].

ILs have a large electrochemical potential window that influence the specific energy and the maximum power obtainable (see Equations 1 and 2) [237]. Ionic liquids are considered to be molten salts with their melting points below room temperature [230,238].

They are non-volatile and non-flammable and are composed of an organic cation and a counter anion [239–241]. ILs have the ability to be modified for a specific purpose by combining specific anions and cations, or by adding different functional groups to acquire certain properties [230]. Mostly, the ions used in these electrolytes for supercapacitor applications are alkyl-substituted imidazolium, pyridinium, halogenated aluminate, cuprate anions and bis(trifluoromethanesulfonimide) ($[N(CF_3SO_2)_2]$) [242]. However, they have limitations such as a high viscosity which decreases the mobility of these ionic species [237], high cost [243] and low electrical conductivities ($\sim$ mS cm^{-1}) compared to aqueous electrolyte [231,244]. The high viscosity limits the wettability, charge transportation and the ease of ions accessibility to the pores on the electrode surface with a lower dielectric constant than other supercapacitor electrolytes.

The current aim by most researchers working with ionic liquid electrolytes is to improve on the low conductivity and reduce its viscosity. For instance, Frackowiak *et al.* [236] were able to decrease the viscosity of ILs by adding a small amount of acetonitrile (ca. 25 wt%). Activated carbons was used as the device electrodes with two phosphonium salts containing trifluoromethylsulfonyl-imide and dicyanamide anions. A specific energy of $\sim$ 40 Wh kg^{-1} was recorded for the electrode with a good stability [236]. Recently, Djire *et al*. [245] compared the electrochemical performance of the vanadium and titanium nitrides electrodes in the protic ionic liquid (2-methylpyridine and trifluoroacetic acid) and aqueous electrolyte (0.1 M H_2SO_4). The VN electrodes gave higher specific capacitance and better cyclic stability than the TiN in both electrolytes [245].

2.6.3 Organic electrolytes

Organic electrolytes have the ability to offer large operating voltage windows of 2.8 V which is the reason for their wide application in commercial-based supercapacitors [246].

The electrical conductivity and specific capacitance of the organic electrolyte are lower (~100 mS cm^{-1}) than that of aqueous systems and can affect the equivalent series resistance (ESR) and charge transfer (R_{CT}) resistance [247]. The organic solvents commonly used in supercapacitors are tetraalkylammonium cations, such as tetramethylammonium (Me4N$^+$), and tetraethylammonium (Et$_4$N$^+$), with tetrafluoroborate (BF$_4^-$), or hexafluorophospate (PF$_6^-$) anions dissolved in acetonitrile (ACN) or propylene carbonate (PC) solvents [248]. ACN provides a higher conductivity due to its low viscosity but its high volatility and toxicity is still a safety-limiting factor when compared to aqueous electrolytes. Propylene carbonate displays a higher viscosity than acetonitrile and thus exhibits lower conductivities as compared to the acetonitrile mixtures [231,242]. For instance, Abdallah *et al.* [249] in their research study were able to reduce both the flammability and the volatility mixture of ionic liquid–molecular solvent (acetonitrile or γ-butyrolactone).

Room temperature ionic liquids (RTILs) were added either to ACN or γ-butyrolactone (GBL) which is another typical solvent for the electrochemical devices. Their study concluded that the RTILs is a promising candidate, (especially TMPA–TFSI), for substitution of the ammonium salt, Et$_4$N$^+$BF$_4^-$, in the standard electrolyte for the safety of the supercapacitor device [249]. Foo *et al.* [250] synthesized a vanadium pentoxide-reduced graphene oxide (V$_2$O$_5$-rGO) free-standing electrodes for supercapacitor application. Their results showed an elimination of the need for current collectors or additives and reducing resistance by using 1 M LiClO$_4$ in propylene carbonate as an organic electrolyte. They presented an asymmetric flexible device based on RGO/V$_2$O$_5$-rGO (VGO) and considered VGO as the negative

electrode and rGO as the positive electrode. The VGO displayed an equivalent series resistance value of 3.36 Ω and an excellent cycling stability up to 8000 cycles [250].

In summary, electrodes materials and the operating electrolytes are equally important in the design or assembly of supercapacitors. The effect of the electrode and electrolyte on the electrochemical performance is summarized in the Figure 2.10 below [247].

The chart is composed of three concentric circles: cycle 1 is the electrolyte with the electrochemical supercapacitors (ESs), cycle 2 presents the parameters that defines the performance of ESs and cycle 3 display the factor of the electrolyte which affect the parameters in cycle 2 [246]. A direct link between the Supercapacitor (main core) and the device parameters (intermediate cycle) is demonstrated. The detailed electrolyte determinants are further elucidated in the outermost cycle of the chart giving a total description of key factors to be considered to obtain good performance metrics.
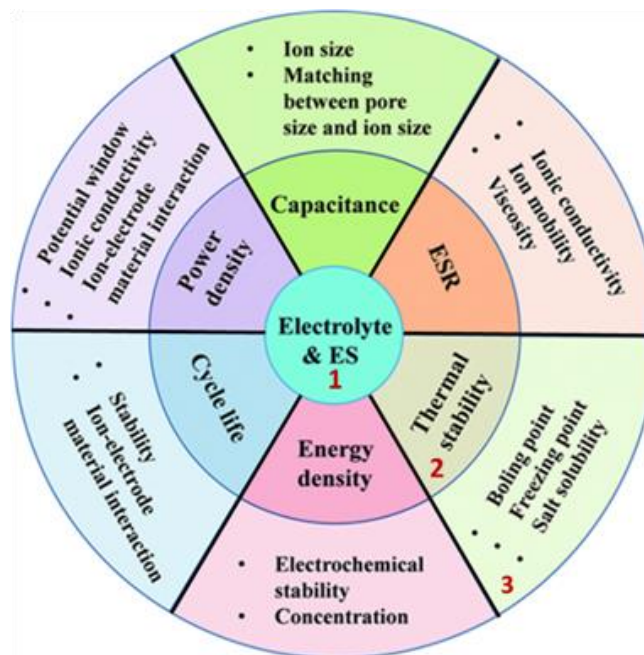
Figure 2.10: Effect of the electrolyte on the supercapacitors performance [247].

2.7 Electrode fabrication, testing and performance evaluation of electrode materials

2.7.1 Electrode fabrication of ECs

The selection of electrochemically-active electrode materials is considered to be key to designing a high-performance supercapacitor. Therefore, having selected the right material, the electrode preparation methodology also constitutes an important step to offering a good interaction between the active material and electrolyte while retaining its original properties (i.e. the electrical conductivity, structure and morphology). Generally, in supercapacitors, the electrodes are prepared from a mixture of an active material with/without a conductive additive and a binding material.

In this method, the conductive additive (such as carbon acetylene black (CB)) is used to slightly increase the conductivity of the electrode materials without contributing to the electrochemical storing capability, the binder (such as polytetrafluoroethylene (PTFE) or polyvinylidene fluoride (PVDF)) is added to prevent the dissolution of the active material on the electrode while immersed in the electrolyte.

Recently, Arunkumar *et al.* [251] proposed an optimization of electrode preparation methodologies for high performance supercapacitors. They used an oxygen-functionalized few-layer graphene as the active material, Nafion, polyvinylidene fluoride and polytetrafluoroethylene were used as binders dissolved in ethylene glycol and N-methyl-2-pyrrolidone (NMP) solvents for active material dispersion. They concluded that the electrodes prepared with the PVDF binder and the NMP solvent presented the best electrochemical performance due to the low viscosity of the solvent and better solubility of the binder in the chosen solvent [251].

2.7.2 Electrochemical evaluation configurations for SC electrode materials
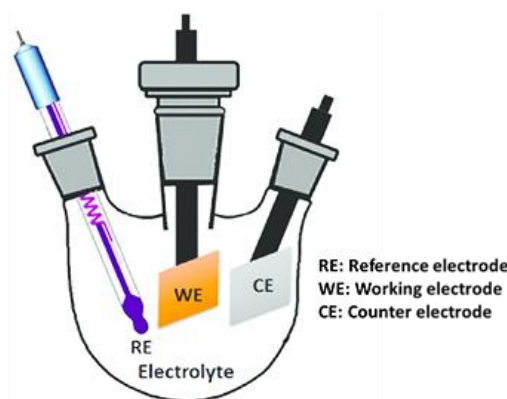
Figure 2.11: An illustration of a half-cell configuration set-up [252].

The evaluation of electrochemical measurements is achieved by initially using a half-cell testing set-up (also known as three electrode or single electrode) configuration and/or subsequently a two-electrode (full-cell/device) configuration.

- The half-cell configuration is generally used to determine the electrode properties including the behaviour of the electrode material, specific capacitance/capacity, working potential, equivalent series resistance and cycling stability in a suitable electrolyte. The set up comprises of a working electrode, a counter electrode, a reference electrode and an operating electrolyte compatible with the set of electrodes as shown in Figure 2.11.

- The working electrode (WE) is the electrode under study to determine its electrochemical properties. The reference electrode (RE) plays the role of measuring and controlling the potential of the working electrode in the half-cell configuration without allowing current to pass through it. The counter electrode (CE, also called auxiliary electrode) is used to close the current circuit in the electrochemical cell. The CE acts to keep the circuit balanced by adjusting to the current produced by the working electrode through a variation of its potential. The high surface area of the counter electrode as compared to the working electrode facilitates the electrochemical kinetics.

The materials used for counter electrodes should be conductive and chemically inert (for e.g. platinum (Pt), gold (Au), graphite rods, glassy carbon discs are the commonly used materials). Generally, the reference electrodes such as saturated calomel electrode (SCE), silver/silver chloride electrode (Ag/AgCl) and mercury/mercury oxide (Hg/HgO) are mostly used in supercapacitors. The selection of the reference electrode and the counter electrodes are slightly governed by the pH-value of the electrolyte used for a specific electrochemical measurement.

- The full-cell configuration (also called two electrode configuration) is characterized by a positive and negative electrode with a separator in-between them in an electrolyte as displayed in Figure 2.12. The two working electrodes in the two-electrode configuration can be similar (symmetric) or dissimilar (asymmetric). The full-cell configuration are generally evaluated using a coin cell or Swagelok with the associated components (e.g. positive case, spacer, spring and negative case).
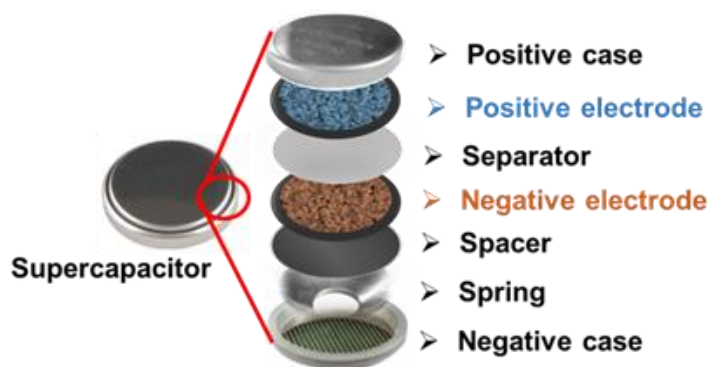
Figure 2.12: An illustration of a full-cell configuration set-up.

Other testing fixtures used to evaluate cell performance in a full-cell configuration include the Swagelok and the T-Cell testing fixtures. This configuration includes both negative and positive working potentials of the electrodes and the evaluation of specific energy, specific power, cycling stability and voltage holding.

These parameters depend widely to the individual electrochemical performance of both electrodes and the electrolyte used to evaluate the full cell.

a) Symmetric device

In this symmetric device, the two working electrodes are identical. For instance, if the active electrodes are EDLC-type materials: the capacitance of the positive and negative electrodes are equal as $C_A = C_B$. The total capacitance is thus half the capacitance of the single electrode ($C_T = C_A/2$). The specific capacitance of the single electrode (C_{sp}) is related to the specific capacitance of the full-cell by:

$$C_{sp} = 4C_T = \frac{4I\Delta t}{M\Delta V} \tag{6}$$

where I is the specific current (in A), Δt is the discharge time from the slope of the galvanostatic charge/discharge curve, ΔV is the cell voltage (V) and M is the total mass (g) of the active material on positive and negative electrodes. In this case, $M = 2\ m$ where m is the mass of single electrode.

b) Asymmetric device

The asymmetric device is composed of different positive and negative electrode with dissimilar electrochemical performance (i.e. C_A is most likely not equal to C_B). The charge equilibrium ($Q_+ = Q_-$) is used to balance the masses of both electrodes in the asymmetric cell. This generates equations (8) – (9) which are used to balance the masses;

$$Q_- = Q_+ \tag{7}$$

where Q_+ and Q_- are the total charge at the positive electrode and negative electrode obtained from the half–cell measurements, respectively.

- In the case where the positive and the negative electrodes are EDLC materials, equations (8) and (9) are applied as follows;

$$Q = C_{sp} \times m \times \Delta V \qquad (8)$$

given that,

$$C_{sp} = \frac{I \times t_D}{m \times \Delta V}$$

where C_{sp} is the specific capacitance of the electrode (F g^{-1}), t_D is the discharge time (s), I_D is the gravimetric applied current (A g^{-1}), ΔV is the working potential (V) and m is the mass (g) of the active material.

Thus, the mass balancing equation is applied as follows:

$$\frac{m+}{m-} = \frac{C_{sp-} \times V_{-}}{C_{sp+} \times V_{+}} \qquad (9)$$

- If the device shows the faradaic behavior, the appropriate name is the "specific capacity" due to the current which is not constant in this device. The specific capacity Q (mA h g^{-1}) is then calculated according to equation 10 [76] expressed as:

$$Q(\text{mA h g}^{-1}) = \frac{I \times t_D}{m \times 3.6} \qquad (10)$$

and the mass balance between the positive and the negative electrodes is given by:

$$\frac{m_{+}}{m_{-}} = \frac{(It_D)_{-}}{(It_D)_{+}} \qquad (11)$$

The general expression of the specific energy (E_d in Wh kg^{-1}) from equation (1) and the specific power (P_d in W kg^{-1}) are calculated using equations (12) and (13) [253–255].

$$E_d(W\ h\ kg^{-1}) = \frac{I_d}{3.6} \int V(t)dt \qquad (12)$$

$$P_d(W\ kg^{-1}) = 3600 \frac{E_d}{t_D} \qquad (13)$$

where I_d is the specific current in A g^{-1}, t_D is the discharge time (s), and V is the working potential window.

2.7.3 Electrochemical techniques adopted in testing electrode material performance

The electrochemical performance of the active electrode is mostly investigated using the cyclic voltammetry (CV), galvanostatic charge-discharge (GCD), electrochemical impedance spectroscopy (EIS) and stability (cycling stability and voltage holding) tests.

a) Cyclic voltammetry (CV)

The cyclic voltammetry (CV) test is largely used as an electrochemical technique to determine the ideal working potential for supercapacitor both in half and full cell configurations. It is considered as a potentio-dynamic electrochemical investigative technique. The CV test measures the output current with an input voltage sweep over a certain potential range [256]. This technique has the possibility to interpret and to determine the electrochemical behaviour of the working electrode in the electrolyte.

In addition, the CV is used as a simple, fast technique employed to identify the reversibility of an electrochemical system. The process of CV is obtained by determining the current at the electrode during the potential scan. The electrochemical mechanism occurs on the surface of the active material [242,257]. The graph obtained is called a "cyclic voltammogram" which is the plot of the current as a function of the voltage generated. The current response of the CV curve is an important parameter and is largely dependent on the interaction between the electrode and electrolyte.
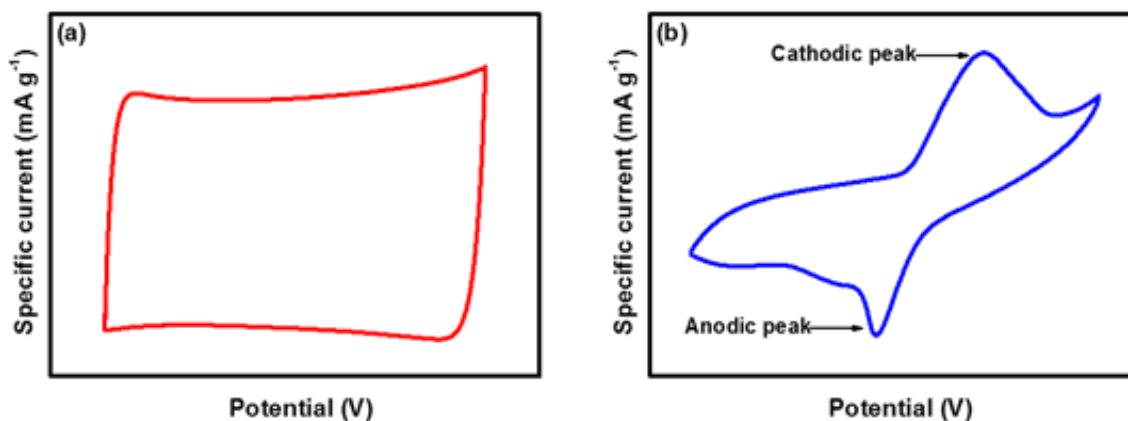
Figure 2.13: Cyclic voltammograms presenting the features for an (a) EDLC system, and (b) overlaid reduction and oxidation peaks for a faradaic system.

In Figure 2.13 (a), the rectangular plot is referred to an EDLC curve which confirms a typical reversible capacitive behavior of the material while the shape with redox peaks in Figure 2.13 (b), is related to the faradaic-type material. This faradaic process presents reversible oxidation and reduction peaks.

The potential difference between these two peaks anodic and cathodic peaks is usually ~ 59 mV n^{-1} with "n" being the number of electrons. The potential window and the potential peak position applied do not affect the oxidation and reduction peak.

b) Galvanostatic charge - discharge (GCD)

Galvanostatic charge-discharge (GCD) or Chronopotientiometry (CP) test is obtained by monitoring the voltage for an applied current between the working and counter electrodes as a function of time.

The GCD curves aid in obtaining the specific capacitance or capacity, specific energy, specific power, rate capability, and cycling stability of a material. The GCD plot is obtained by measuring the generated voltage (V) as a function of discharge time (s). The voltage limit is retained throughout the procedure. The applied current increases with time and is reversed after attained the set potential.

The potential increases to reach the maximum potential, with a current reversal occurring to decrease the potential to the lower present value. The figure 2.14 shows a typical GCD curve for EDLC and faradaic electrode materials. The GCD curve of the EDLC material in figure 2.14 (a) shows a linear or a triangular charge - discharge behavior with a constant IR drop (responsible for the negative resistive ohmic loss which is associated with the resistance of the active material). The specific capacitance is basically unchanged over the entire potential range.
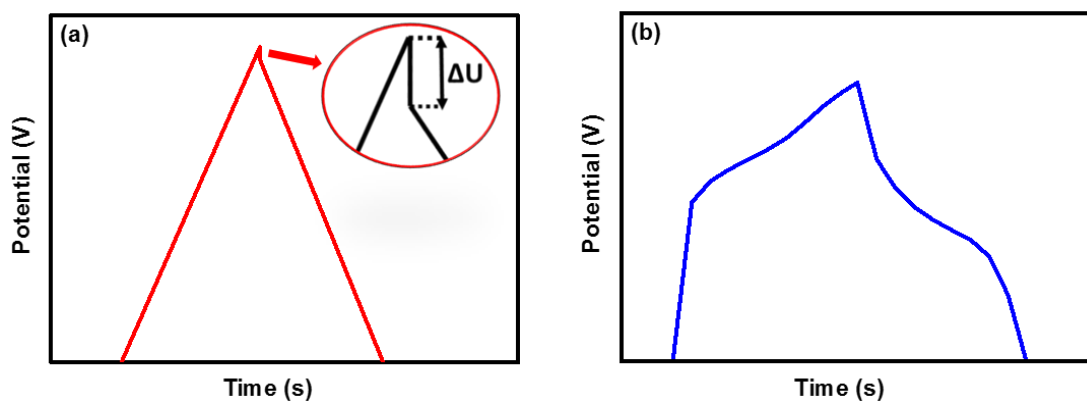
Figure 2.14: GCD plot of (a) an EDLC (the figure inset illustrates the IR drop) and (b) a redox active pseudocapacitor or faradaic.

The GCD plot of a faradaic material in Figure 2.14 (b) is completely different as compared to that EDLC curve. For faradaic, the curve displays a non - linear plot due to the presence of redox reactions occurring during the charge and discharge test.

c) Electrochemical Impedance spectroscopy (EIS)

The electrochemical impedance spectroscopy (EIS) is a powerful and important technique used to evaluate the electrochemical behavior and to establish a hypothesis using equivalent circuit models of an electrode material. A sinusoidal voltage fluctuation of low amplitude (typically ± 5 mV) is superimposed with frequency f ($\omega = 2\pi f$) to a bias voltage (stationary-state).

Electrochemical impedance spectroscopy is generally recorded in the frequency range of 100 kHz - 10 mHz [258,259]. The applied voltage (V) and the response in current are sinusoidal and are obtained by using equations below [260]:

$$V = V_0 + \Delta V \sin(\omega t) \tag{14}$$

$$I(t) = I_0 + \Delta V \sin(\omega t - \varphi) \tag{15}$$

where V_0 and I_0 are the initial state potential (V) and current (I), in this thesis V_0 is the open circuit potential of the material, V_0 and I_0 are 0, ω is the pulsation (where f is the signal frequency) and ΔV and ΔI are the amplitudes of the signal (V), φ of phase is the shifted angle and t is the time [260].

The EIS variation is obtained by the imaginary part of impedance – Im (Z) (or Z″) as a function of the real part Re (Z) (or Z′), generally represented in term of Nyquist plot.

EIS is also used to determine the specific capacitance by investigating the charge transfer (R_{CT}) and the total resistances at the electrolyte-electrode-current collector interface know as solution (R_Ω called equivalent series resistance (ESR)) of the three and two electrodes configurations [261].
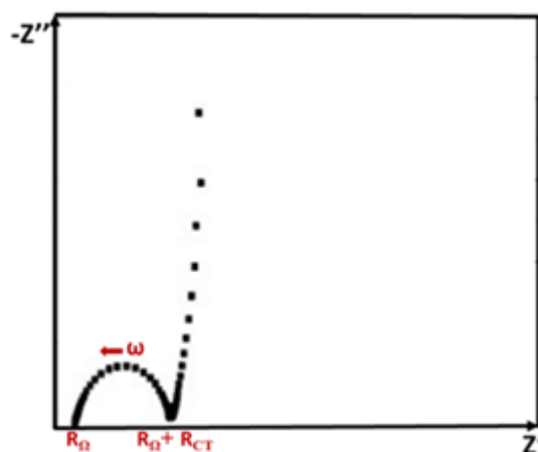
Figure 2.15: Nyquist plot with R_{CT} and R_Ω.

This ESR is also an important parameter to determine the maximum power (as per equation 16) which is the total resistance from the contribution of different resistances.

The conductivity at the interface between the active material and the electrolyte, the thickness of the active material and the porous morphology could influence the value of the R_Ω while R_{CT} shows a faradaic nature which is attributed to the porous electrode [262].

Generally, the EIS curve constitutes two different parts; a semi- circular loop at high frequency ($> 10^4$ Hz) and a linear part at low frequency due to the different electrochemical phenomena occurring during the electrochemical measurement as shown in figure 2.15. At low frequency (< 1 Hz), the Nyquist plot has a pure capacitive behavior which should be a straight line parallel to the y - axis (Z''-axis) and this ideal behavior is usually different to the experimental result.

2.7.4 Stability test
a) Cycle life

As mentioned in Table 2.1, supercapacitors have a large lifetime (~ 1 million cycles). The cycle life is an important parameter used to evaluate the stability of the supercapacitors.

The procedure depends on the specific current, the working potential used and the temperature at which the test is carried out. The GCD profile plays a key role in this case to evaluate the stability metrics of the electrode by repeated charge-discharge cycles.

Generally in supercapacitors, the coulombic efficiency (ε_t), capacitance/capacity retention (specific capacitance/capacity) and the energy efficiency (η_E) are determined from the charge-discharge curves. The coulombic efficiency and energy efficiency can be calculated using the following equations [263]:

$$\varepsilon_t = \frac{t_D}{t_C} \times 100 \tag{16}$$

where t_D and t_C are the discharge and charge time, respectively.

$$\eta_E = \frac{E_D}{E_C} \times 100 \tag{17}$$

where E_D and E_C are the discharge and charge energy, respectively [263].

b) Voltage holding test

The voltage holding (or "potentiostatic floating") test is an additional stability test recently agreed upon by researchers as an idea tool to accurately ascertain the stability of a SC device. The floating test determines the specific capacitance/capacity as a function of time by occasional charge/discharge cycles while keeping the cell under test at a constant maximum operating voltage. (Figure 2.16). The voltage holding test has the ability to gives a direct insight into the possible effect and degradation phenomena which might occur during the electrochemical process [264]. The significant difference between cycle life and voltage holding is that a "constant" voltage is applied to the capacitor increasing the measured life time [265]. Some researchers have confirmed that voltage holding tests are more demanding than respective cycling tests with identical upper voltage limits [266].

During the cycling test, most of the time is consumed at capacitor voltages, which are not critical for the capacitor's stability [266].
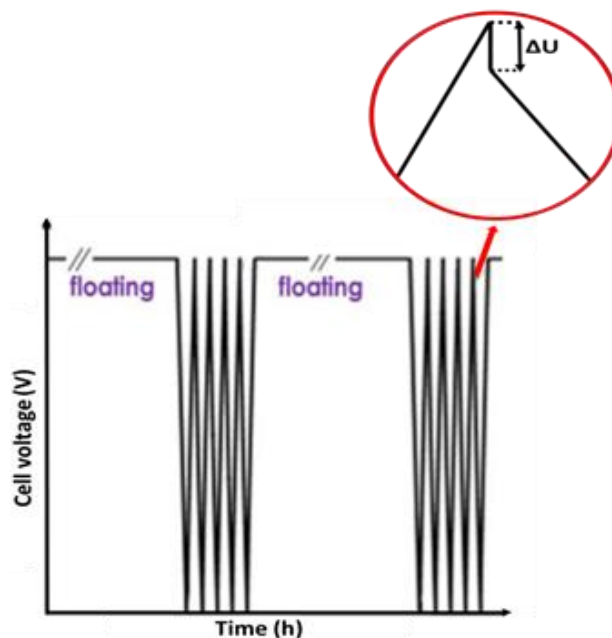
Figure 2.16: Scheme of the voltage holding test [262].

Bibliography

[1]   F. Shi, L. Li, X. Wang, C. Gu, J.-P. Tu, Metal oxide/hydroxide-based materials for supercapacitors, RSC Adv. 4 (2014) 41910–41921.

[2]   J. Jiang, Y. Li, J. Liu, X. Huang, C. Yuan, X.W.D. Lou, Recent Advances in Metal Oxide-based Electrode Architecture Design for Electrochemical Energy Storage, Advanced Materials. 24 (2012) 5166–5180.

[3]   H.D. Abruña, Y. Kiya, J.C. Henderson, Batteries and electrochemical capacitors, Physics Today. 61 (2008) 43–47.

[4]   D. Deng, Li-ion batteries: Basics, progress, and challenges, Energy Science and Engineering. 3 (2015) 385–418.

[5]   V. Augustyn, J. Come, M.A. Lowe, J.W. Kim, P.-L. Taberna, S.H. Tolbert, H.D. Abruña, P. Simon, B. Dunn, High-rate electrochemical energy storage through Li+ intercalation pseudocapacitance, Nature Materials. 12 (2013) 518–522.

[6]   Y. Idota, T. Kubota, A. Matsufuji, Y. Maekawa, T. Miyasaka, Tin-Based Amorphous Oxide: A High-Capacity Lithium-Ion-Storage Material, Science. 276 (1997) 1395–1397.

[7]   P. Thounthong, S. Raël, B. Davat, Energy management of fuel cell/battery/supercapacitor hybrid power source for vehicle applications, Journal of Power Sources. 193 (2009) 376–385.

[8]   H. Wang, Y. Yang, Y. Liang, J.T. Robinson, Y. Li, A. Jackson, Y. Cui, H. Dai, Graphene-Wrapped Sulfur Particles as a Rechargeable Lithium–Sulfur Battery Cathode Material with High Capacity and Cycling Stability, Nano Letters. 11 (2011) 2644–2647.

[9]   K.H. An, W.S. Kim, Y.S. Park, Y.C. Choi, S.M. Lee, D.C. Chung, D.J. Bae, S.C. Lim, Y.H. Lee, Supercapacitors Using Single-Walled Carbon Nanotube Electrodes,

Advanced Materials. 13 (2001) 497–500.

[10]   M. Winter, R.J. Brodd, What Are Batteries, Fuel Cells, and Supercapacitors?, Chem. Rev. 104 (2004) 4245−4269.

[11]   A.K. Mondal, H. Liu, Z.-F. Li, G. Wang, Multiwall carbon nanotube-nickel cobalt oxide hybrid structure as high performance electrodes for supercapacitors and lithium ion batteries, Electrochimica Acta. 190 (2016) 346–353.

[12]   P. Yang, Y. Ding, Z. Lin, Z. Chen, Y. Li, P. Qiang, M. Ebrahimi, W. Mai, C.P. Wong, Z.L. Wang, Low-Cost High-Performance Solid-State Asymmetric Supercapacitors Based on MnO_2 Nanowires and Fe_2O_3 Nanotubes, Nano Letters. 14 (2014) 731–736.

[13]   A. Khaligh, Z. Li, Battery, Ultracapacitor, Fuel Cell, and Hybrid Energy Storage Systems for Electric, Hybrid Electric, Fuel Cell, and Plug-In Hybrid Electric Vehicles: State of the Art, IEEE Transactions on vehicular technology, 59 (2010) 6.

[14]   F. Rafik, H. Gualous, R. Gallay, A. Crausaz, A. Berthon, Frequency, thermal and voltage supercapacitor characterization and modeling, Journal of Power Sources. 165 (2007) 928–934.

[15]   M. Al Sakka, H. Gualous, J. Van Mierlo, H. Culcu, Thermal modeling and heat management of supercapacitor modules for vehicle applications, Journal of Power Sources. 194 (2009) 581–587.

[16]   R. Kötz, M. Hahn, R. Gallay, Temperature behavior and impedance fundamentals of supercapacitors, Journal of Power Sources. 154 (2006) 550–555.

[17]   L. Li, S. Kim, W. Wang, M. Vijayakumar, Z. Nie, B. Chen, J. Zhang, G. Xia, J. Hu, G. Graff, J. Liu, Z. Yang, A Stable Vanadium Redox-Flow Battery with High Energy Density for Large-Scale Energy Storage, Advanced Energy Materials. 1 (2011) 394–400.

[18]   K. Zaghib, M. Dontigny, A. Guerfi, P. Charest, I. Rodrigues, A. Mauger, C.M. Julien,

Safe and fast-charging Li-ion battery with long shelf life for power applications, Journal of Power Sources. 196 (2011) 3949–3954.

[19] Z. Fan, J. Yan, T. Wei, L. Zhi, G. Ning, T. Li, F. Wei, Asymmetric Supercapacitors Based on Graphene/MnO$_2$ and Activated Carbon Nanofiber Electrodes with High Power and Energy Density, Advanced Functional Materials. 21 (2011) 2366–2375.

[20] V.D. Nithya, N.S. Arul, Progress and development of Fe$_3$O$_4$ electrodes for supercapacitors, Journal of Materials Chemistry A. 4 (2016) 10767–10778.

[21] A.M. Rao, Nanotechnology institutions Energy and our future: a perspective from the Clemson Nanomaterials Center, Nanotechnol Rev. 4 (2015) 479–484.

[22] Y. Wang, Y. Xia, Recent Progress in Supercapacitors: From Materials Design to System Construction, Advanced Materials. 25 (2013) 5336–5342.

[23] Z. Chen, V. Augustyn, J. Wen, Y. Zhang, M. Shen, B. Dunn, Y. Lu, High-Performance Supercapacitors Based on Intertwined CNT/V$_2$O$_5$ Nanowire Nanocomposites, Advanced Materials. 23 (2011) 791–795.

[24] Z. Cao, B.B.Q. Wei, A perspective: carbon nanotube macro-films for energy storage, Energy Environ. Sci. 6 (2013) 3183–3201.

[25] W. Deng, X. Ji, Q. Chen, C.E. Banks, Electrochemical capacitors utilising transition metal oxides: an update of recent developments, RSC Advances. 1 (2011) 1171.

[26] Becker H.E., U.S. Patent (General Electric), 1957.

[27] D. I, Boos, U.S. Patent (to Standard Oil, SOHIO), 1970.

[28] T.C. Murphy, R.B. Wright, R.A. Sutula, in: F.M. Delnick, D. Ingersoll, X. Andrieu, K. Naoi, Electrochemical Capacitors II, proceedings, Electrochemical Society, Pennington, NJ. 96–25 (1997) 258.

[29] M. Notarianni, J. Liu, K. Vernon, N. Motta, Synthesis and applications of carbon nanomaterials for energy generation and storage, Beilstein Journal of Nanotechnology.

7 (2016) 149–196.

[30]   A. Balducci, R. Dugas, P.L. Taberna, P. Simon, D. Plée, M. Mastragostino, S. Passerini, High temperature carbon–carbon supercapacitor using ionic liquid as electrolyte, Journal of Power Sources. 165 (2007) 922–927.

[31]   Z. Niu, L. Zhang, L. Liu, B. Zhu, H. Dong, X. Chen, All-Solid-State Flexible Ultrathin Micro-Supercapacitors Based on Graphene, Advanced Materials. 25 (2013) 4035–4042.

[32]   S. Shi, C. Xu, C. Yang, J. Li, H. Du, B. Li, F. Kang, Flexible supercapacitors, Particuology. 11 (2013) 371–377.

[33]   T.D. Dongale, P.R. Jadhav, G.J. Navathe, J.H. Kim, M.M. Karanjkar, P.S. Patil, Development of nano fiber MnO_2 thin film electrode and cyclic voltammetry behavior modeling using artificial neural network for supercapacitor application, Materials Science in Semiconductor Processing. 36 (2015) 43–48.

[34]   M. Jayalakshmi, K. Balasubramanian, Simple Capacitors to Supercapacitors-An Overview, Int. J. Electrochem. Sci. 3 (2008) 1196–1217. www.electrochemsci.org (accessed December 31, 2018).

[35]   R. Kühne, Electric buses – An energy efficient urban transportation means, Energy. 35 (2010) 4510–4513.

[36]   D. Ghosh, S. Giri, M. Moniruzzaman, T. Basu, M. Mandal, C.K. Das, α $MnMoO_4$/graphene hybrid composite: High energy density supercapacitor electrode material, Dalton Transactions. 43 (2014) 11067–11076.

[37]   P.R. Deshmukh, S. V. Patil, R.N. Bulakhe, S.N. Pusawale, J.-J. Shim, C.D. Lokhande, Chemical synthesis of PANI–TiO_2 composite thin film for supercapacitor application, RSC Advances. 5 (2015) 68939–68946.

[38]   L.L. Zhang, R. Zhou, X.S. Zhao, Graphene-based materials as supercapacitor

electrodes, Journal of Materials Chemistry. 20 (2010) 5983.

[39] S. Faraji, F.N. Ani, Microwave-assisted synthesis of metal oxide/hydroxide composite electrodes for high power supercapacitors - A review, Journal of Power Sources. 263 (2014) 338–360.

[40] Z.L. Li, Carbon-based materials as supercapacitor electrodes, National University of Singapore, 2010.

[41] B.S. Singu, U. Male, P. Srinivasan, K.R. Yoon, Preparation and performance of polyaniline–multiwall carbon nanotubes–titanium dioxide ternary composite electrode material for supercapacitors, Journal of Industrial and Engineering Chemistry. 49 (2017) 82–87.

[42] D. Ranjini, A. Sambathkumar, Design of Battery-Super Capacitors Combination in Uninterruptible Power Supply (UPS), 2 (2014).

[43] M.A. Bavio, G.G. Acosta, T. Kessler, A. Visintin, Flexible symmetric and asymmetric supercapacitors based in nanocomposites of carbon cloth/polyaniline-carbon nanotubes, Energy. 130 (2017) 22–28.

[44] J. Zhu, L. Huang, Y. Xiao, L. Shen, Q. Chen, W. Shi, Hydrogenated CoO_x nanowire@$Ni(OH)_2$ nanosheet core–shell nanostructures for high-performance asymmetric supercapacitors, Nanoscale. 6 (2014) 6772.

[45] C. Gao, J. Gao, C. Shao, Y. Xiao, Y. Zhao, L. Qu, Versatile origami micro-supercapacitors array as a wind energy harvester, Journal of Materials Chemistry A. 6 (2018) 19750–19756.

[46] Y. Hu, Carbon and Metal Oxides Based Nanomaterials for Flexible High Performance Asymmetric Supercapacitors, National University of Singapore, 2017.

[47] S. Bose, T. Kuila, A.K. Mishra, R. Rajasekar, N.H. Kim, J.H. Lee, Carbon-based nanostructured materials and their composites as supercapacitor electrodes, J. Mater.

Chem. 22 (2012) 767–784.

[48] A.G. Pandolfo, A.F. Hollenkamp, Carbon properties and their role in supercapacitors, Journal of Power Sources. 157 (2006) 11–27.

[49] O. KI, S. Chen, Nanomaterials in Advanced Batteries and Supercapacitors, 2016.

[50] M. Zhi, C. Xiang, J. Li, M. Li, N. Wu, Nanostructured carbon–metal oxide composite electrodes for supercapacitors: a review, Nanoscale. 5 (2013) 72–88.

[51] L.L. Zhang, X.S. Zhao, Carbon-based materials as supercapacitor electrodes, Chemical Society Reviews. 38 (2009) 2520.

[52] L. Pilon, H. Wang, A. d'Entremont, Recent Advances in Continuum Modeling of Interfacial and Transport Phenomena in Electric Double Layer Capacitors, Journal of The Electrochemical Society. 162 (2015) A5158–A5178.

[53] L.L. Zhang, X.S. Zhao, P.L. Taberna, P. Simon, D. Plee, M. Mastragostino, S. Passerini, D. Zhao, M. Yumura, S. Iijima, Carbon-based materials as supercapacitor electrodes, Chemical Society Reviews. 38 (2009) 2520.

[54] R.B. Marichi, V. Sahu, R.K. Sharma, G. Singh, Efficient, Sustainable, and Clean Energy Storage in Supercapacitors Using Biomass-Derived Carbon Materials, in: Handbook of Ecomaterials, Springer International Publishing, Cham, 2018: pp. 1–26.

[55] O. Stern Z. Elektrochem, No Title, 30 (1924) 508.

[56] S. Ghosh, S.M. Jeong, S.R. Polaki, A review on metal nitrides/oxynitrides as an emerging supercapacitor electrode beyond oxide, Korean Journal of Chemical Engineering. 35 (2018) 1389–1408.

[57] H. Li, Y. Gao, C. Wang, G. Yang, A simple electrochemical route to access amorphous mixed-metal hydroxides for supercapacitor electrode materials, Advanced Energy Materials. 5 (2015) 1401767.

[58] M. Sathiya, A.S. Prakash, K. Ramesha, J. Tarascon, A.K. Shukla, V_2O_5-Anchored

Carbon Nanotubes for Enhanced Electrochemical Energy Storage, J. Am. Chem. Soc. 133 (2011) 16291–16299.

[59] L. Guan, L. Yu, G.Z. Chen, Capacitive and non-capacitive faradaic charge storage, Electrochimica Acta. 206 (2016) 464–478.

[60] M. Toupin, T.B. And, D. Bélanger, Influence of Microstucture on the Charge Storage Properties of Chemically Synthesized Manganese Dioxide, Chem. Mater. 14 (2002) 3946–3952.

[61] J. Xie, X. Sun, N. Zhang, K. Xu, M. Zhou, Y. Xie, Layer-by-layer β-Ni(OH)2/graphene nanohybrids for ultraflexible all-solid-state thin-film supercapacitors with high electrochemical performance, Nano Energy. 2 (2013) 65–74.

[62] S. Boukhalfa, K. Evanoff, G. Yushin, Atomic layer deposition of vanadium oxide on carbon nanotubes for high-power supercapacitor electrodes, Energy & Environmental Science. 5 (2012) 6872.

[63] V. Augustyn, P. Simon, B. Dunn, Pseudocapacitive oxide materials for high-rate electrochemical energy storage, Energy & Environmental Science. 7 (2014) 1597.

[64] E. Herrero, L.J. Buller, H.D. Abruña, Underpotential Deposition at Single Crystal Surfaces of Au, Pt, Ag and Other Materials, Chem. Rev. (2001) 1897−1930.

[65] S. Trasatti, G. Buzzanca, Ruthenium dioxide: A new interesting electrode material. Solid state structure and electrochemical behaviour, Journal of Electroanalytical Chemistry and Interfacial Electrochemistry. 29 (1971) A1–A5.

[66] A. Venkataraman, Pseudocapacitors for Energy Storage, Portland, OR, 2000.

[67] J. Shabani Shayeh, A. Ehsani, M.R. Ganjali, P. Norouzi, B. Jaleh, Conductive polymer/reduced graphene oxide/Au nano particles as efficient composite materials in electrochemical supercapacitors, Applied Surface Science. 353 (2015) 594–599.

[68] A. Borenstein, O. Hanna, R. Attias, S. Luski, T. Brousse, D. Aurbach, Carbon-based

composite materials for supercapacitor electrodes: a review, Journal of Materials Chemistry A. 5 (2017) 12653–12672.

[69] C.Z. Yuan, B. Gao, L.F. Shen, S.D. Yang, L. Hao, X.J. Lu, F. Zhang, L.J. Zhang, X.G. Zhang, Hierarchically structured carbon-based composites: Design, synthesis and their application in electrochemical capacitors, Nanoscale. 3 (2011) 529–545.

[70] K. Zhang, L.L. Zhang, X.S. Zhao, J. Wu, L. Li Zhang, X.S. Zhao, J. Wu, Graphene/Polyaniline Nanofiber Composites as Supercapacitor Electrodes, Chemistry of Materials. 22 (2010) 1392–1401.

[71] Y. Gao, Y.S. Zhou, M. Qian, X.N. He, J. Redepenning, P. Goodman, H.M. Li, L. Jiang, Y.F. Lu, Chemical activation of carbon nano-onions for high-rate supercapacitor electrodes, Carbon. 51 (2013) 52–58.

[72] M. Kaempgen, C.K. Chan, J. Ma, Y. Cui, G. Gruner, Printable Thin Film Supercapacitors Using Single-Walled Carbon Nanotubes, Nano Letters. 9 (2009) 1872–1876.

[73] J. Gamby, P. Taberna, P. Simon, J. Fauvarque, M. Chesneau, Studies and characterisations of various activated carbons used for carbon/carbon supercapacitors, Journal of Power Sources. 101 (2001) 109–116.

[74] Y. He, W. Chen, X. Li, Z. Zhang, J. Fu, C. Zhao, E. Xie, Freestanding Three-Dimensional Graphene/MnO_2 Composite Networks As Ultralight and Flexible Supercapacitor Electrodes, ACS Nano. 7 (2013) 174–182.

[75] J.R. Miller, R.A. Outlaw, B.C. Holloway, K.J. Ganesh, W. Cai, P.J. Ferreira, A. Pirkle, R.M. Wallace, K.A. Cychosz, M. Thommes, D. Su, E.A. Stach, R.S. Ruoff, Graphene Double-Layer Capacitor with ac Line-Filtering Performance, Science. 329 (2010) 1637–1639.

[76] T.M. Masikhwa, D.Y. Momodu, K.O. Oyedotun, A.A. Mirghni, N.M. Ndiaye, N.

Manyala, Asymmetric supercapacitor based on cobalt hydroxide carbonate/GF composite and a carbonized conductive polymer grafted with iron (C-FP), Journal of Alloys and Compounds. 769 (2018) 376–386.

[77]   A.A. Mirghni, M.J. Madito, T.M. Masikhwa, K.O. Oyedotun, A. Bello, N. Manyala, Hydrothermal synthesis of manganese phosphate/graphene foam composite for electrochemical supercapacitor applications, Journal of Colloid and Interface Science. 494 (2017) 325–337.

[78]   D.P. Dubal, O. Ayyad, V. Ruiz, P. Gómez-Romero, Hybrid energy storage: The merging of battery and supercapacitor chemistries, Royal Society of Chemistry, 2015.

[79]   C. Liu, Polyaniline and Graphene Based Symmetric and Asymmetric Solide-State Supercapacitor, University of Akron, Polymer Engineering., 2015. (accessed October 17, 2018).

[80]   A. Brandt, J. Pires, M. Anouti, A. Balducci, An investigation about the cycling stability of supercapacitors containing protic ionic liquids as electrolyte components, Electrochimica Acta. 108 (2013) 226–231.

[81]   H.S. Choi, J.H. Im, T. Kim, J.H. Park, C.R. Park, Advanced energy storage device: a hybrid BatCap system consisting of battery–supercapacitor hybrid electrodes based on $Li_4Ti_5O_{12}$–activated-carbon hybrid nanotubes, Journal of Materials Chemistry. 22 (2012) 16986.

[82]   C.D.D. Lokhande, D.P.P. Dubal, O.-S.S. Joo, Metal oxide thin film based supercapacitors, Current Applied Physics. 11 (2011) 255–270.

[83]   D. Momodu, M. Madito, F. Barzegar, A. Bello, A. Khaleed, O. Olaniyan, J. Dangbegnon, N. Manyala, Activated carbon derived from tree bark biomass with promising material properties for supercapacitors, Journal of Solid State Electrochemistry. 21 (2017) 859–872.

[84] A. Laforgue, P. Simon, J.F. Fauvarque, M. Mastragostino, F. Soavi, J.F. Sarrau, P. Lailler, M. Conte, E. Rossi, S. Saguatti, Activated Carbon/Conducting Polymer Hybrid Supercapacitors, Journal of The Electrochemical Society. 150 (2003) A645.

[85] Q. Yang, Z. Lu, J. Liu, X. Lei, Z. Chang, L. Luo, X. Sun, Metal oxide and hydroxide nanoarrays: Hydrothermal synthesis and applications as supercapacitors and nanocatalysts, Progress in Natural Science: Materials International. 23 (2013) 351–366.

[86] E. Frackowiak, F. Béguin, Carbon materials for the electrochemical storage of energy in capacitors, Carbon. 39 (2001) 937–950.

[87] P.N. Bartlett, R.C. Alkire, J. Lipkowski, Electrochemistry of carbon electrodes, Wiley-VCH, 2015. (accessed October 20, 2018).

[88] Yu Liu, A. Randy L. Vander Wal, V.N. Khabashesku, Functionalization of Carbon Nano-onions by Direct Fluorination, Chem. Mater. 19 (2007) 778–786.

[89] F.-D. Han, B. Yao, Y.-J. Bai, Preparation of Carbon Nano-Onions and Their Application as Anode Materials for Rechargeable Lithium-Ion Batteries, The Journal of Physical Chemistry C. 115 (2011) 8923–8927.

[90] D. Pech, M. Brunet, H. Durou, P. Huang, V. Mochalin, Y. Gogotsi, P.-L. Taberna, P. Simon, Ultrahigh-power micrometre-sized supercapacitors based on onion-like carbon, Nature Nanotechnology. 5 (2010) 651–654.

[91] O. Mykhailiv, M. Imierska, M. Petelczyc, L. Echegoyen, M.E. Plonska-Brzezinska, Chemical versus Electrochemical Synthesis of Carbon Nano-onion/Polypyrrole Composites for Supercapacitor Electrodes, Chemistry - A European Journal. 21 (2015) 5783–5793.

[92] G. Wu, C. Dai, D. Wang, D. Li, N. Li, Nitrogen-doped magnetic onion-like carbon as support for Pt particles in a hybrid cathode catalyst for fuel cells, Journal of Materials Chemistry. 20 (2010) 3059.

[93]   N. Keller, N.I. Maksimova, V. V. Roddatis, M. Schur, G. Mestl, Y. V. Butenko, V.L. Kuznetsov, R. Schlögl, The Catalytic Use of Onion-Like Carbon Materials for Styrene Synthesis by Oxidative Dehydrogenation of Ethylbenzene, Angewandte Chemie International Edition. 41 (2002) 1885.

[94]   S. Tomita, M. Fujii, S. Hayashi, Optical extinction properties of carbon onions prepared from diamond nanoparticles, Physical Review B. 66 (2002) 245424.

[95]   C. Zhu, F. Xu, J. Chen, H. Min, H. Dong, L. Tong, K. Qasim, S. Li, L. Sun, Nitrogen-doped carbon onions encapsulating metal alloys as efficient and stable catalysts for dye-sensitized solar cells, Journal of Power Sources. 303 (2016) 159–167.

[96]   R. Borgohain, J. Li, J.P. Selegue, Y.-T. Cheng, Electrochemical Study of Functionalized Carbon Nano-Onions for High-Performance Supercapacitor Electrodes, The Journal of Physical Chemistry C. 116 (2012) 15068–15075.

[97]   J.K. McDonough, A.I. Frolov, V. Presser, J. Niu, C.H. Miller, T. Ubieto, M. V. Fedorov, Influence of the structure of carbon onions on their electrochemical performance in supercapacitor electrodes, Carbon. 50 (2012) 3298–3309.

[98]   Y. Zhai, Y. Dou, D. Zhao, P.F. Fulvio, R.T. Mayes, S. Dai, Carbon Materials for Chemical Capacitive Energy Storage, Advanced Materials. 23 (2011) 4828–4850.

[99]   M. Vangari, T. Pryor, L. Jiang, Supercapacitors: Review of Materials and Fabrication Methods, Journal of Energy Engineering. 139 (2013) 72–79.

[100] A.L. Kalamkarov, A.V. Georgiades, S.K. Rokkam, V.P. Veedu, M.N. Ghasemi-Nejhad, Analytical and numerical techniques to predict carbon nanotubes properties, International Journal of Solids and Structures. 43 (2006) 6832–6854.

[101] T.W. Ebbesen, H.J. Lezec, H. Hiura, J.W. Bennett, H.F. Ghaemi, T. Thio, Electrical conductivity of individual carbon nanotubes, Nature. 382 (1996) 54–56.

[102] K. Balasubramanian, M. Burghard, Chemically Functionalized Carbon Nanotubes,

Small. 1 (2005) 180–192.

[103] M. Yi, Z. Shen, A review on mechanical exfoliation for the scalable production of graphene, Journal of Materials Chemistry A. 3 (2015) 11700–11715.

[104] Y. Shao, J. Wang, H. Wu, J. Liu, I.A. Aksay, Y. Lin, Graphene Based Electrochemical Sensors and Biosensors: A Review, Electroanalysis. 22 (2010) 1027–1036.

[105] C.N.R. Rao, A.K. Sood, K.S. Subrahmanyam, A. Govindaraj, Graphene: The New Two-Dimensional Nanomaterial, Angewandte Chemie International Edition. 48 (2009) 7752–7777.

[106] S. Park, R.S. Ruoff, Chemical methods for the production of graphenes, Nature Nanotechnology. 4 (2009) 217–224.

[107] R.B. Rakhi, W. Chen, D. Cha, H.N. Alshareef, High performance supercapacitors using metal oxide anchored graphene nanosheet electrodes, Journal of Materials Chemistry. 21 (2011) 16197.

[108] P. Simon, Y. Gogotsi, Capacitive Energy Storage in Nanostructured CarbonÀElectrolyte Systems, Accounts of chemical research. 46 (2013) 1094–1103.

[109] K.S. Novoselov, A.K. Geim, S. V. Morozov, D. Jiang, M.I. Katsnelson, I. V. Grigorieva, S. V. Dubonos, A.A. Firsov, Two-dimensional gas of massless Dirac fermions in graphene, Nature. 438 (2005) 197–200.

[110] C. Lee, X. Wei, J.W. Kysar, J. Hone, Measurement of the elastic properties and intrinsic strength of monolayer graphene., Science (New York, N.Y.). 321 (2008) 385–8.

[111] A.A. Balandin, Thermal properties of graphene and nanostructured carbon materials, Nature Materials. 10 (2011) 569–581.

[112] A.A. Balandin, S. Ghosh, W. Bao, I. Calizo, D. Teweldebrhan, F. Miao, C.N. Lau, Superior Thermal Conductivity of Single-Layer Graphene, Nano Letters. 8 (2008) 902–

907.

[113] J.S. Bunch, S.S. Verbridge, J.S. Alden, A.M. van der Zande, J.M. Parpia, H.G. Craighead, P.L. McEuen, Impermeable Atomic Membranes from Graphene Sheets, Nano Letters. 8 (2008) 2458–2462.

[114] J.S. Bunch, A.M. van der Zande, S.S. Verbridge, I.W. Frank, D.M. Tanenbaum, J.M. Parpia, H.G. Craighead, P.L. McEuen, Electromechanical resonators from graphene sheets., Science (New York, N.Y.). 315 (2007) 490–3.

[115] M. Li, G. Sun, P. Yin, C. Ruan, K. Ai, Controlling the Formation of Rodlike V_2O_5 Nanocrystals on Reduced Graphene Oxide for High-Performance Supercapacitors, Nano Lett. 5 (2013) 11462–11470.

[116] S.-M. Paek, E. Yoo, I. Honma, Enhanced Cyclic Performance and Lithium Storage Capacity of SnO_2/Graphene Nanoporous Electrodes with Three-Dimensionally Delaminated Flexible Structure, Nano Letters. 9 (2009) 72–75.

[117] H. Tateishi, K. Hatakeyama, C. Ogata, K. Gezuhara, J. Kuroda, A. Funatsu, M. Koinuma, T. Taniguchi, S. Hayami, Y. Matsumoto, Graphene Oxide Fuel Cell, Journal of The Electrochemical Society. 160 (2013) F1175–F1178.

[118] Z. Yin, J. Zhu, Q. He, X. Cao, C. Tan, H. Chen, Q. Yan, H. Zhang, Graphene-Based Materials for Solar Cell Applications, Advanced Energy Materials. 4 (2014) 1300574.

[119] C. Yan, J. Wang, W. Kang, M. Cui, X. Wang, C.Y. Foo, K.J. Chee, P.S. Lee, Highly Stretchable Piezoresistive Graphene-Nanocellulose Nanopaper for Strain Sensors, Advanced Materials. 26 (2014) 2022–2027.

[120] R.-J. Shiue, X. Gan, Y. Gao, L. Li, X. Yao, A. Szep, D. Walker, J. Hone, D. Englund, Enhanced photodetection in graphene-integrated photonic crystal cavity, Applied Physics Letters. 103 (2013) 241109.

[121] H. Chen, M.B. Müller, K.J. Gilmore, G.G. Wallace, D. Li, Mechanically Strong,

Electrically Conductive, and Biocompatible Graphene Paper, Advanced Materials. 20 (2008) 3557–3561.

[122] Y. Wang, J. Lu, L. Tang, H. Chang, J. Li, Graphene Oxide Amplified Electrogenerated Chemiluminescence of Quantum Dots and Its Selective Sensing for Glutathione from Thiol-Containing Compounds, Analytical Chemistry. 81 (2009) 9710–9715.

[123] K.S. Novoselov, V.I. Fal'ko, L. Colombo, P.R. Gellert, M.G. Schwab, K. Kim, A roadmap for graphene, Nature. 490 (2012) 192–200.

[124] K.S. Novoselov, A.K. Geim, S. V Morozov, D. Jiang, Y. Zhang, S. V Dubonos, I. V Grigorieva, A.A. Firsov, Electric field effect in atomically thin carbon films., Science (New York, N.Y.). 306 (2004) 666–9.

[125] J. Chen, M. Duan, G. Chen, Continuous mechanical exfoliation of graphene sheets via three-roll mill, Journal of Materials Chemistry. 22 (2012) 19625.

[126] M. Lotya, Y. Hernandez, P.J. King, R.J. Smith, V. Nicolosi, L.S. Karlsson, F.M. Blighe, S. De, Z. Wang, I.T. McGovern, G.S. Duesberg, J.N. Coleman, Liquid Phase Production of Graphene by Exfoliation of Graphite in Surfactant/Water Solutions, Journal of the American Chemical Society. 131 (2009) 3611–3620.

[127] A.B. Bourlinos, V. Georgakilas, R. Zboril, T.A. Steriotis, A.K. Stubos, Liquid-Phase Exfoliation of Graphite Towards Solubilized Graphenes, Small. 5 (2009) 1841–1845.

[128] Y. Hernandez, V. Nicolosi, M. Lotya, F.M. Blighe, Z. Sun, S. De, I.T. McGovern, B. Holland, M. Byrne, Y.K. Gun'Ko, J.J. Boland, P. Niraj, G. Duesberg, S. Krishnamurthy, R. Goodhue, J. Hutchison, V. Scardaci, A.C. Ferrari, J.N. Coleman, High-yield production of graphene by liquid-phase exfoliation of graphite, Nature Nanotechnology. 3 (2008) 563–568.

[129] X. Li, C.W. Magnuson, A. Venugopal, R.M. Tromp, J.B. Hannon, E.M. Vogel, L. Colombo, R.S. Ruoff, Large-Area Graphene Single Crystals Grown by Low-Pressure

Chemical Vapor Deposition of Methane on Copper, J. Am. Chem. Soc. 133 (2011) 2816–2819.

[130] A. Reina, X. Jia, J. Ho, D. Nezich, H. Son, V. Bulovic, M.S. Dresselhaus, J. Kong, Large Area, Few-Layer Graphene Films on Arbitrary Substrates by Chemical Vapor Deposition, 01 (2018) 19.

[131] X. Li, W. Cai, J. An, S. Kim, J. Nah, D. Yang, R. Piner, A. Velamakanni, I. Jung, E. Tutuc, S.K. Banerjee, L. Colombo, R.S. Ruoff, Large-area synthesis of high-quality and uniform graphene films on copper foils., Science (New York, N.Y.). 324 (2009) 1312–4.

[132] K.S. Kim, Y. Zhao, H. Jang, S.Y. Lee, J.M. Kim, K.S. Kim, J.-H. Ahn, P. Kim, J.-Y. Choi, B.H. Hong, Large-scale pattern growth of graphene films for stretchable transparent electrodes, Nature. 457 (2009) 706–710.

[133] A.J. Patil, J.L. Vickery, T.B. Scott, S. Mann, Aqueous Stabilization and Self-Assembly of Graphene Sheets into Layered Bio-Nanocomposites using DNA, Advanced Materials. 21 (2009) 3159–3164.

[134] G. Wang, B. Wang, X. Wang, J. Park, S. Dou, H. Ahn, K. Kim, Sn/graphene nanocomposite with 3D architecture for enhanced reversible lithium storage in lithium ion batteries, Journal of Materials Chemistry. 19 (2009) 8378.

[135] Q. Cheng, J. Tang, J. Ma, H. Zhang, N. Shinya, L.-C. Qin, Graphene and carbon nanotube composite electrodes for supercapacitors with ultra-high energy density, Physical Chemistry Chemical Physics. 13 (2011) 17615.

[136] Y. Huang, J. Liang, Y. Chen, An Overview of the Applications of Graphene-Based Materials in Supercapacitors, Small. 8 (2012) 1805–1834.

[137] Q. Cheng, J. Tang, J. Ma, H. Zhang, N. Shinya, L.-C. Qin, Graphene and nanostructured MnO_2 composite electrodes for supercapacitors, Carbon. 49 (2011)

2917–2925.

[138] Q. Wu, Y. Xu, Z. Yao, A. Liu, G. Shi, Supercapacitors Based on Flexible Graphene/Polyaniline Nanofiber Composite Films, ACS Nano. 4 (2010) 1963–1970.

[139] D. Zhang, X. Zhang, Y. Chen, P. Yu, C. Wang, Y. Ma, Enhanced capacitance and rate capability of graphene/polypyrrole composite as electrode material for supercapacitors, Journal of Power Sources. 196 (2011) 5990–5996.

[140] Z.-S. Wu, D.-W. Wang, W. Ren, J. Zhao, G. Zhou, F. Li, H.-M. Cheng, Anchoring Hydrous RuO_2 on Graphene Sheets for High-Performance Electrochemical Capacitors, Advanced Functional Materials. 20 (2010) 3595–3602.

[141] R.B. Rakhi, B. Ahmed, M.N. Hedhili, D.H. Anjum, H.N. Alshareef, Effect of Postetch Annealing Gas Composition on the Structural and Electrochemical Properties of Ti_2CT_x MXene Electrodes for Supercapacitor Applications, Chemistry of Materials. 27 (2015) 5314–5323.

[142] J. Yan, C.E. Ren, K. Maleski, C.B. Hatter, B. Anasori, P. Urbankowski, A. Sarycheva, Y. Gogotsi, Flexible MXene/Graphene Films for Ultrafast Supercapacitors with Outstanding Volumetric Capacitance, Advanced Functional Materials. 27 (2017) 1701264.

[143] Q. Shan, X. Mu, M. Alhabeb, C.E. Shuck, D. Pang, X. Zhao, X.-F. Chu, Y. Wei, F. Du, G. Chen, Y. Gogotsi, Y. Gao, Y. Dall'Agnese, Two-dimensional vanadium carbide (V_2C) MXene as electrode for supercapacitors with aqueous electrolytes, Electrochemistry Communications. 96 (2018) 103–107.

[144] O. Barbieri, M. Hahn, A. Herzog, R. Kötz, Capacitance limits of high surface area activated carbons for double layer capacitors, Carbon. 43 (2005) 1303–1310.

[145] Q. Cao, K.-C. Xie, Y.-K. Lv, W.-R. Bao, Process effects on activated carbon with large specific surface area from corn cob, Bioresource Technology. 97 (2006) 110–115.

[146] L. Wei, G. Yushin, Nanostructured activated carbons from natural precursors for electrical double layer capacitors, Nano Energy. 1 (2012) 552–565.

[147] J. Hu, H. Wang, Q. Gao, H. Guo, Porous carbons prepared by using metal–organic framework as the precursor for supercapacitors, Carbon. 48 (2010) 3599–3606.

[148] F.O. Ochai-Ejeh, D.Y. Momodu, M.J. Madito, A.A. Khaleed, K.O. Oyedotun, S.C. Ray, N. Manyala, Nanostructured porous carbons with high rate cycling and floating performance for supercapacitor application, AIP Advances. 8 (2018) 055208.

[149] C. Hu, Fluid coke derived activated carbon as electrode material for electrochemical double layer capacitor, University of Toronto, 2008.

[150] N. Le-Minh, E.C. Sivret, A. Shammay, R.M. Stuetz, Factors affecting the adsorption of gaseous environmental odors by activated carbon: A critical review, Critical Reviews in Environmental Science and Technology. 48 (2018) 341–375.

[151] J. Xu, X. Gu, J. Cao, W. Wang, Z. Chen, Nickel oxide/expanded graphite nanocomposite electrodes for supercapacitor application, Journal of Solid State Electrochemistry. 16 (2012) 2667–2674.

[152] G. Chen, C. Wu, W. Weng, D. Wu, W. Yan, Preparation of polystyrene/graphite nanosheet composite, Polymer. 44 (2003) 1781–1784.

[153] Y.-X. Wang, L. Huang, L.-C. Sun, S.-Y. Xie, G.-L. Xu, S.-R. Chen, Y.-F. Xu, J.-T. Li, S.-L. Chou, S.-X. Dou, S.-G. Sun, Facile synthesis of a interleaved expanded graphite-embedded sulphur nanocomposite as cathode of Li–S batteries with excellent lithium storage performance, Journal of Materials Chemistry. 22 (2012) 4744.

[154] Y. Li, X. Zhao, P. Yu, Q. Zhang, Oriented Arrays of Polyaniline Nanorods Grown on Graphite Nanosheets for an Electrochemical Supercapacitor, Langmuir. 29 (2013) 493–500.

[155] L. Wang, G. Mu, C. Tian, L. Sun, W. Zhou, T. Tan, H. Fu, In Situ Intercalating

Expandable Graphite for Mesoporous Carbon/Graphite Nanosheet Composites as High-Performance Supercapacitor Electrodes, ChemSusChem. 5 (2012) 2442–2450.

[156] T.M. Masikhwa, M.J. Madito, D.Y. Momodu, J.K. Dangbegnon, O. Guellati, A. Harat, M. Guerioune, F. Barzegar, N. Manyala, High performance asymmetric supercapacitor based on CoAl-LDH/GF and activated carbon from expanded graphite, RSC Advances. 6 (2016) 46723–46732.

[157] F. Barzegar, A. Bello, D. Momodu, M.J. Madito, J. Dangbegnon, N. Manyala, Preparation and characterization of porous carbon from expanded graphite for high energy density supercapacitor in aqueous electrolyte, Journal of Power Sources. 309 (2016) 245–253.

[158] F. Barzegar, A. Bello, J.K. Dangbegnon, N. Manyala, X. Xia, Asymmetric supercapacitor based on activated expanded graphite and pinecone tree activated carbon with excellent stability, Applied Energy. 207 (2017) 417–426.

[159] F. Barzegar, A. Bello, J.K. Dangbegnon, N. Manyala, X. Xia, Asymmetric Carbon Supercapacitor with Activated Expanded Graphite as Cathode and Pinecone Tree Activated Carbon as Anode Materials, Energy Procedia. 105 (2017) 4098–4103.

[160] T.M. Masikhwa, M.J. Madito, A. Bello, J.K. Dangbegnon, N. Manyala, High performance asymmetric supercapacitor based on molybdenum disulphide/graphene foam and activated carbon from expanded graphite, Journal of Colloid and Interface Science. 488 (2017) 155–165.

[161] B.E. Conway, Electrochemical supercapacitors: scientific fundamentals and technological applications, Springer S, 2013.

[162] B.E. Conway, Transition from "Supercapacitor" to "Battery" Behavior in Electrochemical Energy Storage, Journal of The Electrochemical Society. 138 (1991) 1539.

[163] C. Peng, S. Zhang, D. Jewell, G.Z. Chen, Carbon nanotube and conducting polymer composites for supercapacitors, Progress in Natural Science. 18 (2008) 777–788.

[164] J.T. Mefford, W.G. Hardin, S. Dai, K.P. Johnston, K.J. Stevenson, Anion charge storage through oxygen intercalation in $LaMnO_3$ perovskite pseudocapacitor electrodes, Nature Materials. 13 (2014) 726–732.

[165] Y. Wang, J. Guo, T. Wang, J. Shao, D. Wang, Y.-W. Yang, Y. Wang, J. Guo, T. Wang, J. Shao, D. Wang, Y.-W. Yang, Mesoporous Transition Metal Oxides for Supercapacitors, Nanomaterials. 5 (2015) 1667–1689.

[166] M. Zheng, X. Xiao, L. Li, P. Gu, X. Dai, H. Tang, Q. Hu, H. Xue, H. Pang, Hierarchically nanostructured transition metal oxides for supercapacitors, Science China Materials. 61 (2018) 185–209.

[167] Q. Zhang, Z. Liu, B. Zhao, Y. Cheng, L. Zhang, H.-H. Wu, M.-S. Wang, S. Dai, K. Zhang, D. Ding, Y. Wu, M. Liu, Design and understanding of dendritic mixed-metal hydroxide nanosheets@N-doped carbon nanotube array electrode for high-performance asymmetric supercapacitors, Energy Storage Materials. 16 (2019) 632–645.

[168] C. Huang, X. Song, Y. Qin, B. Xu, H.C. Chen, Cation exchange reaction derived amorphous bimetal hydroxides as advanced battery materials for hybrid supercapacitors, Journal of Materials Chemistry A. 6 (2018) 21047–21055.

[169] D. Choi, G.E. Blomgren, P.N. Kumta, Fast and Reversible Surface Redox Reaction in Nanocrystalline Vanadium Nitride Supercapacitors, Advanced Materials. 18 (2006) 1178–1182.

[170] X. Lu, M. Yu, T. Zhai, G. Wang, S. Xie, T. Liu, C. Liang, Y. Tong, Y. Li, High Energy Density Asymmetric Quasi-Solid-State Supercapacitor Based on Porous Vanadium Nitride Nanowire Anode, Nano Letters. 13 (2013) 2628–2633.

[171] J. Theerthagiri, G. Durai, K. Karuppasamy, P. Arunachalam, V. Elakkiya, P.

Kuppusami, T. Maiyalagan, H.-S. Kim, Recent advances in 2-D nanostructured metal nitrides, carbides, and phosphides electrodes for electrochemical supercapacitors − A brief review, Journal of Industrial and Engineering Chemistry. 67 (2018) 12–27.

[172] A.M. Navarro-Suárez, K.L. Van Aken, T. Mathis, T. Makaryan, J. Yan, J. Carretero-González, T. Rojo, Y. Gogotsi, Development of asymmetric supercapacitors with titanium carbide-reduced graphene oxide couples as electrodes, Electrochimica Acta. 259 (2018) 752–761.

[173] M. Yu, Y. Han, X. Cheng, L. Hu, Y. Zeng, M. Chen, F. Cheng, X. Lu, Y. Tong, Holey Tungsten Oxynitride Nanowires: Novel Anodes Efficiently Integrate Microbial Chemical Energy Conversion and Electrochemical Energy Storage, Advanced Materials. 27 (2015) 3085–3091.

[174] D. Shu, H. Cheng, C. Lv, M.A. Asi, L. Long, C. He, X. Zou, Z. Kang, Soft-template synthesis of vanadium oxynitride-carbon nanomaterials for supercapacitors, International Journal of Hydrogen Energy. 39 (2014) 16139–16150.

[175] J.P. Cheng, J. Zhang, F. Liu, Recent development of metal hydroxides as electrode material of electrochemical capacitors, RSC Adv. 4 (2014) 38893–38917.

[176] V. Gupta, S. Gupta, N. Miura, Potentiostatically deposited nanostructured $Co_xNi_{1−x}$ layered double hydroxides as electrode materials for redox-supercapacitors, Journal of Power Sources. 175 (2008) 680–685.

[177] Z. Wu, Y. Zhu, X. Ji, C.E. Banks, Transition Metal Oxides as Supercapacitor Materials, in: Springer, Cham, 2016: pp. 317–344.

[178] S. Rao Popuri, A. Artemenko, C. Labrugere, M. Miclau, A. Villesuzanne, M. Pollet, $VO_2(A)$: Reinvestigation of crystal structure, phase transition and crystal growth mechanisms, Journal of Solid State Chemistry. 213 (2014) 79–86.

[179] Y. Zhang, J. Zheng, T. Hu, F. Tian, C. Meng, Synthesis and supercapacitor electrode of

VO$_2$(B)/C core–shell composites with a pseudocapacitance in aqueous solution, Applied Surface Science. 371 (2016) 189–195.

[180] Q. Qu, Y. Zhu, X. Gao, Y. Wu, Core-Shell Structure of Polypyrrole Grown on V$_2$O$_5$ Nanoribbon as High Performance Anode Material for Supercapacitors, Advanced Energy Materials. 2 (2012) 950–955.

[181] X. Zhou, Q. Chen, A. Wang, J. Xu, S. Wu, J. Shen, Bamboo-like Composites of V$_2$O$_5$ /Polyindole and Activated Carbon Cloth as Electrodes for All-Solid-State Flexible Asymmetric Supercapacitors, ACS Appl. Mater. Interfaces. 8 (2016) 3776–3783.

[182] H.Y. Lee, J.B. Goodenough, Ideal Supercapacitor Behavior of Amorphous V$_2$O$_5$·nH$_2$O in Potassium Chloride (KCl) Aqueous Solution, Journal of Solid State Chemistry. 148 (1999) 81–84.

[183] M. Yu, Y. Zeng, Y. Han, X. Cheng, W. Zhao, C. Liang, Y. Tong, H. Tang, X. Lu, Valence-Optimized Vanadium Oxide Supercapacitor Electrodes Exhibit Ultrahigh Capacitance and Super-Long Cyclic Durability of 100 000 Cycles, Advanced Functional Materials. 25 (2015) 3534–3540.

[184] G. Wang, X. Lu, Y. Ling, T. Zhai, H. Wang, Y. Tong, Y. Li, LiCl/PVA Gel Electrolyte Stabilizes Vanadium Oxide Nanowire Electrodes for Pseudocapacitors, ACS Nano. 6 (2012) 10296–10302.

[185] S.D. Perera, B. Patel, N. Nijem, K. Roodenko, O. Seitz, J.P. Ferraris, Y.J. Chabal, K.J. Balkus, Vanadium Oxide Nanowire-Carbon Nanotube Binder-Free Flexible Electrodes for Supercapacitors, Advanced Energy Materials. 1 (2011) 936–945.

[186] H. Li, L. Peng, Y. Zhu, X. Zhang, G. Yu, Achieving High-Energy-High-Power Density in a Flexible Quasi-Solid-State Sodium Ion Capacitor, Nano Letters. 16 (2016) 5938–5943.

[187] Y.Z. Lian-Mei Chen, Qiong-Yu Lai, Yan-Jing Hao, Xiao-YangJi, Investigations on

capacitive properties of the AC/V$_2$O$_5$ hybrid supercapacitor in various aqueous electrolytes, Journal of Alloys and Compounds. 467 (2009) 465–471.

[188] J. Yang, T. Lan, J. Liu, Y. Song, M. Wei, Supercapacitor electrode of hollow spherical V$_2$O$_5$ with a high pseudocapacitance in aqueous solution, Electrochimica Acta. 105 (2013) 489–495.

[189] L. Liang, H. Liu, W. Yang, Fabrication of VO$_2$(B) hybrid with multiwalled carbon nanotubes to form a coaxial structure and its electrochemical capacitance performance, Journal of Alloys and Compounds. 559 (2013) 167−173.

[190] B.D. Ngom, M. Chaker, A. Diallo, I.G. Madiba, S. Khamlich, N. Manyala, O. Nemraoui, R. Madjoe, A.C. Beye, M. Maaza, Competitive growth texture of pulsed laser deposited vanadium dioxide nanostructures on a glass substrate, Acta Materialia. 65 (2014) 32–41.

[191] A. Diallo, N.M. Ndiaye, B.D. Ngom, S. Khamlich, K. Talla, S. Ndiaye, N. Manyala, O. Nemraoui, R. Madjoe, A.C. Beye, M. Maaza, Effect of substrate temperature on the structure and the metal insulator transition in pulsed laser deposed VO$_2$\films on soda lime glass, Journal of Optics. 44 (2015) 36–44.

[192] X.-J.J. Ma, W.-B. Bin Zhang, L.-B. Bin Kong, Y.-C.C. Luo, L. Kang, VO$_2$: from negative electrode material to symmetric electrochemical capacitor, RSC Advances. 5 (2015) 97239–97247.

[193] Q.H. Do, C. Zeng, C. Zhang, B. Wang, J. Zheng, Supercritical fluid deposition of vanadium oxide on multi-walled carbon nanotube buckypaper for supercapacitor electrode application Related content, Nanotechnology. 22 (2011) 365–402.

[194] B. Saravanakumar, K.K. Purushothaman, G. Muralidharan, Interconnected V$_2$O$_5$ Nanoporous Network for High-Performance Supercapacitors, ACS Appl. Mater. Interfaces. 4 (2012) 4484−4490.

[195] B. Saravanakumar, K.K. Purushothaman, G. Muralidharan, Interconnected V_2O_5 Nanoporous Network for High-Performance Supercapacitors, ACS Applied Materials & Interfaces. 4 (2012) 4484–4490.

[196] J. Xu, H. Sun, Z. Li, S. Lu, X. Zhang, S. Jiang, Q. Zhu, G.S. Zakharova, Synthesis and electrochemical properties of graphene/V_2O_5 xerogels nanocomposites as supercapacitor electrodes, Solid State Ionics. 262 (2014) 234–237.

[197] Y. Wang, Z. Zhang, Synthesis and field emission property of VO_2 nanorods with a body-centered-cubic structure, Physica E: Low-Dimensional Systems and Nanostructures. 41 (2009) 548–551.

[198] Y. Oka, S. Sato, T. Yao, N. Yamamoto, Crystal Structures and Transition Mechanism of VO_2(A), Journal of Solid State Chemistry. 141 (1998) 594–598.

[199] F. Théobald, Étude hydrothermale du système VO_2-$VO_{2,5}$-H_2O, Journal of the Less Common Metals. 53 (1977) 55–71.

[200] C. Leroux, G. Nihoul, G. Van Tendeloo, From VO_2(B) to VO_2(R): Theoretical structures of VO_2 polymorphs and *in situ* electron microscopy, Physical Review B. 57 (1998) 5111–5121.

[201] C. Chen, Y. Zhu, Y. Zhao, J.H. Lee, H. Wang, A. Bernussi, M. Holtz, Z. Fan, VO_2 multidomain heteroepitaxial growth and terahertz transmission modulation, Applied Physics Letters. 97 (2010) 211905.

[202] X. Xia, D. Chao, C.F. Ng, J. Lin, Z. Fan, H. Zhang, Z.X. Shen, H.J. Fan, VO_2 nanoflake arrays for supercapacitor and Li-ion battery electrodes: performance enhancement by hydrogen molybdenum bronze as an efficient shell material, Mater. Horiz. 2 (2015) 237–244.

[203] Y. Oka, T. Yao, N. Yamamoto, Powder X-ray crystal structure of VO_2(A), Journal of Solid State Chemistry. 86 (1990) 116–124.

[204] X. Pan, Y. Zhao, G. Ren, Z. Fan, Highly conductive VO_2 treated with hydrogen for supercapacitors, Chemical Communications. 49 (2013) 3943.

[205] X.J. Ma, W. Bin Zhang, L. Bin Kong, Y.C. Luo, L. Kang, VO_2: From negative electrode material to symmetric electrochemical capacitor, RSC Advances. 5 (2015) 97239–97247.

[206] X. Xia, D. Chao, C.F. Ng, J. Lin, Z. Fan, H. Zhang, Z.X. Shen, H.J. Fan, VO_2 nanoflake arrays for supercapacitor and Li-ion battery electrodes: performance enhancement by hydrogen molybdenum bronze as an efficient shell material, Mater. Horiz. 2 (2015) 237–244.

[207] O. Kartachova, A.M. Glushenkov, Y. Chen, H. Zhang, X.J. Dai, Y. Chen, Electrochemical capacitance of mesoporous tungsten oxynitride in aqueous electrolytes, Journal of Power Sources. 220 (2012) 298–305.

[208] C. Zhu, Y. Sun, D. Chao, X. Wang, P. Yang, X. Zhang, H. Huang, H. Zhang, H.J. Fan, A 2.0 V capacitive device derived from shape-preserved metal nitride nanorods, Nano Energy. 26 (2016) 1–6.

[209] L. Toth, Transition Metal Carbides and Nitrides., Elsevier Science, 1971.

[210] A.M. Glushenkov, D. Hulicova-Jurcakova, D. Llewellyn, G.Q. Lu, Y. Chen, Structure and Capacitive Properties of Porous Nanocrystalline VN Prepared by Temperature-Programmed Ammonia Reduction of V_2O_5, Chemistry of Materials. 22 (2010) 914–921.

[211] J. Buha, I. Djerdj, M. Antonietti, M. Niederberger, Thermal Transformation of Metal Oxide Nanoparticles into Nanocrystalline Metal Nitrides Using Cyanamide and Urea as Nitrogen Source, Chem. Mater. 19 (2007) 3499–3505.

[212] C. Giordano, C. Erpen, W. Yao, B. Milke, M. Antonietti, Metal Nitride and Metal Carbide Nanoparticles by a Soft Urea Pathway, Chemistry of Materials. 21 (2009)

5136–5144.

[213] R.L. Porto, R. Frappier, J.B.B. Ducros, C. Aucher, H. Mosqueda, S. Chenu, B. Chavillon, F. Tessier, F. Cheviré, T. Brousse, Titanium and vanadium oxynitride powders as pseudo-capacitive materials for electrochemical capacitors, in: Electrochimica Acta, Pergamon, 2012: pp. 257–262.

[214] Y.-J.B. Ting, H. Wu, N.P. Kherani, K. Lian, Development of pseudocapacitive molybdenum oxide–nitride for electrochemical capacitors, Materials Chemistry and Physics. 154 (2015) 118–124.

[215] C.M. Ghimbeu, E. Raymundo-Piñero, P. Fioux, F.F. Béguin, C. Vix-Guterl, Vanadium nitride/carbon nanotube nanocomposites as electrodes for supercapacitors, Journal of Materials Chemistry. 21 (2011) 13268.

[216] A. Morel, Y. Borjon-Piron, R.L. Porto, T. Brousse, D. Bélanger, Suitable Conditions for the Use of Vanadium Nitride as an Electrode for Electrochemical Capacitor, Journal of The Electrochemical Society. 163 (2016) A1077–A1082.

[217] B. Gao, X. Li, X. Guo, X. Zhang, X. Peng, L. Wang, J. Fu, P.K. Chu, K. Huo, Nitrogen-Doped Carbon Encapsulated Mesoporous Vanadium Nitride Nanowires as Self-Supported Electrodes for Flexible All-Solid-State Supercapacitors, Advanced Materials Interfaces. 2 (2015) 1500211.

[218] R. Lucio-Porto, S. Bouhtiyya, J.F. Pierson, A. Morel, F. Capon, P. Boulet, T. Brousse, VN thin films as electrode materials for electrochemical capacitors, Electrochimica Acta. 141 (2014) 203–211.

[219] B.M. Gray, A.L. Hector, M. Jura, J.R. Owen, J. Whittam, Effect of oxidative surface treatments on charge storage at titanium nitride surfaces for supercapacitor applications, Journal of Materials Chemistry A. 5 (2017) 4550–4559.

[220] G.H. An, D.Y. Lee, H.J. Ahn, Vanadium nitride encapsulated carbon fibre networks

with furrowed porous surfaces for ultrafast asymmetric supercapacitors with robust cycle life, Journal of Materials Chemistry A. 5 (2017) 19714–19720.

[221] D. Ruan, R. Lin, K. Jiang, X. Yu, Y. Zhu, Y. Fu, Z. Wang, H. Yan, W. Mai, High-Performance Porous Molybdenum Oxynitride Based Fiber Supercapacitors, ACS Applied Materials and Interfaces. 9 (2017) 29699–29706.

[222] F. Cheng, C. He, D. Shu, H. Chen, J. Zhang, S. Tang, D.E. Finlow, D. Shua, H. Chen, J. Zhang, S. Tang, D.E. Finlow, Preparation of nanocrystalline VN by the melamine reduction of V_2O_5 xerogel and its supercapacitive behavior, Materials Chemistry and Physics. 131 (2011) 268–273.

[223] Y. Shi, L. Peng, Y. Ding, Y. Zhao, G. Yu, Nanostructured conductive polymers for advanced energy storage, Chemical Society Reviews. 44 (2015) 6684–6696.

[224] G.A. Snook, P. Kao, A.S. Best, Conducting-polymer-based supercapacitor devices and electrodes, Journal of Power Sources. 196 (2011) 1–12.

[225] E. Frackowiak, V. Khomenko, K. Jurewicz, K. Lota, F. Béguin, Supercapacitors based on conducting polymers/nanotubes composites, Journal of Power Sources. 153 (2006) 413–418.

[226] D. Alemu, H.-Y. Wei, K.-C. Ho, C.-W. Chu, Highly conductive PEDOT:PSS electrode by simple film treatment with methanol for ITO-free polymer solar cells, Energy & Environmental Science. 5 (2012) 9662.

[227] H. Lin, L. Li, J. Ren, Z. Cai, L. Qiu, Z. Yang, H. Peng, Conducting polymer composite film incorporated with aligned carbon nanotubes for transparent, flexible and efficient supercapacitor, Scientific Reports. 3 (2013) 1353.

[228] P.L.T. J. Chmiola,G. Yushin,Y. Gogotsi, C. Portet,P. Simon, Anomalous Increase in Carbon Capacitance at Pore Sizes Less Than 1 Nanometer, Science, New Series. 313 (2006) 1760–1763.

[229] C. Largeot, C. Portet, J. Chmiola, P.-L. Taberna, Y. Gogotsi, P. Simon, Relation between the Ion Size and Pore Size for an Electric Double-Layer Capacitor, J. AM. Chem. Soc. 130 (2008) 2730–2731.

[230] S. Lindberg, Novel electrolytes for next-generation hybrid supercapacitors, Chalmers University of Technology, Sweden, 2018.

[231] A. Lewandowski, A. Olejniczak, M. Galinski, I. Stepniak, Performance of carbon–carbon supercapacitors based on organic, aqueous and ionic liquid electrolytes, Journal of Power Sources. 195 (2010) 5814–5819.

[232] K. Fic, G. Lota, M. Meller, E. Frackowiak, Novel insight into neutral medium as electrolyte for high-voltage supercapacitors, Energy Environ. Sci. 5 (2012) 5842–5850.

[233] B.E. Conway, V. Birss, J. Wojtowicz, The role and utilization of pseudocapacitance for energy storage by supercapacitors, Journal of Power Sources. 66 (1997) 1–14.

[234] Z. Chen, Y. Qin, D. Weng, Q. Xiao, Y. Peng, X. Wang, H. Li, F. Wei, Y. Lu, Design and Synthesis of Hierarchical Nanowire Composites for Electrochemical Energy Storage, Advanced Functional Materials. 19 (2009) 3420–3426.

[235] L. Deng, G. Zhang, L. Kang, Z. Lei, C. Liu, Z.-H.H. Liu, Graphene/VO$_2$ hybrid material for high performance electrochemical capacitor, Electrochimica Acta. 112 (2013) 448–457.

[236] E. Frackowiak, G. Lota, J. Pernak, Room-temperature phosphonium ionic liquids for supercapacitor application, Physical Properties of Ionic Liquids: Database and Evaluation Journal of Physical and Chemical Reference Data. 86 (2005) 1475.

[237] K.T. Takaya Sato, Gen Masuda, Electrochemical properties of novel ionic liquids for electric double layer capacitor applications, Electrochimica Acta . 49 (2004) 3603–3611.

[238] R.D. Rogers, K.R. Seddon, Perspective article: Ionic Liquids Solvents of the Future?,

Science. 302 (2003) 792.

[239] J.G. Huddleston, A.E. Visser, W.M. Reichert, H.D. Willauer, G.A. Broker, R.D. Rogers, Characterization and comparison of hydrophilic and hydrophobic room temperature ionic liquids incorporating the imidazolium cation, Green Chemistry. 3 (2001) 156–164.

[240] J. Salminen, N. Papaiconomou, R.A. Kumar, J.-M. Lee, J. Kerr, J. Newman, J.M. Prausnitz, Physicochemical properties and toxicities of hydrophobic piperidinium and pyrrolidinium ionic liquids, Fluid Phase Equilibria. 261 (2007) 421–426.

[241] D. Mecerreyes, Polymeric ionic liquids: Broadening the properties and applications of polyelectrolytes, Progress in Polymer Science. 36 (2011) 1629–1648.

[242] A. Oickle, A Systematic study of self-discharge mechanisms in carbon-based, aqueous electrolyte electrochemical capacitors, Dalhousie University Halifax, Nova Scotia, 2013.

[243] A. Brandt, S. Pohlmann, A. Varzi, A. and Balducci, S. Passerini, Ionic liquids in supercapacitors, Ionic Liquids for Energy Applications. 38 (2013) 554–559.

[244] A. Brandt, S. Pohlmann, A. Varzi, A. Balducci, S. Passerini, Ionic liquids in supercapacitors, MRS Bulletin. 38 (2013) 554–559.

[245] A. Djire, J.Y. Ishimwe, S. Choi, L.T. Thompson, Enhanced performance for early transition metal nitrides via pseudocapacitance in protic ionic liquid electrolytes, Electrochemistry Communications. 77 (2017) 19–23.

[246] G.A. Tiruye, Application of ionic liquids, innovative polymer electrlytes and novel carbonaceous materilas in supercapacitors, Electrochemical Process Unit, IMDEA Energy Institute Madrid, Spain, 2016.

[247] C. Zhong, Y. Deng, W. Hu, J. Qiao, L. Zhang, J. Zhang, A review of electrolyte materials and compositions for electrochemical supercapacitors, Chemical Society

Reviews. 44 (2015) 7484–7539.

[248] M. Ue, K. Ida, S. Mori, Electrochemical Properties of Organic Liquid Electrolytes Based on Quaternary Onium Salts for Electrical Double-Layer Capacitors, Journal of The Electrochemical Society. 141 (1994) 2989.

[249] T. Abdallah, D. Lemordant, B. Claude-Montigny, Are room temperature ionic liquids able to improve the safety of supercapacitors organic electrolytes without degrading the performances?, Journal of Power Sources. 201 (2012) 353–359.

[250] C.Y. Foo, A. Sumboja, D.J.H. Tan, J. Wang, P.S. Lee, Flexible and highly scalable V_2O_5-rGO electrodes in an organic electrolyte for supercapacitor devices, Advanced Energy Materials. 4 (2014) 1400236.

[251] A. M., A. Paul, Importance of Electrode Preparation Methodologies in Supercapacitor Applications, ACS Omega. 2 (2017) 8039–8050.

[252] M. Moussa, M.F. El-Kady, Z. Zhao, P. Majewski, J. Ma, Recent progress and performance evaluation for polyaniline/graphene nanocomposites as supercapacitor electrodes, Nanotechnology. 27 (2016) 442001.

[253] A.A. Mirghni, M.J. Madito, K.O. Oyedotun, T.M.M. Masikhwa, N.M. Ndiaye, S.J. Ray, N. Manyala, A high energy density asymmetric supercapacitor utilizing a nickel phosphate/graphene foam composite as the cathode and carbonized iron cations adsorbed onto polyaniline as the anode, RSC Advances. 8 (2018) 11608–11621.

[254] C. Arbizzani, M. Mastragostino, F. Soavi, New trends in electrochemical supercapacitors, Journal of Power Sources. 100 (2001) 164–170.

[255] A. Balducci, W.A. Henderson, M. Mastragostino, S. Passerini, P. Simon, F. Soavi, Cycling stability of a hybrid activated carbon//poly(3-methylthiophene) supercapacitor with N-butyl-N-methylpyrrolidinium bis(trifluoromethanesulfonyl)imide ionic liquid as electrolyte, Electrochimica Acta. 50 (2005) 2233–2237.

[256] M.E. Guittet, Vertically aligned carbon nanotubes for supercapacitor and the effect of surface functionalization to its performance, Ecole polytechnique federale de Lausanne School of life science; California, 2011.

[257] F. Bonaccorso, L. Colombo, G. Yu, M. Stoller, V. Tozzini, A.C. Ferrari, R.S. Ruoff, V. Pellegrini, Graphene, related two-dimensional crystals, and hybrid systems for energy conversion and storage, Science. 347 (2015) 1246501–1246501.

[258] J. Bobacka, Potential Stability of All-Solid-State Ion-Selective Electrodes Using Conducting Polymers as Ion-to-Electron Transducers, Anal. Chem. 71 (1999) 4932–4937.

[259] Y. Lu, F. Zhang, T. Zhang, K. Leng, L. Zhang, X. Yang, Y. Ma, Y. Huang, M. Zhang, Y. Chen, Synthesis and supercapacitor performance studies of N-doped graphene materials using o-phenylenediamine as the double-N precursor, Carbon. 63 (2013) 508–516.

[260] P. Huang, C. Lethien, S. Pinaud, K. Brousse, R. Laloo, V. Turq, M. Respaud, A. Demortiere, B. Daffos, P.L. Taberna, B. Chaudret, Y. Gogotsi, P. Simon, A. Demortière, B. Daffos, P.L. Taberna, B. Chaudret, Y. Gogotsi, P. Simon, On-chip and freestanding elastic carbon films for micro-supercapacitors., Science. 351 (2016) 691–695.

[261] Wataru Sugimoto, Hideki Iwata, Katsunori Yokoshima, and Yasushi Murakami, Y. Takasu, Proton and Electron Conductivity in Hydrous Ruthenium Oxides Evaluated by Electrochemical Impedance Spectroscopy: The Origin of Large Capacitance, (2005).

[262] P. Ratajczak, Design of High Voltage AC/AC Electrochemical Capacitors in Aqueous Electrolyte, Poznan University of Technology, Poland, 2015.

[263] A. Laheäär, P. Przygocki, Q. Abbas, F. Béguin, Appropriate methods for evaluating the efficiency and capacitive behavior of different types of supercapacitors,

Electrochemistry Communications. 60 (2015) 21–25.

[264] A. Bello, F. Barzegar, M.J. Madito, D.Y. Momodu, A.A. Khaleed, T.M. Masikhwa, J.K. Dangbegnon, N. Manyala, Stability studies of polypyrole- derived carbon based symmetric supercapacitor via potentiostatic floating test, Electrochimica Acta. 213 (2016) 107–114.

[265] A. Burke, R&D considerations for the performance and application of electrochemical capacitors, Electrochimica Acta. 53 (2007) 1083–1091.

[266] D. Weingarth, A. Foelske-Schmitz, R. Kötz, Cycle versus voltage hold – Which is the better stability test for electrochemical double layer capacitors?, Journal of Power Sources. 225 (2013) 84–88.

_____

3.0 Synthesis procedure and characterisation techniques

The structural, morphological and textural characterization techniques play importance role in the conception of nanostructures materials. These techniques are crucial in the scientific field to enable the researchers to characterize the synthesized materials. Hydrothermal, freeze-drying and CVD techniques were used in this thesis to synthesize the materials. The techniques adopted to characterize the materials were X-ray diffraction (XRD), Raman spectroscopy, physisorption analysis, scanning electron microscope (SEM), transmission electron microscope (TEM), Brunauer-Emmett-Teller (BET) analysis and X-ray photoelectron spectroscopy (XPS). The electrochemical analysis was carried out to evaluate the electrochemical performance of the electrode materials in supercapacitors through cyclic voltammetry (CV), galvanostatic charge-discharge (GCD), electrochemical impedance spectroscopy (EIS) and stability test.

3.1. Experimental techniques

3.1.1 Hydrothermal and Solvothermal methods

The hydrothermal technique has been widely adopted for synthesizing single crystals such as quartz, metal oxides, semiconductor powders and composite materials [1,2]. The hydrothermal method is a simple technique that takes place in closed system conditions leading to the decomposition or chemical reactions between precursors in the presence of a solvent at a high-temperature. The nanoparticle growth process involves crystal nucleation followed by growth of crystallites as a function of the synthesis temperature, pH value, reaction time, type of solvent and the total autoclave volume. The reaction in the hydrothermal technique is carried out in an apparatus named Teflon lined autoclave.

The hydrothermal process has the capability to control the crystal size, shape distribution as well as the crystallinity of the metal oxide and composites nanostructures [3,4]. The hydrothermal route is similar to the solvothermal process with different solvent used in the reaction. The hydrothermal method commonly uses water as a solvent while for solvothermal method, isopropanol, methanol, acetonitrile dimethyl sulfoxide solutions can be generally used as the solvent at the temperature superior to their boiling point [5]. The homogeneous and heterogeneous nucleation process can also be controlled in a solvothermal method by using inorganic additives [1]. Figure 3.1 shows the hydrothermal and the solvothermal device used in this research.

Figure 3.1: Hydrothermal and solvothermal device used for heating.

3.1.2 Freeze-drying method

The freeze-drying also termed as lyophilisation entails the removal of residual water by cooling a solution in liquid nitrogen under vacuum. Generally, the freeze-dryer is constituted of a drying chamber with temperature controlled shelves which are linked to a condenser

chamber. This method is operated at a very low temperature that is maintained by the series of plates or coils in the condenser chamber.

This process has been reported for various types of electrochemically active materials including carbon [6] and various metal oxides materials [7–9]. The freeze-drying process has also been used successfully for the growth of vanadium oxides and composite materials comprising of different nano-architectures such as nanowire [9], nanosheets [10] and aerogels [11,12] among others

a) Synthesis of three dimensional vanadium pentoxide (3D V$_2$O$_5$) and vanadium pentoxide/graphene foam (V$_2$O$_5$/GF) composites

The pristine 3D V$_2$O$_5$ was synthesized by mixing 0.36 g of bulk V$_2$O$_5$ (analytical grade) and 5 mL of 30% H$_2$O$_2$ to 30 mL of deionized water (DI) under vigorous stirring to obtain a red solution. A 30 mL portion of the red solution was transferred into a sealed 50 mL teflon-lined autoclave and kept at a 190 °C temperature for a period of 20 h to generate a gel. Consequently, the gel was freeze-dried to obtain the final product V$_2$O$_5$ sample. Figure 3.2 displays the synthesis route used to prepare the pristine 3D V$_2$O$_5$.
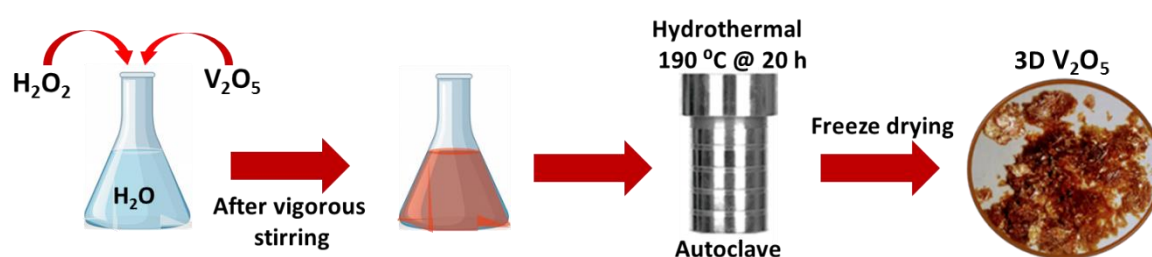
Figure 3.2: Schematic of the synthesis process of 3D V$_2$O$_5$.

The same procedure described for the synthesis of pristine V$_2$O$_5$ was repeated for the synthesis of the V$_2$O$_5$/GF composites with GF being introduced along with the precursors. Simply, varying mass contents of GF (50 – 200 mg) was added to the 30 mL of DI before

adding the precursors to obtain V_2O_5/GF-50 mg, V_2O_5/GF-100 mg, V_2O_5/GF-150 mg and V_2O_5/GF-200 mg composites.

b) Preparation of monoclinic vanadium dioxide VO_2(M)

Figure 3.3 shows the schematic diagram of the synthesis used in the preparation of VO_2 sample at various growth times (2.5, 4, 6 and 12 h) as shown in Figure 2.2. Initially, bulk V_2O_5 powder (1.2 g) and $H_2C_2O_4 \cdot 2H_2O$ in a molar ratio of 1:3 were dissolved in 40 mL of deionized water under vigorous stirring at 80 °C for 3 h until a clear blue VOC_2O_4 solution (0.33 M) was formed.

Then 6 mL of the obtained precursor VOC_2O_4 was added to 60 mL of isopropanol under vigorous stirring for 20 min at 80 °C. The final homogeneous solution was transferred into a sealed Teflon-lined stainless-steel autoclave and kept at a temperature of 200 °C for different growth time varying from 2 h 30 min to 12 h. After cooling to room temperature, the black powder was centrifuged, washed several times with deionized water and ethanol and dried at 60 °C for 6 h to form the VO_2 (A) and VO_2 (B) materials.
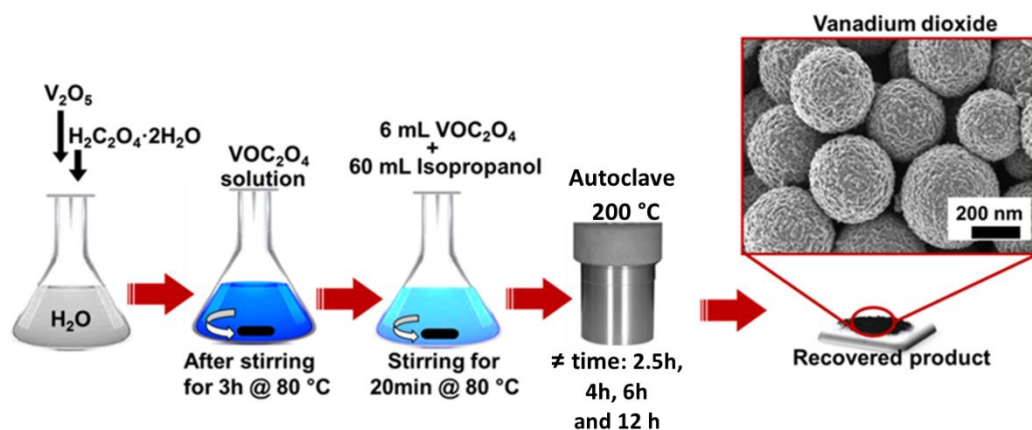
Figure 3.3: Synthesis procedure of the vanadium dioxide (VO_2(M)).

3.1.3 Atmospheric Pressure Chemical Vapour Deposition technique (APCVD)

CVD technique includes photochemical vapor deposition, atmospheric pressure chemical vapor deposition (APCVD), photon (laser) chemical vapor deposition (PHCVD), metal-

organic chemical vapor deposition (MOCVD), chemical beam epitaxy, low pressure chemical vapor deposition (LPCVD), chemical vapor infiltration, plasma-enhanced chemical vapor deposition (PECVD) and plasma-assisted chemical vapor deposition as presented in Figure 3.4. The chemical vapour deposition technique (CVD) is the condensation of a compound or compounds from the gas phase on to a substrate where reaction occurs to produce a solid deposit. The substrate used in CVD method is exposed to numerous volatile precursors which react and/or decompose on the substrate surface to synthesize the intended deposit [13]. The CVD technique is efficient and very popular method due to their ability to grow high quality, large-scale, multiple formats (single layer, multi-layer, composite), uniform layer deposition materials and to control dimensions and structures at reasonably low temperatures [14,15]. The growth route have the ability to grow different form including thin films, powders and single crystals of various materials such as oxides, carbon, nitride, oxynitride and carbides [16–20].

Additionally, the CVD technique is commonly used for the synthesis of the amorphous materials [21]. The CVD process of the materials are primarily controlled by the deposition temperature, reaction time, gas phase reaction, reactant transport to the surface, the chemical reaction on the surface, the desorption of reaction products from the surface and the total pressure gas flows [22]. These numerous variation parameters involve a wide range of different physical and chemical properties of the materials.

However, the APCVD is a preferred fabrication technique for an easy transition into industries due to their lower operating cost, fewer resources, fast growth and generally simpler in design [23]. In this work, the APCVD in Figure 3.4 was used to prepare the vanadium-based materials.
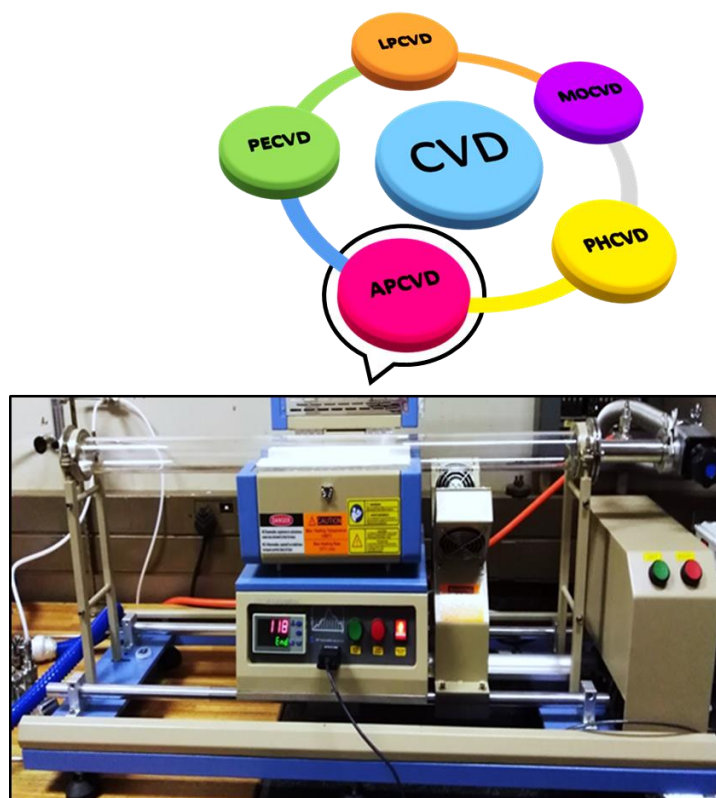
Figure 3.4: Some of different CVD methods on the top, atmospheric pressure chemical vapour deposition technique system.

c) Preparation of Carbon-vanadium oxynitride (C-V$_2$NO) materials

Figure 3.5 presents the diagram illustrating the procedure used to synthesize the C-V$_2$NO sample at a nitridation temperature of 700 °C with the same procedure used for other temperatures. The C-V$_2$NO materials were synthesized by mixing analytical grade chemicals: 0.5 g of ammonium metavanadate (NH$_4$VO$_3$, 99%) and 5 g of melamine (C$_3$H$_6$N$_6$, 99%) in an agate mortar with a few drops of ethanol (CH$_3$CH$_2$OH, 99%) to make a homogeneous slurry. This was inserted into a quartz tube furnace and heated to 700 °C at a heating rate of 18 °C min^{-1} with the nitrogen (N$_2$) flow rate of 200 standard cubic centimeter per minute (sccm) before being kept at that temperature for 2 h. After cooling down to room temperature, the final product was obtained and labelled as C-V$_2$NO@700 °C. This process was repeated at different growth temperatures of 800 °C and 900 °C to form C-V$_2$NO@800 °C and C-V$_2$NO@900 °C.
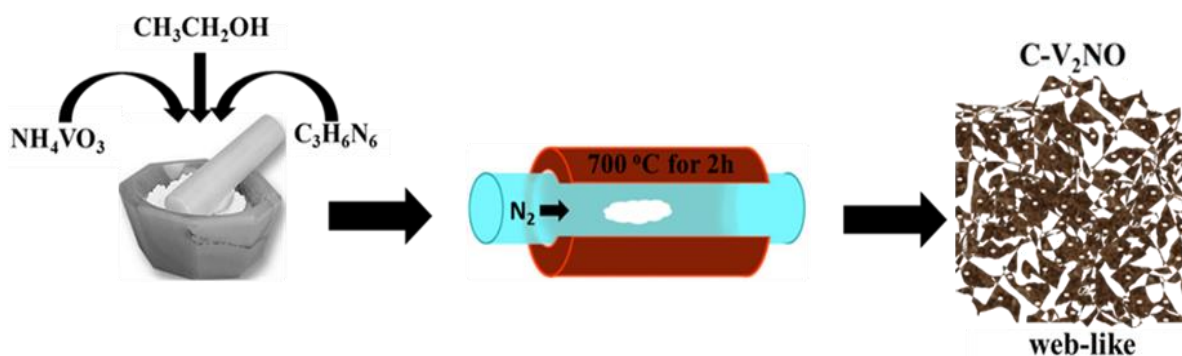
Figure 3.5: Diagram illustration of the preparation method of C-V$_2$NO sample at a nitridation temperature of 700 °C.

d) Synthesis of vanadium dioxide/activated extended graphite composite (VO$_2$/AEG)

Figure 3.6 presents the schematic diagram used to synthesize the C-V$_2$NO sample at a nitridation temperature of 700 °C. The same procedure were used for other temperatures (800 °C and 900 °C). The C-V$_2$NO materials were synthesized by mixing 1.8 g of NH$_4$VO$_3$ and 90 mg of AEG in an agate mortar. The mixture was inserted into a quartz tube furnace and heated to 900 °C at a heating rate of 2 °C min^{-1} and kept at that temperature for 2 h under nitrogen (N$_2$) atmosphere. After cooling down to room temperature under a flow of nitrogen. The resulting black powder was ground in an agate mortar to obtain the final product (VO$_2$/AEG composite).
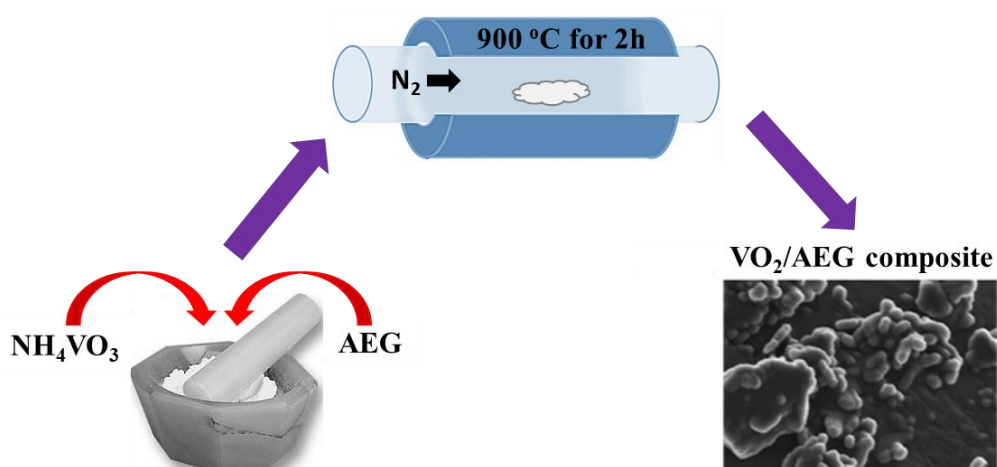
Figure 3.6: Schematic of the synthesis route of VO$_2$/AEG composites.

3.2 Physical Characterization techniques

3.2.1 X-ray diffraction

The X-ray diffraction (XRD) is used for the fine characterization of massive crystallized materials or powders of metals, ceramic minerals, pharmaceutical compounds, organometallic complexes and metallo-organic materials. This technique was discovered in 1912 by Max von Laue which showed that the manner of the diffraction reveals the structure of the crystal [24]. XRD method is developed to investigate the crystallinity, chemical analysis, stress measurement, phase equilibria, particle size and orientation of one crystal or ensemble of orientations in a polycrystalline aggregate [25].

The X-ray diffraction is a powerful, versatile, non-destructive analytical technique. The X-ray diffraction peaks are generated by constructive interference of monochromatic X-ray beam scattered by each set of lattice planes. The Bragg's law is satisfied at a characteristic specific angle on the crystalline material. The Bragg equation [26] is:

$$n\lambda = 2d \sin \theta \tag{1}$$

where n is an integer value (1,2,3...), λ is the wavelength of the incident x-ray, d is the spacing between the diffracting planes and θ is the incident angle. The angle between the projection of the X-ray source and the detector is 2θ.

Consequently, the X-ray diffraction pattern constitute a ̀uniquễ identity card for each material in this study. The XRD pattern of all the as-prepared materials were characterized using an XPERT-PRO diffractometer in a $\theta/2\theta$ configuration, with a cobalt tube at 35 kV and 50 mA (PANalytical BV, Netherlands), located at the Department of Geology, University of Pretoria, South Africa.

3.2.2 Raman Spectroscopy

Raman technique is a spectroscopic study of molecular vibration, rotational, and other low-frequency modes in a system. In this context, the Raman spectroscopic has been considered as a potential and a very promising instrumental technique applied in materials and biological fluids [27]. The technique is also a useful system to have some insight into the chemical composition of the materials. The Raman spectroscopy operates on the inelastic scattering (Raman scattering) of monochromatic light, usually from a laser in the visible, near infrared, or near ultraviolet range [28].

In this process, the molecule is irradiated by electromagnetic radiation which interacts with the bonds or electron cloud of the molecule and emits a scattered light. The interactions of the laser light with molecular vibrations, phonons or other excitations in a material result in the energy or frequency of the laser photons to be varied up or down with respect to the energy or frequency of the original monochromatic light, in a process named Raman Effect [29]. The energy or frequency variations supply information on the vibrational modes in a material.

In this thesis, A WITec confocal Raman microscope (WITec alpha300 R, Ulm Germany) with a 532 nm laser wavelength and spectral acquisition time of 120 s was used to characterize the materials. The Raman system laser power was set as low as 5 mW in order to minimize heating effects. Figure 3.7 presents the WITec confocal Raman microscope used to analysis the vanadium-based materials.
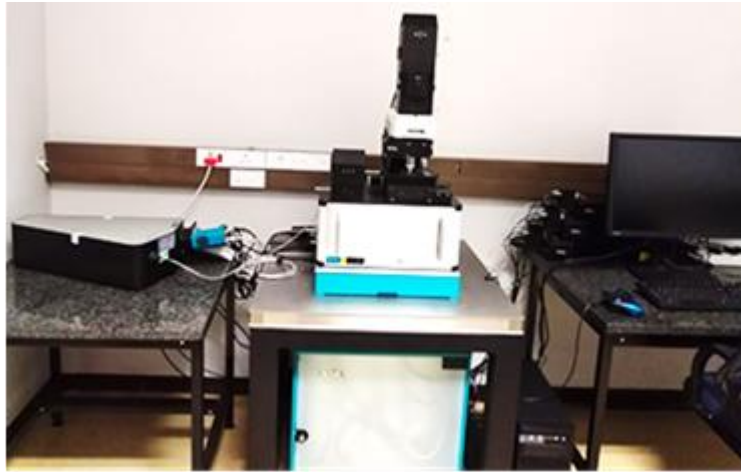
Figure 3.7: WITec confocal Raman microscope (WITec alpha300 R, Ulm Germany).

3.2.3 Scanning electron microscopy (SEM)

The scanning electron microscopy (SEM) is a quick, simple and popular analysis of materials in the field of material science. The SEM has the potential to provide high-resolution analysis and to offer a large variety of analytical modes, which give unique information regarding the surface features of a particular specimen [30].

Scanning electron microscopy process uses a focused electron beam of high-energy electrons to generate a variety of signals at the surface of the solid materials. The different type of signals in the process is produced by using secondary electrons, back-scattered electrons, characteristic X-ray, light cathode luminescence and specimen current. The secondary electron is used for imaging information about the depth and morphology at the material surface. The signals result from interactions of the electron beam with atoms at or near the surface of the material. These signals that are derived reveal information about the sample such as morphology, thickness, porosity and orientation of the microscopic materials that make up bulk material.

In this thesis, the surface of all the materials were not electrically conductive to prevent the accumulation of electrostatic charge on the surface, they were coated with carbon materials by using a carbon sputter coating. The microscopic images and elemental compositions for the vanadium based material were analyzed by the field emission scanning electron microscopy (FESEM) using a high-resolution Zeiss, Ultra Plus 55, (in Figure 3.8) operating at 2.0 kV, coupled with integrated energy dispersive X-ray spectrometer (EDX), operating at 20 kV.

Figure 3.8: High-resolution Zeiss Ultra, Plus 55 instrument.

3.2.4 Transmission electron microscopy (TEM)

Transmission electron microscopy (TEM) is similar to the SEM but it is capable of achieving higher resolution and uses transmitted electrons. TEM is a powerful and very important tool for structure characterization and it is considered to be unique in revealing and quantifying the chemical and lattice parameters of individual nanocrystals [31]. The most important application of TEM is the atomic-resolution real-space imaging of nanoparticles [31,32].

This technique uses a high electron beam to irradiate the specimen area and generates an image through the interaction of the transmitted high accelerating electrons and the ultra-slim specimen as the electrons are transmitted through the specimen.

In this thesis, all the materials were prepared by dissolving the powder of the specimen in an ethanol solvent (100%). The solution were sonicated to form a homogeneous mixture and subsequent the mixture was drop-coated on a carbon-coated copper grid, dried in air before loading onto the analysis chamber. TEM images for the vanadium based material were evaluated by using the high-resolution transmission electron microscopy (HR-TEM) JEOL 2100F equipped with LaB6 filament, a Gartan U1000 camera of 2028 x 2028 pixels and operated at 200 kV as shown in Figure in 3.9.
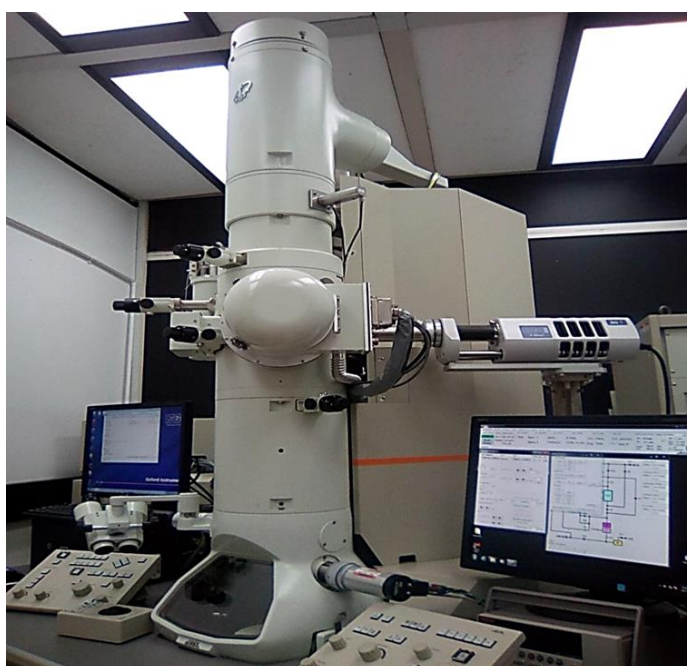
Figure 3.9: Transmission electron microscopy instrument (HR-TEM-JEOL 2100F).

3.2.5 N_2 gas-adsorption-desorption measurement

N_2 gas-adsorption-desorption measurement is very important in electrochemical performance. This technique has the ability to determine the specific surface area (SSA), porosity, average pore volume, and the broad pore size distribution of the powder specimen. Nitrogen adsorption–desorption isotherms were measured at -196 °C using a Micromeritics TriStar II 3020 (version 2.00) for all the vanadium-based materials. This Micromeritics TriStar II

system operated in a relative pressure (P/Po) range of 0.01–1.0 to acquire the adsorption-desorption isotherms.

The specific surface area of the vanadium-based materials was determined by the Brunauer–Emmett–Teller (BET) method. The pore size and average pore volume were acquired by employing the Barrett–Joyner–Halenda (BJH) models from the desorption branch of the corresponding isotherms. All the materials were pre-degassed at 100 °C for 18 h under vacuum prior to the measurement in order to remove any residues of moisture in the sample. The degassed specimens were then transferred to the analysis chamber for the complete analysis using N_2 gas at low pressure and 77 K. This is followed by dosing the sample with a specific amount of gas which is then evacuated to acquire the amount of gas absorbed by the specimens over a relative pressure range, P/P0 (i.e. 0.01<P/P0<0.2). The nature of the isotherm acquired has the capability to indicate the type of pore size in the specimen.

3.2.6 X-ray photoelectron spectroscopy (XPS)

X-ray photoelectron spectroscopy (XPS) is commonly considered as an important and key technique for the surface characterization. Generally, XPS is the most quantitative, the most readily interpretable, and the most informative with regard to chemical and electronic information. XPS method provides a total elemental analysis, except for hydrogen and helium.

XPS spectra are acquired through irradiating the sample surface with a beam of X-rays (Al-Kα or Mg-Kα) while concurrently measuring the kinetic energy and number of elastically scattered electrons (photoelectrons) that break from the top 0 to 10 nm of atomic layers in the sample being analysed. This technique requests high vacuum (P ~ 10^{-8} millibar) or ultra-high vacuum (UHV; P <10^{-9} millibar) conditions. The result of the XPS spectrum is a plot of the number of detected electrons (per unit time) as function of the binding energy of detected

electrons. All the chemistry element generates a typical set of XPS peaks at specific binding energies. The XPS spectrum have the potential to deliver various levels of spectral interpretation including the simple elemental analysis; detailed considerations of chemical shifts and chemical bonding nature in the surface region; and various loss or relaxation structures which provide further information on the chemical nature of the surface. This interpretation becomes progressively more challenging as one goes to more complex surfaces, such as multi-component and multi-phase materials [33] [34].

X-ray photoelectron spectroscopy (XPS) measurements of the vanadium-based materials and vanadium/carbon composites in this work were studied using a Physical Electronics VersaProbe 5000 spectrometer operating with a 100 μm monochromatic Al-Kα exciting source. A 180° hemispherical electron energy analyser collected photoelectrons, with the samples been studied at a 45° angle between the sample surface and the path to the analyser. Survey spectra were taken at pass energy of 117.5 eV, with a step size of 0.1 eV.

3.2.7 Electrochemical characterization

The electrochemical performance of all electrodes coated on nickel foam (NF) as a current collector were evaluated with a Bio Logic VMP300 workstation (Knoxville TN 37,930, USA) controlled by the EC-Lab® V1.40 software in a three and two electrodes configurations as presented in Figure 3.10.

The electrochemical measurements were performed with a glassy carbon as a counter electrode, Ag/AgCl (3 M KCl) as the reference electrode and the vanadium-based materials as the working electrodes. The working electrodes were fabricated by mixing 80% of the active materials (vanadium-based materials) with 10% of carbon black (as a conducting agent) and 10% of polyvinylidene difluoride (PVDF) binder in a proportionate weight ratio to make slurry. A few drops of N-methylpyrrolidone (NMP) solvent was dispersed in the mixture to

form a slurry, which was then coated onto a NF substrate and dried at a particular temperature in an electric oven in order for the NMP to completely evaporate. In this study, the electrochemical measurements of all the electrode materials were performed in a 6 M KOH aqueous electrolyte at room temperature.
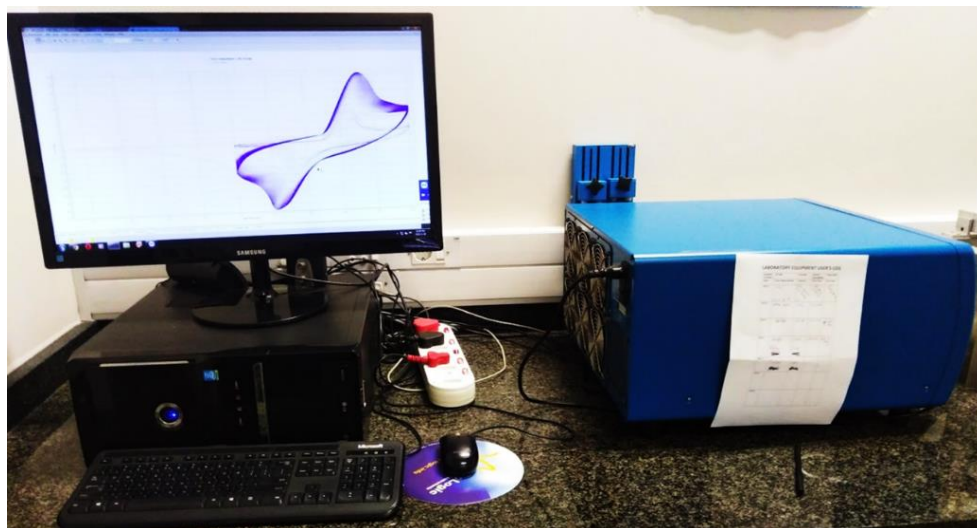
Figure 3.10: Bio Logic VMP300 workstation (Knoxville TN 37,930, USA) controlled by the EC-Lab® V1.40 software.

Bibliography

[1]   S. Komarneni, Y.D. Noh, J.Y. Kim, H. Kim, H. Katsuki, Solvothermal/Hydrothermal Synthesis of Metal Oxides and Metal Powders with and without Microwaves, 65 (2010) 1033–1037.

[2]   T.M. Masikhwa, D.Y. Momodu, K.O. Oyedotun, A.A. Mirghni, N.M. Ndiaye, N. Manyala, Asymmetric supercapacitor based on cobalt hydroxide carbonate/GF composite and a carbonized conductive polymer grafted with iron (C-FP), Journal of Alloys and Compounds. 769 (2018) 376–386.

[3]   L. Jiang, M. Yao, B.B. Liu, Q. Li, R. Liu, Z. Yao, S. Lu, W. Cui, X. Hua, B. Zou, T. Cui, B.B. Liu, Shape-selective synthesis and optical performance of ceria nanocrystal/graphene hybrid composites, CrystEngComm. 15 (2013) 3739.

[4]   J. Zhang, H. Kumagai, K. Yamamura, S. Ohara, S. Takami, A. Morikawa, H. Shinjoh, K. Kaneko, T. Adschiri, A. Suda, Extra-Low-Temperature Oxygen Storage Capacity of CeO $_2$ Nanocrystals with Cubic Facets, Nano Letters. 11 (2011) 361–364.

[5]   A.A. Khaleed, A. Bello, J.K. Dangbegnon, M.J. Madito, O. Olaniyan, F. Barzegar, K. Makgopa, K.O. Oyedotun, B.W. Mwakikunga, S.C. Ray, N. Manyala, Solvothermal synthesis of surfactant free spherical nickel hydroxide/graphene oxide composite for supercapacitor application, Journal of Alloys and Compounds. 721 (2017) 80–91.

[6]   H. Tamon, H. Ishizaka, T. Yamamoto, T. Suzuki, Preparation of mesoporous carbon by freeze drying, Carbon. 37 (1999) 2049–2055.

[7]   A.T. Stone, H.-J. Ulrich, Kinetics and reaction stoichiometry in the reductive dissolution of manganese(IV) dioxide and co(III) oxide by hydroquinone, Journal of

Colloid and Interface Science. 132 (1989) 509–522.

[8]   D.E. WITTMER, R.C. BUCHANAN, Low-Temperature Densification of Lead Zirconate-Titanate with Vanadium Pentoxide Additive, Journal of the American Ceramic Society. 64 (1981) 485–490.

[9]   Q. Wei, J. Liu, W. Feng, J. Sheng, X. Tian, L. He, Q. An, L. Mai, Hydrated vanadium pentoxide with superior sodium storage capacity, Journal of Materials Chemistry A. 3 (2015) 8070–8075.

[10]   J. Zhu, L. Cao, Y. Wu, Y. Gong, Z. Liu, H.E. Hoster, Y. Zhang, S. Zhang, S. Yang, Q. Yan, P.M. Ajayan, R. Vajtai, Building 3D Structures of Vanadium Pentoxide Nanosheets and Application as Electrodes in Supercapacitors, Nano Letters. 13 (2013) 5408–5413.

[11]   E. Baudrin, G. Sudant, D. Larcher, B. Dunn, J.-M. Tarascon, Preparation of Nanotextured VO2[B] from Vanadium Oxide Aerogels, Chem. Mater. 18 (2006) 4369–4374.

[12]   F. Coustier, G. Jarero, S. Passerini, W.H. Smyrl, Performance of copper-doped V2O5 xerogel in coin cell assembly, Journal of Power Sources. 83 (1999) 9–14.

[13]   A. Zhou, Methods of MAX-phase synthesis and densification–II, Advances in Science and Technology of $M_{n+1}AX_n$ Phases. (2012) 21–46.

[14]   G.B. Stringfellow, Organometallic Vapor-Phase Epitaxy: Theory and Practice, Second Edi, Academic Press, 1999.

[15]   C. Drosos, D. Vernardou, Perspectives of energy materials grown by APCVD, Solar Energy Materials and Solar Cells. 140 (2015) 1–8.

[16] W.A. Bryant, Review The fundamentals deposition of chemical vapour, Journal of Materials Science. 12 (1977) 1285–1306.

[17] K.B.K. Teo, S.-B. Lee, M. Chhowalla, V. Semet, V.T. Binh, O. Groening, M. Castignolles, A. Loiseau, G. Pirio, P. Legagneux, D. Pribat, D.G. Hasko, H. Ahmed, G.A.J. Amaratunga, W.I. Milne, Plasma enhanced chemical vapour deposition carbon nanotubes/nanofibres how uniform do they grow?, Nanotechnology. 14 (2003) 204–211.

[18] Y. Wu, P. Qiao, T. Chong, Z. Shen, Carbon Nanowalls Grown by Microwave Plasma Enhanced Chemical Vapor Deposition, Advanced Materials. 14 (2002) 64–67.

[19] I.P. Parkin, G.S. Elwin, Atmospheric pressure chemical vapour deposition of vanadium nitride and oxynitride films on glass from reaction of VCl_4 with NH_3, Journal of Materials Chemistry. 11 (2001) 3120–3124.

[20] X.-J.J. Ma, W.-B. Bin Zhang, L.-B. Bin Kong, Y.-C.C. Luo, L. Kang, VO_2: from negative electrode material to symmetric electrochemical capacitor, RSC Advances. 5 (2015) 97239–97247.

[21] K. Tachibana, M. Nishida, H. Harima, Y. Urano, Diagnostics and modelling of a methane plasma used in the chemical vapour deposition of amorphous carbon films, 1984.

[22] D.W. Greve, Growth of epitaxial germanium-silicon heterostructures by chemical vapour deposition, Materials Science and Engineering: B. 18 (1993) 22–51.

[23] R.Y. Tay, X. Wang, S.H. Tsang, G.C. Loh, R.S. Singh, H. Li, G. Mallick, E.H. Tong Teo, A systematic study of the atmospheric pressure growth of large-area hexagonal

crystalline boron nitride film, Journal of Materials Chemistry C. 2 (2014) 1650.

[24]   M. Eckert, Max von Laue and the discovery of X-ray diffraction in 1912, Annalen Der Physik. 524 (2012) A83–A85.

[25]   B.D. Cullity, S.R. Stock, Elements of x-ray diffraction, ADDISON-WE, Prentice Hall, INC, 2001.

[26]   C.G. Pope, X-Ray Diffraction and the Bragg Equation, Journal of Chemical Education. 74 (1997) 129.

[27]   L.M. Moreira, L.S. Jr, F. V. Santos, J.P. Lyon, R. Rocha, R.A. Zângaro, A.B. Villaverde, M.T.T. Pacheco, Raman spectroscopy: a powerful technique for biochemical analysis and diagnosis, Spectroscopy. 22 (2008) 1–19.

[28]   T.F.A. Rubim J. C, Sousa M. H, Silva J. C. O, Raman Spectroscopy as a Powerful Technique in the Characterization of Ferro uids, Brazilian Journal of Physics. (2001).

[29]   Y.-C. Tseng, Y.-C. Cheng, Y.-C. Lee, D.-L. Ma, B.-Y. Yu, B.-C. Lin, H.-L. Chen, Using Visible Laser-Based Raman Spectroscopy to Identify the Surface Polarity of Silicon Carbide, The Journal of Physical Chemistry C. 120 (2016) 18228–18234.

[30]   J. Orloff, Handbook of charged particle optics, CRC Press, 1997.

[31]   Z.L. Wang, Transmission Electron Microscopy of Shape-Controlled Nanocrystals and Their Assemblies, J. Phys. Chem. B. 10 (2000) 1153–1175.

[32]   C.L. Jackson, H.D. Chanzy, Frank P. Booy, Bartholomew J. Drake, ¶ Donald A. Tomalia, A. Barry J. Bauer, E.J. Amis, Visualization of Dendrimer Molecules by Transmission Electron Microscopy (TEM): Staining Methods and Cryo-TEM of

Vitrified Solutions, Macromolecules. 31 (1998) 6259–6265.

[33] J.D. Andrade, X-ray Photoelectron Spectroscopy (XPS), in: Surface and Interfacial Aspects of Biomedical Polymers, Springer US, Boston, MA, 1985: pp. 105–195.

[34] S. Ghosh, S. Bomma, V.L. Prasanna, P. Srivani, D. Bhanji, New Analytical Methods in Nanotechnology-A Review, Asian J. Res. Pharm. Sci. 3 (2013) 31–41.

_____

4.0 Results and discussion

This chapter describes the results obtained from the material characterization procedure and the electrochemical measurements of the as-synthesized vanadium-based samples, which were outlined in the chapter 3.

4.1 Three dimensional vanadium pentoxide/graphene foam composite as positive electrode for high performance asymmetric electrochemical supercapacitor

4.1.1 Introduction

Transition metal oxide-based electrochemical supercapacitors (ECs) exhibit much higher specific capacity as compared to carbon-based ECs [1] due to their ability to exist in various oxidation states [2]. Research efforts have been invested to find low-cost metal oxides due to the high cost of ruthenium which limits its applications [3]. Amongst the low-cost metal oxides, vanadium pentoxide (V_2O_5) is a promising applicant for ultracapacitors electrodes.

V_2O_5 presents the advantage of unique layered structures, high specific capacity and its wide operating potential window arising due to the mixed oxidation states (V^{2+}, V^{3+}, V^{4+} and V^{5+}) [4,5]. Unfortunately, V_2O_5 exhibits poor electrical conductivity and cyclic stability [6,7].

As a result, numerous V_2O_5-based composites with carbon (V_2O_5/carbon) have been studied to improve the conductivity issues related to its adoption as supercapacitor materials [7–13].

Recently, graphene-based materials have also been considered as an ideal candidate for energy storage due to their outstanding properties such as the good electrical conductivity, high theoretical surface area and thermal stability [14]. The combination of graphene-based

materials with metal oxide results in composite material electrode with improved electrochemical performance.

This is linked to the conductivity of the graphene coupled with the high specific capacity of the metal oxide [15,16]. For instance, Li et al. [5] studied nanocrystals of V_2O_5 integrated onto reduced graphene oxide sheet. In their work, a solvothermal technique was used to synthesize the composite material followed by a subsequent annealing step for device applications. Graphene oxide sheets served as a template to synthesize V_xO_y nanoparticles. The V_2O_5/reduced graphene oxide nanocomposites recorded an improved performance as compared to the V_2O_5 alone [5]. Recently, Hoa et al. [17] reported on the controlled growth of flower-like V_2O_5 onto the graphene@nickel foam. In their study, an in situ growth of V_2O_5 was used to synthesis the NF/G/V_2O_5 composite by hydrothermal method. The NF/G/V_2O_5 composite exhibited an excellent electrode performance [17].

In this work, we report on the synthesis of V_2O_5 and V_2O_5/GF composites with a varying mass of graphene foam (GF) (50 – 200 mg) by hydrothermal method and a freeze-drying process. Furthermore, we evaluate the V_2O_5/GF composites as a positive electrode in a two-electrode asymmetric device with a pyrolyzed iron-PANI polymer material (C-Fe/PANI or C-FP) as a negative electrode. This hybrid capacitor design has been developed in a bid to solve the limitations exhibited by both EDLCs and faradaic-type supercapacitors vis-à-vis the low specific capacitance from the former and the low conductivity coupled with the poor cyclability problems associated with metal oxides/hydroxides [18].

4.1.2 Results and discussion

The characterization and electrochemical results obtained from both V_2O_5 and the V_2O_5/GF composites with varying mass of GF (50 – 200 mg) is detailed in the following paper:

Contents lists available at ScienceDirect

Journal of Colloid and Interface Science

journal homepage: www.elsevier.com/locate/jcis
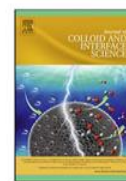
Regular Article

Three dimensional vanadium pentoxide/graphene foam composite as positive electrode for high performance asymmetric electrochemical supercapacitor

Ndeye M. Ndiaye [a], Balla D. Ngom [b], Ndeye F. Sylla [a], Tshifhiwa M. Masikhwa [a], Moshawe J. Madito [a], Damilola Momodu [a], Tshepo Ntsoane [c], Ncholu Manyala [a,*]

[a] Department of Physics, Institute of Applied Materials, SARChI Chair in Carbon Technology and Materials, University of Pretoria, Pretoria 0028, South Africa
[b] Laboratoire d'Energie, de Photonique et de Nano-Fabrication, Faculté des Sciences et Techniques, Université Cheikh Anta Diop de Dakar (UCAD), B.P. 25114, Dakar-Fann Dakar, Senegal
[c] Nuclear Energy Cooperation South Africa, Nuclear Liabilities Waste Management, Pelindaba, South Africa

GRAPHICAL ABSTRACT

Schematic illustration of the synthesized V_2O_5/GF-150 mg composite and Ragone plot of asymmetric cell.
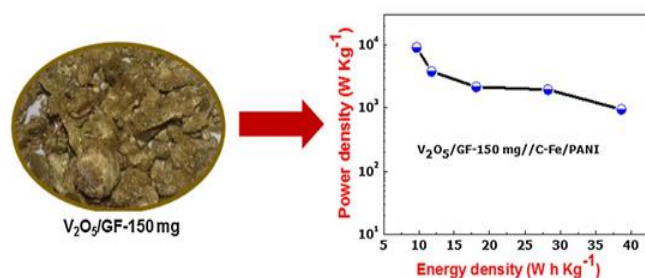
V_2O_5/GF-150 mg

V_2O_5/GF-150 mg//C-Fe/PANI

ARTICLE INFO

ABSTRACT

The electrochemical performance of hydrothermal synthesized three dimensional (3D) orthorhombic vanadium pentoxide (V_2O_5) nanosheets and vanadium pentoxide/graphene foam (V_2O_5/GF) composites at different mass loading of GF were successfully studied. The optimized V_2O_5/GF-150 mg composite provided a high specific capacity of 73 mA h g^{-1}, which was much higher than that the pristine V_2O_5 (60 mA h g^{-1}) nanosheets at a specific current of 1 A g^{-1}. A hybrid capacitor was also fabricated by adopting a carbon-based negative electrode obtained from the pyrolysis of an iron-PANI polymer (C-Fe/PANI) mixture and the 3D V_2O_5/GF-150 mg composite as the positive electrode in 6 M KOH electrolyte. The hybrid device of V_2O_5/GF-150 mg//C-Fe/PANI demonstrated a high energy density of 39 W h kg^{-1} with a corresponding high power density of 947 W kg^{-1} at a specific current of 1 A g^{-1} in an operating voltage window of 0.0–1.6 V. The hybrid device also exhibited an excellent cycling stability with 74% capacity retention recorded for up to 10,000 constant charging–discharge cycles and an excellent ageing test at a specific current of 10 A g^{-1}.

© 2018 Elsevier Inc. All rights reserved.

* Corresponding author.
E-mail address: ncholu.manyala@up.ac.za (N. Manyala).

114

1. Introduction

A lot of proficient high energy storage technologies have been developed due to the increasing demand for conversion of renewable energy resources (such as wind, solar, geothermal, and biomass etc.) into usable energy to efficiently deal with the generated energy for productive use [1–4]. Actually, supercapacitors and batteries are the most common devices for electrical energy storage [5]. Supercapacitors (SCs) or ultracapacitors referred to in some instances as electrochemical capacitors (ECs) are extensively studied mainly due to their high power density [6,7] and their reversible energy storage capability as compared with other energy storage devices such as dielectric capacitors, secondary cells, fuel cells, and lithium-ion batteries [8].

Ultracapacitors could be used concurrently to complement batteries or as complete alternative to batteries. In addition to their high power density, ultracapacitors also exhibit a long cycle life [9,10], high energy efficiency [11,12] among other properties. However, most ultracapacitors possess a low energy density, as compared to batteries/fuel cells and this has aroused researchers to improve their energy density [13,14].

Ultracapacitors are divided into three types in relation to their energy storage mechanism: (1) Electric double-layer capacitors (EDLC), which arises from the accumulation of charges at the electrode/electrolyte interface and the commonly used materials in EDLCs are carbon-based, (2) Faradaic supercapacitors in which the storage results from the fast redox reactions and common materials adopted in this type of capacitors are transition metal oxide and hydroxides (TMOs/TM-OHs), redox polymers and (3) Hybrid capacitors which utilize materials of both EDLC and Faradaic nature [15]. A common subclass of hybrid capacitors is the asymmetric ultracapacitors which are obtained by assembling two dissimilar materials as the positive and negative electrode components of the full device. The positive electrodes are mostly metal oxides [16–21], conductive polymers [22], metal hydroxides [23] and their composites with carbon materials, while the negative electrodes are generally carbon-based materials [17,24–28].

The hybrid capacitor design has been developed and postulated to solve the limitations of both EDLCs and Faradaic-type ultracapacitors via the low specific capacitance from activated carbons and the low conductivity and poor cycleability problems associated with metal oxides/hydroxides [29].

Transition metal oxide-based ECs exhibit much higher specific capacity as compared to carbon-based ECs [15] due to their ability to exist in variable oxidation states [30]. Efforts have been developed to find low-cost metal oxides due to the high cost of ruthenium (RuO_2) which limits its applications [20]. Amongst the low-cost metal oxides, vanadium pentoxide (V_2O_5) is a promising candidate material for ultracapacitors electrodes.

V_2O_5 presents the advantage of unique layered structures, high specific capacity and its wide operating potential window arising due to the mixed oxidation states (V^{2+}, V^{3+}, V^{4+} and V^{5+}) [31–33]. Unfortunately, V_2O_5 exhibits a poor electrical conductivity and cyclic stability [34,35]. As a result, numerous V_2O_5-based composites with carbon (V_2O_5/carbon) have been studied to improve the conductivity issues related to its adoption as supercapacitor material [35–41].

Recently, graphene-based materials have also been considered as an ideal candidate for energy storage because of their outstanding properties such as the good electrical conductivity, high theoretical surface area $\sim 2600\ m^2\ g^{-1}$ and thermal stability [42]. The combination of the metal oxide with graphene-based materials serves generally to improve the electrochemical performance of as-prepared composite electrode due to the excellent conductivity of the graphene coupled with the high specific capacity of the metal oxide [32,43].

Li et al. [33] studied nanocrystals of V_2O_5 integrated onto reduced graphene oxide sheet. In their work, a solvothermal technique was used to synthesize the composite material followed by a subsequent annealing step for device applications. They used graphene oxide sheets as a template to synthesis V_xO_y nanoparticles. The V_2O_5/reduced graphene oxide nanocomposites recorded an improved performance as compared to the V_2O_5 alone [33]. Recently, Hoa et al [44] reported flower-likes of V_2O_5 onto the graphene@nickel foam. In their study, an in situ growth of V_2O_5 was used to synthesise the $NF/G/V_2O_5$ composite by hydrothermal method. The $NF/G/V_2O_5$ composite exhibited an excellent electrode performance [44].

Herein, we report on the electrochemical performance of as-synthesized orthorhombic V_2O_5 nanosheets and its composites with graphene foam, by hydrothermal method and a freeze-drying process. The electrochemical performance of the as-synthesized V_2O_5 and V_2O_5/GF composites were analyzed in half-cell configuration using 6 M KOH aqueous electrolyte. Furthermore, we evaluate V_2O_5 nanosheets with 150 mg of GF (V_2O_5/GF-150 mg) composite which was found to be the best performing composite, as a positive electrode in a two-electrode asymmetric cell device with a carbon-based negative electrode at a high operating cell voltage of 1.6 V in 6 M KOH electrolyte. The full cell device delivered energy and power densities of 39 W h kg^{-1} and 947 W kg^{-1} respectively at a specific current of 1 A g^{-1} with excellent stability demonstrated through 74% capacity retention up to 10,000 cycles and voltage holding up to 130 h techniques.

2. Experimental section

2.1. Materials

Vanadium pentoxide (V_2O_5, purity $\geq 98\%$), Hydrogen peroxide solution (H_2O_2) 30%, aniline hydrochloride ($C_6H_5NH_2 \cdot HCl$, purity 99%), ammonium persulphate (($NH_4)_2S_2O_8$, purity _99%) and iron nitrate nonahydrate ($Fe(NO_3)_3 \cdot 9H_2O$, purity _99.95%) were purchased from Sigma-Aldrich. Nickel foam (NF) substrate (420 g m^2 areal density) was obtained from Alantum (Germany) while Potassium hydroxide (KOH, min 85%) pellet was purchased from Merck (South Africa).

2.2. Synthesis of graphene foam (GF)

The graphene foam (GF) synthesis by chemical vapor deposition (CVD) method was achieved by using a pre-cleaned polycrystalline nickel foam (NF) as a growth template. The NF was placed at the center of a CVD quartz tube. It was annealed under an argon, methane and hydrogen gas mixture at 1000 °C. After cooling down, the graphene/nickel foam was dipped in a 3 M HCl solution at 80 °C to ensure complete etching of the nickel scaffold. Finally, the recovered GF was washed several times with deionized water (DI) and dried at 60 °C [45].

2.3. Synthesis of V_2O_5/GF composites

Firstly, pristine V_2O_5 nanosheets were synthesized by mixing 0.36 g of bulk V_2O_5 (analytical grade) and 5 ml of 30% H_2O_2 to 30 ml of deionized water (DI) under vigorous stirring to obtain a red solution. A 30 ml portion of the red solution was transferred into a sealed 50 ml Teflon-lined autoclave and kept at a 190 °C temperature for a period of 20 h to generate a gel. Consequently, the gel was freeze-dried [51] to obtain the final product V_2O_5 sample. The same procedure described for the synthesis of pristine V_2O_5 was repeated for the synthesis of the V_2O_5/GF composites with GF being introduced along with the precursors. Simply, a

115
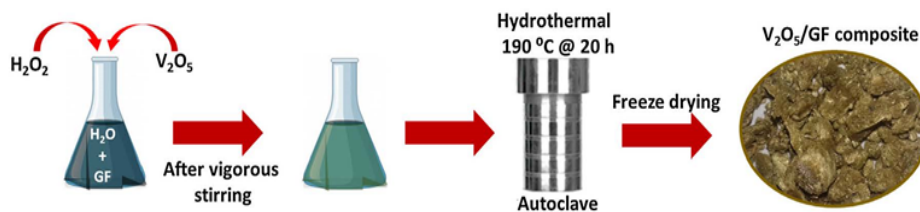
Scheme 1. Schematic of the synthesis process of V_2O_5/GF composite.

varying mass content of GF (50–200 mg) was added to 30 ml of DI before adding the precursors and the process is demonstrated in Scheme 1 below

2.4. Pyrolysis of Fe-cation adsorbed onto polyaniline (C-Fe/PANI) adopted as an anode

Briefly, polyaniline (PANI) was originally synthesized by mixing 50 ml of 0.2 M aniline hydrochloride ($C_6H_5NH_2 \cdot HCl$) solution and 50 ml of 0.25 M ammonium peroxydisulfate ($(NH_4)_2S_2O_8$) solution with a measured volume of 1.0 M HCl. The detailed description of C-Fe/PANI from PANI is described by Rantho et al [46].

2.5. Structural and morphological characterization

X-ray diffraction (XRD) spectra of as-synthesized orthorhombic V_2O_5 nanosheets and the V_2O_5/GF composite were collected using a diffractometer (Brucker D8 Advance) with theta/2theta geometry, operating with a Cu X-ray source at 2θ values ranging from 15° to 60° with a step size of 0.04°. Raman spectroscopy measurements were obtained using a WITec confocal Raman microscope (WITec alpha300 R, Ulm Germany) with a 532 nm laser wavelength and spectral acquisition time of 60 s. The specific surface area (SSA) of the samples was obtained by the Brunauer–Emmet t–Teller (BET) method in the relative pressure range (P/P_0) of 0.01–1.0. The pore size distribution obtained from the desorption branch of the isotherm using the Barrett-Joyner-Halenda (BJH) method and density functional theory (DFT) pore size distribution data. The morphology of the V_2O_5, graphene foam (GF) and V_2O_5/GF composites was obtained from a high-resolution Zeiss Ultra plus 55 field emission scanning electron microscope (FE-SEM), operated at a working voltage of 2.0 kV. Transmission electron microscopy (TEM) analysis was done with a JEOL JEM-2100F microscope operated at 200 kV (Akishima-shi, Japan). X-ray photoelectron spectroscopy (XPS, K-alpha, Thermo Fisher) with a monochromatic Al Kα radiation as the X-ray source was used to irradiate the sample surface in order to determine the surface chemistry of the samples.

2.6. Electrodes preparation and electrochemical characterization

The electrochemical properties of the V_2O_5, V_2O_5/GF and C-Fe/PANI electrodes were analyzed in a three and two electrode configuration using a Bio-Logic VMP-300 (Knoxville TN 37,930, USA) potentiostat to obtain the material's energy storage behavior at various scan rates and specific currents. In the half-cell configuration, a glassy carbon counter electrode and Saturated calomel electrode (SCE) reference electrode were used with the active materials as a working electrode to complete the testing circuit in a 6 M KOH aqueous electrolyte. The half-cell electrochemical characterization was performed to determine the electrode performance for optimization of V_2O_5/GF composites as a positive electrode and the C-Fe/P as a negative electrode for asymmetric device fabrication. The V_2O_5 and V_2O_5/GF electrodes were fabricated by mixing weighed amounts of V_2O_5 and V_2O_5/GF with carbon black conducting additive and polyvinylidene difluoride (PVDF) binder in a mass ratio of 80:10:10. A few drops of N-methylpyrrolidone (NMP) was dispersed in the mixture to form a slurry in an agate mortar. This was pasted onto a pre-annealed nickel foam (NF) substrate with an area of 1×1 cm^2. The coated NF electrodes were dried at 60 °C in an electric oven for 12 h in order for the NMP to completely evaporate. The masses of the V_2O_5, V_2O_5/GF composites electrode with different GF mass loading were approximately kept at 2.0 mg for comparison sake. The electrochemical performance of the V_2O_5/GF electrode was also evaluated in a two-electrode cell. The asymmetric device was carried out using V_2O_5/GF-150 mg as a positive electrode due to its superior electrochemical performances as compared to other composites and C-Fe/PANI as negative electrode assembled in a coin cell (thickness = 0.2 mm and diameter = 16 mm) with glass microfibre filter paper used as a separator in 6 M KOH aqueous electrolyte. The masses per unit area of the V_2O_5/GF and C-FP electrodes were within 2–3 mg cm^{-2} and 2.6–3.9 mg cm^{-2}, respectively.

3. Results and discussions

X-ray diffraction (XRD) analysis results of V_2O_5, GF and V_2O_5/GF composites are presented in Fig. 1. Fig. 1a displays the XRD spectra of the as-prepared V_2O_5. The diffraction peaks of the as-prepared V_2O_5 located at $2\theta = 22.9$, 30.8 and 38.5° correspond to the Miller indices of (0 0 3), (0 0 4) and (0 0 5) of an orthorhombic V_2O_5 (JCPDS Card No. 40-1296) [47,48]. Analysis of the spectra for the as-prepared pristine V_2O_5 reveals a preferred $\langle 0\,0\,1 \rangle$ direction oriented growth for the sample. In Fig. 1b, a typical (0 0 2) distinctive peak is observed which is located at an angle of $2\theta = 26°$ (JCPDS Card No. 75-1621) [49] value which confirms the successful synthesis of a graphitic material.

Fig. 1c displays the diffraction pattern for the V_2O_5/GF composites for different GF mass loading. From the spectra, the characteristic diffraction peaks of the V_2O_5 and GF are recorded, confirming the successful incorporation and presence of GF in the V_2O_5/GF composites [50,51]. Fig. 1d shows the XRD pattern of the freestanding C-Fe/PANI powder sample without the Ni foam template. The diffraction peaks for C-Fe/PANI material is linked to an orthorhombic Fe_3C structure (ICSD card no. 16593). Other forms of Fe-based compounds were also recorded in the XRD spectra such as orthorhombic FeS (ICSD card no. 35008) and metallic Fe recorded at a 2θ value of 52° [46]. Detailed elucidation of the origin of these peaks has been discussed in Ref. [46].

Raman spectroscopy was further used to study the phase structure and identify different phases of the as-prepared materials at the molecular level. The Raman spectroscopy analysis of the GF, V_2O_5 and V_2O_5/GF composites are shown in Fig. 2a. The Raman spectrum of graphene foam contains two peaks at ~1570 and 2700 cm^{-1} corresponding to the characteristic G and 2D band of graphene as shown in Fig. 2a. The G and 2D peaks positions observed are related to the vibration mode of carbon sp^2 and double resonance process, respectively [49,52].
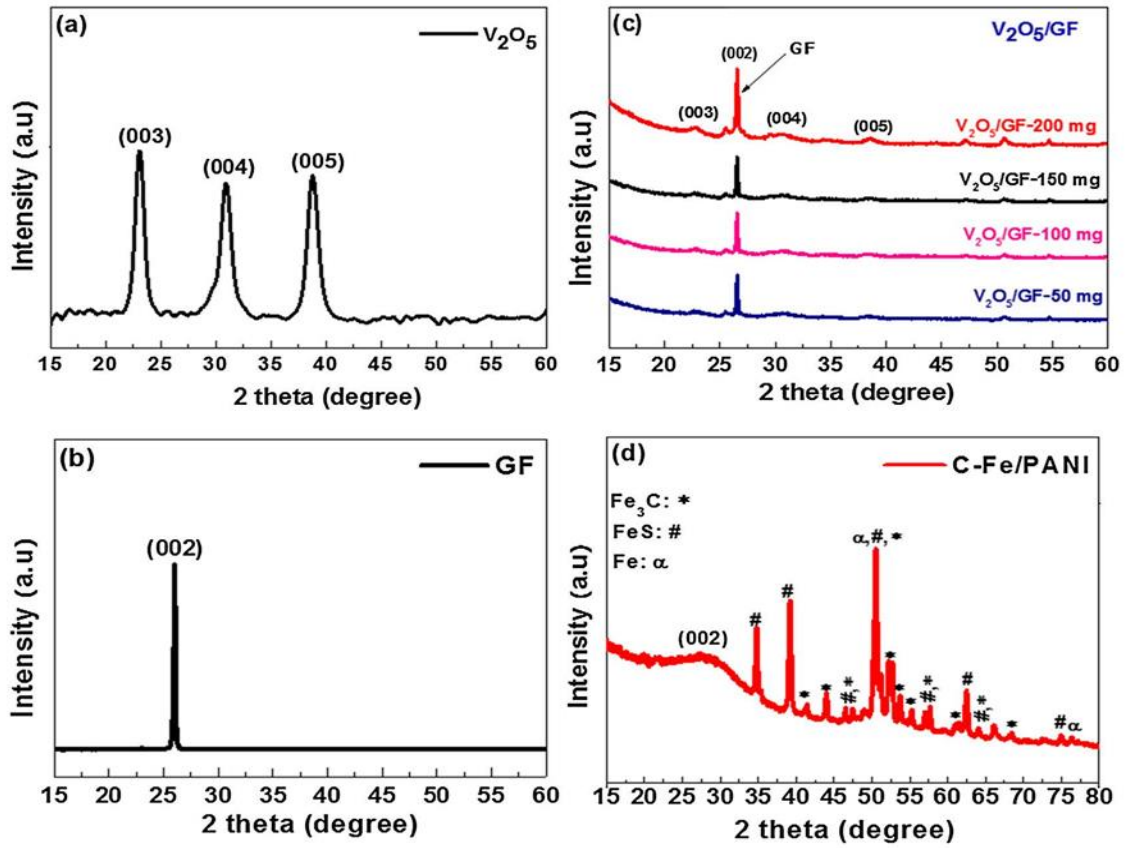
Fig. 1. XRD spectra of (a) V_2O_5, (b) graphene foam (GF), (c) V_2O_5/GF composites and (d) C-Fe/PANI.
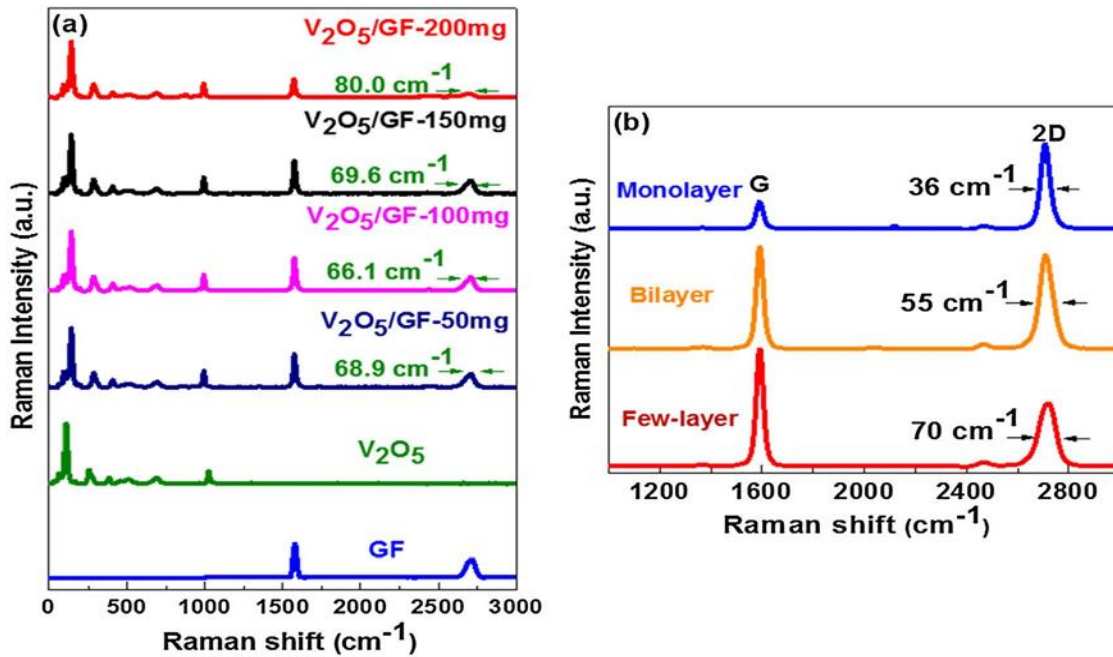

Fig. 2. The Raman spectra of the (a) GF, V_2O_5 and V_2O_5/GF composites. (b) The Raman spectra of as-grown graphene foam.

These two peaks G and 2D of the graphene foam are also observed in the V_2O_5/GF composites which are located at ~1572 and 2702 cm^{-1}, respectively. It also shows that the 2D-to-G peaks intensities ratio (I_{2D}/I_G) of the graphene in the composites is ≤0.58 and the 2D peak full width at half maximum (FWHM) is in the range of 70–80 cm^{-1} which confirms the few-layer graphene into the V_2O_5 matrix. As observed in Fig. 2a, the I_{2D}/I_G ratio decrease significantly as the GF mass loading is increased. Since 2D peak is very susceptible to the impurities its reduction is an indication of more interaction of graphene with V_2O_5. The Raman band at 95.3, 142, 283, 405, 518, 693, 993 cm^{-1} are seen in V_2O_5, and the V_2O_5/GF composite and are associated with the orthorhombic V_2O_5 nanosheets stretching mode [33,53]. The low intensity at 95.3 cm^{-1} is related to the bending vibration (A_g) which can be described in terms of external modes of V_2O_5 units [54]. The high intensity peak at 142 cm^{-1} wavenumbers is linked to the bending vibration (B_{3g} species) associated with the layered structure [55,56]. The Raman band located at 283, 405, 540, 693 cm^{-1} are due to the bending vibrations of O—V—O bond (B_{2g} mode) and asymmetric stretching of the V—O—V bond (A_g mode). The band at 993 cm^{-1} is attributed to the stretching of the V=O arising from of the typical bands of V_2O_5 crystallites [53,57]. Fig. 2a shows also the Raman spectrum of as-synthesized graphene foam.

Fig. 2b shows the Raman data of as-grown graphene foam taken from different spots of the same sample. From the figure, it is clear that GF consists of different thicknesses throughout the sample ranging from monolayers, bilayers and a few layers. The layer distribution can be crudely determined by using I_{2D}/I_G and FWHM of 2D peak where for instance, $I_{2D}/I_G > 3$ and the 2D peak with the FWHM in the range of 28–38 cm^{-1} demonstrate the characteristics of a monolayer graphene. The I_{2D}/I_G ratio of ~1 and the 2D peak with FWHM in the range of 40–65 cm^{-1} demonstrates characteristics of bilayer graphene and the I_{2D}/I_G ratio <0.6 and the FWHM approximately >70 cm^{-1} are features of few-layer graphene. Moreover, the absence of the D-band (at ~1350 cm^{-1}) in the spectra shows high-quality of as-grown graphene foam since its presence demonstrates defects in the translational symmetry of the carbon lattice. The values obtained from the I_{2D}/I_G ratio and the 2D peaks FWHM in Fig. 2a can confirm the incorporation of graphene into the V_2O_5.

Fig. 3 displays the results from the BET analysis with the N_2 adsorption-desorption isotherms for the V_2O_5 and V_2O_5/GF composite with different GF mass loading. A type III isotherm with an H3 hysteresis loop was recorded for the V_2O_5, V_2O_5/GF-150 mg
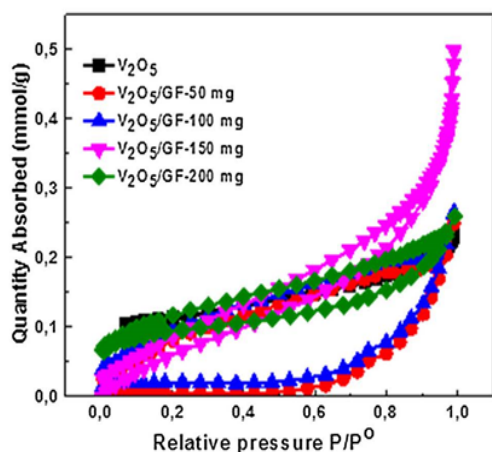
and V_2O_5/GF-200 mg while a type II isotherm with an H3 hysteresis loop was depicted for the V_2O_5/GF-50 mg and V_2O_5/GF-100 mg samples. These H3 hystereses for the V_2O_5 and V_2O_5/GF composites with different GF mass loading indicate the presence of non-rigid aggregates of plate-like particles [58].

The noticeable difference in the N_2 adsorption-desorption isotherms (type II and III) of the V_2O_5/GF composites could be due to different integration to the varying amount of GF in the V_2O_5 network which could influence the specific processes of structure evolution during the crystallization; nucleation, island growth, coalescence of islands, formation of polycrystalline islands and channels. The specific surface areas (SSAs) calculated for GF, V_2O_5 and V_2O_5/GF composites with different GF mass loading are summarized in Table 1. As observed, the specific surface area increases with increasing amount of GF added up to 150 mg. Then, it decreases with an increase in the mass of GF at 200 mg.

The BET analysis revealed that the V_2O_5/GF-150 mg has higher SSA than all other composites. This is due to the fact that initial incorporation of GF into the pristine material framework is still too little for enhancement of pore development. Sufficient amounts of GF incorporated into the pristine V_2O_5 framework yield the V_2O_5/GF-150 material which demonstrates a high specific surface area coupled with an optimized pore network which could contribute to an excellent transport of electrons and ions in device energy storage applications.

The results from the morphological analysis of the V_2O_5, graphene foam and V_2O_5/GF nanosheet-like composite samples are presented in Fig. 4. The SEM micrograph of the V_2O_5 sample (Fig. 4a) is composed of a nanosheet-like structure with very thin-flakes. The interconnected V_2O_5 sheets are built from numerous nanosheets randomly merged into three-dimensional (3D) architectures.

Fig. 4b shows the SEM image of the graphene foam showing a sheet-like morphology [45] which are connected by weak van der Waals interactions [59]. Fig. 4c–f show the SEM image of as-synthesized V_2O_5/GF composites for varying the mass content of GF present (50–200 mg). Fig. 4c, d and f show a partial integration of the GF on the surface of the V_2O_5 and could negatively affect the electrochemical performance of these composites because of the composites not being able to take advantage of each material's properties. However, a complete and efficient integration of the GF is seen in Fig. 4e when 150 mg of the graphene is added. A good interaction between the GF sheets and the V_2O_5 nanosheets is exhibited which could provide efficient channels for charge and ionic transport within the composite when adopted as electrochemical device electrodes because of the good electrical conductivity, high specific surface area and stability provided by GF.

Based on the results obtained from the BET and SEM analysis in Figs. 3 and 4 respectively, further analysis of the V_2O_5 and V_2O_5/GF-150 mg composite was done using TEM and X-ray photoelectron spectroscopy (XPS). The TEM images were further used to investigate the morphology of the V_2O_5 and V_2O_5/GF-150 mg as shown in Fig. 5. The TEM micrograph revealed the presence of thin-sheets of flake-like vanadium pentoxide architectures shown in Fig. 5a. In Fig. 5b, the V_2O_5/GF-150 mg composite material clearly exhibits an overlapping of the GF and V_2O_5 nanosheets. It confirms the complete integration of the GF into the V_2O_5 matrix without an alteration of morphologies of both materials.

X-ray photoelectron spectroscopy (XPS) was used to study the chemical/oxidations states of GF, V_2O_5 and V_2O_5/GF-150 mg composite. Fig. 6(a) shows the wide scan XPS spectra of the GF, as-synthesized V_2O_5 nanosheets and V_2O_5/GF-150 mg composite. The wide scan XPS spectrum of the GF shows mostly C 1s peak with no traces of nickel suggesting that nickel template was successfully etched away, while the observed O1s peak could be due to handling of sample in the air. The wide scan XPS spectra of the as-

Fig. 3. N2 absorption/desorption isotherms of V_2O_5 and V_2O_5/GF composites.

118

Table 1
A summary of specific surface area for the V$_2$O$_5$, GF and V$_2$O$_5$/GF with different GF mass loading.

Material	V$_2$O$_5$	GF	V$_2$O$_5$/GF-50 mg	V$_2$O$_5$/GF-100 mg	V$_2$O$_5$/GF-150 mg	V$_2$O$_5$/GF-200 mg
SSA (m^2/g)	4.9	208.8	5.1	8.0	9.5	6.2
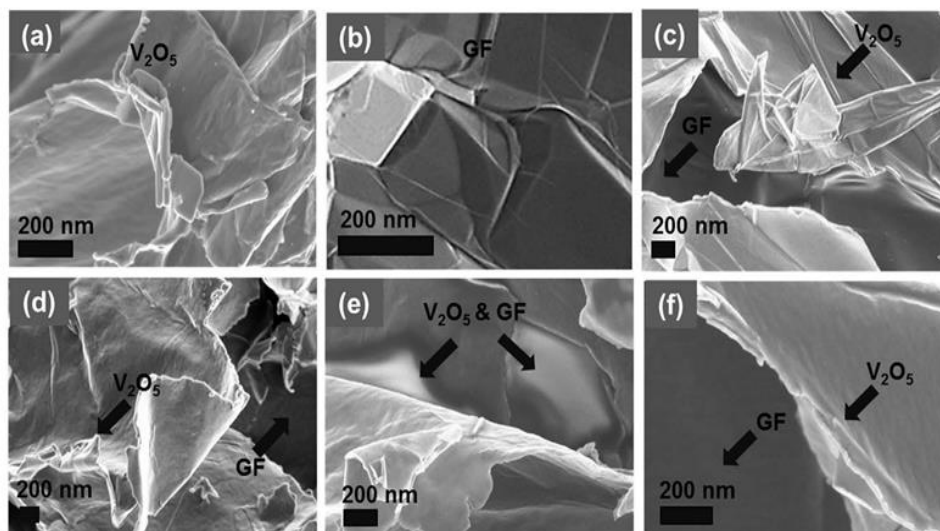
Fig. 4. SEM image of (a) as synthesized V$_2$O$_5$, (b) graphene foam (GF), (c) V$_2$O$_5$/GF-50 mg composite, (d) V$_2$O$_5$/GF-100 mg composite, (e) V$_2$O$_5$/GF-150 mg composite and (f) V$_2$O$_5$/GF-200 mg composite at high magnification.
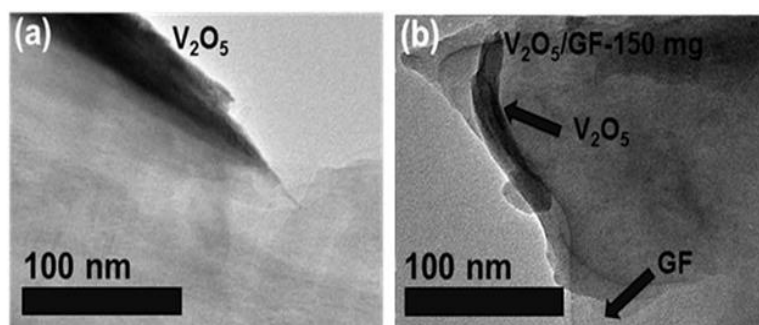
Fig. 5. TEM images of as-synthesized (a) V$_2$O$_5$ nanosheets and (b) V$_2$O$_5$/GF-150 mg composite, of the V$_2$O$_5$ into the composite.

synthesized V$_2$O$_5$ and V$_2$O$_5$/GF-150 mg composite display the main elements of the composition of the samples. The same element composition is expected for other compositions and hence it is not necessary to include them in the manuscript. Fig. 6(b) shows the fitted core level spectrum of C1s of a GF. The fitted binding energy peaks, i.e. sp^2 C=C (284.4 eV), C–O–C (285.0 eV), C=O (286.4 eV), O–C=O (288.4 eV) and π–π^* (291.2 eV) [60–62], reveal the sp^2 hybridization component of GF, traces of oxide components and the π–π^* electrons transition [61–63]. It is worth mentioning that the fitted core level spectrum of C1s of a GF shows a form of high-quality graphene. In the V$_2$O$_5$/GF-150 mg composite (Fig. 6 (c)), it shows a broad and asymmetric core level spectrum of C1s compared to GF which is due to an increase in the oxide components of the GF confirming an interaction between V$_2$O$_5$ and GF in the composite. In fact, due to unpaired π-electron in C (GF) and high electronegativity of oxygen, a chemical interaction

between GF and V$_2$O$_5$ in the composite has occurred during synthesis.

In Fig. 6d, two peaks (2p$_{3/2}$ and 2p$_{1/2}$) are shown from the core level spectrum of V2p of as-synthesized V$_2$O$_5$.

The core level spectrum of V2p reveals the binding energy peaks at 517.1 and 524.6 eV which correspond to the V2p$_{3/2}$ and V2p$_{1/2}$ respectively [64–66]. The V2p core level spectrum suggests a vanadium oxidation state of 5$^+$ which confirms the formation of V$_2$O$_5$ [67,68]. The core level spectrum of V2p from both as-synthesized V$_2$O$_5$ nanosheets and the V$_2$O$_5$/GF-150 mg composite is the same, as shown in Fig. 6(e), confirming the same chemical/oxidation state of the vanadium in both samples. Furthermore, as shown in Fig. 6 (f), the core level spectra of O1s from both as-synthesized V$_2$O$_5$ nanosheets and the V$_2$O$_5$/GF-150 mg composite is broad and asymmetric, which indicate the existence of different oxygen components with predominant component assigned to oxygen in V$_2$O$_5$.
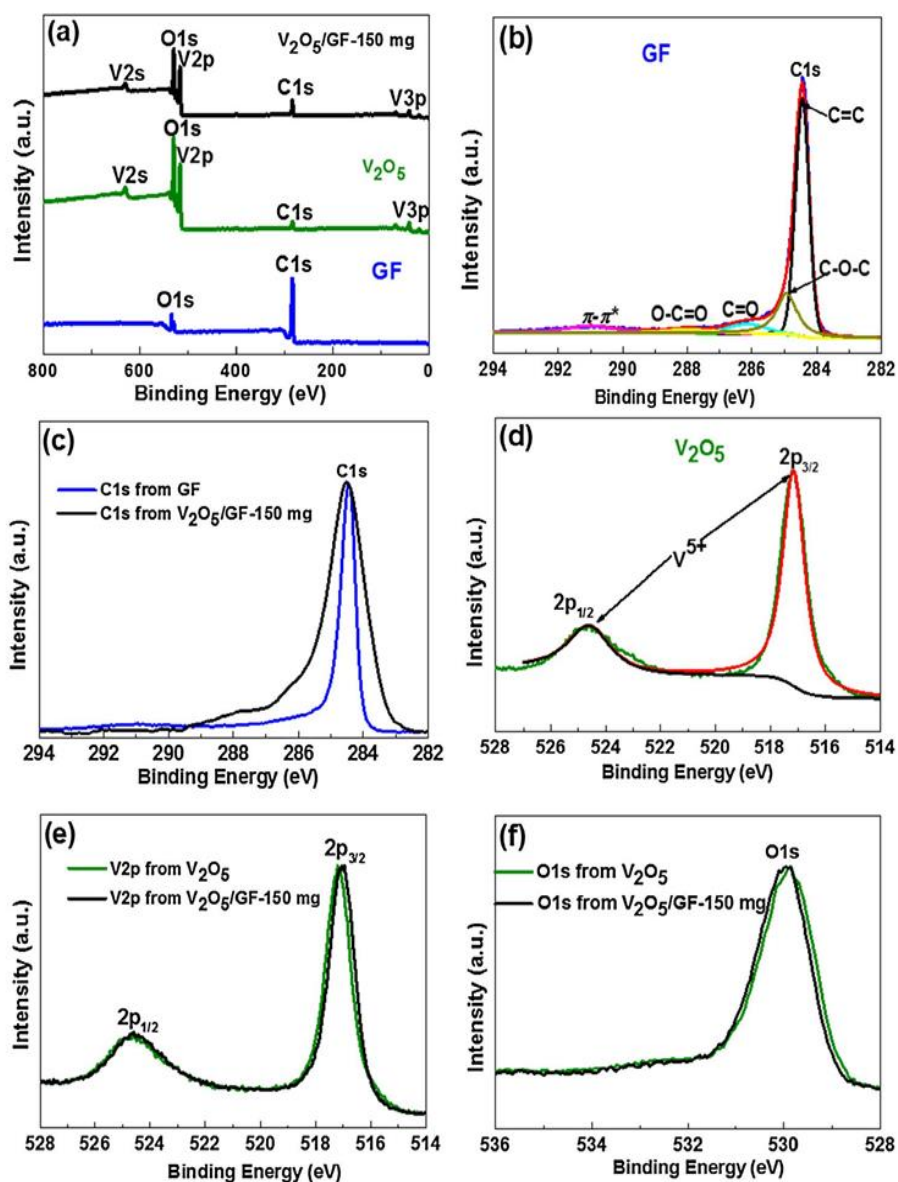
Fig. 6. (a) The wide scan XPS spectra of the GF, as-synthesized V_2O_5 nanosheets and V_2O_5/GF-150 mg composite. (b) The fitted core level spectrum of C1s of a GF. (c) The core level spectra of C1s from GF and V_2O_5/GF-150 mg composite. (d) The fitted core level spectrum of V2p of V_2O_5 nanosheets. (e) The core level spectrum of V2p from both as-synthesized V_2O_5 nanosheets and V_2O_5/GF-150 mg composite. (f) The core level spectra of O 1s from both as-synthesized V_2O_5 nanosheets and V_2O_5/GF composite.

3.1. Electrochemical performance of electrodes

The electrochemical measurements of the V_2O_5 and V_2O_5/GF composites with varying mass of GF (50–200 mg) in three electrode configuration in 6 M KOH electrolytes are shown in Fig. 7.

Fig. 7a shows the cyclic voltammogram (CV) plots for the V_2O_5 and the V_2O_5/GF composites with varying mass of GF (50–200 mg) at 50 mV s^{-1}. Fig. 7b and c show the specific capacity Q_S calculated using Eq. (1) as a function of GF mass loading at 1 A g^{-1} and specific current respectively:

$$Q_S = \frac{I_d \times t_D}{3.6} \qquad (1)$$

where I_d is the gravimetric specific current in A g^{-1}, t_D is the discharge time (s) and Q_S is the specific capacity (mA h g^{-1}).

Fig. 7a–c clearly shows that V_2O_5/GF-150 mg composite displayed the highest current response, specific capacity as a function of GF mass loading and the specific capacity for all specific currents considered. Fig. 7d also shows that V_2O_5/GF-150 mg has displays better stability in terms of both Columbic efficiency (99%) and capacity retention (95%) as compared to the pristine sample with 98% Columbic efficiency and 93% capacity retention respectively over 5000 cycles. It is therefore clear that V_2O_5/GF-150 mg sample presents the best electrochemical performance as compared to other composites due to the successful interaction of the V_2O_5 nanosheets with the GF.

120
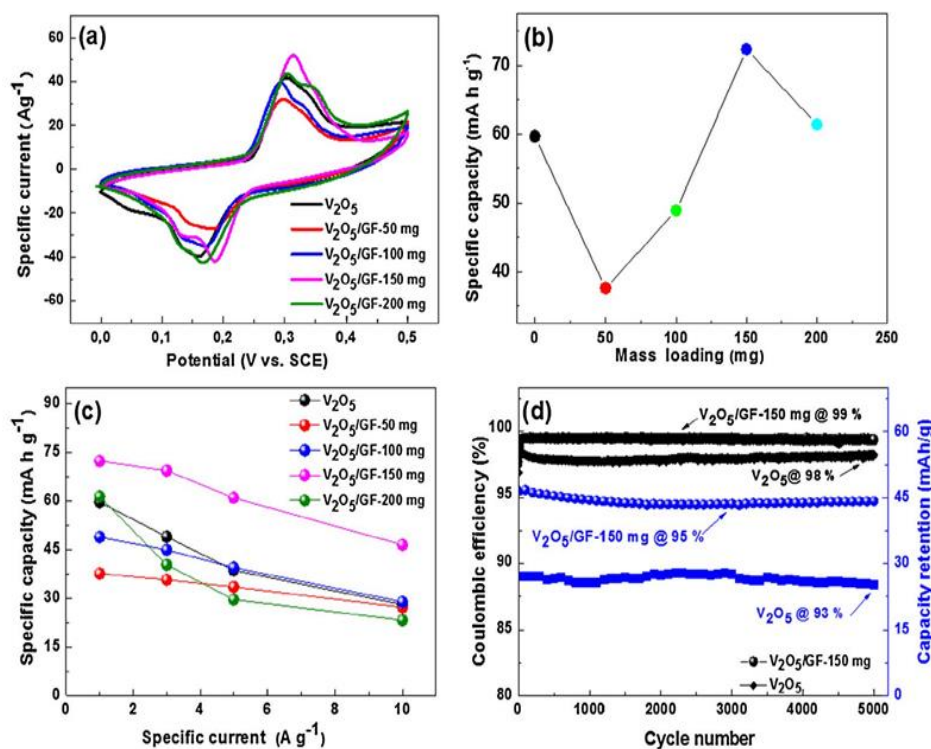
Fig. 7. The comparison of V_2O_5 and V_2O_5/GF composites (a) the CV curves at $50\,mV\,s^{-1}$, (b) the specific capacity of $1\,A\,g^{-1}$ as a function of GF mass loading, (c) the specific capacity as function of specific current and (d) Coulombic efficiency and capacity retention as a function of cycle number at a specific current of $10\,A\,g^{-1}$ V_2O_5 and V_2O_5/GF-150 mg samples.

Because of the excellent electrochemical performance that is displayed by V_2O_5/GF-150 mg, further electrochemical measurements will be done on it including the asymmetric device where it will be used as a cathode electrode. Fig. 8a shows the CV curves of the V_2O_5/GF-150 mg composite electrode at different scan rates from 5 to $100\,mV\,s^{-1}$ within an operating potential range of 0.0–0.5 V. The CV curves shows reduction and oxidation peaks linked to the electrochemical redox reactions at the electrode/electrolyte interface, indicating the conventional behaviour of a battery-type electrode. The CV curve at a scan rate of $50\,mV\,s^{-1}$ show a pair of redox peaks corresponding to the anodic peak at ~0.15 V and cathodic peak at ~0.30 V. The results suggest that the CV curves are mainly based on a redox mechanism.

Fig. 8b shows the corresponding galvanostatic charge-discharge (GCD) curves at different specific currents within the same operating potential range as in CV tests. Each GCD plot displays a non-linear charge-discharge pattern, confirming the existence of a Faradaic behavior as seen earlier in the CV plots for the pristine V_2O_5 and the V_2O_5/GF-150 mg composite.

Fig. 8c shows the Nyquist plot of the V_2O_5/GF-150 mg composite, recorded in the frequency range of 100 kHz–10 mHz. The equivalent series resistance (ESR) value of the V_2O_5/GF-150 mg composite was 0.44 Ω which indicates good interaction of material/electrolyte and also current collector/material interaction.

Upon evaluation of the optimal performance of the V_2O_5/GF-150 mg electrode and C-Fe/PANI electrodes extensively, an asymmetric cell was assembled using V_2O_5/GF-150 mg as a positive electrode and C-Fe/PANI as a negative electrode in 6 M KOH. To account for charge balance in the asymmetric cell, the masses of both electrodes were calculated by adopting the following Eqs. (2) and (3):

$$Q_{V_2O_5/GF-150mg} = Q_{C-Fe/P} \qquad (2)$$

$$\frac{m_{V_2O_5/GF-150mg}}{m_{C-Fe/PANI}} = \frac{(I.t_D)_{C-Fe/PANI}}{(I.t_D)_{V_2O_5/GF-150mg}} \qquad (3)$$

where m_{VO_2} and $m_{C-Fe/PANI}$ are mass loading of the V_2O_5 and C-Fe/PANI electrodes and $Q_{V_2O_5/GF-150mg}$ and Q_{C-FP} are the total charge on the V_2O_5 electrode and C-Fe/PANI electrodes respectively, I the current and t_D is the discharge time.

Fig. 9a shows the superposition of the individual CV profiles for the V_2O_5/GF-150 mg and C-Fe/PANI electrodes measured in their respective stable working potential windows of −1.2 to 0.0 V and 0.0 to 0.5 V at a scan rate of $50\,mV\,s^{-1}$.

Fig. 9b shows the calculated specific capacities of both electrodes at different specific currents of $1–10\,A\,g^{-1}$. This clearly shows the range of specific capacity of both electrodes which clearly gives an idea of the variance of the specific capacity over a wide gravimetric specific current. These two materials have specific capacities values of 72 and $79\,mA\,h\,g^{-1}$ respectively recorded for both electrodes materials at $1\,A\,g^{-1}$ which are quite close to each other and hence this should lead to similar masses from Eq. (3).

Fig. 9c shows the CV curves of the V_2O_5/GF-150 mg//C-Fe/PANI asymmetric device at different scan rates from 5 to $100\,mV\,s^{-1}$ within the large combined stable operating voltage of 1.6 V. The nature of the CV plots indicates a combination of both EDLC and Faradaic charge storage mechanisms confirming the existence of a hybrid-type device with an extended operating voltage in aqueous electrolyte.

Fig. 9d shows the related galvanostatic charge–discharge (GCD) curves of the V_2O_5/GF-150 mg//C-Fe/PANI hybrid device at differ-
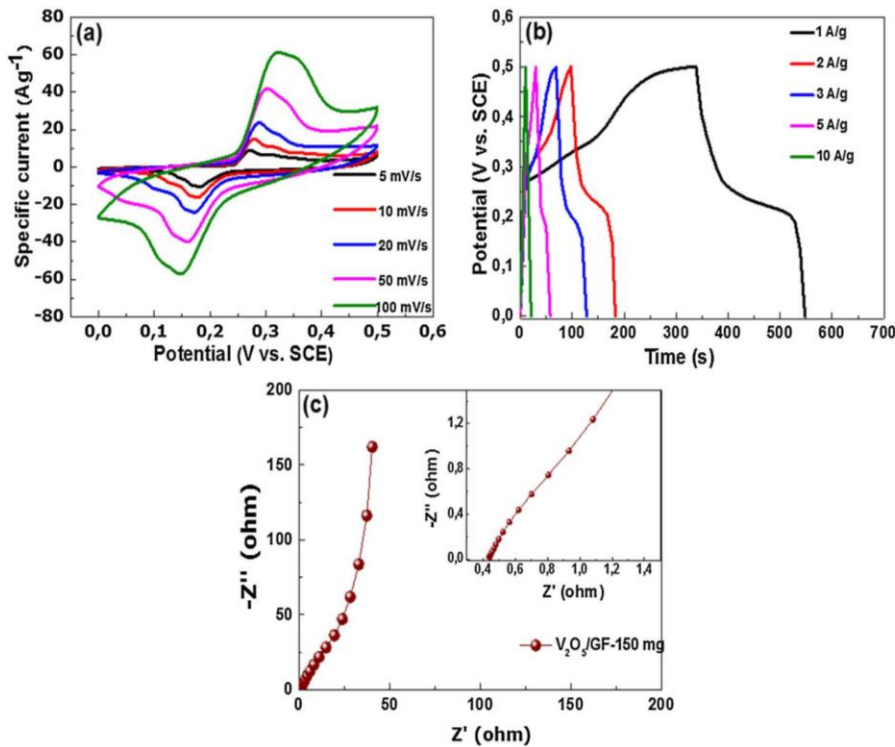
Fig. 8. (a) CV curves at different scan rates, (b) GCD curves at different specific currents and (c) Nyquist plot (the inset to (c) is the magnified plot showing) of the V_2O_5/GF-150 mg composite.

ent specific currents of 1–10 A g^{-1} in a similar operating voltage of 0.0–1.6 V. From the GCD curves, the specific capacity Q (mA h g^{-1}) of the V_2O_5/GF-150 mg//C-Fe/PANI device was calculated using Eq. (1). The plot of the specific capacity as a function of the specific current is shown in Fig. 9e. A specific capacity of 41 mA h g^{-1} was calculated for the asymmetric V_2O_5/GF-150 mg//C-Fe/PANI device at a gravimetric specific current of 1 A g^{-1}.

A decrease in specific capacity with increasing specific current is linked to the inability of ions to adequately access porous sites with higher charge kinetics. Fig. 9f shows the plot of the power density as a function of energy density for the asymmetric V_2O_5/GF-150 mg//C-Fe/PANI at different specific currents. The energy density (E_d), power density (P_d) and the maximum power density of the asymmetric device were calculated using Eqs. (4) and (5):

$$E_d(\text{W h kg}^{-1}) = \frac{I_d}{3.6} \int V(t)dt \tag{4}$$

$$P_d(\text{W kg}^{-1}) = 3600\frac{E_D}{t} \tag{5}$$

$$P_{max}(\text{W kg}^{-1}) = \frac{V^2}{4 \times m \times R_S} \tag{6}$$

where I_d is the specific current in A g^{-1}, t is the discharge time (s), and V is the potential window (V), m is the total mass (mg) of anode and cathode and R_s is the solution resistance (Ω) (obtained from the Nyquist plot) of the V_2O_5/GF-150 mg//C-Fe/PANI.

The energy density of 39 W h kg^{-1} was recorded for the V_2O_5/GF-150 mg//C-Fe/PANI hybrid device with a corresponding power density of 947 W kg^{-1} at a specific current of 1 A g^{-1}. The energy and power densities are higher than those reported in the literature. Kim et al. synthesized V_2O_5/carbon nanofiber composites

(CNFCs) electrode by electrospinning method in 6 M KOH for supercapacitor application. They then produced symmetric device with energy and power densities of 18.8 Wh kg^{-1} and 400 W kg^{-1} respectively [68]. Bonso et al. reported the exfoliated graphite nanoplatelet (xGnP) and V_2O_5 nanotube (VNT) composite electrodes by ultrasonication and a sol-gel method in 1 M LiTFSI. They fabricated an asymmetric device using activated carbon (AC) cloth as the positive electrode and xGnP-VNT composite as the negative electrode. The energy and power densities were 28 Wh kg^{-1} and 303 W kg^{-1}, respectively, at 250 mA g^{-1} [69].

Qian et al. prepared the V_2O_5/PPy core/shell by a "seeding approach" with a Ni substrate and a double hydrolysis for solid-state supercapacitors in LiNO$_3$/PVA (polyvinyl alcohol) gel electrolyte. The symmetric device of V_2O_5/PPy displayed an energy density of 14.2 W h kg^{-1} at a power density of 250 W kg^{-1} at 0.5 A g^{-1} [70]. Chen et al. synthesized the carbon nanotubes and vanadium pentoxide (V_2O_5) electrodes by in situ hydrothermal processes for supercapacitor composite in 1 M Na$_2$SO$_4$. The asymmetric devices of the V_2O_5//CNT exhibited an energy density of 16 W h kg^{-1} at a power density of 75 W kg^{-1} at 0.25 A g^{-1} [71]. The maximum power density of the asymmetric device was also calculated to be 7.75 kW kg^{-1} using the R_S value of 1.18 Ω from Eq. (6). This high energy and power densities recorded for the asymmetric V_2O_5/GF-150 mg//C-Fe/PANI device is due to the reasonable specific capacity and large working potential window, fast charge/discharge process kinetics [72].

Fig. 10a shows the initial stability tests carried out on the asymmetric V_2O_5/GF-150 mg//C-Fe/PANI cell in order to evaluate the cyclic performance of the device. The hybrid device was subjected to continuous charge-discharge cycling for up to 10,000 cycles at the high 10 A g^{-1} specific current. An excellent coulombic efficiency of 99% and a good capacity retention of 74.5% were obtained
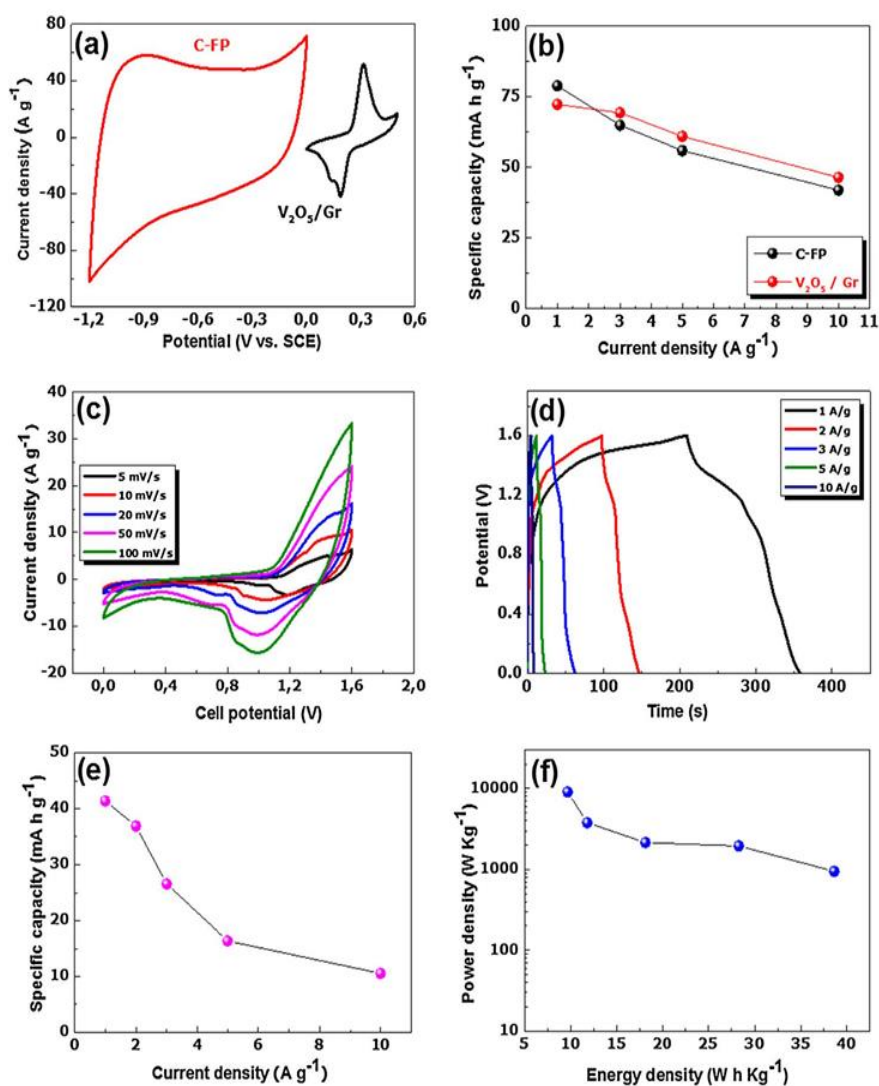
Fig. 9. (a) CV curves of V_2O_5/GF and C-Fe/PANI electrodes at 50 mV s^{-1} showing both negative and positive potential windows, (b) specific capacities as a function of specific current for the V_2O_5/GF-150 mg and C-Fe/PANI electrodes for three-electrode measurements, (c) CV of the V_2O_5/GF-150 mg//C-Fe/PANI asymmetric cell devise at different scan rates (d) GCD curves of the cell device at specific currents of 1–10 A g^{-1}, (e) specific capacity as a function of specific current for the V_2O_5/GF-150 mg//C-Fe/PANI asymmetric cell device and (f) Ragone plot for the V_2O_5/GF-150 mg//C-Fe/PANI.

which is an indication of the excellent electrochemical stability of the device. The stability of the asymmetric V_2O_5/GF-150 mg//C-Fe/PANI device also showed the considerable increase in the coulombic efficiency after the first 4000 cycles and maintained 99% throughout the cycling of up to 10,000 cycles which could be due to phase activation of the active materials.

The floating test or voltage holding test was also used to assess further the stability of the V_2O_5/GF-150 mg//C-Fe/PANI. During the floating test, each 10 h potential holding step is followed by three galvanostatic charge-discharge cycles and calculated the specific capacity from the third discharge for up to 130 h. Fig. 10b exhibits the stability of specific capacity with a rapid increase after 30 h of floating test before reaching a plateau. This increase in specific capacity value after the first 30 h could be due to the increase in accessible redox sites during the aging time.

Fig. 10c shows the Nyquist plots of the asymmetric device before stability, after 10,000 cycling and after voltage holding carried out in the frequency range of 100 kHz to 10 mHz. R_S values of 1.18 Ω before cycling tests, 1.19 Ω after cycling and 1.20 Ω after voltage holding were recorded for the hybrid device which is quite close to each other. The high maximum power density for the V_2O_5/GF-150 mg//C-Fe/PANI hybrid device can also be due to the low equivalent series resistance (ESR) value recorded which suggests a good electrical conductivity in the asymmetric cell. The Nyquist plot after 10,000 cycling as shows a small deviation to the initial curve. However, the diffusion length before stability is shorter than others but diffusion length after voltage holding shows the ideal electrochemical feature with respect to the vertical axis which has shifted slightly more towards the imaginary impedance (Z) axis compared to the one before stability and after 10,000 cycling.

Fig. 10. (a) Cycle stability and capacity retention for up to 10,000 cycles at specific current of 10 A g^{-1}, (b) plot of specific capacity at maximum operating voltage for up to 130 h at 10 A g^{-1}, (c) Nyquist plot before stability, after 10,000 cycling and after voltage holding at a specific current of 10 A g^{-1} (the inset to (c) is the magnified plot showing) and (d) plot of energy density at maximum operating voltage as function of floating time up to 130 h at 10 A g^{-1} of the asymmetric device.

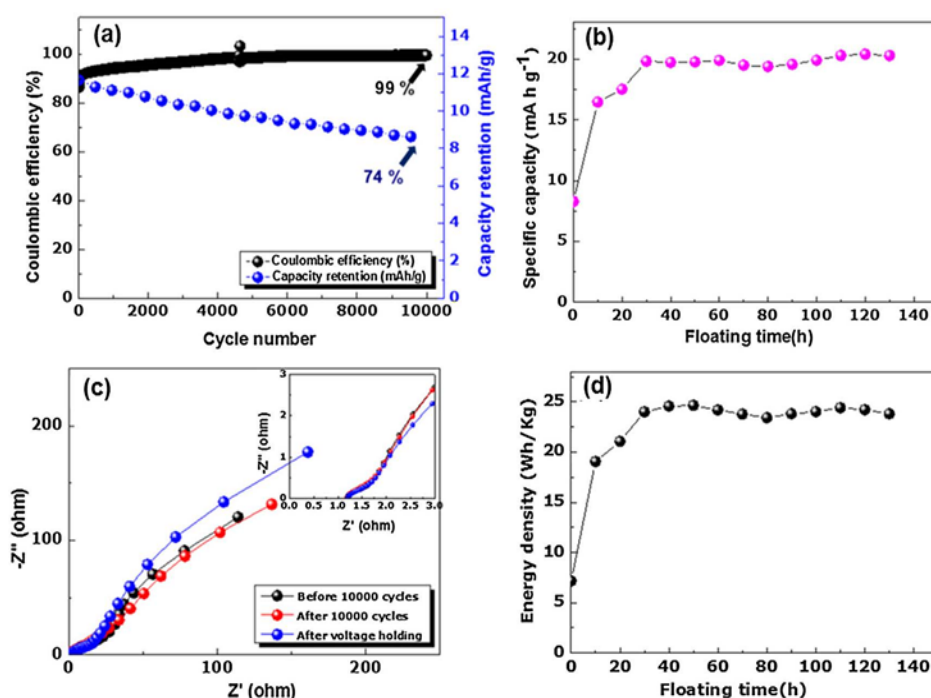In addition, the energy density as a function of voltage holding time up to 130 h is shown in Fig. 10d. It shows that the energy density increases by 55% after the first 30 h of floating test which is consistent with the similar increase in specific capacity. The excellent cycling test of the V$_2$O$_5$/GF-150 mg//C-Fe/PANI device showed that this asymmetric device presents a long-term stability with a small degree of degradation.

4. Conclusion

We have successfully synthesized 3D V$_2$O$_5$/GF composites by hydrothermal method and freeze drying process. The optimized incorporation of GF into 3D V$_2$O$_5$ matrix was found to correspond to 150 mg GF mass loading as evidenced by the best specific surface area, CV current response, specific capacity and stability.

An asymmetric device assembled with the optimized V$_2$O$_5$/GF-150 mg and the pyrolysis of Fe cation absorbed onto polyaniline (C-Fe/PANI) exhibited an energy density of 39 Wh kg^{-1} with a corresponding power density of 947 W kg^{-1} at a specific current of 1 A g^{-1} in a wide operating voltage of 1.6 V which are higher than those reported in the literature for the similar materials and device. The hybrid supercapacitor also showed an excellent cycling stability with 99% coulombic efficiency and 74% capacity retention up to 10,000 charge-discharge cycles at a specific current of 10 A g^{-1}. Additionally, an excellent stability was displayed from the voltage holding tests done for over 130 h showing much improved specific capacity and energy density after 30 h as an indication that the electrodes materials became better after voltage holding measurements. These results clearly make these materials suitable for high-performance electrode materials for supercapacitor applications. The good electrochemical performance of the V$_2$O$_5$/GF-150 mg//C-Fe/PANI can be improved by using an ionic liquid as an electrolyte to increase the potential window and hence the energy density without compromising its power density.

References

[1] M.H. Nehrir, C. Wang, K. Strunz, H. Aki, R. Ramakumar, J. Bing, Z. Miao, Z. Salameh, I.E.E.E. Trans, Sustain. Energy 2 (2011) 392–403.
[2] P.S.L. Vipin Kumar, Sangbaek Park, Kaushik Parida, Venkateswarlu Bhavanasi, Mater. Today Energy 4 (2017) 41–57.
[3] P.A. Østergaard, B.V. Mathiesen, B. Möller, H. Lund, Energy 35 (2010) 4892–4901.
[4] I.G. Mason, S.C. Page, A.G. Williamson, Energy Policy 38 (2010) 3973–3984.
[5] Y.H. Lu Wang, B.W. Xiao Feng, Junwen Zhou, Pengfei Qi, Coord. Chem. Rev. 307 (2016) 361–381.
[6] C. Du, J. Yeh, N. Pan, Nanotechnology 16 (4) (2005) 350–353.
[7] X. Wang, Y. Zhang, C. Zhi, X. Wang, D. Tang, Y. Xu, Q. Weng, X. Jiang, M. Mitome, D. Golberg, Y. Bando, Nat. Commun. 4 (2013) 2905.
[8] J. Chmiola, C. Largeot, P.L. Taberna, P. Simon, Y. Gogotsi, Science 328 (2010) 480–483.
[9] S. Rold, M. Granda, R. Men Endez, R. Santamaría, C. Blanco, J. Phys. Chem. C 115 (2011) 17606–17611.
[10] F. Zhang, T. Zhang, X. Yang, L. Zhang, K. Leng, Y. Huang, Y. Chen, Energy Environ. Sci. 6 (2013) 1623.

[11] H.W. Haichao Chen, Jianjun Jiang, Li Zhang, Dandan Xia, Yuandong Zhao, Danqing Guo, Tong Qi, J. Power Sources 254 (2014) 249–257.
[12] M. Uno, H. Toyota, IEEE Power Electron. Spec. Conf., IEEE, 2008, pp. 755–760.
[13] C. Liu, Z. Yu, D. Neff, A. Zhamu, B.Z. Jang, Nano Lett. 10 (2010) 4863–4868.
[14] Z. Tang, C. Tang, H. Gong, Adv. Funct. Mater. 22 (2012) 1272–1278.
[15] M. Zhi, C. Xiang, J. Li, M. Li, N. Wu, Nanoscale 5 (2013).
[16] B. Rong-Rong, W. Xing-Long, C. Fei-Fei, J. Ling-Yan, G. Yu-Guo, Wan Li-Jun, J. Phys. Chem. C 114 (2010) 2448–2451.
[17] H. Jiang, C. Li, T. Sun, J. Ma, Nanoscale 4 (2012) 807–812.
[18] J. Zhu, L. Huang, Y. Xiao, L. Shen, Q. Chen, W. Shi, Nanoscale 6 (2014) 6772.
[19] J.-W. Lang, L.-B. Kong, W.-J. Wu, Y.-C. Luo, L. Kang, Chem. Commun. 104 (2008) 4213.
[20] L.M. Chen, Q.Y. Lai, Y.J. Hao, Y. Zhao, X.Y. Ji, J. Alloys Compd. 467 (2009) 465–471.
[21] W. Xiao, University of Akron, 2014.
[22] A. Rudge, J. Davey, I. Raistrick, S. Gottesfeld, J.P. Ferraris, J. Power Sources 47 (1994) 89–107.
[23] H. Li, Y. Gao, C. Wang, G. Yang, Adv. Energy Mater. 5 (2015) 1401767.
[24] D. Salinas-Torres, J.M. Sieben, D. Lozano-Castelló, D. Cazorla-Amorós, E. Morallón, Electrochim. Acta 89 (2013) 326–333.
[25] J. Huang, P. Xu, D. Cao, X. Zhou, S. Yang, Y. Li, G. Wang, J. Power Sources 246 (2014) 371–376.
[26] R.R. Salunkhe, J. Lin, V. Malgras, S.X. Dou, J.H. Kim, Y. Yamauchi, Nano Energy 11 (2015) 211–218.
[27] J. Yan, Z. Fan, W. Sun, G. Ning, T. Wei, Q. Zhang, R. Zhang, L. Zhi, F. Wei, Adv. Funct. Mater. 22 (2012) 2632–2641.
[28] B.G. Choi, S.-J. Chang, H.-W. Kang, C.P. Park, H.J. Kim, W.H. Hong, S. Lee, Y.S. Huh, Nanoscale 4 (2012) 4983.
[29] M. Afzal, Faraj A. Adeel, Amir Habib Abuilaiwi, M.A. Waje Awais, Samaila B. Atieh, J. Power Sources 352 (2017) 174–186.
[30] E. Umeshbabu, G. Ranga Rao, J. Colloid Interface Sci. 472 (2016) 210–219.
[31] B. Saravanakumar, K.K. Purushothaman, G. Muralidharan, A.C.S. Appl. Mater. Interfaces 4 (2012) 4484–4490.
[32] Q. Qu, Y. Zhu, X. Gao, Y. Wu, Adv. Energy Mater. 2 (2012) 950–955.
[33] M. Li, G. Sun, P. Yin, C. Ruan, K. Ai, Nano Lett. 5 (2013) 11462–11470.
[34] X. Zhou, Q. Chen, A. Wang, J. Xu, S. Wu, J. Shen, A.C.S. Appl. Mater. Interfaces 8 (2016) 3776–3783.
[35] B. Saravanakumar, K.K. Purushothaman, G. Muralidharan, J. Electroanal. Chem. 758 (2015) 111–116.
[36] K.K.T. Kudo, Y. Ikeda, T. Watanabe, M. Hibino, M. Miyayama, H. Abe, Solid State Ionics 152–153 (2002) 833–841.
[37] D. Imamura, Masaru Miyayama, Solid State Ionics 161 (2003) 173–180.
[38] A. Kuwahara, S. Suzuki, M. Miyayama, Solid State Ionics 179 (2008) 1890–1896.
[39] H. Zhang, A. Xie, C. Wang, H. Wang, Y. Shen, X. Tian, ChemPhysChem 15 (2014) 366–373.
[40] H. Zhao, A. Yuan, B. Liu, S. Xing, X. Wu, J. Xu, J. Appl. Electrochem. 42 (2012) 139–144.
[41] D. Chao, X. Xia, J. Liu, Z. Fan, C.F. Ng, J. Lin, H. Zhang, Z.X. Shen, H.J. Fan, Adv. Mater. 26 (2014) 5794–5800.
[42] R.B. Rakhi, W. Chen, D. Cha, H.N. Alshareef, J. Mater. Chem. 21 (2011) 16197.
[43] S.D. Perera, B. Patel, N. Nijem, K. Roodenko, O. Seitz, J.P. Ferraris, Y.J. Chabal, K.J. Balkus, Adv. Energy Mater. 1 (2011) 936–945.

[44] J.-J.S. Nguyen Van Hoa, Tran Thi Hoang Quyen, Nguyen Huu Nghia, Nguyen Van Hieu, J. Alloys Compd. 702 (2017) 693–699.
[45] A.A. Mirghni, M.J. Madito, T.M. Masikhwa, K.O. Oyedotun, A. Bello, N. Manyala, J. Colloid Interface Sci. 494 (2017) 325–337.
[46] M.N. Rantho, M.J. Madito, N. Manyala, Electrochim. Acta 262 (2018) 82–96.
[47] G. Li, S. Pang, L. Jiang, Z. Guo, Z. Zhang, J. Phys. Chem. B 110 (2006) 9383–9386.
[48] G. Du, K.H. Seng, Z. Guo, J. Liu, W. Li, D. Jia, C. Cook, Z. Liu, H. Liu, RSC Adv. 1 (2011) 690–697.
[49] X. Dong, Y. Cao, J. Wang, M.B. Chan-Park, L. Wang, W. Huang, P. Chen, RSC Adv. 2 (2012) 4364.
[50] Z.S. Ting Lu, Yanping Zhang, Haibo Li, Likun Pan, Yinlun Li, Electrochim. Acta 55 (2010) 4170–4173.
[51] H. Chen, M.B. Müller, K.J. Gilmore, G.G. Wallace, D. Li, Adv. Mater. 20 (2008) 3557–3561.
[52] N. Li, Q. Zhang, S. Gao, Q. Song, R. Huang, L. Wang, L. Liu, J. Dai, M. Tang, G. Cheng, Sci. Rep. 3 (2013) 1604.
[53] M. Lee, S. Kannan Balasingam, H. Young Jeong, W.G. Hong, H.-B.-R. Lee, B. Hoon Kim, Y. Jun, Sci. Rep. 5 (2015) 8151.
[54] R. Baddour-Hadjean, V. Golabkan, J.P. Pereira-Ramos, A. Mantoux, D. Lincot, J. Raman Spectrosc. 33 (2002) 631–638.
[55] S.-H. Lee, H.M. Cheong, M.J. Seong, P. Liu, C.E. Tracy, A. Mascarenhas, J.R. Pitts, S.K. Deb, Solid State Ionics 165 (2003) 111–116.
[56] S.-H. Lee, H.M. Cheong, M.J. Seong, P. Liu, C.E. Tracy, A. Mascarenhas, J.R. Pitts, S.K. Deb, J. Appl. Phys. 921 (2002) 1893–21604.
[57] M. Shanmugam, A. Alsalme, A. Alghamdi, R. Jayavel, A.C.S. Appl. Mater. Interfaces 7 (2015) 14905–14911.
[58] T.M. Masikhwa, M.J. Madito, A. Bello, J.K. Dangbegnon, N. Manyala, J. Colloid Interface Sci. 488 (2017) 155–165.
[59] Y.Z. Kangfu Zhou, S.L. Xiaoling Yang, Jie Luo, Chunzhong Li, Electrochim. Acta 55 (2010) 3055–3060.
[60] Y.V. Butenko, S. Krishnamurthy, A.K. Chakraborty, V.L. Kuznetsov, V.R. Dhanak, M.R.C. Hunt, L. Šiller, Phys. Rev. B 71 (2005) 075420.
[61] M. Hsiao, S. Liao, M. Yen, C. Teng, S. Lee, N. Pu, C. Wang, Y. Sung, M. Ger, C. Ma, M. Hsiao, J. Mater. Chem. 20 (2010) 8496.
[62] S. Ogawa, T. Yamada, S. Ishizuka, A. Yoshigoe, M. Hasegawa, Y. Teraoka, Y. Takakuwa, Jpn. J. Appl. Phys. 52 (2013) 110122.
[63] H. Aoki, M.S. Dresselhaus (Eds.), Physics of Graphene, Springer, New York, 2014.
[64] G. Kiss, H. Paulus, O. Krafcsik, F. Réti, K.-H. Müller, J. Giber, Fresenius. J. Anal. Chem. 365 (1999) 203–207.
[65] V. Bondarenka, H. Tvardauskas, M. Senulis, A. Pašiškevičius, S. Grebinskij, S. Mickevičius, I. Vitkut, Acta Phys.Pol. A 119 (2011).
[66] S. Gan, X.-M. Yan, Q. Yang, Met. Nano-Metal Chem. 45 (2015) 24–27.
[67] Q.H. Wu, A. Thißen, W. Jaegermann, Surf. Sci. 578 (2005) 203–212.
[68] B.H. Kim, C.H. Kim, K.S. Yang, A. Rahy, D.J. Yang, Electrochim. Acta 83 (2012) 335–340.
[69] J.S. Bonso, A. Rahy, S.D. Perera, N. Nour, O. Seitz, Y.J. Chabal, K.J. Balkus, J.P. Ferraris, D.J. Yang, J. Power Sources 203 (2012) 227–232.
[70] T. Qian, N. Xu, J. Zhou, T. Yang, X. Liu, X. Shen, J. Liang, C. Yan, J. Mater. Chem. A 3 (2015) 488–493.
[71] Z. Chen, Y. Qin, D. Weng, Q. Xiao, Y. Peng, X. Wang, H. Li, F. Wei, Y. Lu, Adv. Funct. Mater. 19 (2009) 3420–3426.
[72] A. Leela Mohana Reddy, F. Estaline Amitha, I. Jafri, S. Ramaprabhu, Nanoscale Res. Lett. 3 (2008) 145–151.

4.1.3 Concluding Remarks

We have successfully synthesized 3D V_2O_5/GF composites by hydrothermal and freeze-drying processes. The optimized incorporation of GF into the 3D V_2O_5 matrix was found to correspond to a 150 mg GF mass loading as shown from the SEM, the BET and electrochemical measurements. An asymmetric device assembled with the optimized V_2O_5/GF-150 mg and the pyrolysis of Fe cation adsorbed onto polyaniline (C-Fe/PANI) exhibited a specific energy of 39 W h kg^{-1} with a corresponding 947 W kg^{-1} specific power at a specific current of 1 A g^{-1} in a wide operating potential of 1.6 V. The hybrid supercapacitor also showed an excellent cycling stability with a 99% coulombic efficiency and 74% capacity retention for up to 10,000 charge–discharge cycles at a specific current of 10 A g^{-1}. These results clearly make these materials suitable high performance electrode materials for supercapacitor applications.

125

4.2 Effect of growth time on solvothermal synthesis of vanadium dioxide for electrochemical supercapacitor application

4.2.1 Introduction

The vanadium dioxide (VO_2) is an interesting electrode material for supercapacitor applications which is a low band-gap semiconductor with relatively high conductivity among the transition metal oxides [19]. Different methods have been used to synthesize the VO_2 with various morphology such us nanobelts, nanoflowers, nanowires and microspheres.

Recently, Y. Zhang et al. [20] proposed a novel synthesis method of V_2O_3 solid microspheres structures by a hydrothermal route. The morphology of the V_2O_3 can be controlled by the decomposition of VOC_2O_4, CO and CO_2 gas with oxalic acid serving as a soft template to control the structure of the V_2O_3. They concluded that this process could be successfully explored as a standard methodology in preparing different metal oxides microspheres using the oxalic acid template approach within the hydrothermal method [20].

In this work, we then considered the time-dependent morphological evolution of the as-prepared monoclinic $VO_2(M)$ by a solvothermal method for supercapacitor applications. Compared to the synthetic route proposed by Y. Zhang et al. [20] which uses the hydrothermal; our approach uses the solvothermal method at different growth times and temperatures. Different morphologies of VO_2 (i.e., microspheres and nanosheets) were successfully synthesised and the electrochemical performance of the samples was analysed in a three-electrode cell configuration using 6 M KOH aqueous electrolyte as a function of growth time.

4.2.2 Result and discussion

The detailed results of the study is presented in the paper below:

Effect of growth time on solvothermal synthesis of vanadium dioxide for electrochemical supercapacitor application

N.M. Ndiaye [a], T.M. Masikhwa [a], B.D. Ngom [b], M.J. Madito [a], K.O. Oyedotun [a], J.K. Dangbegnon [a], N. Manyala [a, *]

[a] Department of Physics, Institute of Applied Materials, SARChI Chair in Carbon Technology and Materials, University of Pretoria, Pretoria, 0028, South Africa
[b] Laboratoire de Photonique et de Nano-Fabrication, Faculté des Sciences et Techniques Kabi (UCAD) B.P. 25114, Dakar-Fann Dakar, Senegal

HIGHLIGHTS

- The effect of growth time on the morphology and electrochemical results on VO$_2$.
- The grown VO$_2$ as a function of time show two monoclinic phases.
- 6 M KOH electrolyte was found to be the best electrolyte for VO$_2$ electrochemical performance.
- 6 h was found to be the optimum growth time for best physical and electrochemical results.

GRAPHICAL ABSTRACT
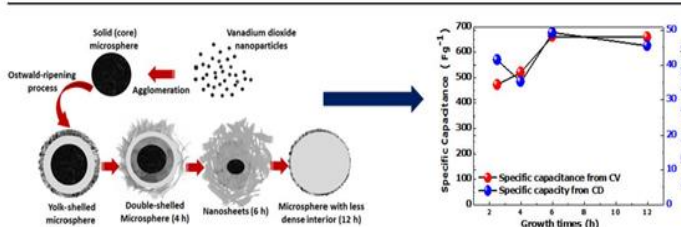
ARTICLE INFO

ABSTRACT

In this work, we report the time-dependent morphological evolution of the as-prepared vanadium dioxide (VO$_2$) and its electrochemical performance for supercapacitor applications. VO$_2$ with different morphologies (microspheres and nanosheets) were successfully synthesised by solvothermal method for time growth ranging from 2 h 30min to 12 h at a temperature of 200 °C. X-ray diffraction (XRD), Raman spectroscopy, scanning electron microscope (SEM), high resolution transmission electron microscopy (HRTEM), energy dispersive spectroscopy (EDS), gas adsorption/desorption analysis and X-ray photoelectron spectroscopy (XPS) were used to characterize the structure, morphology, composition and the oxidation state of the as-prepared samples. The electrochemical behaviour of the as-prepared VO$_2$ samples were analysed in a three-electrode cell configuration using 6 M KOH aqueous electrolyte. The VO$_2$ samples revealed monoclinic crystal structure (with VO$_2$ (B) monoclinic phase for the samples prepared for 4 h and 6 h and VO$_2$ (A) monoclinic phase for the samples grown for 2 h 30min and 12 h). The VO$_2$ samples grown for 4 h and 6 h displayed nanoflakes and nanosheets-like morphology, respectively, whereas VO$_2$ samples grown for 2 h 30min and 12 h revealed nanorods-like morphology. The 6 h grown sample also showed more porous structure leading to much higher specific surface area, pore volume and enhanced electrochemical performance with highest specific discharge capacity of 49.28 mA h g^{-1} at current density of 0.5 A g^{-1} and the corresponding specific capacitance of 663 F g^{-1} at a scan rate of 5 mV s^{-1} with excellent cycling stability as compared to others samples. Accordingly, the 6 h is considered to be optimal growth time for VO$_2$ nanosheets for considerable potential as an electrode material for supercapacitor applications.

© 2018 Elsevier B.V. All rights reserved.

---

* Corresponding author.
E-mail address: ncholu.manyala@up.ac.za (N. Manyala).

1. Introduction

The energy storage has become a key technological challenge due to the energy crisis and greenhouse effect in the past few decades [1,2]. The global scientific community has not only been developing strategies and rules for efficient energy generation and use, but has also been developing cutting-edge storage technologies to complement the energy production [3–5]. Supercapacitors (SCs), also called ultracapacitors or electrochemical capacitors (ECs) have been extensively explored in the field of energy storage compared with other storage devices such as dielectric capacitors, secondary cells and fuel cells. They exhibit higher power density and a broader range of working temperature compared to batteries, for example [6,7]. Moreover, SCs also exhibit longer cycling life and an enhanced efficiency for energy utilization hence they can store energy from various renewable energy sources such as solar energy, wind power and fast delivery on demand [8,9]. However, SCs suffer from low energy density [10], hence an improvement of their energy density will definitely increase their large-scale industrialization. In view of the energy storage mechanism, SCs can be divided into two types of capacitors, namely, electric double layer capacitors (EDLCs) that stores energy based on the electrostatic charge accumulation on the surface between the electrode and electrolyte and faradaic supercapacitors mostly depend on fast and reversible faradic reactions to store energy [6]. Generally, the capacitive property and performance of SCs are influenced by both the electrolyte and electrode material [3,11,12]. In this work, our focus will be on designing better active faradic material for SCs.

The most common electrodes used for SCs are based on carbon materials. Although, such electrodes can deliver high power density with high cycling stability, most of their energy densities are still less than $10 \, W \, h \, kg^{-1}$ and this is related to the limitation of the charge storage mechanism involved for carbonaceous materials [13]. In other words, pure non-faradaic charge separation in an electric field gives rise to EDLC which is influenced by the active surface area of the material and its pore size distribution. The bulk of the carbon material is not involved in the charge storage and the charge stored on the surface could be drawn out rapidly, explaining the high power and low energy densities. Metal oxides have also been explored, especially on the sub-bulk where electrochemical redox or faradaic reactions occur. However, in contrast to carbon materials, in metal oxides a faradaic reaction involves to some extend the bulk (sub-bulk) of the material in charge storage. As a result, metal oxide electrode materials exhibit higher capacity, but at a slower discharge rate compared to carbon electrode materials. Therefore, by tuning the structural properties of the metal oxides, for instance, the morphology of the materials, the electrochemical performance could be enhanced. In view of this, vanadium oxides which have high faradaic activity, adopt different structures (VO, V_2O_3, V_2O_5, VO_2, V_3O_5, V_4O_7) due to their variable oxidation states and can easily be engineered to a two-dimensional structure are quite interesting to be investigated as electrodes for energy storage applications.

Currently, vanadium oxides have been widely investigated as electrode materials for supercapacitors. They can be modified with reduced graphene oxides [10], CNTs [14,15], conducting polymers [16]. It is worth mentioning that for one-electron redox reaction for VO_2, the theoretical specific capacity value is as high as $323 \, mA \, h \, g^{-1}$ [17]. Thus, this material can be an excellent candidate for energy storage application.

Furthermore, Deng et al. reported the graphene/VO_2 (RG/VO_2) hybrid material for high-performance electrochemical capacitor by hydrothermal reduction technology and the material exhibited a specific capacitance of $225 \, F \, g^{-1}$ at a current density of $0.25 \, A \, g^{-1}$ in $0.5 \, M \, K_2SO_4$ aqueous solution [10]. Wang et al. prepared 3D

graphene/VO_2 nanobelt for high-performance supercapacitors by hydrothermal strategy which exhibited a specific capacitance of $191 \, F \, g^{-1}$ at a current density of $1 \, A \, g^{-1}$ in $0.5 \, M \, K_2SO_4$ aqueous solution [1]. Rakhi et al. reported VO_2 nanosheets electrodes in organic gel electrolyte for supercapacitor applications by hydrothermal method and the electrodes exhibited a specific capacitance of $405 \, F \, g^{-1}$ at a current density of $1 \, Ag^{-1}$ [18]. Xiao et al. reported the composite of metastable vanadium dioxide [$VO_2(B)$] nanobelts on reduced graphene oxide (RGO) layers by one-step hydrothermal process which exhibited a specific capacitance of $290.4 \, F \, g^{-1}$ at a current density of $0.2 \, A \, g^{-1}$ in $1 \, M \, Na_2SO_4$ aqueous solution [19]. Liming et al. prepared VO_2/ordered mesoporous carbon (CMK-3) composites for hybrid capacitors by solid-state reaction process which exhibited a specific capacitance of $131 \, F \, g^{-1}$ in $1 \, M \, KNO_3$ aqueous solution [20]. In brief, previously reported VO_2 based electrodes are mainly composites which exhibited specific capacitance values in the range of about $130–430 \, F \, g^{-1}$ [10,14,18,20,21], and were not evaluated in 6 M KOH as the electrolyte. In fact, to the best of our knowledge, no report exist on the electrochemical performance of VO_2 electrode in 6 M KOH aqueous electrolyte until the present. Usually, a choice of KOH is motivated by its high ionic conductivity (i.e. with 73.5 and $198 \, S \, cm^2 \, mol^{-1}$ for K^+ and OH^-, respectively [22]) as compared to other neutral electrolytes [23,24].

Herein, we report the time-dependent morphological evolution of the as-prepared monoclinic $VO_2(M)$ by a solvothermal method for supercapacitor applications. The synthetic route in this work for the synthesis of the VO_2 microspheres is similar to a novel route for synthesis and growth formation of metal oxides microspheres proposed by Y. Zhang et al. [25]. However, compared to the synthetic route proposed by Y. Zhang et al. [25] which uses the hydrothermal; our approach uses the solvothermal method at different growth times and temperatures. Different morphologies of VO_2 (i.e., microspheres and nanosheets) were successfully synthesised and the electrochemical performance of the samples were analysed in a three-electrode cell configuration using 6 M KOH aqueous electrolyte as a function of growth time. The as-prepared 6 h grown VO_2 nanosheets showed a significant improvement in the porous nature and exhibited enhanced electrochemical performance compared to VO_2 microspheres obtained from other growth times. The VO_2 nanosheets show a considerable potential as an electrode material for supercapacitor applications.

2. Experimental

2.1. Materials

Vanadium (V) oxide (V_2O_5, purity $\geq$ 98%), oxalic acid dehydrate ($C_2H_2O_4 \cdot 2H_2O$ purity 99%) and propan-2-ol ($CH_3CHOHCH_3$) were purchased from Sigma-Aldrich. Polycrystalline Nickel (Ni) foam (3D scaffold template with an areal density of $420 \, g \, m^2$ and thickness of 1.6 mm was purchased from Alantum (Munich, Germany)). Potassium hydroxide (KOH, min 85%) was purchased from Merck (South Africa).

2.2. Synthesis of VO_2 microspheres and nanosheets using solvothermal method

Scheme 1 shows the schematic view of the procedure used in the preparation of VO_2 sample for 2 h 30 min growth time of which the similar procedure was repeated for other different growth times of 4, 6 and 12 h. Initially, bulk V_2O_5 powder (1.2 g) and $H_2C_2O_4 \cdot 2H_2O$ in a molar ratio of 1:3 were dissolved in 40 mL of deionized water under vigorous stirring at 80 °C for 3 h until a clear blue VOC_2O_4 solution (0.33 M) was formed. Then 6 mL of the obtained precursor VOC_2O_4 was added to 60 mL of isopropanol under

Scheme 1. Preparation procedure of vanadium dioxide.

vigorous stirring for 20 min at 80 °C. The final homogeneous solution was transferred into a sealed Teflon-lined stainless-steel autoclave and kept at a temperature of 200 °C for different growth time varying from 2 h 30 min to 12 h. After cooling to room temperature, the black powder was centrifuged, washed several times with deionized water and ethanol and dried at 60 °C for 6 h. The final product has different morphologies depending on the growth time as illustrate by SEM micrograph as the last image in Scheme 1. Generally, the reactions to obtain VO_2 can be expressed as follows:

$$V_2O_5 + 3H_2C_2O_4 \rightarrow 2VOC_2O_4 + 2CO_2 + 3H_2O \tag{1}$$

$$VOC_2O_4 \rightarrow VO_2 + CO_2 + CO \tag{2}$$
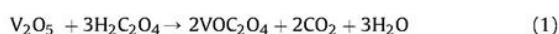
3. Structural, morphological and composition characterization

X-ray diffraction (XRD) spectra of the as-prepared VO_2 sample were collected using an XPERT-PRO diffractometer (PANalytical BV, Netherlands) with theta/2theta geometry, operating at 50 kV and 30 mA and reflection geometry at 2θ values ranging from 10 to 80° with a step size of 0.01°. Raman spectroscopy measurements were obtained using a T64000 micro-Raman spectrometer (HORIBA Scientific, Jobin Yvon Technology) with a 514 nm laser wavelength and spectral acquisition time of 120 s was used to characterize the as-prepared vanadium oxide samples. The morphology of the as-prepared VO_2 samples was studied using a high-resolution Zeiss Ultra Plus 55 field emission scanning electron microscope (FE-SEM) operated at a voltage of 2.0 kV. T High resolution transmission electron microscopy (HRTEM) micro-images was carried out with a JEOL JEM-2100F microscope operated at 200 kV (Akishima-shi, Japan). X-ray photoelectron spectroscopy (XPS, K-alpha, Thermo Fisher) with monochromatic Al $K\alpha$ radiation as the X-ray source was used to irradiate the sample surface and determine the chemistry of the samples. Nitrogen adsorption–desorption isotherms were measured at −196 °C using a Micromeritics ASAP 2020. All the samples were degassed at 180 °C for more than 12 h under vacuum conditions. The surface area was calculated by the Brunauer–Emmett–Teller (BET) method from the adsorption branch in the relative pressure range (P/P₀) of 0.01−1.0.

4. Electrochemical characterization

The electrochemical properties were studied using a Bio-Logic VMP-300 potentiostat in a three-electrode configuration controlled by the EC-Lab® V10.37 software. The vanadium dioxide material served as the working electrode, glassy carbon plate as the counter electrode and Ag/AgCl (3 M KCl) as the reference electrode in 6 M KOH electrolyte. The vanadium dioxide electrode was prepared according to the following steps: 85 wt% of vanadium dioxide was mixed with 10 wt% carbon black as conducting additive and

5 wt% polyvinylidene difluoride (PVdF) binder in an agate mortar. The mixture was then dissolved with 1-methyl-2-pyrrolidinone (NMP) to form slurry. The slurry was then uniformly pasted on a nickel foam current collector and dried at 60 °C in an electrical oven for 8 h to ensure complete evaporation of the NMP. The masses of the materials pasted on the current collector were approximately 2 mg, for comparison sake. The cyclic voltammetry tests were carried out in the potential range of 0−0.5 V (vs. Ag/AgCl) at different scan rates ranging from 5 to 100 mV s⁻¹. The galvanostatic charge−discharge measurements were also carried out at different current densities from 0.5 to 10 A g⁻¹ and the electrochemical impedance spectroscopy (EIS) measurements were done in the frequency range of 100 kHz−10 mHz in open circuit voltage. All the electrochemical tests were performed at room temperature.

5. Results and discussion

5.1. Structural, morphological, and composition characterization

Fig. 1(a) shows the XRD patterns of the as-prepared vanadium dioxide samples grown at 200 °C for 2 h 30 min, 4 h, 6 h and 12 h, respectively. The XRD patterns of the as-prepared samples display diffraction peaks confirming the samples crystallinity. In Fig. 1(a), it can be seen that for a growth times of 2 h 30 min, and 12 h, the XRD patterns are similar, while samples for a growth times of 4 h and 6 h show similar XRD patterns as well. Although, the XRD patterns for the growth times of 4 h and 6 h appear noticeably different from those of 2 h 30 min and 12 h, one is looking at the same material.
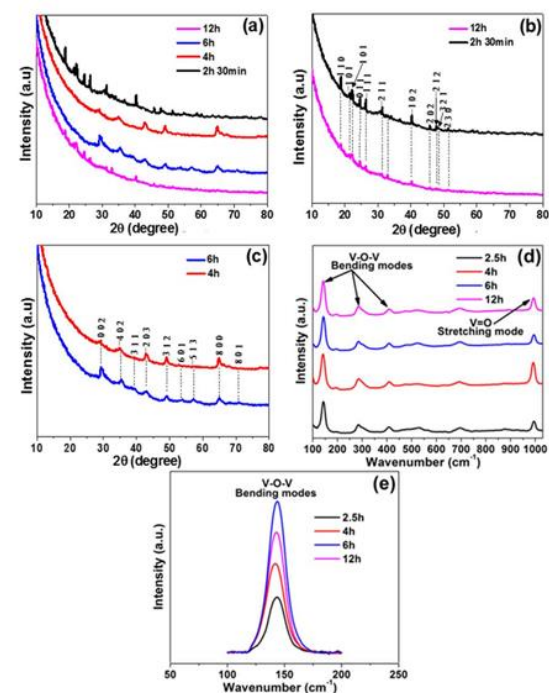

Fig. 1. (a) The XRD patterns of the as-prepared vanadium dioxide samples grown at 200 °C for 2 h 30 min, 4, 6 and 12 h. The XRD patterns for samples grown at (b) 2 h 30 min and 12 h (c) 4 h and 6 h (d) The Raman spectra of the samples synthesised at growth times shown in the figure, and (e) a comparison of the intensity of the prominent Raman band at the different growth times.

Furthermore, the XRD patterns of the as-prepared vanadium dioxide samples grown for 2 h 30 min, 4 h, 6 h and 12 h were indexed to a monoclinic structure with different phases.

The XRD patterns of the vanadium dioxide samples grown for 2 h 30 min and 12 h can be indexed as VO_2 (A) monoclinic structure with a space group $P\ 1\ 2/m\ 1$ and lattice parameters of $a = 9.0600$ Å, $b = 5.8000$ Å, $c = 4.5217$ Å, $\beta = 91.85°$ using the best matching inorganic crystal structure database (ICSD) card #1503 for VO_2, as shown in Fig. 1(b). The XRD patterns for growth times of 4 h and 6 h were indexed as VO_2 (B) monoclinic structure with a space group of $C\ 1\ 2/m\ 1$, lattice parameters of $a = 12.03$ Å, $b = 3.693$ Å, $c = 6.42$ Å, $\beta = 106.1°$ using the best matching inorganic crystal structure database (ICSD) card #199, as shown in Fig. 1(c).

The noticeable difference in the crystallographic phases in the monoclinic structure of the grown vanadium dioxide samples, could be ascribed to preferential crystallographic growth orientation, influenced by the specific processes of structure evolution during the crystallization; nucleation, island growth, coalescence of islands, formation of polycrystalline islands and channels, development of a continuous structure, and grains growth. The evolution of the structure in polycrystalline structure is a very complex phenomenon and exhibits different features at different stages during the grains growth.

A comprehensive description of the formation of these peculiar structural features is possible using the structure-forming phenomena mentioned above as a basis (nucleation, crystal growth, grain growth). These phenomena are composed of elementary atomic processes as reported by Ngom et al. [26], which can account for their global effects on the structure evolution. It is important to note that not only the temperature controls the atomic processes, but also the structural conditions characteristic of the actual growth stage.

To further confirm the phase of the as-prepared vanadium dioxide, the Raman spectra of the samples were obtained as shown in Fig. 1(d). For vanadium oxides, the Raman bands exist within the wavenumber range of ~100–400 cm^{-1}, ~400 - 800 cm^{-1} and 800 - 1100 cm^{-1} attributable to V–O–V bending modes, V–O–V stretching modes and V=O stretching modes respectively [27,28]. In addition, VO_2 monoclinic (VO_2 (M)) has prominent Raman band at approximately 145 cm^{-1} (V–O–V bending mode) [29,30]. As shown in Fig. 1(d), the Raman bands of as-prepared vanadium dioxide were mainly observed for V–O–V bending modes and V=O stretching mode suggesting that these modes are dominant in the prepared VO_2, and the prominent Raman band at ~145 cm^{-1} further suggests that the samples are predominantly VO_2(M) as expected. At low-frequency vibrations (wavenumber of ~100 cm^{-1}), the Raman bands typically originate from large-scale vibrations, such as the whole crystal lattice vibrating hence could be useful in distinguishing between amorphous and crystalline material or even between different crystalline forms (polymorphs). Of course, Raman scattering is sensitive to the degree of crystallinity in a sample [31]. Fig. 1(e) shows a comparison of the intensity of the prominent Raman band at ~145 cm^{-1} as a function of growth time. It can be seen that as growth time increases from 2 h 30 min to 6 h the Raman intensity increases significantly suggesting an enhancement in the crystallinity of the samples. The high-frequency Raman located ~1000 cm^{-1} is attributed to the terminal oxygen which results from an unshared oxygen. Prolonged growth time decreases the Raman intensity, as illustrated by the Raman spectrum of the sample prepared for 12 h. This could mean that the sample obtained for 4 h and 6 h growth times have a different crystallinity compared to others samples prepared for 2 h 30 min and 12 h. This observation confirms our XRD findings on the different VO_2 monoclinic phases for the prepared samples. So one could suggest that the changes on the Raman intensity from 2 h

30 min to 4 h and from 6 h to 12 h are due to the changes in the monoclinic phases from VO_2(A) to VO_2(B) and vice versa.

Fig. 2(a)–(d) show SEM micrographs (low and high magnifications) of the samples grown at 200 °C for 2 h 30 min, 4 h, 6 h and 12 h, respectively. It can be seen that all the samples are composed of microspheres (see the insert figures), but the sample grown for 4 h is showing nanoflakes-like structure on the surface of the microspheres as compared to closed distinct microsphere surface morphology for the 2 h 30 min grown sample which is composed of nanorods-like structure. In other words, for a growth time of 2 h 30 min the surfaces of the microspheres show relatively shorter nanorods which are flat and more compact on the surfaces of the microspheres, while, for a growth time of 4 h the surface of the microspheres shows nanoflakes which are relatively perpendicular to the surfaces. It is worth mentioning that at this growth time of 4 h the nanosheets-like structure starts developing and become noticeable at a longer growth time of 6 h which clearly shows nanosheets-like morphology on the surface of the microspheres. However, for a longer growth time of 12 h the material shows microspheres surface morphology similar to that of 2 h 30 min growth time but the nanorods are relatively perpendicular to the surface of the microspheres.

The morphology of the samples was further confirmed by TEM as shown in Fig. 2 (e) to 2 (h). TEM micrographs for a growth time of 2 h 30 min (Fig. 2(e)) and 4 h (Fig. 2(f)) clearly show the microspheres with distinct microsphere surface morphology. In this
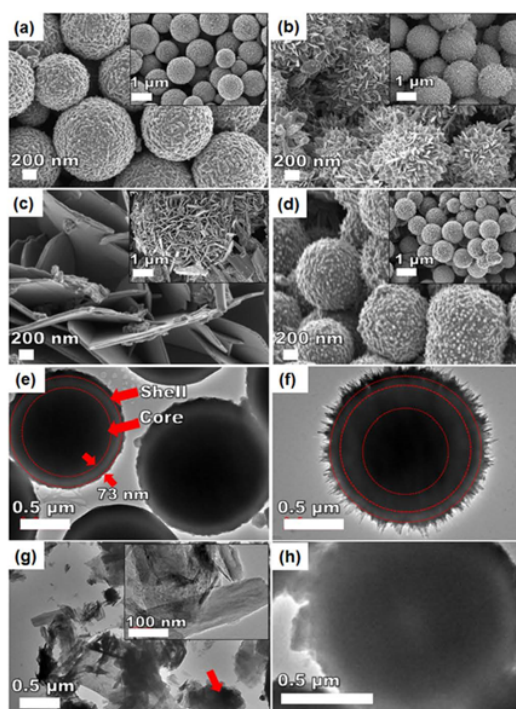

Fig. 2. The SEM images of the as-prepared vanadium dioxide samples grown at 200 °C for (a) 2 h 30 min, (b) 4 h, (c) 6 h and (d) 12 h. The insert figures show the corresponding low magnification micrographs. The corresponding TEM micrographs for growth time of (e) 2 h 30 min, (f) 4 h, (g) 6 h and (h) 12 h. The insert figure in (g) shows the high magnification micrograph.

regards the surface of the microsphere for 4 h growth time shows nanoflakes in accordance with SEM results.

In Fig. 2(e), the interior structure of the microspheres reveals the yolk-shelled sphere-like with a gap distance of approximately 73 nm between the core and the shell, and for 4 h the interior structure of the microsphere reveals the double-shelled microsphere. For further prolongation of the growth time, i.e. 6 h, the nanosheets evolved, as shown in Fig. 2(g) and the formation of these nanosheets could be viewed as a coalescence from the nanoflakes observed on the surface of the microsphere for 4 h growth time which confirms the time-dependence grown from 4 h to 6 h with a noticeable change of the interior of the microsphere with time. In fact, the growth of the outer part of the microsphere consumes the inner substances (the core). The red arrow in Fig. 2(g) shows the core which has been consumed in the transformation of the interior of the microsphere to nanosheets. Furthermore, based on the morphology and the XRD results analysis a correlation could be made between these two findings. The obtained morphology could be correlated to the observed different VO_2 monoclinic phases. The 2 h 30min and 12 h growth times corresponding to the VO_2 monoclinic phase A give the same morphology with almost no time dependence effect, while the 4 h and 6 h growth times corresponding to the VO_2 monoclinic B phase show different morphology but with a time-dependence resulting from the coalescence of the nanoflakes seen on the sample prepared for 4 h that gives the nanosheets seen on the sample grown for 6 h. The difference on the morphology for the two different phases could be explained as result of the influence of the crystal growth on the final grains growth. It is well known that, crystals growing from the nuclei are randomly oriented due to the random orientation of the nuclei themselves. The complete coalescence of the crystals touching each other constitutes grain coarsening, which also results in the development of discrete single crystals and is connected to some changes in the orientation controlled mainly by the minimization of the crystals interface energy. But, the observed morphology evolution of the as-prepared vanadium dioxide samples for 4 h and 6 h is well-thought-out to emerge from the inside-out Ostwald ripening process as depicted in Scheme 2. Firstly, vanadium dioxide nanoparticles are formed and aggregated to form solid (core) microsphere which undergoes the inside-out Ostwald-ripening process and transform to the yolk-shelled microsphere. Upon further prolongation of the growth time, the secondary Ostwald-ripening process takes place on the initial solid core, resulting in the formation of the double-shelled microsphere with nanoflakes on the surface. The nanoflakes on the microsphere surface evolved into nanosheets upon longer growth time by consuming the inner core through coalescence. In fact, under hydrothermal conditions, the particles on the outer surface grow relatively easy because the recrystallization preferentially occurs at the solid−liquid interface [32].

The vanadium oxidation state of the as-prepared vanadium dioxide was analysed by XPS, since the binding energy of the V $2p_{3/2}$ is dependent on the vanadium cationic oxidation state [33]. Fig. 3(c) shows the wide scan XPS spectrum of the as-received (i.e., without sputter cleaning) vanadium dioxide grown for 6 h. Similar to EDS, the wide scan XPS spectrum displays the main elements, V (23.48 at%) and O (49.51 at%) of the sample, and the observed C (27.01 at%) may be due to contamination from the precursor and/or the surface-adsorbed CO_2 and O_2. The core level spectrum of V 2p reveals the binding energy peaks at 524 eV and 516 eV which correspond to the V $2p_{1/2}$ and V $2p_{3/2}$ core levels, respectively, as shown in Fig. 3(d) [33]. The core level spectrum of V 2p suggests that the oxidation state of the as-prepared vanadium dioxide is predominantly V^{4+}.

The surface area and the pore size distribution of the as-
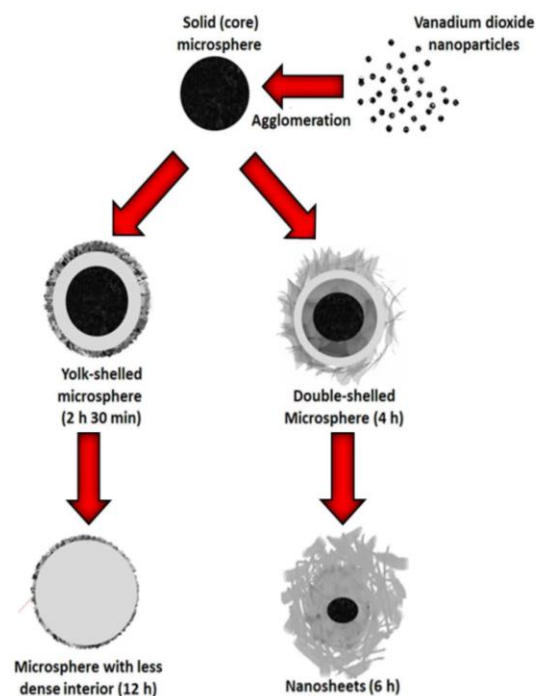
Scheme 2. Schematic illustration of the growth time-dependent morphological evolution of the as-prepared vanadium dioxide.

prepared vanadium dioxide were analysed by BET. Fig. 3(e) and (f) show the N_2 gas isotherms and pore size distribution obtained using Barrett-Joyner-Halenda (BJH) method, respectively for the as-prepared vanadium dioxide samples. The nitrogen adsorption-desorption isotherm of the vanadium dioxide shows a type III isotherm with H3 hysteresis, indicating a weak interaction between the N_2 adsorbent and the material and the hysteresis indicating non-rigid aggregates of plate-like particles or assemblages of slit-shaped pores. From Fig. 3(e) the specific surface area (SSA) was calculated as 16.0, 23.82, 34.14 and 25.12 $m^2 g^{-1}$ for vanadium dioxide samples grown for 2 h 30 min, 4, 6 and 12 h, respectively. Fig. 3(f) shows a concentration of pore volume ranging from ~5 to 20 nm, signifying that the pores which exist in these materials are predominantly meso-pores. Consequently, the BET results reveal that the sample grown for 6 h has larger SSA and high pore volume which would provide the probability of efficient transport of electrons and ions facilitating the electrolyte ion diffusion and deliver more electroactive sites for fast energy storage through redox reaction, contributing to higher electrochemical capacity.

5.2. Electrochemical performances of vanadium oxide

To evaluate the supercapacitive performance of the as-prepared vanadium dioxide samples we performed the cyclic voltammograms (CVs), galvanostatic charge-discharge (GCD) and electrochemical impedance spectroscopy (EIS) in a three-electrode half-cell configuration using 6 M KOH aqueous electrolyte. Fig. 4(a) shows the CV curves acquired at a scan rate of 50 mV s^{-1} within a potential range of 0.0−0.5 V for all electrode materials. These CV curves show a pair of redox peaks corresponding to the anodic peak at ~0.15 V and cathodic peak ~0.35 V, indicating the conventional behaviour of a battery-type electrode. The results suggest that the CV curves are mainly based on a redox mechanism of V^{4+} to V^{5+}
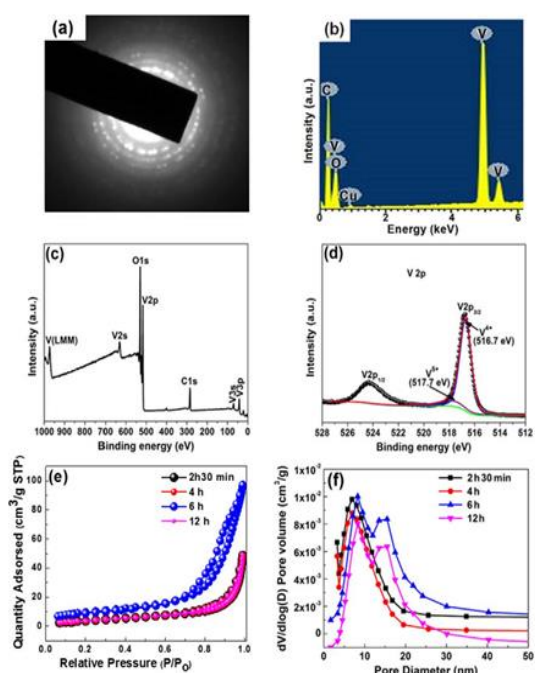
Fig. 3. (a) The selected area electron diffraction (SAED) pattern of the as-prepared vanadium dioxide sample grown at 200 °C for 6 h and (b) the EDS spectra of the vanadium dioxide grown at 200 °C for 6 h (c) The wide scan XPS spectrum of the as-received (i.e., without sputter cleaning) vanadium dioxide grown at 200 °C for 6 h, and (d) the corresponding core level spectrum of V 2p. (e) N_2 absorption/desorption isotherms; and (f) pore size distribution of vanadium dioxide samples grown at 200 °C for 2 h 30 min, 4, 6 and 12 h.
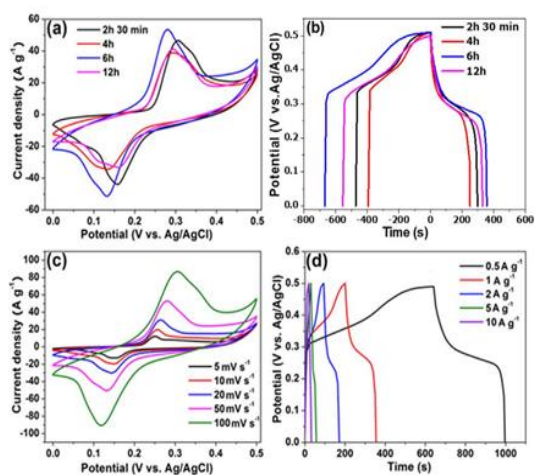

Fig. 4. The comparison of (a) The CV curves acquired at a scan rate of 50 mV s^{-1} within a potential range of 0.0–0.5 V, (b) the GCD curves for all vanadium dioxide samples grown at 200 °C at a current density of 0.5 Ag^{-1}, (c) CV curves versus scan rate and (d) GCD curves versus as function of current density respectively.

which takes place at the surface of the VO_2 material according to the following reaction [22].

$$VO_2 + OH^- \leftrightarrow VO_2(OH) + e^- \qquad (3)$$
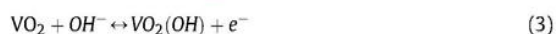
It can also be clearly seen that the electrode made of the sample grown for 6 h exhibits better current response as compared to the other electrode materials grown at different times. This could be related to the higher degree of crystallinity of this sample which could enhance its electrical conductivity, but also to its higher SSA providing more sites for the redox reaction to occur.

Fig. 4(b) shows the overlaid GCD curves acquired at a current density of 0.5 Ag^{-1} for all vanadium dioxide electrodes. Beside the typical non-linear charge-discharge curves observed for faradaic capacitors, the discharge time for the electrode material grown for 6 h is significantly longer than the other electrode materials, signifying better rate of discharge. This is in good agreement with the CV curves in Fig. 4(a) and could be related to the same reasons for the high current response of the CV. This electrode was further characterized to understand its electrochemical performance. In other words, detailed CV and GCD measurements of this electrode were carried out at scan rates ranging from 5 to 100 mV s^{-1} and current densities ranging from 0.5 to 10 Ag^{-1}, respectively. Fig. 4(c) shows the CV of this electrode at scan rate range of 5–100 mV s^{-1}.

It can be seen that the CV curves maintain a similar shape even at a high sweep rate, demonstrating the excellent reversible process and fast diffusion of electrolyte ions into the vanadium nanosheets. This also signifies that the kinetics of the interfacial faradic reactions and the rate of electronic transport are fast enough at these scan rates [34]. Fig. 4(d) shows the charge-discharge curves at different current densities in the potential window of 0.0–0.5 V for the electrode material grown for 6 h, which shows the same faradaic charge-discharge behaviour for different current densities. Typical reduction in discharge time with increasing current density is also observed, which is related to the limited access to the electrolyte ions to the surface of the electrode material at high current density.

Based on the CV and GCD curves, the specific capacitance, C_S (F g^{-1}) and the specific capacity q_s (mA h g^{-1}) were calculated using the following equation (4) for CV curves and (5) for CD curves, respectively [35,36]:

$$C_s = \frac{1}{mv\left(V_f - V_i\right)} \int_{V_i}^{V_f} I(V)dV \qquad (4)$$

$$q_s = \frac{It}{3.6.m} \qquad (5)$$

where V is the potential window, v is the scan rate (V s^{-1}), V_f and V_i are the integration potential limits of the CV curve, I is the discharge current (A), m is the active mass of the electrode material (g) and t is the discharge time (s).

The plot of the specific capacitance and specific capacity as a function of growth time is shown in Fig. 5(a), respectively, for all electrodes. Overall, the specific capacity increasing with increasing growth time from 2 h 30 min to 6 h, thereafter decrease with increase growth time (to 12 h) showing that 6 h growth time is optimum growth time. In other words, in both measurements, the electrode grown for 6 h exhibits higher specific capacitance and capacity values as compared to the other electrodes. A decrease in these values for the electrode grown for 12 h confirms that 6 h is indeed the optimum growth time. In brief, the sample grown for 6 h shows better capacitive performance, due to a more diffuse structure and large SSA of the nanosheets which can provide large electrochemical active sites and easy access for the electrolyte ions. However, for prolonged growth time (i.e., 12 h), the specific capacity and capacitance decrease because of the microsphere structure of the electrode which has reduced SSA limiting the OH$^-$
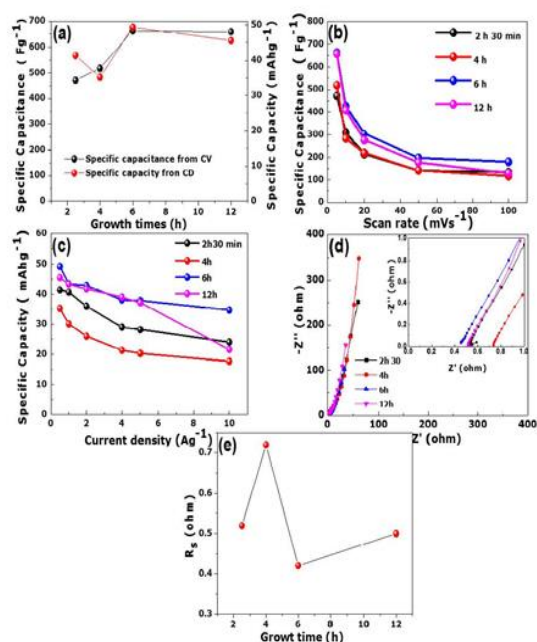
Fig. 5. (a) comparison of specific capacitance and specific capacity of vanadium dioxide at a scan rate of 5 mV s^{-1} and current density of 0.5 A/g, respectively (b) specific capacitance vs. scan rate, (c) specific capacity vs. current density, (d) EIS of vanadium dioxide samples grown at different times shown in the figure. The inset to (d) is the magnified plot showing the R_S values for different electrodes. (e) Equivalent series resistance (R_S) of vanadium dioxide samples grown at different times shown in the main figure.

ion diffusion into the electrode surface. In Fig. 5(b) and (c), the specific capacitance and capacity gradually decrease with increasing current density and scan rate, due to the decrease of effective interaction between the ions and the electrode at higher current density and sweep rate [37]. To further evaluate the conductivity of the electrode materials, the electrochemical impedance spectroscopic (EIS) measurement was carried out at an open potential and within a frequency range of 100 kHz - 10 mHz (Fig. 5(d)). At high frequency, the intercept with the Z′ represents the equivalent series resistance (R_S) attributed to the diffusion of ions to/from the interface between the electrode and electrolyte [38]. As shown in Fig. 5(d), the electrode material grown for 6 h exhibits the shorter diffusion length as well as smaller R_S value of 0.42 Ω (Fig. 5(e)) due to the easiness of the movement of ions and the charge transfer towards the electrode/electrolyte interface.

Table 1 presents a summary of the pore size distribution, specific capacitance, specific capacity and the solution resistance for the as-prepared vanadium dioxide electrode materials grown at 200 °C with different growth times. It can be seen in Table 1 that there is a clear correlation among different parameters such as SSA, micropore volume, R_s, C_s, and q_s that 6 h samples is always showing the best results. In other words this a clear evidence that the sample

grown for 6 h is the best performing samples which makes this growth time to be optimum for producing VO$_2$ electrode material with the excellent physical and electrochemical properties.

Furthermore, the cycling performance is an important factor in determining the supercapacitor electrodes for practical applications. To evaluate the cycle behaviour of the vanadium dioxide nanosheets structure (i.e. a sample grown for 6 h), the sample was subjected to 5000 cycles at current density of 10 A g^{-1}, as shown in Fig. 6(a). It can be seen that the sample shows good cycle stability with 99.4% coulombic efficiency up to 5000 charge-discharge cycles, signifying good electrochemical stability of the active material. Furthermore, an increase in the capacity retention with cycle number is also observed. This means that more accessible sites were made available during cycling without significant deterioration of the electrode material. Fig. 6(b) shows the Nyquist plots of the sample grown for 6 h, before and after the last cycle recorded in the frequency range of 100 kHz to10 mHz. Both plots show similar curves with similar R_S values of 0.42 and 0.45 Ω before and after cycling, respectively and much shorter diffusion length after cycling which the indication that the electrode has been somehow improved after cycling. To further asses the cycle of the electrode material, the CV curves at a scan rate of 50 mV s^{-1} were obtained before and after cycling, as shown in Fig. 6(c). A shift in the redox peak current is observed after stability. This is tentatively related to a variation of the pH of the electrolyte due to the consumption of the OH$^-$ or deposition of KOH during the stability test. This could decrease the pH of the solution, engendering the shift observed here [39]. This shift is followed by an increase in current response suggesting excellent cycling stability and highly reversible redox reaction of the vanadium dioxide, confirming results obtained in Fig. 6(a).

Our results were also compared with other vanadium dioxide electrode materials in Table 2. This work shows significant
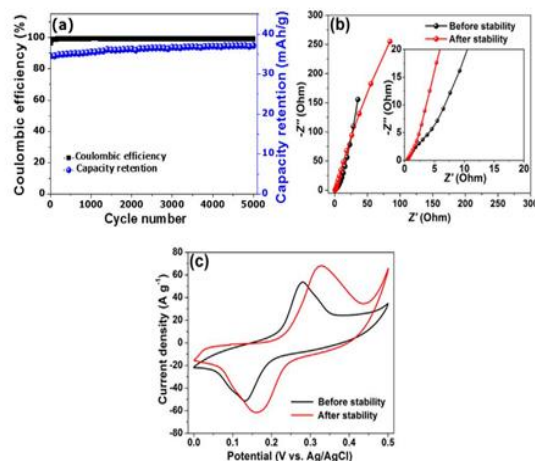
Fig. 6. (a) Coulombic efficiency as a function of cycle number at a current density of 10 A g^{-1}, (b) Nyquist plot before and after cycling and (c) cyclic voltammetry before and after cycling for vanadium dioxide sample grown at 200 °C for 6 h.

Table 1
A summary SSA, micropore volume, R_s, C_s and q_s for all electrode materials.

Growth time	SAA (m^2 g^{-1})	Micropore volume (cm^{3}g^{-1})	R_S (Ω)	C_S (Fg^{-1}) at 0.5 A g^{-1}	q_s (mAhg^{-1})
2 h 30 min	16.00	0.14	0.52	471.30	41.42
4 h	23.82	0.11	0.72	518.92	35.24
6 h	**34.14**	**0.19**	**0.42**	**663.22**	**49.28**
12 h	25.12	0.16	0.50	659.31	45.55

Table 2
A comparison of specific capacitance obtained in this work and other previously published reports.

Electrodes	Methods	Electrolytes	Specific capacitance (F g^{-1})	Capacitance retentions	References
RG (1.0)/VO$_2$	One-step simultaneous hydrothermal reduction	0.5 M K$_2$SO$_4$	225 @ 0.25 A g^{-1}	65% after 1000 cycles @ 5 A g^{-1}	[10]
VO$_2$	technology		136 @ 0.25 A g^{-1}	47% after 1000 cycles @ 5 A g^{-1}	
Gr/VO$_2$	One-step hydrothermal strategy	0.5 M K$_2$SO$_4$	426 @ 1 A g^{-1}	92% after 5000 cycles @ 10 A g^{-1}	[1]
VO$_2$ nanobelts			243 @ 1 A g^{-1}	59% after 5000 cycles @ 10 A g^{-1}	
VO$_2$ nanosheets	Hydrothermal	Gel electrolyte	405 @ 1 A g^{-1}	82% after 6000 cycles @ 10 A g^{-1}.	[18]
VO$_2$(B)/RG	One step hydrothermal	1 M Na$_2$SO$_4$	290.4 @ 0.2 A g^{-1}	82.3% after 1000 cycles @ 2 A g^{-1}	[19]
VO$_2$			–	37.9% after 1000 cycles @ 2 A g^{-1}	
VO$_2$/CMK-3	Solid-state reaction	1 M KNO$_3$	131 (current density not given)	–	[20]
VO$_2$(B)/WCNTs	Sol–gel method assisted with freeze-drying	1 M Na$_2$SO$_4$	250 @ 0.5 A g^{-1}	71% after 200 cycles @ 10 A g^{-1}	[14]
VOx @ carbon	One-step method using phenolic	1 M KNO$_3$	171 @ 100 mA g^{-1}	–	[21]
VOx			88 @ 100 mA g^{-1}		
VO$_2$-6 h nanosheets	Solvothermal	6 M KOH	663 @ 5 mV s^{-1}	99.4% after 5000 cycles @ 10 A g^{-1}	This work

improvement on the specific capacitance of vanadium dioxide electrode compared with the vanadium dioxide-based electrode materials listed in Table 2. However, it is worth mentioning that all the previous works were done in neutral electrolytes, which generally give a pseudocapacitor behaviour with extended voltage windows. In fact, different redox reactions may occur when changing from a neutral electrolyte to a more alkaline electrolyte which could narrow the voltage window. But the low ionic conductivity of these neutral electrolytes hampers the specific capacitance value, as shown in this table.

6. Conclusions

In this work, the time-dependent morphological evolution of the as-prepared monoclinic VO$_2$(M) through solvothermal method with growth time varied from 2 h 30 min to 12 h had been studied. In addition, the electrochemical performance of the as-prepared monoclinic VO$_2$ for supercapacitor applications was evaluated in a three-electrode cell configuration using 6 M KOH aqueous electrolyte. The VO$_2$ sample grown for 6 h displayed nanosheets-like morphology compared to other VO$_2$ samples grown for 2 h 30 min, 4 and 12 h which revealed microsphere-like morphology. Furthermore, the 6 h sample showed the best results for all measurements carried out. This sample showed best specific surface area and pore volume, enhanced electrochemical performance with highest specific discharge capacity of 49.28 mAh g^{-1} at current density of 0.5 A g^{-1} and the corresponding specific capacitance of 663 F g^{-1} at a scan rate of 5 mV s^{-1}. The samples also showed 99.4% coulombic efficiency up to 5000 charge-discharge cycles at current density of 10 A g^{-1}. Accordingly, the VO$_2$ nanosheets (6 h sample) show a considerable potential as an electrode material for supercapacitor applications.

Acknowledgements

References

[1] H. Wang, H. Yi, X. Chen, X. Wang, D.W. Liu, J. Liu, G.Z. Cao, P.M. Ajayan, F. Wei, J. Mater. Chem. A 2 (2014) 1165–1173.
[2] J.W. Lee, A.S. Hall, J.D. Kim, T.E. Mallouk, Chem. Mater. 24 (2012) 1158–1164.
[3] C. Liu, F. Li, L.-P. Ma, H.-M. Cheng, Adv. Mater. 22 (2010) E28–E62.
[4] S. Chu, A. Majumdar, Nature 488 (2012) 294–303.
[5] J. Yang, T. Lan, J. Liu, Y. Song, M. Wei, Electrochim. Acta 105 (2013) 489–495.
[6] P. Simon, Y. Gogotsi, Nat. Mater. 7 (2008) 845–854.
[7] J. Chmiola, C. Largeot, P.L. Taberna, P. Simon, Y. Gogotsi, Science (80) 328 (2010) 480–483.
[8] M.F.E.-K, R.B. Kaner, Nat. Commun. 4 (2013) 1475.
[9] J. Miller, P. Simon, Sci. Mag. 321 (2008) 651–652.
[10] L. Deng, G. Zhang, L. Kang, Z. Lei, C. Liu, Z.-H. Liu, Electrochim. Acta 112 (2013) 448–457.
[11] L.L. Zhang, X.S. Zhao, P.L. Taberna, P. Simon, D. Plee, M. Mastragostino, S. Passerini, D. Zhao, M. Yumura, S. Iijima, Chem. Soc. Rev. 38 (2009) 2520.
[12] E. Frackowiak, Phys. Chem. Chem. Phys. 9 (2007) 1774.
[13] H.-Y. Li, C. Wei, L. Wang, Q.-S. Zuo, X. Li, B. Xie, M. Wu, L.-H. Chen, B.-L. Su, J. Chen, C.G. Hu, Y.X. Tong, J. Zhou, Z.L. Wang, Z.L. Wang, Y.L. Chueh, Z.L. Wang, J. Zhou, J. Mater. Chem. A 3 (2015) 22892–22901.
[14] L. Liang, H. Liu, W. Yang, J. Alloys Compd. 559 (2013) 167–173.
[15] M. Sathiya, A.S. Prakash, K. Ramesha, J.M. Tarascon, A.K. Shukla, J. Am. Chem. Soc. 133 (2011) 16291–16299.
[16] L. Mai, F. Dong, X. Xu, Y. Luo, Q. An, Y. Zhao, J. Pan, J. Yang, Nano Lett. 13 (2013) 740–745.
[17] X. Xia, D. Chao, C.F. Ng, J. Lin, Z. Fan, H. Zhang, Z.X. Shen, H.J. Fan, Mater. Horiz. 2 (2015) 237–244.
[18] R.B. Rakhi, D.H. Nagaraju, P. Beaujuge, H.N. Alshareef, Electrochim. Acta 220 (2016) 601–608.
[19] X. Xiao, S. Li, H. Wei, D. Sun, Y. Wu, G. Jin, F. Wang, Y. Zou, J. Mater. Sci. Mater. Electron. 26 (2015) 4226–4233.
[20] L. Hu, L. Yu, C. Zhao, X. Long, W. Chen, J. Wuhan Univ. Technol. Sci. Ed. 25 (2010) 574–578.
[21] C. Zhao, J. Cao, Y. Yang, W. Chen, J. Li, J. Colloid Interface Sci. 427 (2014) 73–79.
[22] Y.-G. Wang, L. Cheng, Y.-Y. Xia, J. Power Sources 153 (2006) 191–196.
[23] D. Jiménez-Cordero, F. Heras, M.A. Gilarranz, E. Raymundo-Piñero, Carbon N. Y. 71 (2014) 127–138.
[24] H. Wu, X. Wang, L. Jiang, C. Wu, Q. Zhao, X. Liu, B. Hu, L. Yi, J. Power Sources 226 (2013) 202–209.
[25] Y. Zhang, C. Huang, C. Meng, T. Hu, Mater. Chem. Phys. 177 (2016) 543–553.
[26] B.D. Ngom, M. Chaker, A. Diallo, I.G. Madiba, S. Khamlich, N. Manyala, O. Nemraoui, R. Madjoe, A.C. Beye, M. Maaza, Acta Mater. 65 (2014) 32–41.
[27] F.D. Hardcastle, I.E. Wachs, Solid State Ionics 45 (1991) 201–213.
[28] S. Lee, I.N. Ivanov, J.K. Keum, H.N. Lee, Sci. Rep. 6 (2016) 19621.
[29] G.I. Petrov, V.V. Yakovlev, J. Squier, Appl. Phys. Lett. 81 (2002) 1023–1025.
[30] M. Pan, J. Liu, H. Zhong, S. Wang, Z.F. Li, X. Chen, W. Lu, J. Cryst. Growth 268 (2004) 178–183.
[31] L.S. Taylor, G. Zografi, Pharm. Res. 15 (1998) 755–761.
[32] T. Ye, Z. Dong, Y. Zhao, J. Yu, F. Wang, S. Guo, Y. Zou, CrystEngComm 13 (2011) 3842.
[33] M.J. Miller, J. Wang, J. Appl. Phys. 117 (2015).

[34] Y. Zhang, Y. Huang, Mater. Lett. 182 (2016) 285–288.
[35] B. Akinwolemiwa, C. Peng, G.Z. Chen, J. Electrochem. Soc. 162 (2015) A5054–A5059.
[36] A. Laheäär, P. Przygocki, Q. Abbas, F. Béguin, Electrochem. Commun. 60 (2015) 21–25.
[37] D. Jiang, Q. Xu, S. Meng, C. Xia, M. Chen, J. Alloy. Compd. 706 (2017) 41–47.
[38] T.M. Masikhwa, M.J. Madito, A. Bello, J.K. Dangbegnon, N. Manyala, J. Colloid Interface Sci. 488 (2017) 155–165.
[39] A.H. Shah, W. Zaid, A. Shah, U.A. Rana, H. Hussain, M.N. Ashiq, R. Qureshi, A. Badshah, M.A. Zia, H.-B. Kraatz, J. Electrochem. Soc. 162 (2014) H115–H123.

4.2.3 Conclusion Remarks

The time-dependent morphological evolution of the monoclinic $VO_2(M)$ through the solvothermal method with growth time varied from 2 h 30 min to 12 h has been studied. The VO_2 sample grown for 6 h displayed a nanosheets-like morphology compared to other VO_2 samples grown for 2 h 30 min, 4 and 12 h which revealed a microspheric morphology. Furthermore, the as-prepared 6 h sample showed the highest specific surface area with an associated pore volume and a remarkable electrochemical performance with a specific discharge capacity of 49.28 mA h g^{-1} at a current density of 0.5 A g^{-1}.

This electrode also displayed a 99.4% coulombic efficiency of up to 5000 charge-discharge cycles at a current density of 10 A g^{-1}. According to the results obtained, the electrochemical performance of the monoclinic VO_2 could be improved by varying the growth time via the solvothermal technique.

4.3 High-performance asymmetric supercapacitor based on vanadium dioxide and carbonized iron-polyaniline electrodes

4.3.1 Introduction

In the section 4.2, we synthesized the vanadium dioxide monoclinic (VO_2 (B)) through a solvothermal method at different growth time frames. In the three electrode configuration, the VO_2(B) material grown for 6 h displayed the highest electrochemical performance as compared to other growth times in 6 M KOH. To further investigate the electrochemical performance of this electrode material, an asymmetric supercapacitor was assembled in an attempt to further extend the device operating voltage to achieve a higher energy density.

The fabrication of a novel asymmetric supercapacitor based on the VO_2 (B) monoclinic material as a positive electrode and carbonized iron-polyaniline (C-FP) as a negative electrode was undertaken. The VO_2//C-FP asymmetric device was able to operate a voltage window of 1.6 V with high a specific energy and power densities of 30 W h kg^{-1} and 713 W kg^{-1} respectively at 1 A g^{-1}. In addition, the VO_2//C-FP exhibited an 89% energy efficiency after 10,000 galvanostatic charge-discharge cycles with a large improvement in device specific capacity and specific energy after an ageing test at a gravimetric current of 10 A g^{-1}.

4.3.2 Result and discussion

The detailed results of the asymmetric device assembled using VO_2(B) and C-FP electrodes is presented in the paper below:

High-performance asymmetric supercapacitor based on vanadium dioxide and carbonized iron-polyaniline electrodes

N. M. Ndiaye, M. J. Madito, B. D. Ngom, T. M. Masikhwa, A. A. Mirghni, and N. Manyala

ARTICLES YOU MAY BE INTERESTED IN

AVS Quantum Science
Co-published with AIP Publishing

Coming Soon!

High-performance asymmetric supercapacitor based on vanadium dioxide and carbonized iron-polyaniline electrodes

View Online   Export Citation   CrossMark

N. M. Ndiaye,[1] M. J. Madito,[1] B. D. Ngom,[2] T. M. Masikhwa,[1] A. A. Mirghni,[1] and N. Manyala[1,a] (iD)

AFFILIATIONS

[1] Department of Physics, Institute of Applied Materials, SARChI Chair in Carbon Technology and Materials, University of Pretoria, Pretoria 0028, South Africa

[2] Laboratoire de Photonique Quantique d'Energie et de Nano Fabrication, Groupe de Physique du Solide et Science des Matériaux, Département de Physique FST-UCAD BP 5005 Dakar-Fan, Dakar, Sénégal

[a] Corresponding author email: ncholu.manyala@up.ac.za, **Tel.:** + (27)12 420 3549 **Fax:** + (27)12 420 2516

ABSTRACT

Vanadium dioxide (VO_2) monoclinic nanosheets were synthesized by a solvothermal method and carbonized iron-polyaniline (C-FP) nanograins were prepared by pyrolysis of iron-polyaniline (PANI) mixture under nitrogen ambient. An asymmetric device (VO_2//C-FP) was evaluated with VO_2 and C-FP as positive and negative material electrodes in aqueous 6 M KOH electrolyte respectively. The asymmetric supercapacitor (VO_2//C-FP) exhibited a 47 mA h g^{-1} specific capacity and a specific energy of 30 W h kg^{-1} with an associated specific power of 713 W kg^{-1} at a gravimetric current of 1 A g^{-1} in a potential window of 1.6 V. It also displayed an 89% energy efficiency after 10000 galvanostatic charge-discharge cycles with a large improvement after ageing test at a gravimetric current of 10 A g^{-1}.

I. INTRODUCTION

Supercapacitors (SCs), also called electrochemical capacitors (ECs) have been on the forefront of research owing to their relatively high power density (15 kW kg^{-1}), low specific energy (<10 W h kg^{-1}) and a long lifetime.[1-6] To date, the scientific community is working towards increasing the specific energy of SCs by using ingenious device design.[7] SCs can be classified into three types of capacitors based on their charge storage mechanism: (i) The electrical double-layer capacitors (EDLCs), where charge build-up at the boundary between the electrode and the electrolyte is responsible for the energy storage and the common materials used are carbon-based materials.[2,8] (ii) The faradaic capacitor which as their names suggest, involve redox or faradaic reaction and is mainly displayed in transition metal oxides, metal hydroxides, metal sulfides and conducting polymers.[9-13] (iii) The hybrid capacitors which are the combination of both EDLC and faradaic materials. A subclass of hybrid capacitors is the asymmetric supercapacitor (ASC) which are composed of a positive and a negative electrodes with dissimilar charge storage mechanisms. Generally, the positive electrodes are

the faradaic materials[14-21] while the negative electrodes are mostly made of carbon-based materials.[22-26] The Hybrid capacitors have been proposed and considered as a promising solution to improve the low specific capacitance from carbon-based materials and the low conductivity and poor cycle stability of the transition metal oxides/hydroxides.[27]

Carbon-based materials such as activated carbon,[28] carbon nanotube[29] and graphene[30] have been demonstrated to be a good electrode materials in supercapacitor due to their excellent conductivity combined with their good stability.[31]

The transition metal oxide used as supercapacitor electrode materials exhibit a high specific capacity as compared to carbon-based materials owing to its multiple oxidations states.

Amongst the low-cost metal oxides, vanadium oxides (e.g. VO_2, V_2O_5, V_2O_3, and V_4O_7) have received recent attention[32-40] which is linked to their abundant sources, and ability to exist in variable oxidation states.[41]

Vanadium dioxide (VO_2) has an exciting phase with a rich polymorphic stable and metastable forms included VO_2 (A), VO_2 (M), VO_2 (R), VO_2 (B), VO_2 (T) and VO_2 (bcc).[42,43] VO_2 (A),

138

VO_2 (M) and VO_2 (B) are the most attractive due to their tuneable and the relatively easy synthesis process.[42,44] The VO_2 materials change from monoclinic (at a temperature about 68°C) to tetragonal structure reversibly (at a temperatures higher than the 68 °C) and can undergo semiconductor-to-metal transition.[45–50] VO_2 (B) electrodes with a metastable monoclinic structure is a potential electrode material in supercapacitor.[51]

As compared to vanadium pentoxide (V_2O_5), there are few report on vanadium dioxide for asymmetric supercapacitor. For instance, Wang et al. synthesized a graphene/VO_2 composite material for a positive and a negative electrodes. They assembled a symmetric supercapacitor (graphene/VO_2//graphene/VO_2) using 0.5 M Na_2SO_4 as an aqueous electrolyte. The graphene/VO_2//graphene/VO_2 symmetric device showed a specific energy of 21.3 W h kg^{-1} at 1 A g^{-1}. The graphene/VO_2 composite showed a cycling stability with 92% after 5000th cycles at 10 A g^{-1}.[52] Similarly Ma et al.[48] prepared a vanadium dioxide electrode using for a symmetric supercapacitor in 1 M Na_2SO_4. The VO_2//VO_2 symmetric device exhibited a specific energy of 21.3 W h kg^{-1} corresponding to a specific power of 207.2 W kg^{-1} at a gravimetric current of 0.25 A g^{-1}. They reported a cycling efficiency of 78.7% after 5.000 cycles at a specific current of 0.5 A g^{-1}.[48]

In our previous study, we synthesized the vanadium dioxide monoclinic (VO_2 (B)) through a solvothermal method. In a three electrode configuration the VO_2 (B) displayed a specific capacity of 49.28 mAh g^{-1} at current density of 0.5 A g^{-1} in aqueous electrolyte (6 M KOH).[53]

The present work reports the fabrication of a novel asymmetric supercapacitor (ASC) based on VO_2 (B) monoclinic as a positive electrode and carbonized iron-polyaniline (C-FP) as a negative electrode. The VO_2//C-FP ASC tested in aqueous electrolyte (6 M KOH) was able to reach a potential window of 1.6 V. The asymmetric device exhibited a specific energy and power of 30 W h kg^{-1} and 713 W kg^{-1} respectively at 1 A g^{-1}. In addition, the ASC showed an 89% energy efficiency after 10000 galvanostatic charge-discharge cycles with a large improvement after ageing test at a gravimetric current of 10 A g^{-1}.

II. EXPERIMENTAL

A. Chemicals

Vanadium (V) oxide (V_2O_5, purity ≥98%), oxalic acid dehydrate ($C_2H_2O_4\cdot2H_2O$ purity 99%), iron (III) nitrate (Fe(NO_3)$_3\cdot9H_2O$ purity 99-100%), ammonium peroxydisulfate ((NH_4)$_2S_2O_8$) purity 98%), aniline hydrochloride ($C_6H_5NH_2\cdot$HCl purity ≥99%) and propan-2-ol ($CH_3CHOHCH_3$ purity 99.5%) were purchased from Sigma-Aldrich. Potassium hydroxide (KOH) and ethanol (C_2H_6O purity 99%) were purchased from Merck (South Africa). Polycrystalline nickel foam (thickness of 1.6 mm) was obtained from Alantum (Munich, Germany).

B. Synthesis technique

1. Preparation of vanadium dioxide (VO₂)

The synthesis of the VO_2 material was carried out using solvothermal method. Initially, 1.2 g of V_2O_5 powder and 2.49 g of $H_2C_2O_4\cdot2H_2O$ was added to 40 mL of deionized water and stirred for 3 h, thereafter, a 6 mL of the homogeneous solution

was added to 60 mL of isopropanol under continuous stirring for 20 min.

The solution was transferred into a Teflon-lined stainless steel autoclave and kept at 200 °C for 6 h. The recovered powder was washed several times with deionized water followed by ethanol and dried at 60 °C in an electric oven.[53]

2. Synthesis of polyaniline (PANI)

0.2 M aniline hydrochloride ($C_6H_5NH_2\cdot$HCl) (2.59 g dissolved in 50 mL deionized water) was added to 0.25 M ammonium peroxydisulfate ((NH_4)$_2S_2O_8$) (5.71 g in 50 mL deionized water) and mixed overnight.

3. Preparation of carbonized iron-PANI (C-FP)

Briefly, 0.2 g of Fe(NO_3)$_3\cdot9H_2O$ and 0.0125 g of PANI were dissolved in 50 ml of ethanol and sonicated in the ultra-sonication bath.

After ethanol was almost completely evaporated, the mixture was coated on a nickel (Ni) foam acting as a current collector and pyrolyzed for 2 h under the N_2 atmosphere at 850 °C. The full detailed description of the C-FP can be found in our previous paper.[54]

C. Structural characterization

The structural properties of the samples were analysed by X-ray diffraction (XRD) powder using an XPERT-PRO diffractometer (PANalytical BV, The Netherlands) with theta/2theta configuration. The morphology of the materials synthesized was characterized by a high-resolution Zeiss Ultra plus 55 field emission scanning electron microscope (FE-SEM), operated at a voltage of 2.0 kV and a JEOL JEM-2100F transmission electron microscope (TEM). The selected area electron diffraction (SAED) pattern were taken with a JEOL JEM-2100F transmission electron microscope (TEM) and were used to evaluate the elemental composition of the produced materials. The X-ray photoelectron spectroscopy (XPS, K-alpha, Thermo Fisher) was used to analyse the elemental composition of the materials with a monochromatic Al-Kα radiation.

D. Electrodes preparation and characterization of supercapacitors

Three - and two electrode configurations were adopted to study the electrochemical properties of the VO_2 and C-FP electrodes.

The electrochemical characterizations were carried out using a Bio-Logic VMP-300 (Knoxville TN 37,930, USA) potentiostat monitored by the EC-Lab® V10.37 software. In the three-electrode configuration, Ag/AgCl (KCl saturated) served as the reference electrode, a glassy carbon plate as the counter electrode and 6 M KOH as the electrolyte. The VO_2 electrode was prepared as follows: 85 wt% of the active material was added to 10 wt% of carbon black as conducting additive and 5 wt% of polyvinylidene difluoride (PVDF) binder in an agate mortar. Few drops of 1-methyl-2-pyrrolidinone (NMP) were added to the mixture to form a slurry, which was pasted on nickel foam (NiF) acting as a current collector and dried at 60 °C in the electric oven for overnight.

Thereafter, the asymmetric supercapacitor consisting of VO_2 positive electrode and C-FP negative electrode was coupled in a coin cell with glass micro-fiber filter paper was used as a separator.

139

III. RESULTS AND DISCUSSION

A. Structural characterizations

Figure 1 display the X-ray diffraction patterns of VO₂ and C-FP materials. The diffraction peaks of the VO₂ materials are indexed as VO₂(B) monoclinic structure as shown in Fig. 1(a). It also shows that vanadium dioxide synthesized at 200 °C has a space group of *C 1 2/m 1*.[53] XRD pattern of C-FP powder material without pasting on the substrate (Ni foam) is shown in Fig. 1(b). The diffraction peaks of C-FP material are indexed to orthorhombic structures of Fe₃C and FeS with a space group of *P nma*.[54,55]

Figure 2 present the SEM micrographs of the as-prepared VO₂ and C-FP materials at low and high magnifications.

Figure 2(a) shows the SEM micrographs of the VO₂ which reveals the nanosheets-like structure on the microspheres surface. In Fig. (2b), the micrographs of VO₂ exhibits a vertically grown sheet-like structure. Figure 2(c–d) shows SEM micrographs of the C-FP which unveiled agglomerated nanograin morphology. The micrographs of the C-FP materials were showed lattice fringes attributed to the Fe cations on PANI and have been discussed in References 51 and 54.

The morphologies and the elemental composition of VO₂ materials were further studied with transmission electron microscope (TEM) and the selected area electron diffraction (SAED) analysis.

Figure 3(a) displays the TEM micrograph of VO₂ at high magnification which reveals clearly the nanosheets structure as shown in Fig. 2(b). The SAED pattern of the VO₂(B) nanosheets in Fig. 3(b) exhibits the presence of well-defined rings, indicates the poly-crystallinity of the VO₂ monoclinic.

To further evaluate the surface characterization of VO₂ material, the X-ray photoelectron spectroscopy (XPS) was used to determine the chemistry of the material. The core level spectrum of V2p reveals two chemical states of vanadium which are related to excitations of electrons from the V2p₃/₂ and V2p₁/₂ core levels, respectively, as shown in Fig. 4(a).

The predominant peak located at 516.5 eV in the V2p₃/₂ binding energy suggests a vanadium oxidation state of 4⁺ which confirms the formation of VO₂.[56] Futhermore, as presented in Fig. 4(b), the core level spectrum of O1s displayed the main peak located at 529.7 eV which is ascribed to the component associated to oxygen in VO₂.[57]
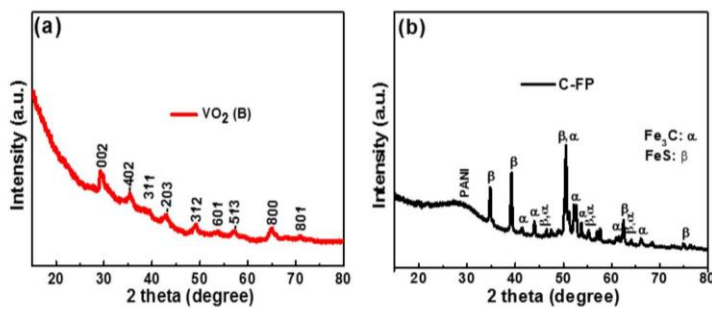

FIG. 1. The XRD patterns of (a) vanadium dioxide (VO₂) and (b) carbonized iron-polyaniline (C-FP).
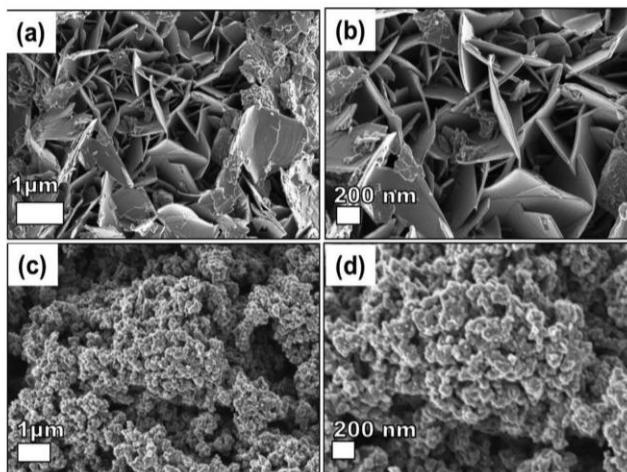

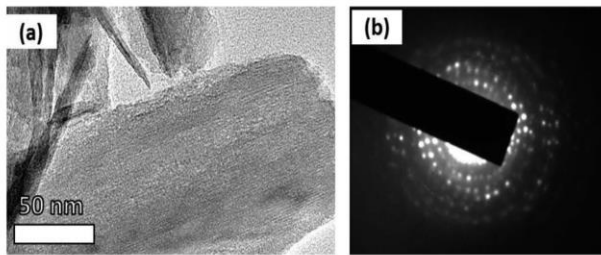**FIG. 2**. The SEM images of the as-prepared (a-b) VO₂ and (c-d) C-FP at low and high magnifications.

140

FIG. 3. (a) TEM at high magnification micrograph and (b) selected area electron diffraction (SAED) pattern of the VO$_2$ nanosheets.

B. Electrochemical performances of VO$_2$//C-FP

To construct the asymmetric hybrid supercapacitor of VO$_2$//C-FP, we, firstly, evaluated the electrochemical performance of the positive VO$_2$ and negative C-FP electrodes in a three-electrode system using 6 M KOH electrolyte with Ni foam and Ag/AgCl (KCl saturated) as a current collector and reference electrode, respectively.

Figure 5(a) shows the cyclic voltammogram (CV) profile of the VO$_2$ electrode at different sweep rates (from 5 to 100 mV s^{-1}) within a potential window range of 0.0 - 0.5 V. The appearance of a pair of redox peaks associated with an anodic peak at ~0.13 V and cathodic peak ~0.23 V at 5mV s^{-1} reveal a faradaic material. As observed in Fig. 5(a), these peaks are broader compared to those exhibited by battery-like material which is typically narrower and indicative of the occurrence of a redox reaction at a constant potential.[58]

The broadness of the peak in faradaic materials is expected as a result of the presence of non-standard sites and defects in the polycrystalline structure. This agrees with the low crystallinity of the VO$_2$ as recorded from XRD diffraction pattern.[58]

Figure 5(b) shows the charge-discharge (CD) of the vanadium dioxide curve at different specific currents. Each discharge curve displays a non-linear curve confirming the faradaic behavior of this electrode material.

Moreover, even at a low specific current of 1 A g^{-1}, the discharge profile does not show an extended plateau as is the case for batteries.[59] Figure 5(c) shows the CV curve of the C-FP electrode at different sweep rates from 5 to 100 mV s^{-1} in a negative potential window range of -1.2 - 0.0 V.

These CV curves show non-rectangular shapes with no apparent redox peaks. However, Fig. 5(d) which shows the charge-discharge curves at different specific currents in the voltage window of -1.2 to 0.0 V of the C-FP electrode, depicting a non-linear charge-discharge, suggesting a pseudocapacitive activity in this electrode material.

From the chronopotentiometry profile of the VO$_2$ and C-FP electrodes, the specific capacity, Q (measured in mA h g^{-1}) of the VO$_2$ and C-FP electrodes was determined using:

$$Q = \frac{I_d \times t_D}{3.6} \quad (1)$$

where I_d is defined as the specific current measured in A g^{-1} and t_D is the time in second (s) for a complete discharge cycle.

Figure 5(e) depicts the values of the specific capacity for the VO$_2$ and C-FP electrodes as a function of increasing specific current. The specific capacity values of 49.3 and 107 mA h g^{-1} were recorded for the VO$_2$ and C-FP material electrodes respectively, at a gravimetric current of 0.5 A g^{-1}. This can be related to the thin nanosheets structure of VO$_2$, which will ensure faster ion and electron transport. Also, the high capacitive characteristic observed in the C-FP can be attributed to the conductive framework, which allows an excellent electric contact and consequently enhances the capacitance performance. Additionally, it can be observed that these two materials (VO$_2$ and C-FP) are stable in each of its potential windows.

With the aim of optimizing the performance of ASC, the device was assembled using VO$_2$ as positive and C-FP as negative electrodes, respectively, in 6 M KOH.

The charge equilibrium ($Q_{VO_2(B)} = Q_{c-FP}$) was used to balance the masses of both electrodes in the asymmetric cell. This generates equation 2 and 3 which were used to balance the masses:

$$Q_{VO_2(B)} = Q_{c-FP} \quad (2)$$
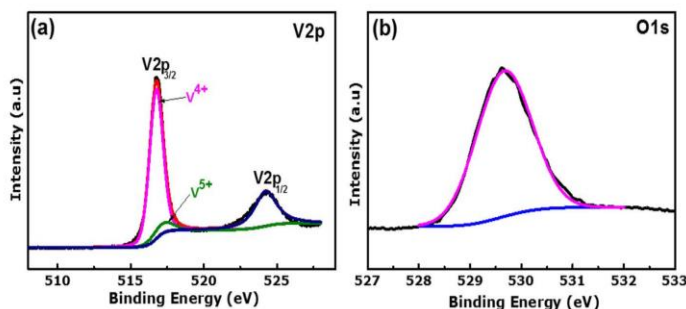
FIG. 4. (a) V2p binding energy region and (b) O1s binding energy regions of the VO$_2$ nanosheets.

141
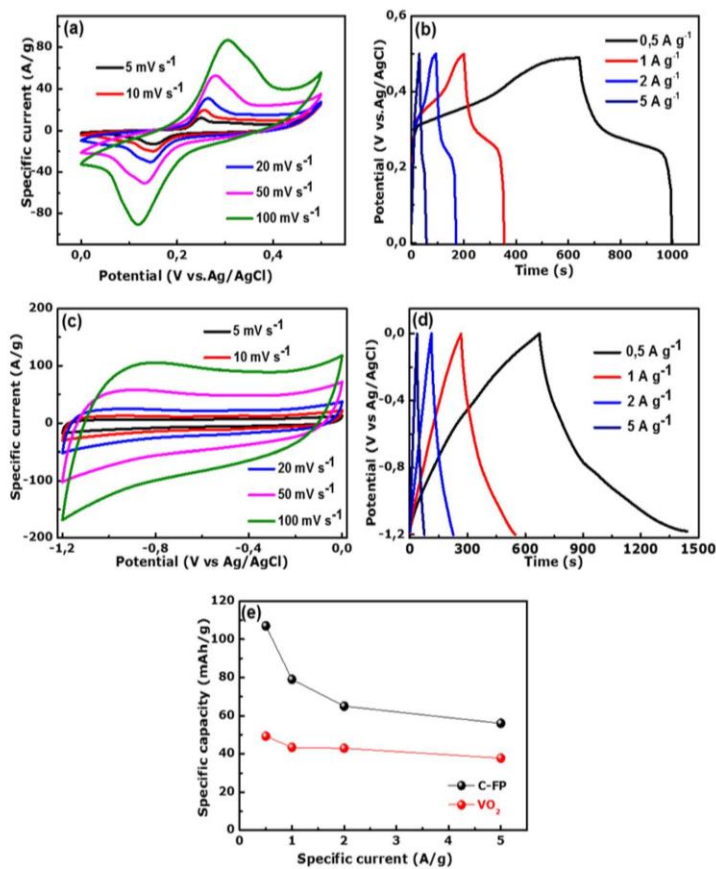
FIG. 5. (a) cyclic voltammogram (CV) curves at different sweep rates, (b) charge and discharge (CD) curves of the VO_2 at different specific current, (c) CV curves at different scan rates, (d) CD curves of the C-FP at different specific current and (e) specific capacities for the VO_2 and C-FP at different specific current.

$$\frac{m_{VO_2(B)}}{m_{c-FP}} = \frac{(I \cdot t_D)_{C-FP}}{(I \cdot t_D)_{VO_2(B)}} \qquad (3)$$

where $m_{VO_2(B)}, m_{c-FP}, Q_{VO_2(B)}, Q_{c-FP}$ describes the mass loading and total charge of the VO_2 and C-FP electrodes, I is given as the applied current and t_D is the time of discharge to 0 V. The mass ratio of the VO_2 to C-FP was adopted as 2:1 and the mass loading per unit area of the VO_2 and C-FP electrodes was recorded as 2.24 and 1.12 mg cm^{-2}, respectively) According to the charge balance, the mass loading of active VO_2 and C-FP on the current collector were measured as 4 and 2 mg, respectively in line with equation 3 above.

Figure 6(a) shows the CV curves of VO_2 and C-FP measured in the stable working potential window at a sweep rate of 50 mV s^{-1}, a working potential window of 1.7 V could be predicted for the asymmetric device.

Figure 6(b) shows the CV graphs of the VO_2//C-FP asymmetric device at different sweep rates (5 to 200 mV s^{-1}). However, the maximum working potential limit of the VO_2//C-FP device was recorded to be 1.6 V.

There is no apparent current leap within the operating cell potential window of 1.6 V, suggesting the stability of the device within this potential window. The CD curves of VO_2//C-F at different specific currents (1 to 10 Ag^{-1}) are shown in Fig. 6(c). The CD curves exhibit faradaic behavior owing to the high redox activity observed from the CV curves of the asymmetric device. The specific capacity of the VO_2//C-FP device was calculated using equation (1) and is shown in Fig. 6(d) as a function of specific current.

The specific capacity of the VO_2//C-FP device reaches a value of 47 mA h g^{-1} at a gravimetric current of 1 A g^{-1}. This value is well positioned between those obtained for VO_2 and C-FP electrodes from the three electrode measurements, at the same specific current. In other words, the specific capacity value of the hybrid device is much higher than that of VO_2 (43.4 mA h g^{-1}) and lower than that of C-FP (79 mA h g^{-1}) calculated in the three-electrode configuration at a gravimetric current of 1 A g^{-1}. This shows a good synergistic improvement by combining these two materials to form a hybrid device.
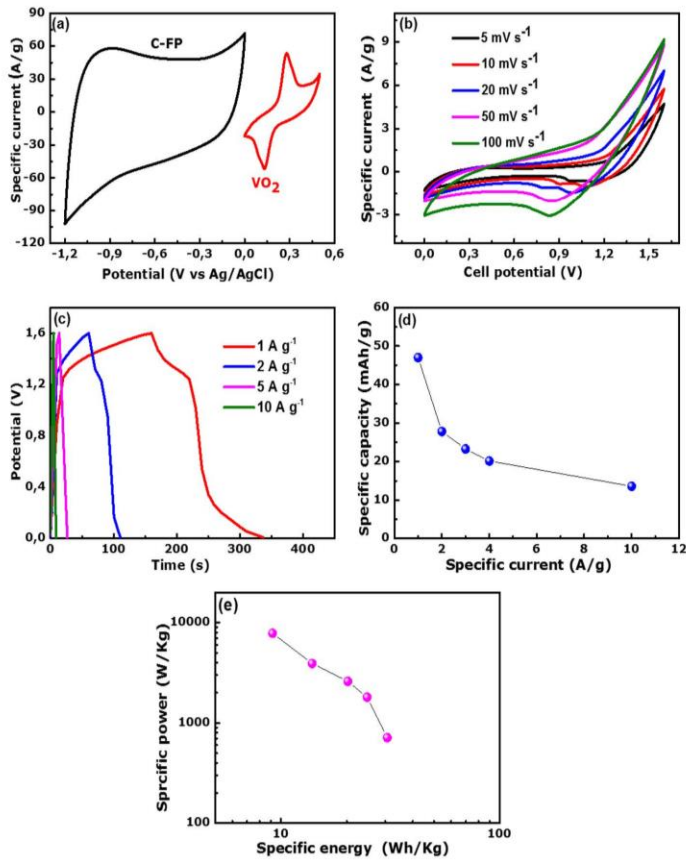
FIG. 6. (a) cyclic voltammograms (CVs) of VO_2 and C-FP electrodes at 50 mV s^{-1} for three-electrode setup, for the asymmetric device of the VO_2//C-FP (b) CV, (c) CD and (d) specific capacity at different specific current and (e) Ragone plot.

Figure 6(e) displays the Ragone plot presenting the specific power versus the specific energy of the asymmetric device obtained at different specific currents. The specific energy and the specific power of the device were obtained using equations (4) and (5) respectively.[60]

$$E_d(\text{W h kg}^{-1}) = \frac{I_d}{3.6} \int V(t)dt \qquad (4)$$

$$P_d(\text{W kg}^{-1}) = 3600\frac{E_D}{t} \qquad (5)$$

where E_d (W h kg^{-1}) and P_d (W kg^{-1}) are the total specific energy and specific power respectively. I_d is the specific current in A g^{-1}, t is the discharge time (s) and V is the working potential window (V) of the VO_2//C-FP device.

The maximum specific energy value of 30 Wh kg^{-1} was recorded for the VO_2//C-FP device with an associated specific power value of 713 W kg^{-1} at a 1 A g^{-1} specific current. This is maintained at 9.1 W h kg^{-1} for a specific power of 7.9 kW kg^{-1} at 10 A g^{-1}. The

high specific energy and specific power of the ASC are attributed to a high specific capacity and device wide operating voltage. This is also related to the good stability, fast kinetics of charge/discharge process[61] and the high ionic conductivity of the electrolyte ions, i.e., 73.5 and 198 Scm^2 mol^{-1} for K$^+$ and OH$^-$, respectively.[26]

In order to study the stability of the device, it was subjected to 10 000 cycles at the high gravimetric current of 10 A g^{-1} and the results are shown in Fig. 7(a).

An energy efficiency of the device was calculated using equation (6)

$$\eta_E = \frac{E_d}{E_c} \times 100 \qquad (6)$$

where η_E, E_d and E_c are energy efficiency, discharge energy and charge energy from the charge-discharge curve of the VO_2//C-FP device respectively.

The energy efficiency of 89% is obtained with good capacity retention of 78.5% at the 10 000th constant charge-discharge cycle, signifying good electrochemical stability of the device. The further

143
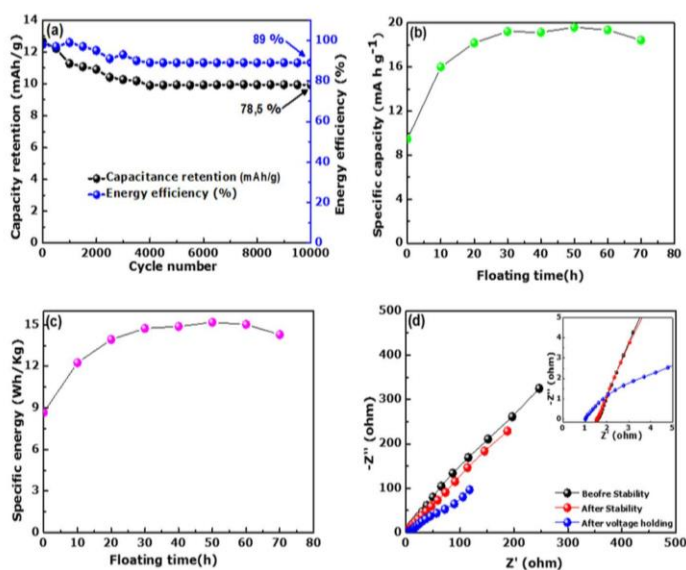
FIG. 7. (a) Stability test showing energy efficiency and capacity retention for up to 10000th cycles at a constant gravimetric current of 10 A g^{-1}, (b) specific capacity as function of floating time at 10 A g^{-1}, (c) specific energy as function of holding time at 10 A g^{-1}, (d) EIS before and after 10000th cycles and 70h voltage holding of the VO$_2$//C-FP asymmetric cell.

additional stability test was performed after cycling measurement on the cell using the voltage holding test (also called floating test).[62] It has the ability to determine a direct insight into the possible effect and degradation phenomena which might occur during the electrochemical process.[63] The voltage holding test was designed to analyse the device specific capacity at each 10 h period of the potential holding step for up to 70 h. This is following by three GCD to exhibit any change in the cell device with floating over a time of 70 h. The specific capacity as a function of floating time is presented in Fig. 7(b) for 70 h at 10 A g^{-1}.

It exhibits an increase in the specific capacity value for up to 30 h period of voltage holding time before becoming constant. The increase in the specific capacity could be linked to the evolution of accessible redox sites during the ageing experiment.

This improvement is even more striking when the specific energy was calculated after each voltage holding as shown in Fig. 7(c). Within the first 10 h of voltage holding, the specific energy increases by 32% to finally stabilize after 30 h of floating test, at 15 W h kg^{-1}, corresponding to an impressive increase of 65% from the original 9.1 W h kg^{-1} at 10 A g^{-1}. It shows that the cell voltage (1.6 V) is stable using 6 M KOH. As compared to other hybrid devices our group has reported this increase is better than that of Co$_3$(PO$_4$)$_2$·4H$_2$O/GF//C-FP (2.2% from the original value of 9.1 W h Kg^{-1})[64] as earlier reported for hybrid asymmetric capacitors. Thus, the floating test should be considered as a viable option for optimizing the properties of this cell.

The electrochemical impedance spectroscopic (EIS) measurement of the device was performed in an open voltage from 0.01 Hz to 100 kHz frequencies. The Nyquist plot of the asymmetric device (VO$_2$//C-FP), before stability, after the 10.000 constant galvanostatic cycles and after voltage holding are shown in Fig. 7(d). The equivalent series resistance (ESR) value of the asymmetric device

(VO$_2$//C-FP) was 1.55 Ω before and after 10000th cycles. However, after voltage holding, the ESR decreased to 1 Ω followed by a shorter diffusion length of the electrolyte ions. This low value of ESR confirm the good contact between the electrolyte and the surface of the electrode materials. Thus, any degradation of the cell has been not observed after the voltage holding. More explicitly, no change in the equivalent series resistance was noticed after stability. Two main changes in the impedance could explain the electrochemical improvement of the cell after voltage holding. However, the diffusion was reduced after the stability test. Upon voltage holding, the diffusion length is markedly reduced followed by reduction of the solution resistance. These reductions can significantly enhance the performance of the cell by a fast collection of charges.

Table I compares the asymmetric VO$_2$//C-FP device with some others devices reported in the literature. The cell shows higher

TABLE I. Comparison of electrochemical properties of VO$_2$//C-FP with previous supercapacitors comprised of VO$_2$.

Materials	Specific current (A/g)	Specific energy (Wh/Kg)	Specific power (W/Kg)	References
GF(0.1)/VO$_2$//GF	0.25	22.8	425	4
VO$_2$//VO$_2$	0.25	21.3	207.2	48
Graphene/VO$_2$//graphene/VO$_2$	1	21.3	-	52
GF+VO$_2$//HMB	2	14.5	720	65
VO$_2$//C-FP	1	30	713	This work
	2	25	1806	

144

values when compared with other devices.[4,48,52,65] This demonstrates the excellent choice of tandem materials for this asymmetric device.

IV. CONCLUSIONS

We have successfully synthesized $VO_2(B)$ nanosheets by a solvothermal method and C-FP material by pyrolysis of an iron-PANI mixture under nitrogen atmosphere. An ASC cell was fabricated from VO_2 adopted as positive and C-FP as the negative electrodes operated with an aqueous 6 M KOH electrolyte. The asymmetrical device exhibited a specific capacity of 47 mA h g^{-1} with a high specific energy of 30 W h kg^{-1} and the corresponding specific power of 713 W kg^{-1} at 1 A g^{-1} with 1.6 cell potential. These values are far better as compared to those studies previously published for related devices as indicated in Table I above. The excellent stability performance of the VO_2//C-FP device was demonstrated up to 10000 cycles at a specific current of 10 A g^{-1}. In addition, the voltage holding data obtained after testing for a period of 70 h shows a significant improvement in device specific capacity and energy after a period of 10 h at 10 A g^{-1}. This result confirms that the performance of the VO_2//C-FP device increase after the voltage holding test. This asymmetric supercapacitor from VO_2/C-FP exhibits impressive electrochemical performance and hence making the device excellent for energy storage applications.

ACKNOWLEDGMENTS

REFERENCES

[1] W. Y. Tsai, P. C. Gao, B. Daffos, P. L. Taberna, C. R. Perez, Y. Gogotsi, F. Favier, and P. Simon, Electrochemistry Communications 34, 109 (2013).

[2] H. Li, B. Wang, X. He, J. Xiao, H. Zhang, Q. Liu, J. Liu, J. Wang, L. Liu, and P. Wang, J. Mater. Chem. A 3, 9754 (2015).

[3] P. Simon and Y. Gogotsi, Nat. Mater. 7, 845 (2008).

[4] L. Deng, G. Zhang, L. Kang, Z. Lei, C. Liu, and Z.-H. H. Liu, Electrochimica Acta 112, 448 (2013).

[5] P. S. J. R. Miller, J. Miller, P. Simon, and P. S. J. R. Miller, Science 321, 651 (2008).

[6] B. E. Conway, Kluwer Academic 10, 221 (1999).

[7] Z. Yu, L. Tetard, L. Zhai, and J. Thomas, Energy Environ. Sci. 8, 702 (2015).

[8] P. Simon, Y. Gogotsi, and B. Dunn, Science 343, 1210 (2014).

[9] B. E. Conway, Journal of the Electrochemical Society 138, 1539 (1991).

[10] J. T. Mefford, W. G. Hardin, S. Dai, K. P. Johnston, and K. J. Stevenson, Nature Materials 13, 726 (2014).

[11] Y. Xiao, W.-Y. Wang, S.-W. Chou, T.-W. Lin, and J.-Y. Lin, Journal of Power Sources 266, 448 (2014).

[12] M.-N. Lu, C.-S. Dai, S.-Y. Tai, T.-W. Lin, and J.-Y. Lin, Journal of Power Sources 270, 499 (2014).

[13] T.-W. Lin, M.-C. Hsiao, S.-W. Chou, H.-H. Shen, and J.-Y. Lin, Journal of the Electrochemical Society 162, A1493 (2015).

[14] B. Rong-Rong, W. Xing-Long, C. Fei-Fei, J. Ling-Yan, G. Yu-Guo, and W. Li-Jun, The Journal of Physical Chemistry C 114, 2448 (2010).

[15] H. Jiang, C. Li, T. Sun, and J. Ma, Nanoscale 4, 807 (2012).

[16] J. Zhu, L. Huang, Y. Xiao, L. Shen, Q. Chen, and W. Shi, Nanoscale 6, 6772 (2014).

[17] J.-W. Lang, L.-B. Kong, W.-J. Wu, Y.-C. Luo, and L. Kang, Chemical Communications 104, 4213 (2008).

[18] L.-M. M. Chen, Q.-Y. Y. Lai, Y.-J. J. Hao, Y. Zhao, X.-Y. Y. Ji, Y. Z. Lian-Mei Chen, Q.-Y. Lai, H. Yan-Jing, and X.-Y. Ji, Journal of Alloys and Compounds 467, 465 (2009).

[19] W. Xiao, Asymmetric Capacitor Based on Vanadium Dioxide/Graphene/Nickle and Carbon Nanotube Electrode (University of Akron, 2014).

[20] A. Rudge, J. Davey, I. Raistrick, S. Gottesfeld, and J. P. Ferraris, Journal of Power Sources 47, 89 (1994).

[21] H. Li, Y. Gao, C. Wang, and G. Yang, Advanced Energy Materials 5, 1401767 (2015).

[22] J. Huang, P. Xu, D. Cao, X. Zhou, S. Yang, Y. Li, and G. Wang, Journal of Power Sources 246, 371 (2014).

[23] R. R. Salunkhe, J. Lin, V. Malgras, S. X. Dou, J. H. Kim, and Y. Yamauchi, Nano Energy 11, 211 (2015).

[24] J. Yan, Z. Fan, W. Sun, G. Ning, T. Wei, Q. Zhang, R. Zhang, L. Zhi, and F. Wei, Advanced Functional Materials 22, 2632 (2012).

[25] B. G. Choi, S.-J. Chang, H.-W. Kang, C. P. Park, H. J. Kim, W. H. Hong, S. Lee, and Y. S. Huh, Nanoscale 4, 4983 (2012).

[26] Y.-G. Wang, L. Cheng, and Y.-Y. Xia, Journal of Power Sources 153, 191 (2006).

[27] D. P. Dubal, O. Ayyad, V. Ruiz, and P. Gómez-Romero, Hybrid Energy Storage: The Merging of Battery and Supercapacitor Chemistries (Royal Society of Chemistry, 2015), pp. 1777–1790.

[28] D. Salinas-Torres, J. M. Sieben, D. Lozano-Castelló, D. Cazorla-Amorós, and E. Morallón, Electrochimica Acta 89, 326 (2013).

[29] Q. Wang, J. Yan, Y. Wang, G. Ning, Z. Fan, T. Wei, J. Cheng, M. Zhang, and X. Jing, Carbon 52, 209 (2013).

[30] Y. Fang, B. Luo, Y. Jia, X. Li, B. Wang, Q. Song, F. Kang, and L. Zhi, Advanced Materials 24, 6348 (2012).

[31] L. L. Zhang and X. S. Zhao, Chemical Society Reviews 38, 2520 (2009).

[32] W. F. Mak, G. Wee, V. Aravindan, N. Gupta, S. G. Mhaisalkar, and S. Madhavi, Journal of the Electrochemical Society 159, A1481 (2012).

[33] E. Umeshbabu and G. Ranga Rao, Journal of Colloid and Interface Science 472, 210 (2016).

[34] H. Zhao, L. Pan, S. Xing, J. Luo, and J. Xu, Journal of Power Sources 222, 21 (2013).

[35] M. H. Bai, L. J. Bian, Y. Song, and X. X. Liu, ACS Applied Materials and Interfaces 6, 12656 (2014).

[36] X. Pan, G. Ren, M. N. F. Hoque, S. Bayne, K. Zhu, and Z. Fan, Advanced Materials Interfaces 1, 1400398 (2014).

[37] H. Li, K. Jiao, L. Wang, C. Wei, and B. Xie, Journal of Materials Chemistry A: Materials for Energy and Sustainability 2, 18806 (2014).

[38] G. P. Nagabhushana and G. T. Chandrappa, Journal of Materials Chemistry A 1, 11539 (2013).

[39] I. Derkaoui, M. Khenfouch, I. Elmokri, S. J. Moloi, B. M. Mothudi, M. S. Dhlamini, M. Maaza, I. Zorkani, and A. Jorio, Graphene 5, 14 (2016).

[40] S. Kachi, T. Takada, and K. Kosuge, Journal of the Physical Society of Japan 18, 1839 (1963).

[41] H. Hosseini and S. Shahrokhian, Applied Materials Today 10, 72 (2018).

[42] S. Rao Popuri, A. Artemenko, C. Labrugere, M. Miclau, A. Villesuzanne, and M. Pollet, Journal of Solid State Chemistry 213, 79 (2014).

[43] Y. Wang and Z. Zhang, Physica E: Low-Dimensional Systems and Nanostructures 41, 548 (2009).

[44] Y. Oka, S. Sato, T. Yao, and N. Yamamoto, Journal of Solid State Chemistry 141, 594 (1998).

[45] X. Pan, Y. Zhao, G. Ren, and Z. Fan, Chemical Communications 49, 3943 (2013).

[46] S. Surnev, M. G. Ramsey, and F. P. Netzer, Progress in Surface Science 73, 117 (2003).

145

[47] X. Xiao, S. Li, H. Wei, D. Sun, Y. Wu, G. Jin, F. Wang, and Y. Zou, Journal of Materials Science: Materials in Electronics **26**, 4226 (2015).

[48] X.-J. J. Ma, W.-B. Bin Zhang, L.-B. Bin Kong, Y.-C. C. Luo, and L. Kang, RSC Advances **5**, 97239 (2015).

[49] K. Tang, Y. Li, Y. Li, H. Cao, Z. Zhang, Y. Zhang, and J. Yang, Electrochimica Acta **209**, 709 (2016).

[50] L. Danxia, H. Wanxia, S. Limwei, and S. Qiwu, Advanced Materials Research **1120**, 158 (2015).

[51] Y. Oka, T. Yao, and N. Yamamoto, Journal of Solid State Chemistry **86**, 116 (1990).

[52] H. Wang, H. Yi, X. Chen, X. Wang, D. W. Liu, J. Liu, G. Z. Cao, P. M. Ajayan, and F. Wei, Journal of Materials Chemistry A **2**, 1165 (2014).

[53] N. M. M. Ndiaye, T. M. M. Masikhwa, B. D. D. Ngom, M. J. J. Madito, K. O. O. Oyedotun, J. K. K. Dangbegnon, and N. Manyala, Materials Chemistry and Physics **214**, 192 (2018).

[54] M. N. Rantho, M. J. Madito, and N. Manyala, Electrochimica Acta **262**, 82 (2018).

[55] T. M. Masikhwa, D. Y. Momodu, K. O. Oyedotun, A. A. Mirghni, N. M. Ndiaye, and N. Manyala, Journal of Alloys and Compounds **769**, 376 (2018).

[56] C.-T. Wang and H.-H. Huang, Journal of Non-Crystalline Solids **354**, 3336 (2008).

[57] E. Z. Kurmaev, V. M. Cherkashenko, Y. M. Yarmoshenko, S. Bartkowski, A. V Postnikov, M. Neumann, L.-C. Duda, J. H. Guo, J. Nordgren, V. A. Perelyaev, and W. Reichelt, Journal of Physics: Condensed Matter **10**, 4081 (1998).

[58] A. Eftekhari and M. Mohamedi, Materials Today Energy **6**, 211 (2017).

[59] A. Eftekhari, Sustainable Energy & Fuels **1**, 2053 (2017).

[60] X. X. Wang, Y. Zhang, C. Zhi, X. X. Wang, D. Tang, Y. Xu, Q. Weng, X. Jiang, M. Mitome, D. Golberg, and Y. Bando, Nature Communications **4**, 2905 (2013).

[61] A. Leela Mohana Reddy, F. Estaline Amitha, I. Jafri, and S. Ramaprabhu, Nanoscale Research Letters **3**, 145 (2008).

[62] D. Weingarth, H. Noh, A. Foelske-Schmitz, A. Wokaun, and R. Kötz, Electrochimica Acta **103**, 119 (2013).

[63] A. Bello, F. Barzegar, M. J. Madito, D. Y. Momodu, A. A. Khaleed, T. M. Masikhwa, J. K. Dangbegnon, and N. Manyala, Electrochimica Acta **213**, 107 (2016).

[64] A. A. Mirghni, D. Momodu, K. O. Oyedotun, J. K. Dangbegnon, and N. Manyala, Electrochimica Acta **283**, 374 (2018).

[65] X. Xia, D. Chao, C. F. Ng, J. Lin, Z. Fan, H. Zhang, Z. X. Shen, and H. J. Fan, Mater. Horiz. **2**, 237 (2015).

146

4.3.3 Concluding Remarks

We have successfully fabricated an asymmetric device from $VO_2(B)$ nanosheets adopted as a positive electrode and C-FP as the negative electrode using 6 M KOH electrolyte. The $VO_2//$C-FP device exhibited a high specific energy of 30 W h kg^{-1} with a corresponding specific power of 713 W kg^{-1} at 1 A g^{-1} with a 1.6 V operating cell voltage. The excellent stability performance of the $VO_2//$C-FP device was demonstrated for up to 10000 cycles at a specific current of 10 A g^{-1}.

In addition, the voltage holding data obtained after subjecting the hybrid device to floating tests for a period of 70 h showed a significant improvement in device specific capacity and specific energy at 10 A g^{-1}. This was due to the evolution of accessible redox sites during the ageing experiment.

In summary, the asymmetric supercapacitor from $VO_2//$C-FP exhibits good electrochemical performance and hence making the device excellent for energy storage applications.

4.4 Generation of a mesoporous web-like carbon-vanadium oxynitride as an electrode material for symmetric supercapacitors

4.4.1 Introduction

Due to the high faradaic activity and the variable oxidation states, metal oxides have been widely used for energy storage applications [21,22]. However, metal oxides suffer low conductivity and poor cyclic stability. This drawback has hinted the need to synthesize new electrode materials applicable in faradaic capacitors. Recently, metal nitrides/oxynitrides have been demonstrated to exhibit high theoretical capacity, high specific surface area, excellent electrical conductivity and good thermal stability suitable for supercapacitors.

In this study, we synthesized a unique design and facile hydrothermal synthesis method of mesoporous web-like carbon-vanadium oxynitride (C-V_2NO) nanostructures at different nitridation temperature of 700 °C, 800 °C and 900 °C using ammonium metavanadate (NH_4VO_3) and melamine ($C_3H_6N_6$) as precursors. The as-prepared C-V_2NO was extensively characterized by using different techniques. In a three-electrode configuration, the electrochemical measurements of the C-V_2NO@800°C depicted a superior electrochemical performance as compared to others.

A symmetric capacitor was assembled with C-V_2NO@800 °C as positive and negative electrodes in the cell potential of 0 – 1.8 V. The C-V_2NO@800 °C//C-V_2NO@800 °C device delivered a specific energy of 38 Wh kg^{-1} with corresponding a specific power of 735 W kg^{-1} at a specific current of 1 A g^{-1}, with 84.7% capacity retention at 10 000th cycles and excellent voltage holding stability up to 100 h at a high specific current.

4.4.2 Result and discussion

The detailed results from the symmetric capacitor fabricated using a mesoporous web-like C-V_2NO nanostructures electrode is presented in the paper below which still under review:

Generation of a mesoporous web-like carbon-vanadium oxynitride as a novel electrode material for symmetric supercapacitors

Ndeye. M. Ndiaye [a], Ndeye. F. Sylla [a], Balla. D. Ngom [b], Bridget K. Mutuma [a], J. K. Dangbegnon [a], S. C. Ray [c]. and Ncholu. Manyala [a]*

[a] Department of Physics, Institute of Applied Materials, SARChI Chair in Carbon Technology and Materials, University of Pretoria, Pretoria 0028, South Africa

[b] Laboratoire de photonique Quantique d'Energie et de NanoFabrication, Groupe de Physique du Solide et Science des Matériaux, Département de Physique FST-UCAD BP 5005 Dakar-Fan, Dakar, Sénégal

[c] Department of Physics, College of Science, Engineering and Technology, University of South Africa, Private Bag X6, Florida, 1710, Science Campus, Christiaan de Wet and Pioneer Avenue, Florida Park, Johannesburg 1710, South Africa

*Corresponding author email: ncholu.manyala@up.ac.za, Tel: + (27)12 420 3549

Fax: + (27)12 420 2516

ABSTRACT

Unique mesoporous web-like carbon-vanadium oxynitride (C-V_2NO) have been synthesized at different nitridation temperatures of 700 °C, 800 °C and 900 °C using the ammonium metavanadate (NH_4VO_3) and melamine ($C_3H_6N_6$) as precursors by a facile chemical vapor deposition (CVD) method. The N_2 physisorption data of the C-V_2NO materials displayed a high specific surface area (SSA) (from 91.6 to 121.6 m^2 g^{-1}) with a pore diameter ranging from ~ 2 to 8 nm. The electrochemical performance of C-V_2NO electrodes at different temperatures was carried out using a 6 M KOH aqueous electrolyte, with the C-V_2NO synthesized at 800 °C revealing the highest electrochemical performance compared to other temperatures in a three electrode configuration. A symmetric capacitor was assembled using the C-V_2NO@800 °C as both positive and negative electrodes and evaluated in a wide potential window range of 0.0 - 1.8 V. The C-V_2NO//C-V_2NO displayed a specific capacity of 58 mA h g^{-1} with a specific energy of 38 Wh kg^{-1} and a corresponding specific power of 735 W kg^{-1} at a specific current of 1 A g^{-1}. These results make this simply synthesized material to be a potential candidate for supercapacitor application.

1 Introduction

The growing demand for conversion of renewable energy resources and a foreseeable shortage of fossil fuels into usable energy is a major challenge for energy storage. However, many high energy storage systems have also been developed to efficiently deal with the generated energy for productive use and cost-effectiveness such as in battery and supercapacitor devices [1,2]. Supercapacitors (SCs), also named ultracapacitors have been largely studied in the field of energy storage. They exhibit a high power density, a longer cycling life and safety as compared to batteries [3,4]. However, ultracapacitors possess a low energy [5], and their improvement may be achieved by the synthesis of materials that display unique morphologies with high performance.

Typically, SCs can be classified into two types based on their charge storage mechanism: Electric Double-Layer Capacitors (EDLCs) and Faradaic capacitors [6,7]. EDLCs can store the charge in double layer capacitance. The materials used are carbon-based active materials with high specific surface area (SSA), good electronic conductivity, good stability and low specific capacitance [6].

In faradaic capacitors, charge storage mechanism is based on fast reversible redox reactions such as in transition metal oxides, hydroxides (TMOs/TM-OHs) and redox polymers [8,9].

For decades, metal oxides have been widely used for energy storage applications due to their high faradaic activity and their variable oxidation states by adopting different structures [10]. Nevertheless, metal oxides suffer low SSA and low conductivity which leads to low specific power [11]. Thus, it is necessary to synthesize new electrode materials applicable in faradaic capacitors. Recently, several achievements geared at improving the stability of faradaic

150

materials have been reported such as the adoption of transition metal nitride materials: CoN [12], CrN [13], TiN [14], VN [15] TiN-VN [16] and Fe_3N [17]. The metal nitride have shown prominent electrochemical capacitive properties by replacing the oxides/hydroxides completely with nitrogen atoms [18]. Among the greatest recent achievements in transition metal nitride materials, vanadium nitrides (VN) has been considered to be an excellent candidate due to its environmental friendliness, low cost [19], high molar density ($\approx$6 g cm^{-3}), excellent chemical resistance [20] and its good electronic conductivity ($\sigma_{bulk} = 1.67 \times 10^6 \ \Omega^{-1}$ m^{-1}) [21] leading to an excellent specific capacitance of 1340 Fg^{-1} at a scan rate of 2 mV s^{-1} in a three-electrode configuration. Although the metal nitride exhibits a high specific capacity. They still suffer from poor rate performance and cycling life [22]. However, the electrochemical performance of the vanadium nitrides can be investigated on the surface functionalization and an introduction of oxygen containing groups (oxidation process) and surface [19,23]. The metal oxynitrides displayed a good redox reaction as compared to VN [24] due to the wettability of the electrode material which is higher than that of the VN [25]. These characteristics make this material interesting as a potential electrode for supercapacitor application. Metal nitrides/oxynitrides have been demonstrated to exhibit a high theoretical capacity, high specific surface area, excellent electrical conductivity and good thermal stability suitable for supercapacitors.

The main challenge, however lies in the bid to experimentally realize this high capacity, good stability and rate performance with the use of a simple synthesis method [22]. In the literature, there are few reports related to the use of vanadium oxynitride as an electrode material for supercapacitors. For instance, Porto *et al.* [26] synthesized vanadium oxynitride VO_xN_y rather than vanadium nitride by a conventional nitridation method using as-prepared VO_2 from the commercial V_2O_5. The specific capacitance of the VO_xN_y powders was found to be 80 Fg^{-1}. In their report, they concluded that the low specific capacitance observed for the VO_xN_y

electrodes was highly influenced by the low specific surface area of the material ($\sim$29 m^2 g^{-1}) [26].

However, most reports on vanadium nitride and oxynitride materials entail the use of vanadium oxide precursors such as VO_2 or V_2O_5 resulting in the generation of aggregated VN and VO_xN_y particles owing to the low melting point of the vanadium oxides [27]. This consequently limits the electrochemical performance of these materials due to their low specific surface areas [26,27]. To overcome this drawback, an appropriate and efficient vanadium precursor is requisite. Although various researchers have reported on the use of vanadium chloride and vanadium oxychloride precursors to obtain well crystalline VN and VO_xN_y nanostructures [20,26], a controlled working environment is required due to the high reactivity and toxicity of the chlorides [28].

Ammonium metavanadate (NH_4VO_3) is less toxic, less corrosive and safer as compared to the chloride-based precursors and thus, a suitable alternative for the preparation of VO_xN_y materials. In addition, a recent approach on the use of organic precursors in the growth of vanadium nitride and oxynitride materials has resulted in a controlled particle formation, generation of a crystalline structure as well as the ability to tune the specific surface areas of the final product [16].

In this regard, polyvinylpyrrolidone, urea, cyanamide and melamine are commonly used organic precursors as they serve as both carbon and nitrogen sources with the melamine providing a higher nitrogen and carbon contents. For instance, Cheng *et al.* [27] studied $VN_{1.02}O_{0.1}$ material by calcining a mixture of melamine and V_2O_5 xerogel in a furnace at 800 °C under an N_2 atmosphere. They obtained a carbon content of 52.6 % and a nitrogen content of 22.6 % after melamine decomposition. A specific capacitance of 273 F g^{-1} was reported for the $VN_{1.02}O_{0.1}$ material at a scan rate of 30 mV s^{-1} in a 1 M KOH [27]. The deposited carbons

prevented aggregation of the VN particles and improved the pseudocapacitive properties of the $VN_{1.02}O_{0.1}$ material. Similarly, Shu *et al*. [29] synthesized the VN materials from the melamine and V_2O_5 xerogel at 800 °C under a N_2 atmosphere.

The specific capacitance of VN electrode was 413 F g^{-1} at a specific current of 1 A g^{-1}. They reported that the electrochemical performance of the material was improved by the presence of the carbon remains [29]. Recently, a different synthesis approach of remodelling the vanadium oxynitride materials with carbon has been proposed to enhance the structural, textural and electrochemical properties VO_xN_y [28]. For example, Shu and co-workers [28] reported on a porous structure of VO_xN_y-C nano-material using polyvinylpyrrolidone (PVP) as a template followed by NH_3 reduction of V_2O_5/PVP xerogel by a CVD method. They demonstrated that the VO_xN_y-C electrode exhibited higher electrochemical performance than the VO_xN_y electrode in 1 M KOH aqueous electrolyte. This good performance of the VO_xN_y-C can be ascribed to their superior specific surface area (40.8 m^2 g^{-1}) as compared to the VO_xN_y (28.8 m^2 g^{-1}) which improved the electrochemical capability. The presence of carbon in the vanadium oxynitride matrix can greatly influence the specific surface area, structure and morphology of the VO_xN_y and as a result, improve their electrochemical capacitance [28]. In this case, the vanadium based active electrode materials were generated by ammonia reduction of V_2O_5 xerogel in the presence of PVP.

In this study, we report a unique design and facile CVD synthesis method of mesoporous web-like carbon-vanadium oxynitride (C-V$_2$NO) nanostructures at different nitridation temperature of 700 °C, 800 °C and 900 °C using ammonium metavanadate (NH_4VO_3) and melamine ($C_3H_6N_6$) as precursors. The C-V$_2$NO was generated by the in-situ decomposition of ammonium metavanadate in the presence of melamine precursor. The ammonia gas was obtained from ammonium metavanadate and by using melamine precursor, a higher carbon content (67 %) was achieved as compared to a soft template such as PVP (~9 %). The high

carbon content is beneficial for the growth of a high surface area mesoporous C-V$_2$NO with nanometer-sized pores and appropriate pore distribution that is beneficial for enhanced electrochemical performance. The electrochemical performance of the cubic C-V$_2$NO was evaluated using 6 M KOH aqueous electrolyte in both positive and negative potential windows. A symmetric capacitor was assembled with C-V$_2$NO@800 °C as positive and negative electrodes in the cell potential of 0 – 1.8 V. The C-V$_2$NO@800 °C//C-V$_2$NO@800 °C delivered high specific energy and specific power of 38 Wh kg^{-1} and 764 W kg^{-1} at 1 A g^{-1}, respectively with 84.7% capacity retention at 10 000th cycles and excellent voltage holding stability up to 100 h at a high specific current. To our knowledge, this is the first time a symmetric device has been fabricated for a C-V$_2$NO electrode material showing the potential for applicability of these materials in high-performance supercapacitors.

2. EXPERIMENTAL

2.1 Synthesis of C-V$_2$NO by CVD technique

Scheme 1 presents the diagram illustrating the facile procedure used to synthesize the C-V$_2$NO sample at a nitridation temperature of 700 °C with the same procedure used for other temperatures.

The C-V$_2$NO materials were synthesized by using analytical grade chemicals: 0.5 g of ammonium metavanadate (NH$_4$VO$_3$, 99%) and 5 g of melamine (C$_3$H$_6$N$_6$, 99%) were mixed in an agate mortar with a few drops of ethanol (CH$_3$CH$_2$OH, 99%) to make a homogeneous slurry. This was inserted into a quartz tube furnace and heated to 700 °C at a heating rate of 18 °C min^{-1} before being kept at that temperature for 2 h under a stream of nitrogen (N$_2$, 99%) gas flow. After cooling down to room temperature, the final product was obtained and labelled as C-V$_2$NO@700 °C. This process was repeated at different growth temperatures of 800 °C and 900 °C and labelled accordingly.
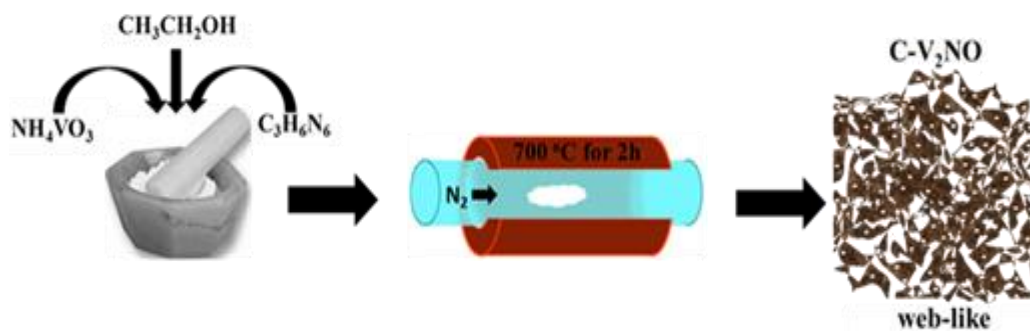
Scheme. 1: Preparation steps of carbon-vanadium oxynitride.

2.2 Structure, morphology and composition characterization

X-ray diffraction (XRD) analysis of as-prepared C-V$_2$NO was studied using a XPERT-PRO diffractometer (PANalytical BV, Netherlands) using a cobalt X-ray source at 50 mA and 35 kV with θ /2θ geometryin the range from 10°–90° 2θ. Raman spectroscopy analysis of the materials were achieved using a WITec confocal Raman microscope (WITec alpha300 R, Ulm Germany at a laser wavelength of 532 nm.

The morphology of the C-V$_2$NO was investigated using a resolution Zeiss Ultra plus 55 field emission scanning electron microscope (FE-SEM) operated at a voltage of 2.0 kV. Transmission electron microscopy (TEM) analysis was carried out at 200 kV on a JEOL JEM-2100F microscope (Akishima-shi, Japan). X-ray photoelectron spectroscopy (XPS, K-alpha, Thermo Fisher) was used to analyse the elemental composition of the materials with a monochromatic Al-Kα radiation.

The porosimetry tests of the C-V$_2$NO materials were evaluated with a nitrogen adsorption–desorption isotherms at -196°C using a Micromeritics ASAP 2020. The surface area of the materials were obtained by the Brunauer–Emmett–Teller (BET) analysis from the adsorption branch in the relative pressure range (P/P0) of 0.01–1.0.

2.3 Electrochemical characterization of C-V₂NO

The electrochemical measurements of the C-V$_2$NO electrodes were studied using a Bio-Logic VMP-300 (Knoxville TN 37,930, USA) potentiostat at room temperature and evaluated in a three-and two electrode configurations. The C-V$_2$NO electrodes were prepared by mixing weighed amounts of C-V$_2$NO active material, carbon black additive and polyvinylidene difluoride (PVDF) binder in a mass ratio of 80:10:10 with a N-methylpyrrolidone (NMP) as a solvent. The slurry was applied on a NiF (3D scaffold template with an area density of 420 g/m^2, Merck (South Africa)) as a current collector. The electrodes were kept at 60 °C in an electric oven overnight to completely evaporate the NMP. The masses of the C-V$_2$NO electrodes fabricated for the different nitridation temperatures were maintained at the same value for comparison purposes. The three-electrode configuration was used to evaluate the electrochemistry of the electrodes with a glassy carbon plate counter electrode and Ag/AgCl (3 M KCl saturated) reference electrode in a 6 M KOH aqueous electrolyte. The two-electrode configuration of a symmetric device was studied using the C-V$_2$NO@800 C as both positive and negative electrodes. The electrodes were separated by a microfibre glass filter paper with a thickness of 0.2 mm in a Swagelok cell.

The specific capacity, Q$_S$ (mA h g^{-1}) of the electrodes was calculated using Eqn. (1) as a function of the specific current:

$$Q = \frac{I_d \times t_D}{3.6} \tag{1}$$

where I_d is defined as the specific current measured in A g^{-1} and t_D is the time in second (s) for a complete discharge cycle.

The specific energy E_d (W h kg^{-1}) and specific power P_d (W kg^{-1}) of the C-V$_2$NO//C-V$_2$NO device were calculated using Eqn. (2) and (3) at different specific currents:

$$E_d \,(\text{W h kg}^{-1}) = \frac{I_d}{3.6} \int V(t)dt \tag{2}$$

$$P_d \, (\text{W kg}^{-1}) = 3600 \frac{E_D}{t_D} \tag{3}$$

where I_d is the specific current in A g^{-1}, t_D is the discharge time (s), and V is the potential window (V) of the symmetric capacitor.

3. Results and discussion

X-ray diffraction (XRD) analysis results of the carbon-vanadium oxynitride materials synthesis at 700 °C, 800 °C and 900 °C, respectively are presented in Fig. 1(a). The XRD patterns of C-V$_2$NO showed three diffraction peaks confirming the crystallinity of the material and were indexed to a cubic structure with a single phase. The diffraction peaks are located at 2θ value of 44.0 °, 51.3 ° and 75.5 ° corresponding to the (111), (200) and (220) crystallographic planes, respectively. The XRD pattern of the C-V$_2$NO cubic structure exhibited a *Fm-3m* space group with lattice parameters of: *a* = 4.1313(1) Å *a/b* = 1.0000, *b/c* = 1.0000 and *c/a* = 1.0000 using the matching inorganic crystal structure Database (ICSD) card # 43182. Indeed, the peaks of C-V$_2$NO@800 °C and C-V$_2$NO@900 °C were narrower and much pronounced than the ones for C-V$_2$NO@700 °C.

Also, the peak intensity of the peak of C-V$_2$NO was found to increase with nitridation temperature indicating an increase in crystallinity.

The presence of the carbon in the as-prepared C-V$_2$NO materials was nonetheless confirmed from the Raman spectra at 700 – 900 °C as shown in Fig 1(b) with the characteristic D and G bands attributed to carbonaceous material present in the C-V$_2$NO at different nitridation temperatures. The Raman spectra for the C-V$_2$NO materials also displayed Raman bands at wavenumbers of 145 cm^{-1}, 192 cm^{-1}, 285 cm^{-1}, 479.1 cm^{-1}, 520.7 cm^{-1}, 693 cm^{-1}, 822 cm^{-1}, 873 cm^{-1}, and 995 cm^{-1} as seen in Fig. 1(b) which can be associated to the V$_2$NO stretching mode in the carbon- metal oxynitride.

The three peaks D, G and D' of the C-V$_2$NO materials are also observed in Fig 1(b). The D peak positions were observed at (1346 – 1373 cm^{-1}) as indicated in Table 1 and is associated to the disorders present in the carbon lattice structure [30,31].
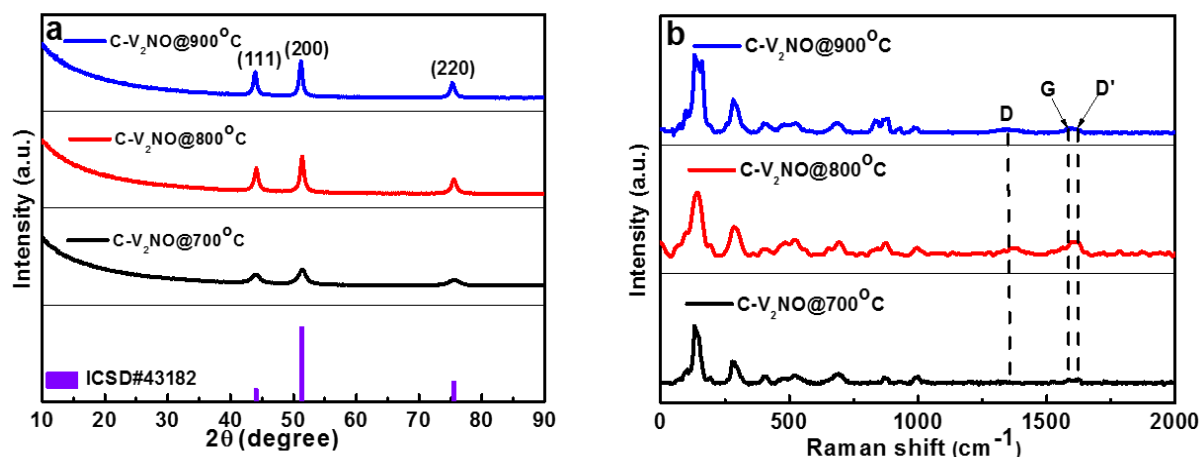
Fig. 1: (a) the XRD patterns and (b) the Raman spectra of the C-V$_2$NO materials grown at 700 °C, 800 °C and 900 °C.

The G peak positions observed at (1585 - 1593) is related to the vibration modes of the graphitic sp^2 carbon present [30,32]. A small shoulder was observed near the G peak suggesting a graphene-like carbon present in the C-V$_2$NO material.

In fact the D' peak is ascribed to the lattice vibration of G band but mainly due to the graphene layers at the surface of the carbon material present in the material [33,34]. A similar D' peak has also been observed in boron carbon oxynitride films due to lattice distortions [35].

Table 1: D, G, D' band positions and I$_D$/I$_G$ ratio of the C-V$_2$NO samples

Material	D peak position (cm^{-1})	G peak position (cm^{-1})	D' peak position (cm^{-1})	I$_D$/I$_G$ ratio
C-V$_2$NO@700°C	1349	1585	1611	0.47
C-V$_2$NO@800°C	**1373**	**1593**	**1621**	**0.84**
C-V$_2$NO@900°C	1346	1588	1618	0.56

The high I_D/I_G ratio of the C-V$_2$NO@800°C recorded in Table 1 suggests that the presence of defects could result from the nitrogen incorporated in the carbon lattice and also the strong interaction between the metal oxynitride and the carbon. The highest graphitization among in the C-V$_2$NO@800°C can contribute to high electrochemical capacity.

The morphological analysis of the C-V$_2$NO synthesized at different temperatures is presented in Fig. 2. The morphologies of the C-V$_2$NO materials at different temperatures showed a web-like structure with irregular porous cavities (Fig. 2(a, c and e). At higher magnifications, C-V$_2$NO@700°C shows densely packed nanoparticles that are non-uniformly distributed (Fig. 2(b)). In contrast, the surface morphology of the C-V$_2$NO@800°C shows interconnecting particles to form a mesoporous web structure (Fig. 2(d)). At 900 °C, a disintegrated network of the C-V$_2$NO is observed (Fig. 2(f)).

In the C-V$_2$NO@ 800°C, it can be seen clearly that the porous cavity can penetrate deep into the material with a non-uniform distribution compared to the C-V$_2$NO obtained at other temperatures.
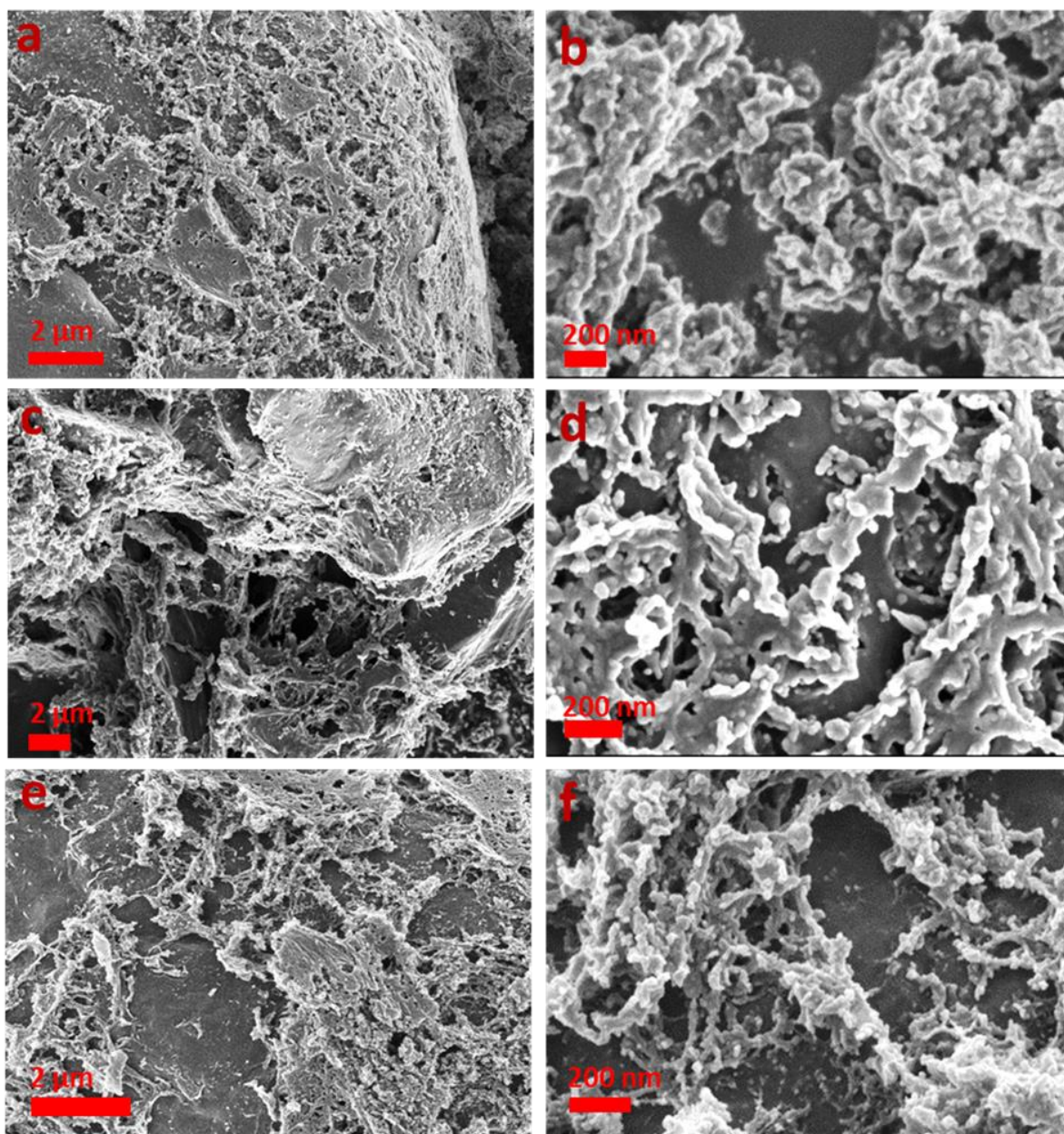
Fig. 2: The SEM images of the as synthesized C-V$_2$NO samples at low and high magnification (a-b) C-V$_2$NO@700 °C, (c-d) C-V$_2$NO@800 °C and (e-f) C-V$_2$NO@900 °C.

The TEM images of the C-V$_2$NO were also used for further morphological analysis (Fig. 3). The micrographs reveals the presence of a mesoporous architecture confirms the web-like structure. However, the carbon formed after melamine decomposition leads to the irregular behaviour and can prevents the re-crystallization of the C-V$_2$NO nanoparticles [27,29].
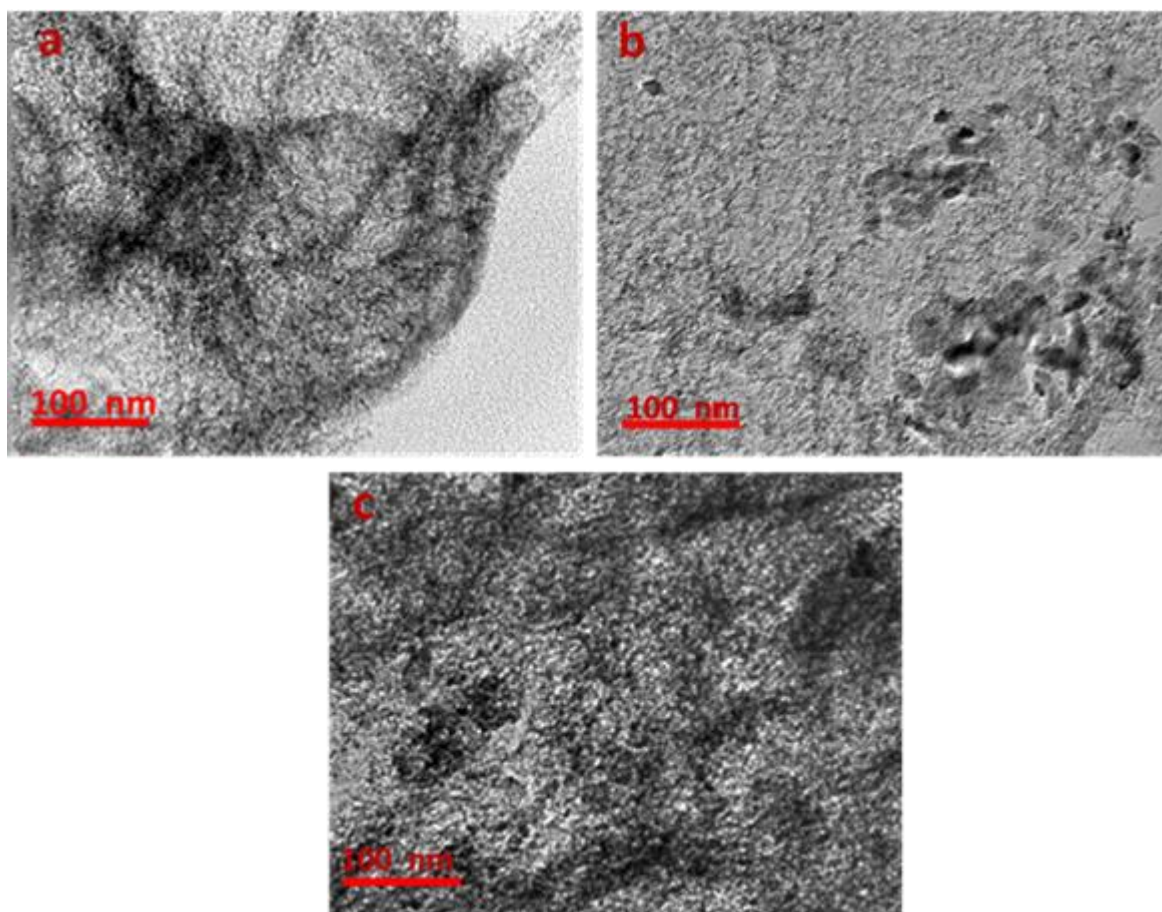
Fig. 3: The TEM images of the as synthesized C-V$_2$NO samples: (a) C-V$_2$NO@700 °C, (b) C-V$_2$NO@800 °C and (c) C-V$_2$NO@900 °C.

To investigate the porosity properties of the materials, N$_2$ adsorption-desorption measurement was carried out on C-V$_2$NO materials at 700 °C, 800 °C and 900 °C, as shown in Fig. (4).

The N$_2$ isotherm of the C-V$_2$NO materials in Fig. 4(a) is depicted a type IV adsorption–desorption isotherm with a H3 hysteresis behaviour associated with plate-like particles giving rise to slit-shaped pores [36]. The as-obtained specific surface area (SSA) of the different carbon-vanadium oxynitride materials was 91.6 m^2 g^{-1}, 121.6 m^2 g^{-1} and 113 m^2 g^{-1} at 700 °C, 800 °C and 900 °C, respectively.

The synthesis of these mesoporous interconnected web-like structures with controlled growth temperature yielded higher values of the specific surface area as compared to those reported for TiO$_x$N$_y$ [37] , VO$_x$N$_y$ and VO$_x$N$_y$-C [28].

Fig. 4(b) shows the pore size distribution with a pore diameter ranging from ~ 2 to 8 nm which signifies the presence of a predominantly mesoporous C-V$_2$NO material. It shows clearly that the pore diameter of the C-V$_2$NO material decrease with increasing the nitridation temperature. The C-V$_2$NO@700 °C shows a broad pore size distribution whereas a narrow pore size distribution was observed for the C-V$_2$NO materials at 800 °C and 900 °C

As seen in Fig. 4(a - b), the C-V$_2$NO@800 °C exhibited a higher specific surface area and a higher pore volume than the C-V$_2$NO@700 °C and C-V$_2$NO@900 °C with a small pore diameter of 2 nm. This mesoporous structure of the C-V$_2$NO@800 °C could greatly increase the mass transport of electrolytes ions within the electrodes for fast redox reactions and thus further enhance the electrochemical performance.
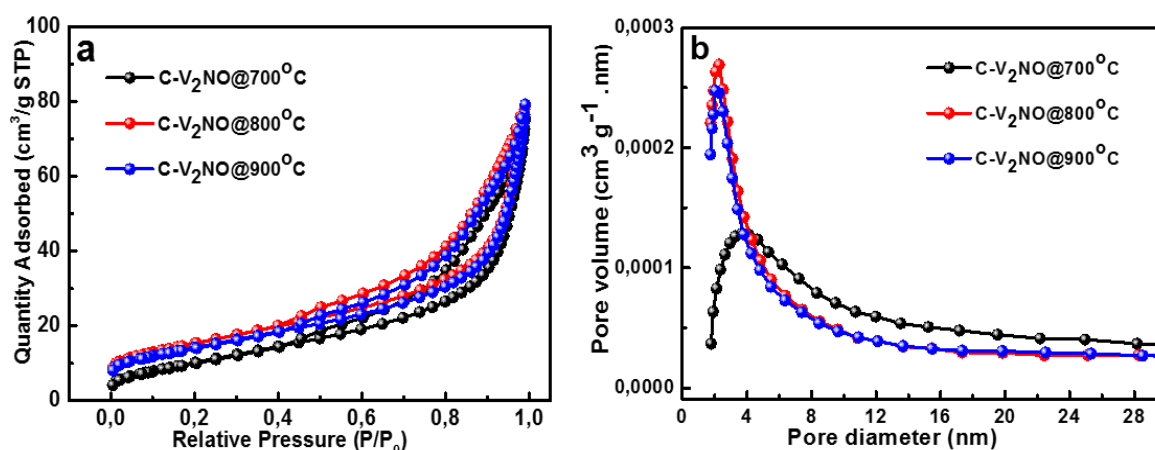
Fig. 4: (a) N$_2$ absorption/desorption isotherms and (b) pore size distribution of C-V$_2$NO at 700 - 900 °C nitridation temperature.

To highlight the merits of the unique and novel design of the C-V$_2$NO@800 °C material, a further surface characterization was performed using X-ray photoelectron spectroscopy (XPS) as shown in Fig. 5.

The chemical states of the C-V$_2$NO@800 °C is quantitatively evaluated to determine the amount of active vanadium, nitrogen, oxygen and carbon content in the carbon-vanadium oxynitride.
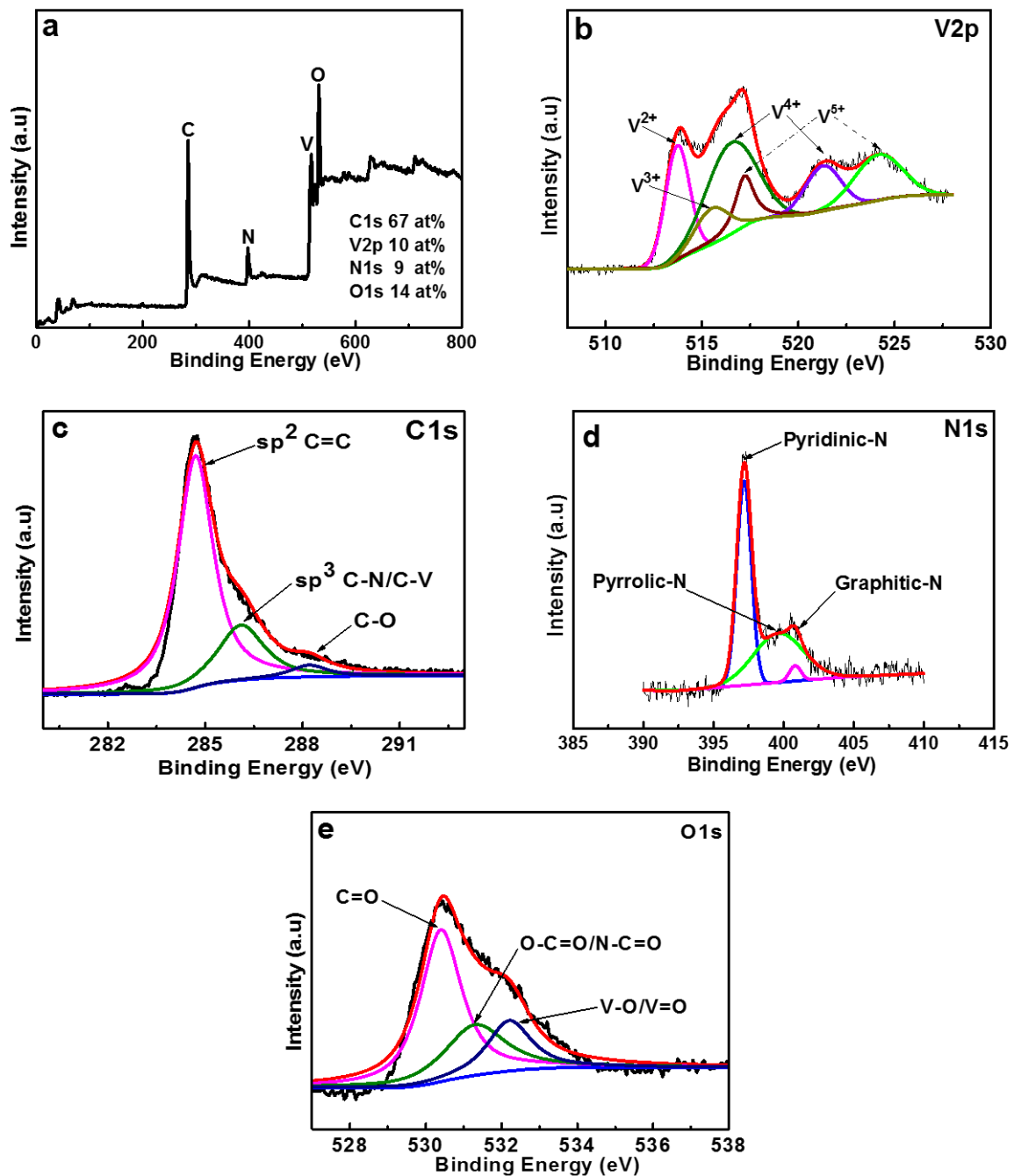
Fig. 5: (a) The wide scan XPS spectrum of the as- received (i.e., without sputter cleaning) C-V$_2$NO@800 °C, indicating deconvoluted spectra of (b) V2p binding energy region, (c) C1s binding energy region, (d) N1s binding energy region and (e) O1s binding energy regions, respectively.

The elemental composition (at %) of the C-V_2NO was carbon (C) (67 at%), vanadium (V) (10 at%), oxygen (O) (14 at%) and nitrogen (N) (9 at%) as determined from the integral peak areas of the XPS survey spectra (Fig 5a).

The core level spectrum of V2p reveals two chemical states of vanadium (V) which are related to excitations of electrons from the V2p$_{3/2}$ and V2p$_{1/2}$ core levels, respectively, as shown in Fig. 5(b).The vanadium-based peaks at binding energies of 513.7 eV, 515.5 eV, 516.5 eV, 517.7 eV, 521.2 eV and 524.1 eV can be attributed to all the different vanadium ions V^{2+}, V^{3+}, V^{4+} and V^{5+} respectively [10,38,39].

The core level spectrum of C1s exhibited four peaks as shown in Fig. 5(c). The high binding energy at 284.6 eV corresponds to the sp^2 C=C bond which further confirms the predominant content of graphitic carbon sp^2 in the material [40,41]. The peaks located at 286.1 eV and 288.2 eV are attributed to the sp^3 C-N/C-V and C-O bonding structures, respectively [42–45].

In Fig. 5(d), the XPS signal of the N1s can be deconvoluted into a three peak Gaussian components. The peak at 397.3 eV binding energy value was attributed to N from vanadium oxynitride [21]. The other two peaks at 399.4 eV and 400.5 eV were assigned to the pyrrolic-N and graphitic-N, respectively [46].

Fig. 5(e) shows the core level spectrum of O1s which reveals two peaks located at 530.5 eV, 531.3 eV and 532.2 eV. The peaks located at 530.5 eV and 531.3 eV were ascribed to C=O and O-C=O/N-C=O, respectively [46] and the peak at 532.2 eV is attributed to the V-O/V=O [47].

The formation of mesoporous carbon-vanadium oxynitride can be postulated to result from the reaction of vanadium metavanadate and melamine at higher temperatures.

Typically, at high temperatures (> 220 °C), the melamine decomposes to give –CH_2, -C-N and nitrogen groups which form the matrix ring (N-C matrix) at higher temperatures [48] and the NH_4VO_3 decomposes at (>300 °C) to yield vanadium oxides, NH_3 gas and H_2O [49,50].

The NH$_3$ gas can further reduce the vanadium oxides in the presence –CH$_2$ and N-C matrix from melamine decomposition leading to the formation of vanadium oxynitride material at higher temperatures (500 - 1500 °C) [51]. The presence of the metal oxide and N-C, as well as the NH$_3$, favoured the formation of the carbon-vanadium oxynitride at high nitridation temperatures.

At 700 °C, small nanoparticles of C-V$_2$NO were formed and connected in a web network with a high degree of graphitized carbon. When the temperature was further increased to 800 °C, the particles is strongly interconnected to form a more mesoporous network (higher surface area) that favoured a better interaction of the C-V$_2$NO surface with the electrolyte.

Consequently, the carbon network became more defective resulting in a lower degree of graphitization. At 900 °C however, the highly mesoporous network was disintegrated resulting in a decreased specific surface area and a moderately graphitized carbon network. Thus, nitridation temperature influenced the morphology, structure and surface area of the C-V$_2$NO.

3.1 Electrochemical performances

To evaluate the electrochemical performances of the C-V$_2$NO synthesized at different growth temperature, the electrodes were initially tested in a three electrode configuration operated in 6 M KOH electrolyte (as seen in Fig. 6). Fig. 6(a - b) shows the cyclic voltammogram (CV) plots of the different C-V$_2$NO materials in a positive potential window of 0.0 to 0.40 V and a negative potential window of -1.20 to 0.0 V at a 50 mV s^{-1} scan rate.

As observed in these figures, the CV plots of C-V$_2$NO@800°C exhibits a higher current response compared to the other C-V$_2$NO samples prepared at different temperatures in both operating potential ranges. Fig. 6(c) shows clearly that the C-V$_2$NO@800°C electrode presents the highest specific capacity as function of the nitration temperature in both positive and negative potential windows.

Fig. 6(d) shows the Nyquist plot and the equivalent serial resistance (ESR) for the C-V$_2$NO electrodes carried out in the frequency range of 100 kHz to 10 mHz. The Nyquist plot of all C-V$_2$NO samples shows a slight deviation from the vertical line with 800 °C sample showing a shorter diffusion length than others. As observed, the C-V$_2$NO at 800 °C also presents a better capacitive response and a smaller ESR (see inset to the figure) than other materials.
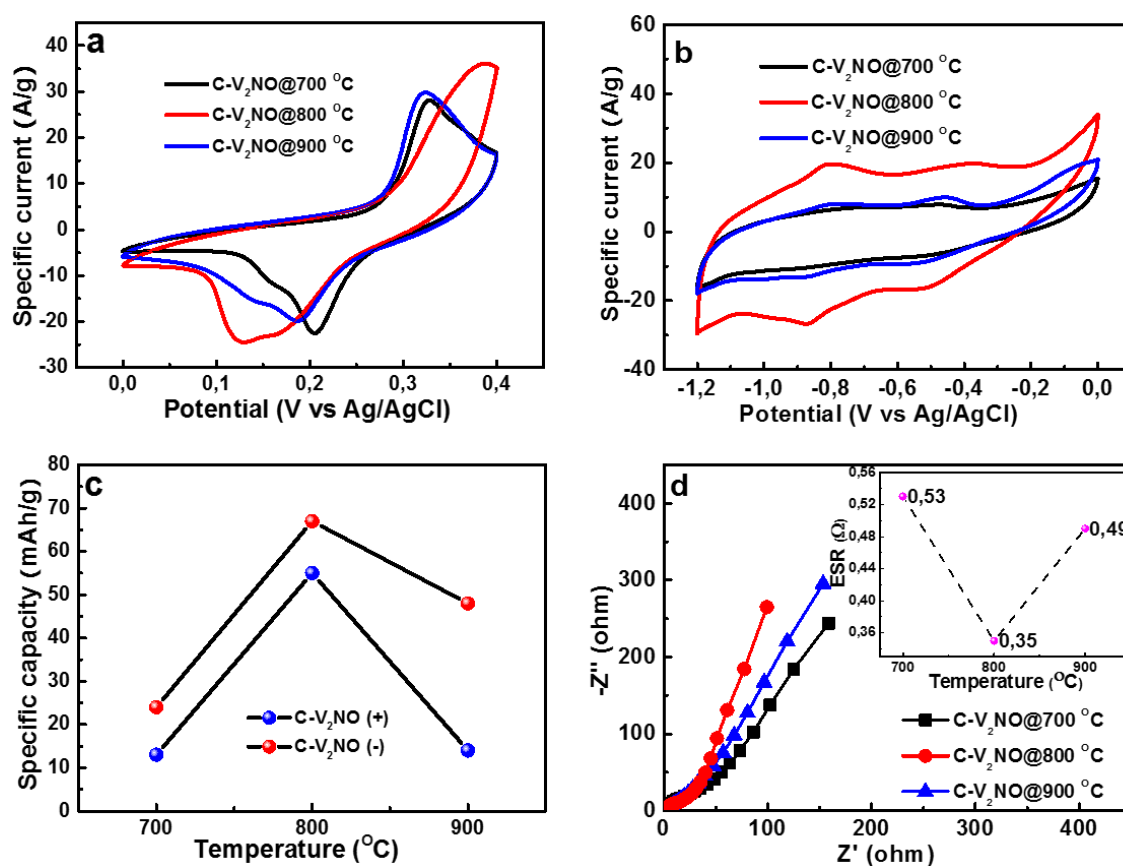
Fig. 6: (a) the CV curve of the C-V$_2$NO electrodes in a potential window range of 0.0 to 0.4 V at 50 mV s^{-1}, (b) the CV curve of the C-V$_2$NO electrodes in a potential window range of -1.2 to 0.0 V at 50 mV s^{-1} (c) the specific capacity of the C-V$_2$NO as positive and negative electrodes as function of nitration temperature at a specific current of 1 A g^{-1} and (d) the Nyquist plot (the inset is the ESR at different nitration temperatures) for the C-V$_2$NO electrodes material

In three-electrode configuration, the electrochemical measurements of C-V$_2$NO@800°C depicted a superior electrochemical response based on the result in Fig. 6. This is linked to the mesoporous web-like morphology of the C-V$_2$NO@800°C coupled with the high SSA and a

small pore diameter which provides an efficient contact between the surface of electroactive web-like and the 6M KOH even at high rates to build up an good path for fast electron transport. From this result, the electrochemical measurements for full cell device is carried out using C-V$_2$NO@800°C samples as both negative and positive electrode to produce a symmetric device.

Fig. 7(a - b) shows the CV curves of the C-V$_2$NO@800 °C electrode in a positive and a negative potential window range of 0.0 to 0.4 V and -1.2 V to 0.0 V, respectively, at different scan rates from 5 to 100 mV s^{-1}. The CV curve depicts a faradaic electrode material in the positive potential window as shown in Fig. 7(a). This behaviour was confirmed by the presence of a pair of redox peaks at a scan rate of 50 mV s^{-1} corresponding to the anodic peak at ~ 0.12 V and cathodic peak ~ 0.35 V, respectively. Fig. 7(b) shows a pseudocapacitive behavior in the negative potential window with two redox peaks during the anodic (-0.80 V, -0.38 V) and the cathodic ((-0.87 V, -0.53 V. These behaviours in the positive and in the negative potential windows are due to the presence of the vanadium oxide in the material which indicates a reversible redox reaction of the vanadium. Based in the literature, vanadium oxides in the negative potential window may led to a redox reaction, but it is a challenge to assign the peak to an individual oxide [19].

Fig. 7(c) displays the associated galvanostatic charge-discharge (GCD) curves at different specific current values. The existence of a faradaic behaviour is depicted with the non-linear discharge profile in the potential window of 0.0 to 0.4 V.

Fig. 7(d) shows the GCD curves at different specific currents in the potential window of -1.2 to 0.0 V. It confirmed the existence of a pseudocapacitive behavior as shown in Fig. 7(b).

Fig. 7(e) shows the specific capacity of the C-V$_2$NO@ 800 °C calculated in the positive and the negative potential window at different specific currents from 1 A g^{-1} to 10 A g^{-1}.

The specific capacities of the C-V$_2$NO@800°C were found to be 55 and 67 mA h g^{-1} in the positive and in the negative potential window, respectively, at a specific current of 1 A g^{-1}.

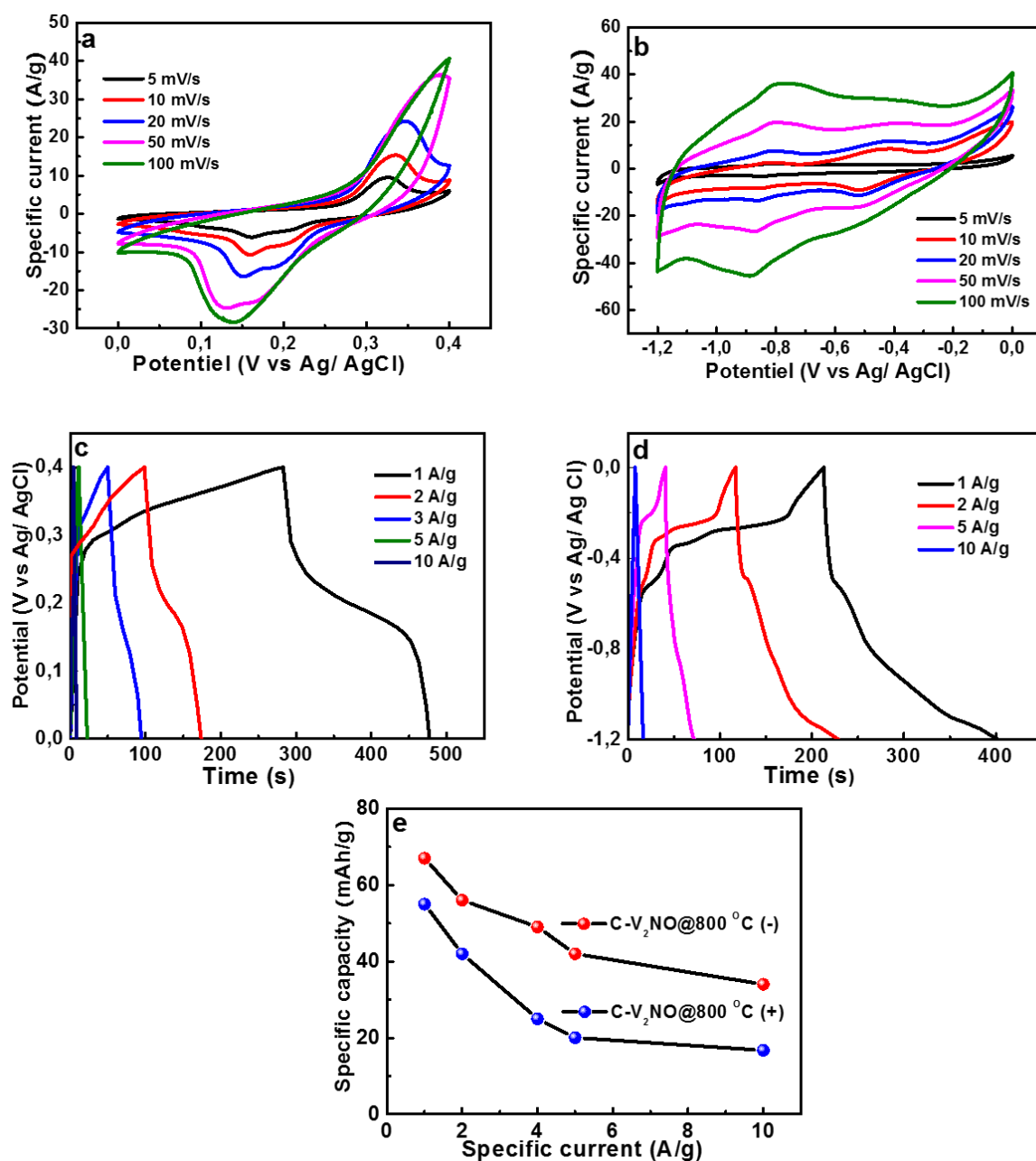**Fig. 7:** The electrochemical measurements of **C**-V$_2$NO@800 °C: (a) CV curves at different scan rates, (b) GCD curves at different specific currents in a potential window of 0.0 to 0.4 V, (c) CV curves at different scan rates, (d) GCD curves at different specific currents in a potential window of -1.2 to 0.0 V and (e) specific capacity of the positive and the negative electrodes as a function of the specific current.

To further demonstrate the electrochemical performance of the C-V$_2$NO@800°C electrode extensively, a symmetric capacitor was assembled using C-V$_2$NO@800°C as a positive and a negative electrodes (C-V$_2$NO// C-V$_2$NO) in 6 M KOH.

Fig. 8(a) shows the CV profiles of the C-V$_2$NO@800°C measured in a stable working potential windows of -1.2 to 0.0 V and 0.0 to 0.4 V, respectively at a scan rate of 50 mV s^{-1}, an estimation of the working potential window of 1.6 V could be waited for the symmetric device.

Fig. 8(b) presents CV curves at different potentials window such as 1.6 V, 1.7 V and 1.8 V at a scan rate of 30 mV s^{-1}. The CV curve at 1.8 V shows the highest current response and good contribution of the two behaviours of C-V$_2$NO@800°C in the positive and the negative potential windows compared to other potential windows (1.6 V and 1.7 V). Moreover, the current leap at large potential window of 1.8 V was not observed, suggesting the stability of the symmetric device in this potential window (Fig. 8(b)). It can therefore be concluded that the maximum stable working potential of the C-V$_2$NO//C-V$_2$NO symmetric device is 1.8 V.

Fig. 8(c) shows the CV curves of the C-V$_2$NO//C-V$_2$NO symmetric device at different scan rates from 5 - 400 mV s^{-1} within the large stable operating voltage of 1.8 V. The CV plots indicate a combination and the contribution of pseudocapacitive and faradaic charge storage mechanisms. As observed, the CV curves present the same behavior from 5 to 500 mV s^{-1} scan rates, indicating rapid redox reactions at high scan rates. The specific current increases proportionally as a function of increased scan rate indicating the good rate capability of the symmetric device.
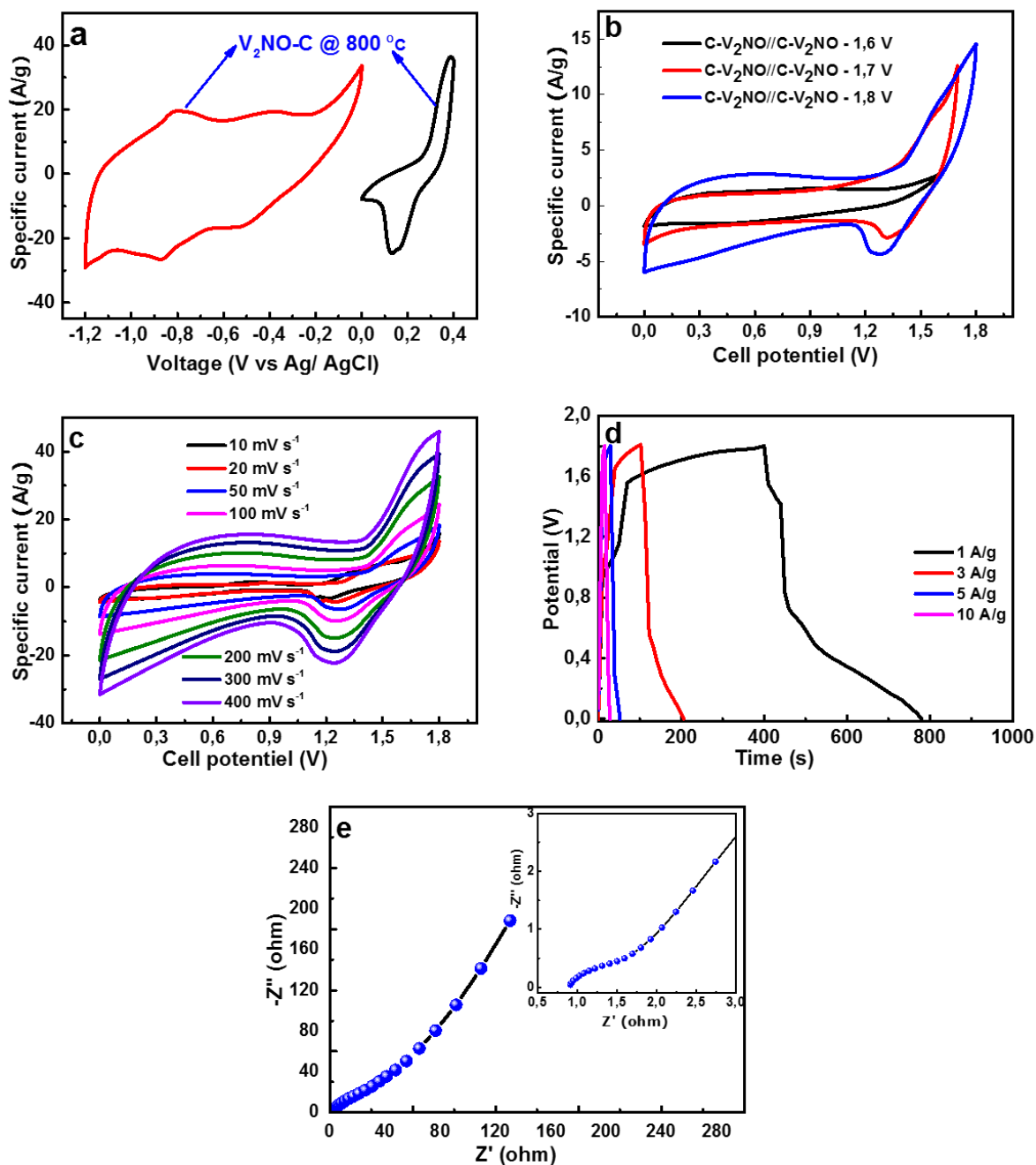
Fig. 8: (a) Combined CV plots from the negative and positive potential window of the C-V$_2$NO@800°C electrode at 50 mV s^{-1}, (b) CV at 1.6 V, 1.7 V and 1.8 V at 30 mV s^{-1}, (c) CV plot at different scan rates for cell potential of 1.8 V, (d) GCD plot of the device at different specific currents and (e) EIS plot of the C-V$_2$NO//C-V$_2$NO symmetric device.

Fig. 8(d) shows the GCD profiles of C-V$_2$NO//C-V$_2$NO symmetric device at different specific currents of 1 − 10 A g^{-1} in the large cell potential of 0.0 - 1.8 V. The GCD curves exhibited faradaic behavior for the symmetric device in agreement with CV curves from Fig. 8 (b). Fig. 8(e) presents the Nyquist plot of the symmetric device, which was carry out in the frequency

range of 100 kHz-10 mHz. An equivalent series resistance (ESR) value of 0.88 Ω was recorded for the symmetric device.

Fig. 9(a) shows the profile of the specific capacity as a function of specific current. A specific capacity of 58 mA h g^{-1} of the symmetric device was recorded at a specific current of 1 A g^{-1}. This was retained at 18.7 mA h g^{-1} as the specific current was increased to 10 A g^{-1}. Fig. 9(b) displays the Ragone plot which describes the power density as a function of energy density for the symmetric capacitor at different specific currents range of 1- 10 A g^{-1}. The specific energy of the C-V$_2$NO//C-V$_2$NO was 38 W h kg^{-1} with an associated specific power of 764 W kg^{-1} at a specific current of 1 A g^{-1}. At 10 Ag^{-1} the specific energy was 12.4 W h kg^{-1} with an equivalent specific power of 6.6 kW kg^{-1}. The high specific energy and high specific power observed in our device are both linked to the excellent electrochemical performance of the C-V$_2$NO@800°C working in a stable cell potential of 1.8 V.
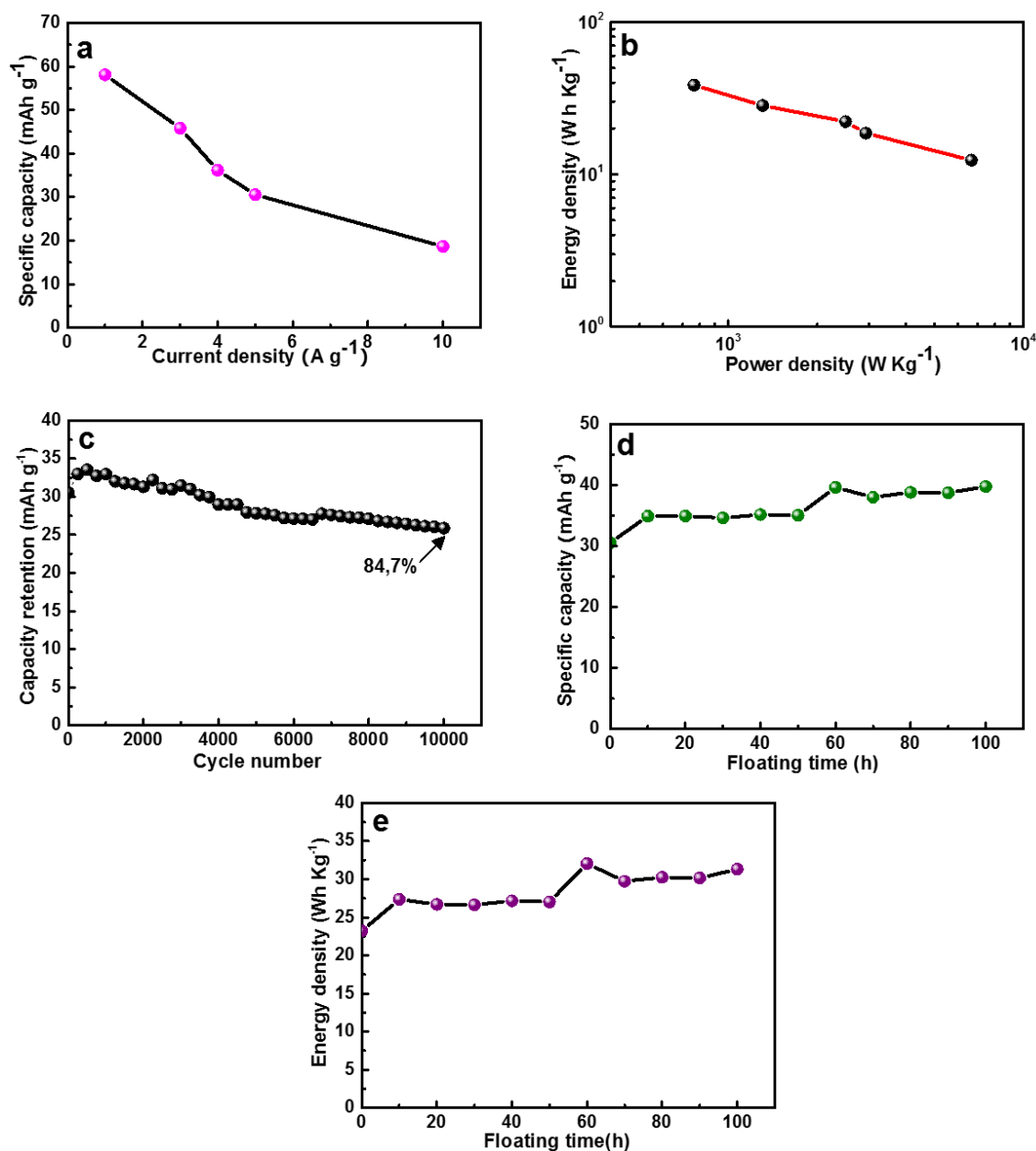
Fig. 9: (a) specific capacity, (b) Ragone plot, (c) stability test showing capacity retention for up to 10000 cycles, (d) specific capacity and (e) energy density as function of holding time at a constant specific current of 10 A g^{-1} up to 100 h of the symmetric device.

To evaluate the device stability of the C-V$_2$NO//C-V$_2$NO, constant cycling (charging-discharging) and voltage holding tests were performed in order to study device degradation with varying set parameters. Fig. 9(c) shows the plot of capacity retention of the symmetric device as a function of cycle number at a high gravimetric current of 10 Ag^{-1}. The cycling

stability presented an excellent capacity retention of 84.7 % up to 10.000 constant charge-discharge cycles, signifying a good electrochemical stability of the device.

The floating test was evaluated after 10.000 stability test at 10 Ag^{-1} with monitoring the specific capacity after very 10 h interval for up to 100 h and the result is shown in Fig. 9(d). A considerable increase in the specific capacity value after 50 h of floating time was observed which was attributed to the increase in accessible redox sites. This appreciable improvement can be seen clearly after calculating the energy density for each voltage holding time as shown in Fig. 9(e). In the first 10 h of voltage holding, the energy density increases by 22% and after 50 h the increase was 23% before stabilizing at a value of 20 W h kg^{-1}, corresponding to an increase of 14% from the original value of 12.4 W h kg^{-1}. These cycling test of the device indicated that the symmetric device showed a good long-term stability without any significant degradation.

4. Conclusion

In this work, the C-V_2NO mesoporous web-like structure were synthesized at different nitridation temperatures of 700 °C, 800 °C and 900 °C using the NH_4VO_3 and $C_3H_6N_6$ as precursors by a facile CVD method, as a novel supercapacitor material. The N_2 physisorption data of the C-V_2NO materials displayed a high specific surface area (SSA) (from 91.6 to 121.6 m^2 g^{-1}) with a pore diameter ranging from ~ 2 to 8 nm. The electrochemical performance of the C-V_2NO evaluated confirmed 800 °C as the optimum synthesis temperature based on the preliminary results obtained. A symmetric capacitor constructed using C-V_2NO@800°C as both positive and negative electrode in a 6 M KOH revealed an specific energy of 38 Wh kg^{-1} with an associated specific power value of 764 W kg^{-1} at a specific current of 1 A g^{-1} in a wide cell potential of 1.8 V. The C-V_2NO//C-V_2NO exhibited a good cycling stability with 84.7% capacity retention up to 10,000 cycles at 10 A g^{-1}.

This excellent stability performance of the device was also confirmed through floating/aging test for up to 100 h exhibiting a further improved device electrochemical performance. The results obtained demonstrate the potential of adopting the C-V$_2$NO as a good electrode material for supercapacitors operated in aqueous electrolytes.

References

[1]   Surendran S, Shanmugapriya S, Shanmugam S, Vasylechko L and Kalai Selvan R 2018 Interweaved Nickel Phosphide Sponge as an Electrode for Flexible Supercapattery and Water Splitting Applications *ACS Applied Energy Materials* **1** 78–92

[2]   Huang P, Lethien C, Pinaud S, Brousse K, Laloo R, Turq V, Respaud M, Demortiere A, Daffos B, Taberna P L, Chaudret B, Gogotsi Y, Simon P, Demortière A, Daffos B, Taberna P L, Chaudret B, Gogotsi Y and Simon P 2016 On-chip and freestanding elastic carbon films for micro-supercapacitors. *Science* **351** 691–5

[3]   Kang Y J, Chung H, Han C-H and Kim W 2012 All-solid-state flexible supercapacitors based on papers coated with carbon nanotubes and ionic-liquid-based gel electrolytes *Nanotechnology* **23** 065401

[4]   Su F and Miao M 2014 Asymmetric carbon nanotube–MnO_2 two-ply yarn supercapacitors for wearable electronics *Nanotechnology* **25** 135401

[5]   Deng L, Zhang G, Kang L, Lei Z, Liu C and Liu Z-H H 2013 Graphene/VO_2 hybrid material for high performance electrochemical capacitor *Electrochimica Acta* **112** 448–57

[6]   Simon P, Gogotsi Y, Simon, Patrice; Gogotsi Y, Simon P and Gogotsi Y 2008 Materials for electrochemical capacitors *Nat. Mater.* **7** 845–854.

[7]   Yu L and Chen G Z 2016 High energy supercapattery with an ionic liquid solution of $LiClO_4$ *Faraday Discuss.* **190** 231–40

[8]   Yu L and Chen G Z 2016 Redox electrode materials for supercapatteries *Journal of Power Sources* **326** 604–12

[9]   Zhi M, Xiang C, Li J, Li M and Wu N 2013 Nanostructured carbon–metal oxide composite electrodes for supercapacitors: a review *Nanoscale* **5** 72–88

[10]   Silversmit G, Depla D, Poelman H, Marin G B and De Gryse R 2004 Determination of the V2p XPS binding energies for different vanadium oxidation states (V^{5+} to V^{0+}) *Journal of Electron Spectroscopy and Related Phenomena* **135** 167–75

[11]   Cherusseri J, Sambath Kumar K, Choudhary N, Nagaiah N, Jung Y, Roy T and Thomas J 2019 Novel mesoporous electrode materials for symmetric, asymmetric and hybrid supercapacitors *Nanotechnology* **30** 202001

[12]   Das B, Behm M, Lindbergh G, Reddy M V. and Chowdari B V R 2014 High performance metal nitrides, MN (M = Cr, Co) nanoparticles for non-aqueous hybrid supercapacitors *Advanced Powder Technology* **26** 1–6

[13]   Arif M, Sanger A and Singh A 2018 Sputter deposited chromium nitride thin electrodes for supercapacitor applications *Materials Letters* **220** 213–7

[14]   Yang P, Chao D, Zhu C, Xia X, Zhang Y, Wang X, Sun P, Tay B K, Shen Z X, Mai W J and Fan H J 2015 Ultrafast-charging supercapacitors based on corn-like titanium nitride nanostructures *Advanced Science* **3** 1500299

[15]   Lu X, Yu M, Zhai T, Wang G, Xie S, Liu T, Liang C, Tong Y and Li Y 2013 High Energy Density Asymmetric Quasi-Solid-State Supercapacitor Based on Porous Vanadium Nitride Nanowire Anode *Nano Letters* **13** 2628–33

[16]   Zhou X, Shang C, Gu L, Dong S, Chen X, Han P, Li L, Yao J, Liu Z, Xu H, Zhu Y, Cui G and Qingdao § † 2011 Mesoporous Coaxial Titanium Nitride-Vanadium Nitride Fibers of CoreÀshell Structures for High-Performance Supercapacitors *ACS Appl. Mater. Interfaces* **3** 3058–63

[17]   Zhao Z-Y, Zhang W-B, Ma X-J, Li K, Zhao Y, Gao J-F, Kang L and Kong L-B 2018 A Novel Capacitive Negative Electrode Material of Fe3N *Nano* **13** 1850002

[18]   Zhu C, Sun Y, Chao D, Wang X, Yang P, Zhang X, Huang H, Zhang H and Fan H J 2016 A 2.0 V capacitive device derived from shape-preserved metal nitride nanorods *Nano Energy* **26** 1–6

[19]   Ghimbeu C M, Raymundo-Piñero E, Fioux P, Béguin F F and Vix-Guterl C 2011 Vanadium nitride/carbon nanotube nanocomposites as electrodes for supercapacitors *Journal of Materials Chemistry* **21** 13268

[20]   Choi D, Blomgren G E and Kumta P N 2006 Fast and Reversible Surface Redox Reaction in Nanocrystalline Vanadium Nitride Supercapacitors *Advanced Materials* **18** 1178–82

[21]   Gao B, Li X, Guo X, Zhang X, Peng X, Wang L, Fu J, Chu P K and Huo K 2015 Nitrogen-Doped Carbon Encapsulated Mesoporous Vanadium Nitride Nanowires as Self-Supported Electrodes for Flexible All-Solid-State Supercapacitors *Advanced Materials Interfaces* **2** 1500211

[22]   Ghosh S, Jeong S M and Polaki S R 2018 A review on metal nitrides/oxynitrides as an emerging supercapacitor electrode beyond oxide *Korean Journal of Chemical Engineering* **35** 1389–408

[23]   Gray B M, Hector A L, Jura M, Owen J R and Whittam J 2017 Effect of oxidative surface treatments on charge storage at titanium nitride surfaces for supercapacitor applications *Journal of Materials Chemistry A* **5** 4550–9.

[24]   An G H, Lee D Y and Ahn H J 2017 Vanadium nitride encapsulated carbon fibre networks with furrowed porous surfaces for ultrafast asymmetric supercapacitors with robust cycle life *Journal of Materials Chemistry A* **5** 19714–20

[25]   Ruan D, Lin R, Jiang K, Yu X, Zhu Y, Fu Y, Wang Z, Yan H and Mai W 2017 High-Performance Porous Molybdenum Oxynitride Based Fiber Supercapacitors *ACS Applied Materials and Interfaces* **9** 29699–706

[26]   Porto R L, Frappier R, Ducros J B B, Aucher C, Mosqueda H, Chenu S, Chavillon B, Tessier F, Cheviré F and Brousse T 2012 Titanium and vanadium oxynitride powders as pseudo-capacitive materials for electrochemical capacitors *Electrochimica Acta* **82** 257–62

[27]   Cheng F, He C, Shu D, Chen H, Zhang J, Tang S, Finlow D E, Shua D, Chen H, Zhang J, Tang S and Finlow D E 2011 Preparation of nanocrystalline VN by the melamine

reduction of V2O5 xerogel and its supercapacitive behavior *Materials Chemistry and Physics* **131** 268–73

[28]   Shu D, Cheng H, Lv C, Asi M A, Long L, He C, Zou X and Kang Z 2014 Soft-template synthesis of vanadium oxynitride-carbon nanomaterials for supercapacitors *International Journal of Hydrogen Energy* **39** 16139–50

[29]   Shu D, Lv C, Cheng F, He C, Yang K, Nan J and Long L 2013 *Enhanced Capacitance and Rate Capability of Nanocrystalline VN as Electrode Materials for Supercapacitors Int. J. Electrochem. Sci* **8** 1209-1225

[30]   Chhowalla M, Ferrari A C, Robertson J and Amaratunga G A J 2000 Evolution of sp2 bonding with deposition temperature in tetrahedral amorphous carbon studied by Raman spectroscopy *Applied Physics Letters* **76** 1419.

[31]   Roy D, Chhowalla M, Wang H, Sano N, Alexandrou I, Clyne T W and Amaratunga G A J 2003 Characterisation of carbon nano-onions using Raman spectroscopy *Chemical Physics Letters* **373** 52–6

[32]   Mohiuddin T M G, Lombardo A, Nair R R, Bonetti A, Savini G, Jalil R, Bonini N, Basko D M, Galiotis C, Marzari N, Novoselov K S, Geim A K and Ferrari A C 2009 Uniaxial strain in graphene by Raman spectroscopy: G peak splitting, Grüneisen parameters, and sample orientation *Physical Review B - Condensed Matter and Materials Physics* **79** 205433

[33]   Barzegar F, Bello A, Momodu D, Madito M J, Dangbegnon J and Manyala N 2016 Preparation and characterization of porous carbon from expanded graphite for high energy density supercapacitor in aqueous electrolyte *Journal of Power Sources* **309** 245–53

[34]   Fabiane M, Madito M J, Bello A and Manyala N 2017 Raman spectroscopy and imaging of Bernal-stacked bilayer graphene synthesized on copper foil by chemical vapour deposition: growth dependence on temperature *Journal of Raman Spectroscopy* **48** 639–46

[35]   Matsoso B J, Ranganathan K, Mutuma B K, Lerotholi T, Jones G and Coville N J 2017 Synthesis and characterization of boron carbon oxynitride films with tunable composition using methane, boric acid and ammonia *New Journal of Chemistry* **41** 9497–504

[36]   Yu J, Wang G, Cheng B and Zhou M 2007 Effects of hydrothermal temperature and time on the photocatalytic activity and microstructures of bimodal mesoporous TiO_2 powders *Applied Catalysis B: Environmental* **69** 171–80

[37]   Wang Z, Li Z and Zou Z 2015 Application of binder-free TiO_xN_{1-x} nanogrid film as a high-power supercapacitor electrode *Journal of Power Sources* **296** 53–63

[38]   Hryha E, Rutqvist E and Nyborg L 2012 Stoichiometric vanadium oxides studied by XPS *Surface and Interface Analysis* **44** 1022–5

[39] Ferran Urena-Begara, Aurelian Crunteanu and Raskin J-P 2017 full-textRaman and XPS characterization of vanadium oxide thin films with temperature *Applied Surface Science* **403** 717–727

[40] Marton D, Boyd K J, Al-Bayati A H, Todorov S S and Rabalais J W 1994 Carbon nitride deposited using energetic species: A two-phase system *Physical Review Letters* **73** 118–21

[41] Sevilla M and Fuertes A B 2009 The production of carbon materials by hydrothermal carbonization of cellulose *Carbon* **47** 2281–9

[42] Rantho M N N, Madito M J J and Manyala N 2018 Symmetric supercapacitor with supercapattery behavior based on carbonized iron cations adsorbed onto polyaniline *Electrochimica Acta* **262** 82–96

[43] Mutuma B K, Matsoso B J, Ranganathan K, Keartland J M, Wamwangi D and Coville N J 2017 Generation of radical species in CVD grown pristine and N-doped solid carbon spheres using H $_2$ and Ar as carrier gases *RSC Advances* **7** 21187–95

[44] Hong Z, Shen B, Chen Y, Lin B and Gao B 2013 Enhancement of photocatalytic H$_2$ evolution over nitrogen-deficient graphitic carbon nitride *Journal of Materials Chemistry A* **1** 11754

[45] Fang J, Fan H, Li M and Long C 2015 Nitrogen self-doped graphitic carbon nitride as efficient visible light photocatalyst for hydrogen evolution *Journal of Materials Chemistry A* **3** 13819–26

[46] Dwivedi N, Kumar S, Carey J D, Malik H K and Govind 2012 Photoconductivity and characterization of nitrogen incorporated hydrogenated amorphous carbon thin films *Journal of Applied Physics* **112** 113706

[47] Liu Y, Liu L, Tan Y, Kong L, Kang L and Ran F 2018 Well-Dispersed Vanadium Nitride on Porous Carbon Networks Derived from Block Copolymer of PAN-b-PDMC-b-PAN Absorbed with Ammonium Metavanadate for Energy Storage Application *Journal of Physical Chemistry C* **122** 143–9

[48] Levchik S V., Balabanovich A I, Levchik G F and Costa L 1997 Effect of melamine and its salts on combustion and thermal decomposition of polyamide 6 *Fire and Materials* **21** 75–83

[49] Twu J, Shih C-F, Guoa T-H and Chenb K-H 1997 Raman spectroscopic studies of the thermal decomposition mechanism of ammonium metavanadate *J. Mater. Chem.* **7 (11)** 2273–2277

[50] Selim S A, Philip C A and Mikhail R S 1980 Thermal decomposition of ammonium metavanadate *Thermochimica Acta* **36** 287–97

[51] Brown M E, Glasser L and Stewart B V 1974 The thermal decomposition of ammonium metavanadate II The kinetics and mechanism of the decomposition *Journal of Thermal Analysis* **6** 529–514

4.4.3 Concluding Remarks

The C-V$_2$NO mesoporous web-like structure was successfully synthesized at different nitridation temperatures of 700 °C, 800 °C and 900 °C using the NH$_4$VO$_3$ and C$_3$H$_6$N$_6$ as precursors by a facile hydrothermal method, as a novel supercapacitor material.

The N$_2$ physisorption data of the C-V$_2$NO materials displayed a high specific surface area (SSA) (from 91.6 to 121.6 m^2 g^{-1}) with a pore diameter ranging from ~ 2 to 8 nm.

The electrochemical performance of the C-V$_2$NO evaluated confirmed 800 °C as the optimum synthesis temperature based on the preliminary results obtained. A symmetric capacitor constructed using C-V$_2$NO@800°C as both positive and negative electrode in a 6 M KOH revealed a specific energy of 38 Wh kg^{-1} with an associated 764 W kg^{-1} specific power value at a specific current of 1 A g^{-1} in a wide cell voltage of 1.8 V. The C-V$_2$NO//C-V$_2$NO exhibited a good cycling stability with 84.7% capacity retention up to 10,000 cycles at 10 A g^{-1}. The results obtained demonstrate the potential of adopting the C-V$_2$NO as a new good electrode material for supercapacitors operated in aqueous electrolytes.

4.5 High-performance asymmetric supercapacitor based on vanadium dioxide/activated expanded graphite composite and carbon-vanadium oxynitride nanostructures

4.5.1 Introduction

In the literature, numerous researchers focus the synthesis of composite materials comprising of vanadium dioxide (VO_2) with activated carbon, graphene and carbon nanotubes to improve the electrochemical performance of the VO_2. The use of activated expanded graphite (AEG) has been rarely explored for supercapacitor applications.

In this work, we report on the synthesis of a vanadium dioxide/activated expanded graphite composite (VO_2/AEG) as an electrode material in supercapacitors. The VO_2/AEG materials were obtained by a facile CVD process. The distribution of the VO_2 rods on the AEG surface leads to an enhanced interaction which maximizes the electrochemically accessible area.

This good integration yields good electrochemical performance by providing efficient channels for charge and ionic transport. An asymmetric supercapacitor was assembled by combining the VO_2/AEG composite as a positive electrode and C-V_2NO@800°C (C-V_2NO) as a negative. The device displayed high specific energy of 41.6 W h kg^{-1} associated with a specific power of 904 W kg^{-1} at a specific current of 1 A g^{-1} and capacity retention of 93% up to 10,000 cycles.

4.5.2 Result and discussion

The results obtained of the asymmetric device assembled used VO_2/AEG composite and C-V_2NO electrodes are presented in the paper below:

High-performance asymmetric supercapacitor based on vanadium dioxide/activated expanded graphite composite and carbon-vanadium oxynitride nanostructures

Ndeye M. Ndiaye [a, b], Ndeye F. Sylla [a, b], Balla D. Ngom [b], Farshad Barzegar [c], Damilola Momodu [a], Ncholu Manyala [a, *]

[a] Department of Physics, Institute of Applied Materials, SARChI Chair in Carbon Technology and Materials, University of Pretoria, Pretoria, 0028, South Africa
[b] Laboratoire de Photonique Quantique d'Energie et de NanoFabrication, Groupe de Physique du Solide et Science des Matériaux, Département de Physique FST-UCAD BP, 5005, Dakar-Fan, Dakar, Senegal
[c] Electrical, Electronic and Computer Engineering Department, University of Pretoria, Pretoria, 0002, South Africa

ABSTRACT

The vanadium dioxide/activated expanded graphite (VO_2/AEG) composite and carbon-vanadium oxynitride ($C-V_2NO$) porous web-like structures were successfully synthesized by chemical vapor deposition (CVD) method. The X-ray diffraction analysis of the VO_2/AEG composite revealed the diffraction peaks of the monoclinic VO_2 and hexagonal AEG structures respectively while for the $C-V_2NO$ material, a cubic crystal structure was observed. The Raman spectroscopy analysis of VO_2/AEG composite and $C-V_2NO$ depicted vibration brands linked to vanadium dioxide with the distinct D, G, and D' peaks confirming the presence of disordered carbon into the main vanadium-based matrix. The electrochemical performance of the electrode material (VO_2/AEG//$C-V_2NO$) was evaluated in a two-electrode asymmetric device with the VO_2/AEG composite as the positive electrode and $C-V_2NO$ as the negative electrode operating in a 6 M KOH electrolyte. The asymmetric device exhibited a specific energy of 41.6 Wh kg^{-1} with a corresponding specific power of 904 W kg^{-1} at a 1 A g^{-1} specific current in a large operating voltage of 1.8 V. The specific energy was still retained at 9 Wh kg^{-1} at an amplified specific current of 20 A g^{-1} with a specific power of 18 kW kg^{-1}. The supercapacitor showed a 93% capacity retention for up to 10,000 constant gravimetric current cyclic stability test at a specific current of 10 A g^{-1} with a good rate capability. A notable device stability was maintained without any failure via voltage floating tests for up to 100 h.

© 2019 Elsevier Ltd. All rights reserved.

1. Introduction

Supercapacitors also known as electrochemical capacitors (ECs) have been known to be great candidates for the future generation of energy storage [1–3]. ECs are high power devices which can store and deliver energy relatively faster than batteries [4]. Currently, the spotlight is on these devices due to their application merits which include their high power density, long cycle life and safety [5]. Although supercapacitors still suffer low energy density as compared to batteries [6], they have higher energy density than conventional capacitors [7–9].

Generally, supercapacitors are mainly classified into three classes based on their energy storage mechanism; the Electrochemical Double Layer Capacitors (EDLCs) are the first class which arise from the accumulation of charges at the electrode/electrolyte interface [6]. EDLC storage behavior is mainly exhibited in carbon-based materials. The pseudocapacitors and faradaic capacitors are next class which are governed by a chain of Faradaic reactions which store the charges via redox reactions. Common materials in this class of supercapacitors include transition metal oxides, hydroxides (TMOs/TM-OHs) and redox polymers. Lastly, the hybrid capacitors that are considered as a combination of both EDLC and Faradaic materials [10]. In this storage category, the materials usually exist combined mechanisms as either a composite material or separate individual electrodes in non-symmetric device architecture. The positive electrode is composed of metal oxides/hydroxide [11–14] and conductive polymers [15,16] that give higher specific capacity [8,10] than the negative electrode which is usually

made up of EDLC consisting of carbon-based materials. Activated carbon (AC) [17,18], carbon nanotubes (CNT) [19], graphene [20,21] and carbon nitride/oxynitride-based nanostructures are examples of materials which have been successfully used in these devices [22–24]. These carbon nanomaterials possess high specific surface area, good electronic conductivity, and long cycle stability [25–27] as compared to faradaic materials.

Asymmetric capacitors (AsyCs) are considered as a subclass of hybrid capacitors obtained by combining two different materials as a positive and an negative electrodes in the same cell. AsyCs are considered as a promising candidate and reliable approach to maximizing the specific capacitance and to extend the cell potential in order to improve the energy density [28].

Among all transition metal oxides, vanadium oxides family such as vanadium dioxide (VO_2) vanadium pentoxide (V_2O_5) and divanadium trioxide V_2O_3 have received great consideration in energy storage devices [29–38] due to their multiple oxidation states, low cost and non-toxic chemical properties [39,40]. In addition Vanadium dioxide (VO_2) has been largely studied as a potential electrode material in ECs due to its structural stability [39] and excellent reactivity [41]. However, as all metal oxides, VO_2 also displays a poor electrical conductivity and cyclic stability as compared to carbon-based materials [42]. Numerous scholars have studied different methods with an aim to improve the electrochemical performance of the VO_2 materials. For instance, the synthesis of carbon/VO_2 composite materials such as graphene/VO_2 [39], VO_2/CNTs [40] and VO_2@PANi [43] have been recently explored as an electrodes for electrochemical capacitors. Carbon/VO_2 composites have been demonstrated as suitable electrode materials to enhance the electrochemical properties of supercapacitors owing to their synergistic properties but most studies focus on either the positive electrode or negative electrode alone. For instance, Chen et al. [44] assembled an asymmetric supercapacitors by considering a CNT/V_2O_5 nanowire composite as a negative electrode and AC as a positive electrode in an organic electrolyte. The asymmetric capacitor showed a specific energy of

40 W h kg^{-1} at a power density of 210 W kg^{-1} at 0.5 mA cm^{-2} [44]. Recently, Zhou et al. [45] fabricated an asymmetric device where a bamboo-like V_2O_5/polyindole@activated carbon cloth (V_2O_5/PIn@ACC) was used as a positive electrode whereas a reduced graphene oxide@activated carbon cloth (rGO@ACC) was employed as a negative electrode.

The asymmetric capacitor displayed a specific energy of 38.7 W h kg^{-1} at the power density of 900 W kg^{-1} by using a specific current of 1 A g^{-1} [45]. Fleischmann et al. [46] successfully fabricated an asymmetric capacitor by using an AC as a positive electrode and vanadium oxide/carbon onion (VO_2/OLC) composite as a negative electrode with 1 M LiClO$_4$ in acetonitrile (ACN) electrolyte. The asymmetric device exhibited a specific energy of 45 W h kg^{-1} and a specific power of 58 kW kg^{-1} at 0.05 A g^{-1} [46]. Similarly, Hosseini et al. [47] assembled an asymmetric device by adopting a VO_2 nanosheet array grown on porous carbon nanofibers (VO_2@PCNFs) as a positive electrode and a porous carbon nanofibers (PCNFs) as a negative electrode in Na$_2$SO$_4$ poly(vinyl alcohol) (Na$_2$SO$_4$/PVA) gel electrolyte. The asymmetric capacitor displayed a specific energy of 75.06 W h kg^{-1} and a specific power of 1.275 kW kg^{-1} at a specific current of 1 A g^{-1} [47]. No studies have considered the use of vanadium oxides/carbon composites in both electrodes for an asymmetric design with the idea of harnessing both the porosity and conductivity known to carbon-based materials.

In this paper, we report a novel design of a vanadium dioxide/activated expanded graphite composite (VO_2/AEG) and carbon-vanadium oxynitride (C-V_2NO) porous web-like structures produced by the CVD method. The outstanding electrochemical

performance of porous AEG reported in our previous work [48] inspired its introduction into the VO_2 main frame to create a good interaction between VO_2 and AEG using a facile method.

On the other hand, the C-V_2NO displayed a specific surface area value of 121.6 m^2 g^{-1} and a unique morphology with irregular porous cavities which could deliver a good electrochemical performance in supercapacitors. An AsyC was assembled by combining the merits of both materials based on VO_2/AEG composite as a positive electrode and C-V_2NO as a negative. The device displayed high specific energy of 41.6 W h kg^{-1} associated with a specific power of 904 W kg^{-1} at a specific current of 1 A g^{-1} and capacity retention of 93% up to 10,000 cycles.

2. Experimental

Ammonium metavanadate (NH$_4$VO$_3$, purity 99%), Melamine (C$_3$H$_6$N$_6$, purity 99%), Hydrochloric acid (HCl, 37% AR grade) and 10 wt% Polyvinylpyrrolidone (PVP) were purchased from Sigma-Aldrich and used without further purification. Polycrystalline Nickel foam (NiF) (3D scaffold template with an areal density of 420 g m^{-2} and a thickness of 1.6 mm was purchased from Alantum (Munich, Germany). Potassium hydroxide (KOH, min 85%) was purchased from Merck (South Africa). Graphite grade ES 250 B5 was obtained from Qingdao Kropfmuehl Graphite of 10 wt%.

2.1. Synthesis technique

2.1.1. Synthesis of AEG and VO2 materials
Activated expanded graphite (AEG) was prepared from the expanded graphite (EG) using a microwave-assisted method. The EG was carbonized by using a CVD method at 800 °C under argon and hydrogen for 2 h to obtain the final product. The detailed description of AEG is previously reported by Barzegar et. al [48]. The vanadium dioxide (VO_2) was synthesized by a temperature CVD-assisted route at 900 °C for 2 h under nitrogen (N$_2$) atmosphere. The detailed description of VO_2 is presented in the report by Ma et al. [49].

2.1.2. Synthesis of VO2/AEG composite
The VO_2/AEG composite was prepared by simply mixing 1.8 g of NH$_4$VO$_3$ and 90 mg of AEG in an agate mortar. The mixture was inserted into a quartz tube furnace and heated to 900 °C at a heating rate of 2 °C min^{-1} and kept at that temperature for 2 h under nitrogen (N$_2$) atmosphere. After cooling down to room temperature under a flow of nitrogen, the resulting black powder was ground in an agate mortar to obtain the final product.

2.1.3. Synthesis of C-V2NO nanostructures
The C-V_2NO was synthesized following a similar process as that of the VO_2/AEG composite as follows: 0.5 g of NH$_4$VO$_3$ and 5 g of C$_3$H$_6$N$_6$ were mixed in an agate mortar with a few drops of ethanol to make a homogeneous slurry. The slurry was subsequently calcined in a tube furnace from room temperature to 800 °C at a heating rate of 18 °C min^{-1} and left to dwell at this temperature for 2 h under nitrogen (N$_2$) atmosphere. After naturally cooling down, the final carbon-vanadium oxynitride product was obtained.

2.2. Structural and morphological characterization

The X-ray diffraction (XRD) patterns for the VO_2/AEG composite and the C-V_2NO materials were recorded using a XPERT-PRO diffractometer (PANalytical BV, Netherlands, CoKα ($\lambda = 0.178,901$ nm) radiation) with 2θ values ranging from 10°–90°. The Raman spectroscopy measurements of the materials were studied using a WITec confocal Raman microscope (WITec

alpha300 R, Ulm Germany) with a 532 nm laser wavelength and a spectral acquisition time of 60 s. The Raman system laser power was set as low as 5 mW in order to minimize heating effects. The porosimetry test of the materials was evaluated with a nitrogen adsorption−desorption isotherms at −196 °C using a Micromeritics ASAP 2020. The specific surface area of the materials were evaluated by the Brunauer−Emmett−Teller (BET) analysis from the adsorption branch in the relative pressure range (P/P0) of 0.01−1.0. The morphology and the element distribution mapping of the composite and the carbon-vanadium oxynitride were characterized using a high-resolution Zeiss Ultra plus 55 field emission scanning electron microscope (FE-SEM), operated at a voltage of 2.0 kV and a JEOL JEM-2100F high resolution transition electron microscope (HRTEM) at 200 kV. The X-ray photoelectron spectroscopy (XPS, K-alpha, Thermo Fisher) was used to analyse the elemental composition of the materials with a monochromatic Al-Kα radiation.

2.3. Electrodes preparation and electrochemical characterization

The VO$_2$, VO$_2$/AEG composite and carbon-vanadium oxynitride electrodes were prepared by mixing 80 wt% of the active material with 10 wt% of carbon black (as conducting additive) and 10 wt% of polyvinylidene difluoride (PVDF) binder in an agate mortar. The mixture was then dissolved with a few drops of 1-methyl-2-pyrrolidinone (NMP) to form a slurry which was coated onto NiF current collectors with an area of 1×1 cm^2. The electrodes were dried at 60 °C for 12 h to ensure complete evaporation of the NMP.

The electrochemical properties of the VO$_2$, VO$_2$/AEG composite and C-V$_2$NO electrodes were evaluated using a Bio-Logic VMP-300 (Knoxville TN 37,930, USA) controlled by the EC-lab V 11.40 software in a three (half-cell) electrode configuration. Ag/AgCl (KCl saturated) as reference electrode, a glassy carbon plate as counter electrode and VO$_2$/AEG composite and C-V$_2$NO electrodes as working electrodes were used to investigate the electrochemical measurements in a 6 M KOH aqueous electrolyte.

The asymmetric device was fabricated using VO$_2$/AEG composite as a positive and C-V$_2$NO as a negative electrodes respectively in 6 M KOH electrolyte. The VO$_2$/AEG//C-V$_2$NO was assembled in a Swagelok cell with a microfiber filter paper as a separator.

The cyclic voltammetry (CV) measurements were carried out to determine the behavior of the VO$_2$/AEG and C-V$_2$NO electrodes and their ideal working potential in three- and -two configurations cell. The galvanostatic charge-discharge (GCD) measurements aid to obtain the specific capacity and the stability test of the VO$_2$/AEG and C-V$_2$NO electrodes.

The electrochemical impedance test was used to investigate the capacitive properties and conductivity of the VO$_2$/AEG and C-V$_2$NO electrodes in the frequency range of 100 kHz−10 mHz in open circuit voltage. All the electrochemical tests were performed at room temperature.

2.3.1. Structural and morphological properties

X-ray diffraction (XRD) analysis results of VO$_2$/AEG composite and C-V$_2$NO materials are presented in Fig. 1. The XRD patterns of VO$_2$/AEG composite (Fig. 1(a)) showed diffraction peaks of the VO$_2$ and AEG materials confirming a stable composite of AEG with the VO$_2$ material.

The XRD patterns of the VO$_2$ material can be indexed to a VO$_2$ monoclinic structure (black indices in the Fig. 1(a)) with a *P1 2$_1$/c(14)* space group and lattice parameters; $a = 5.3532$ Å, $b = 4.5380$ Å, $c = 5.3830$ Å, and $\beta = 115.2°$ using the matching inorganic crystal structure database (ICSD) card #4033. However, Fig. 1(a) also shows a satellite peaks located at 17.6 and 20.5 which correspond to trace amounts of V$_6$O$_{13}$ [48]. The diffraction peaks of the AEG in Fig. 1(a) exhibited a hexagonal structure which can be indexed to the (002), (100), (101), (102), (004) and (103) planes of the graphite labelled blue in the figure, with a *P6$_3$/mmc* space group. The lattice parameters in this case were given as $a = 2.4704$ Å, $b = 2.4704$ Å, $c = 6.7244$ Å, $ã = 120.0°$ using the matching inorganic crystal structure database (ICSD) card #1487.

In Fig. 1(b), the XRD patterns of C-V$_2$NO were indexed to a cubic structure with a single phase with the diffraction peaks corresponding to (111), (200) and (220). An *Fm-3m(225)* space group with lattice parameters $a = 4.1313(1)$ Å, $a/b = 1.0000$, $b/c = 1.0000$ and $c/a = 1.0000$ was obtained with the matching inorganic crystal structure Database (ICSD) card # 43,182.

The Raman spectroscopy of the VO$_2$/AEG composite and C-V$_2$NO materials were used to identify different phases at the molecular level.

The Raman vibrational modes of the VO$_2$ material are located at 139, 194, 287, 410, 527, 688 and 1000 cm^{-1} wavenumbers as shown in Fig. 2(a). At wavenumber ranging from 100 to 400 cm^{-1}, the V−O−V bending modes are observed. At 400−800 cm^{-1} wavenumber range, the bands recorded are attributed to the V−O−V stretching modes. The Raman bands located at 800−1100 cm^{-1}, are attributed to the V=O stretching modes which are linked to the monoclinic VO$_2$ (M) [50−52]. The Raman vibrational modes of the VO$_2$ material have been assigned to well-known vibrational modes of the material except for the 527 cm^{-1} (B$_g$ species) as shown in Table 1 [53]. The band at 1000 cm^{-1} is attributed to the stretching of the V=O arising from the typical bands of V$_2$O$_5$. This revealed the presence of the V$_2$O$_5$ in the composite material [54].
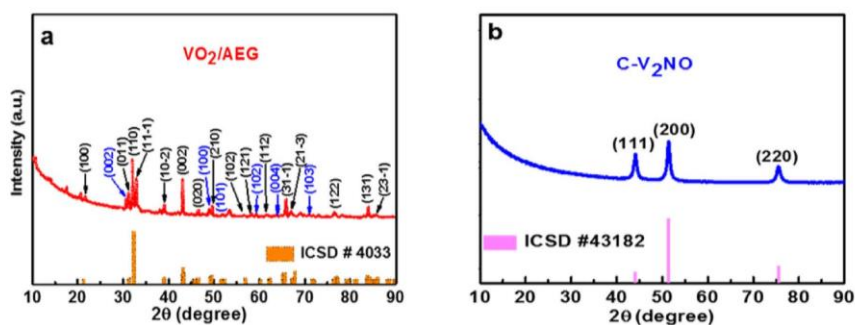

Fig. 1. The XRD patterns of (a) VO$_2$/AEG composite (with black and blue indexes for VO$_2$ and AEG (carbon peaks) respectively) and (b) C-V$_2$NO nanostructures.
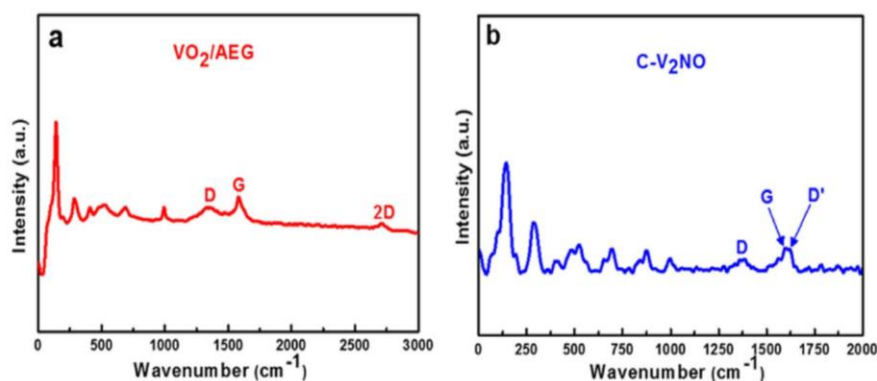
Fig. 2. The Raman spectra of the (a) VO$_2$/AEG composite and (b) C-V$_2$NO nanostructures.

Table 1
Raman modes of VO$_2$ [53].

Raman frequency (cm^{-1})	Vibration assignment
139	A$_g$
194	A$_g$
287	A$_g$
410	A$_g$
527	B$_g$
688	A$_g$

Fig. 2(a) also shows three peaks at 1349, 1583 and 2710 cm^{-1} which are attributed to the D-band (linked to defects or the disorders present in the carbon lattice structure [55,56]), G-band (carbon-carbon vibration mode [55,57]) and the 2D-band (originating from the double resonance process) band of AEG, respectively [48]. All these confirm the presence of both AEG and VO$_2$ materials in the composite.

In Fig. 2(b), the Raman bands indicated that different vanadium species are formed during the growth of the carbon-vanadium oxynitride materials. For instance, the Raman bands at 145, 285 and 479 cm^{-1} confirm the existence of V$_2$O$_5$ and VO$_2$ respectively, in the metal oxynitride–carbon. The high-intensity peak at 142 cm^{-1} wavenumbers is linked to the bending vibration (B$_{3g}$ species) associated with the layered structure [58]. The Raman band located at 285 cm^{-1} is due to the bending vibrations of O-V-O bond (B$_{2g}$ mode) while for the 479 cm^{-1} is attributed to the

stretching of the V–O–V (B$_g$) [59–61]. In addition, these two high intensities peaks at 145 cm^{-1} and 285 cm^{-1} could be associated with the cubic symmetry of the vanadium oxynitride [62].

However, it also showed a D peak at 1373 cm^{-1}, G peak at 1593 cm^{-1} and D′-peak at 1621 cm^{-1}. The D′-peak observed near the G peak showed that the carbon present in the C-V$_2$NO is a graphene-like carbon. The D′ peak is attributed to the lattice vibration of the G band but mainly due to the graphene layers at the surface of the carbon material present in the material [48,63].

The presence of the three peaks (D, G, and D′) confirmed the presence of the carbon element in the as-prepared carbon-vanadium oxynitride.

The specific surface area of the VO$_2$, VO$_2$/AEG composite and the C-V$_2$NO materials were determined by the BET method. Fig. 3 and Fig. S1 display the nitrogen adsorption-desorption isotherm of the materials.

In Fig. 3(a) and Fig.S1, a type III isotherm with an H3 hysteresis loop was depicted for the VO$_2$ and VO$_2$/AEG composite which indicated a weak interaction between the N$_2$ adsorbent and the material. The C-V$_2$NO in Fig. 3(b) shows a type IV isotherm with H3 hysteresis which is indicative of a mesoporous structure. These hysteresis behavior of the materials indicated non-rigid aggregates of plate-like particles or assemblages of slit-shaped pores [64]. The specific surface areas (SSA) recorded for VO$_2$, VO$_2$/AEG composite and the C-V$_2$NO materials were 1.5 m^2 g^{-1}, 4.6 m^2 g^{-1} and 121.6 m^2 g^{-1}, respectively.

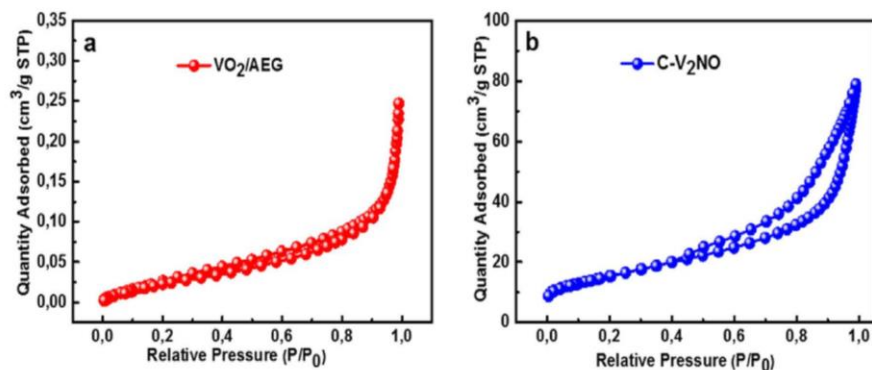As compared to VO$_2$, the high SSA of VO$_2$/AEG composite can be

Fig. 3. The N$_2$ absorption/desorption isotherms of (a) VO$_2$/AEG composite and (b) C-V$_2$NO nanostructures.

184

attributed to the presence of AEG in the network VO_2 which could facilitate the formation of polycrystalline islands and channels. For the C-V_2NO material, the value of the SSA is higher as compared to other vanadium-based oxynitride materials [65,66] which could be associated to the mesoporous structure.

The morphology analysis of the VO_2/AEG composite and C-V_2NO materials is presented in Fig. 4 by scanning electron microscopy (SEM). The SEM micrograph of the pristine VO_2 sample revealed a rod morphology with an agglomerated particles (Fig. S2).

Fig. 4(a) shows the network of an interconnected sheet-like structure of the AEG [48] and the structure of VO_2, respectively. Fig. 4(b) presents the SEM morphology of the VO_2/AEG composite which displays clearly the VO_2 rods grown on the surface of the activated expanded graphite (AEG) sheet-like structure. The VO_2 rods on the surface of the AEG showed a non-uniform structure with an agglomerated rods. The distribution of the VO_2 rods on the AEG surface leads to an enhanced interaction which maximizes the electrochemically accessible area that yields a good electrochemical performance in supercapacitors by providing efficient channels for charge and ionic transport.

The morphology of the C-V_2NO in Fig. 3(c and d) showed a web-like structure with irregular porous cavities. As seen, the surface morphology of the C-V_2NO showed the agglomeration of porous granular with an interconnected network with cavities to form a web-like structure which aids electrolyte efficient penetration [67].

Fig. 5 presented the element distribution mapping of the composite and the web-like C-V_2NO nanostructures. It displayed the presence of V, C and O atoms in the VO_2/AEG composite while for the C-V_2NO, shows V, C, O, and N atoms in the materials. The Fig. 5 (a - d) clearly indicates that all the elements in these composites are uniformly distributed.

The TEM images were further used to study the morphology of the VO_2/AEG composite and C-V_2NO materials in Fig. 5. The TEM micrograph of the VO_2/AEG composite in Fig. 5(a) shows an overlapping of the AEG sheet-like structure and the rods morphology of VO_2(M). The VO_2(M) rods are verified by using high-resolution TEM (inset to Fig. 5 (a)). The HRTEM revealed the crystallinity structure of the VO_2(M) with clear lattice fringes. The interplanar spacing is 3.3 Å which corresponded to the (011) lattice planes, further confirming the existence in VO_2 (M) in the composite material [68].

In Fig. 5(b), the micrograph of the C-V_2NO at low and high magnification (inset to Fig. 5 (b)) showed clearly the presence of the porous structure which confirms the observations from SEM analysis.

The surface characterization of both materials was further investigated by using the X-ray photoelectron spectroscopy (XPS) as shown in Fig. 6. The chemical states of both materials are quantitatively evaluated to determine the amount of active vanadium, nitrogen, oxygen and carbon content in the materials. Fig. 6 (a) and (b) display the wide scan XPS spectrum of the as-received VO_2/AEG composite and C-V_2NO@800 °C materials respectively.

The core level of V$2p_{3/2}$ from the VO_2/AEG composite exhibited three peaks as shown in Fig. 6 (c). The high binding energy at 516.5 eV suggests that the oxidation state of the composite is predominantly V^{4+} which confirm the formation of VO_2 [69]. The other peaks located at 516.9 eV and 517.7 eV were attributed to the mixed-valence of the vanadium ions (V^{4+} and V^{5+} respectively) of the satellite V_6O_{13} [70,71]. The XPS spectrum clearly shows that the phase synthesized herein is VO_2 with a trace presence of V_6O_{13}.

In Fig. S3, the XPS signal of the N1s from the C-V_2NO@800 °C was deconvoluted into a three peak Gaussian components. The peak at 397.3 eV binding energy value was attributed to N from vanadium nitride. The other two peaks at 399.4 eV and 400.5 eV were assigned to the pyrrolic-N and graphitic-N, respectively.

The V$2p_{3/2}$ binding energies of the C-V_2NO@800 °C is presented in Fig. 6(d). The core level of V$2p_{3/2}$ reveals four peaks located at
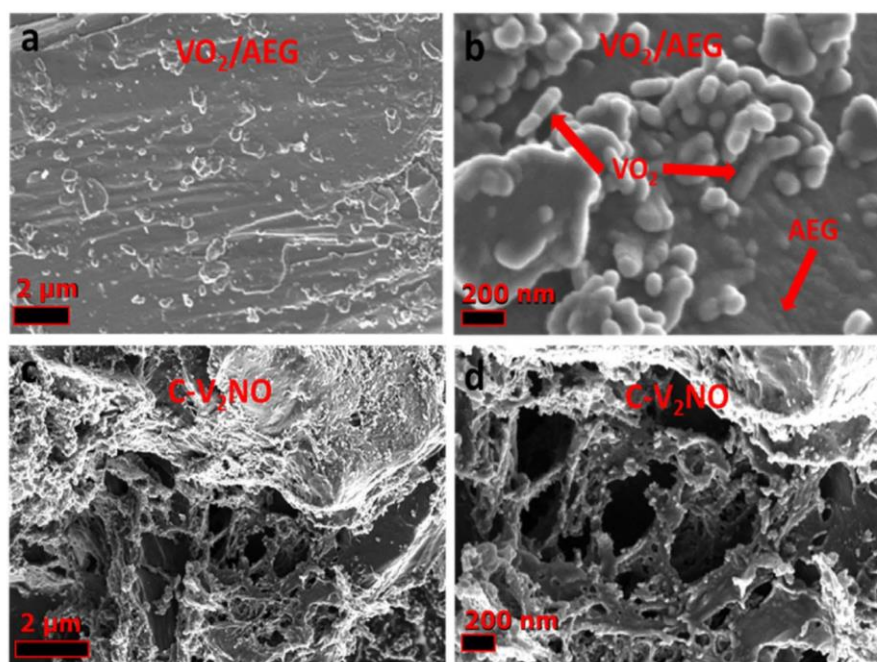

Fig. 4. The SEM images of the as-synthesized (a–b) VO_2/AEG composite and (c–d) C-V_2NO nanostructures.
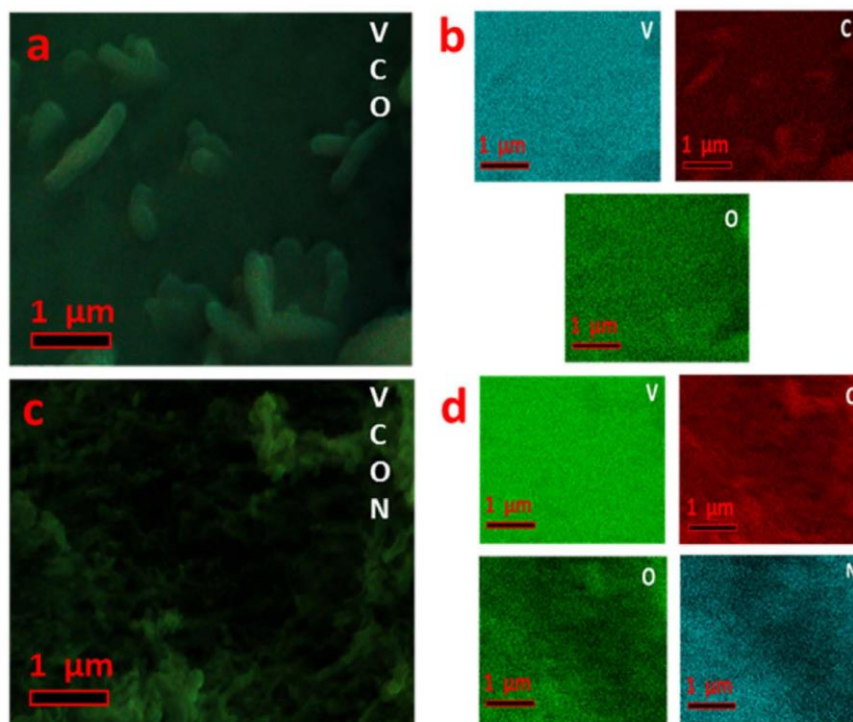
185

Fig. 5. (a) VO₂/AEG composite elemental mapping, (b) distribution of individual elements in the VO₂/AEG composite, (c) C-V₂NO elemental mapping and (d) distribution of individual elements in the C-V₂NO.
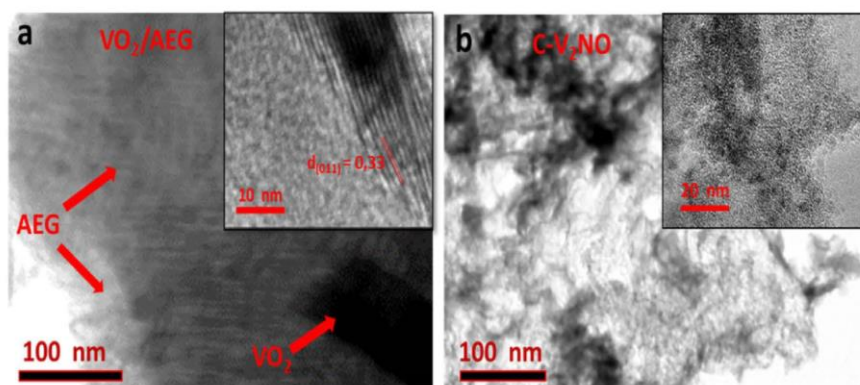

Fig. 6. The TEM images of the synthesized (a) VO₂/AEG composite (the inset is the HRTEM of the composite material) and (c) C-V₂NO nanostructures (the inset shows the HRTEM).

513.7 eV, 515.5 eV, 516.5 eV and 517.7 eV which are ascribed to the vanadium ions V^{2+}, V^{3+}, V^{4+} and V^{5+} respectively [72,73].

Fig. 6 (e) and (f) show the fitted core level spectrum of C1s of both materials. The high binding energy peaks of VO₂/AEG composite (at 284.4 eV) and C-V₂NO@800 °C (at 284.6 eV) correspond to the sp^2 C = C bond which confirms the predominant content of graphitic carbon in the material [74,75]. The peaks located at 285.2 eV for VO₂/AEG composite and 285.5 eV for C-V₂NO@800 °C were ascribed to the carbon (C) sp^3 linked to the nitrogen (N) or the vanadium (V) atoms [76,77]. The low binding energy peaks of VO₂/AEG composite (at 286.3 eV) and C-V₂NO@800 °C (at 288.2 eV) are attributed to the sp^3 C-O bonding structures [78,79].

2.3.2. Electrochemical performances of VO₂/AEG//C-V₂NO

2.3.2.1. Electrochemistry of the VO₂/AEG and C-V₂NO. Electrochemistry involves charge transfer between two electrodes (positive and negative electrodes), and an interconnecting electrolyte [80]. The chemical reaction arises at the electrode/electrolyte interface which can either be driven by electrical energy or yield electrical energy. The electrode materials in electrochemistry must have the ability to possess high electronic conductivity while the electrolyte should have a low electronic conductivity with high ionic conductivity [81]. A typical design to realize the electrochemical measurements is by using a so-called three (3)-electrode configuration setup. It is adopted to minimize the energy lost in the

system by reducing the distance between the components [82]. Generally, the operation of electrochemical capacitors is determined by the type of electrode material used. In this work, faradaic materials were used and thus, the mode of charge storage was based on redox reactions. All the electrochemical measurements were evaluated in 6 M KOH with a high ionic conductivity (i.e. 73.5 and 198 Scm^2mol^{-1} for K^+ and OH^-, respectively [83]), and VO_2, VO_2/AEG and C-V_2NO were used as electrode materials. The mechanism reaction of the VO_2 electrode in 6 M KOH is based on this equation:

$$VO_2 + OH^- \leftrightarrow VO_2(OH) + e^- \qquad (1)$$

The VO_2/AEG and C-V_2NO materials have higher electronic

conductivities than the VO_2 sample. This is linked to the presence of carbon in the materials which could increase the specific surface area enhancing the electrochemical performance of the VO_2 materials.

2.3.3. Three (3)-electrode configuration of the VO_2/AEG composite and C-V_2NO electrodes

In three electrode configuration, the electrochemical measurements of the VO_2/AEG composite and C-V_2NO electrodes were evaluated using 6 M KOH as an aqueous electrolyte.

As seen in Fig. S4 (supporting information), the VO_2/AEG composite exhibited higher current response and specific capacity as a function of the specific current than the pristine material. It also
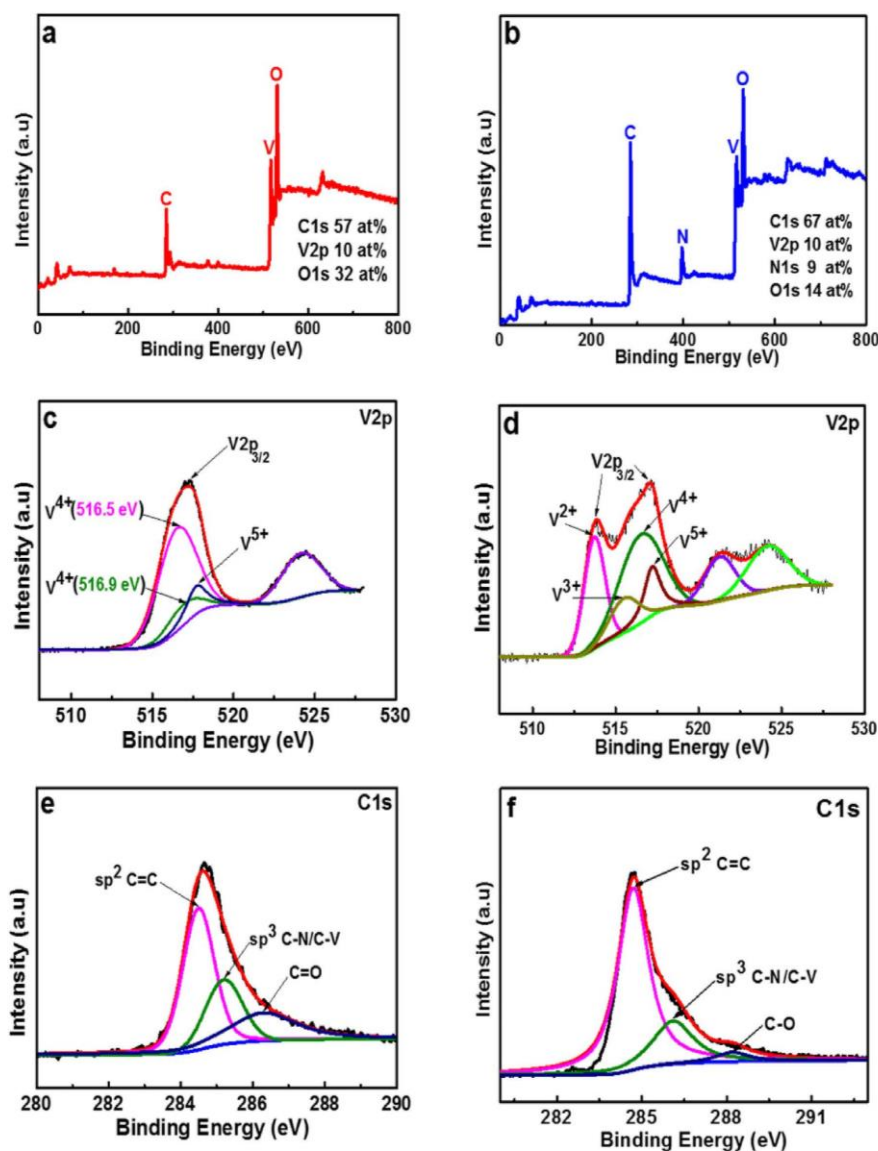

Fig. 7. The wide scan XPS spectrum of the as-received (i.e., without sputter cleaning) of (a) VO_2/AEG composite and (b) C-V_2NO@800 °C. The fitted core level spectrum of V2p from (c) VO_2/AEG composite and (d) C-V_2NO@800 °C. The core level spectra of C1s from (e) VO_2/AEG composite and (f) C-V_2NO@800 °C.

showed a better coulombic efficiency (99%) as compared to the VO_2 electrode with 97% coulombic efficiency up to 5000 cycles at 10 A g^{-1}.

Thus, the VO_2/AEG composite shows the best electrochemical performance as compared to the VO_2 electrode. This is due to the strong synergy between the two materials where AEG improves both good electrical conductivity and high specific surface area to VO_2, but has much high specific capacity as being oxide material as compared AEG carbon material.

Fig. 7 shows the individual electrochemical performance of both electrode materials. The cyclic voltammograms (CV) curves of the VO_2/AEG composite electrode were shown in Fig. 7(a) at scan rates ranging from 5 to 100 mV s^{-1} within a potential window range of

0.0–0.5 V. The curves exhibits reduction and oxidation peaks related to the electrochemical redox reactions at the electrode/electrolyte interface. The CV curves reveal the conventional behavior of a faradaic-type electrode.

The CV curves of the C-V_2NO electrode were shown in Fig. 7(b) at different scan rates from 5 to 100 mV s^{-1} in a negative potential window range of −1.2 V to 0.0 V. The CV curve at 50 mV s^{-1} displayed a two-pairs of redox peaks corresponding to the anodic peaks at −0.80 V and −0.38 V and cathodic peaks at −0.87 V and −0.53 V, respectively. Mostly, two pairs of broad redox peaks in the CV curve could be related to M−O/M−O−OH, in which M is V in this work [84].

As observed, the reversibility of these redox reactions confirmed

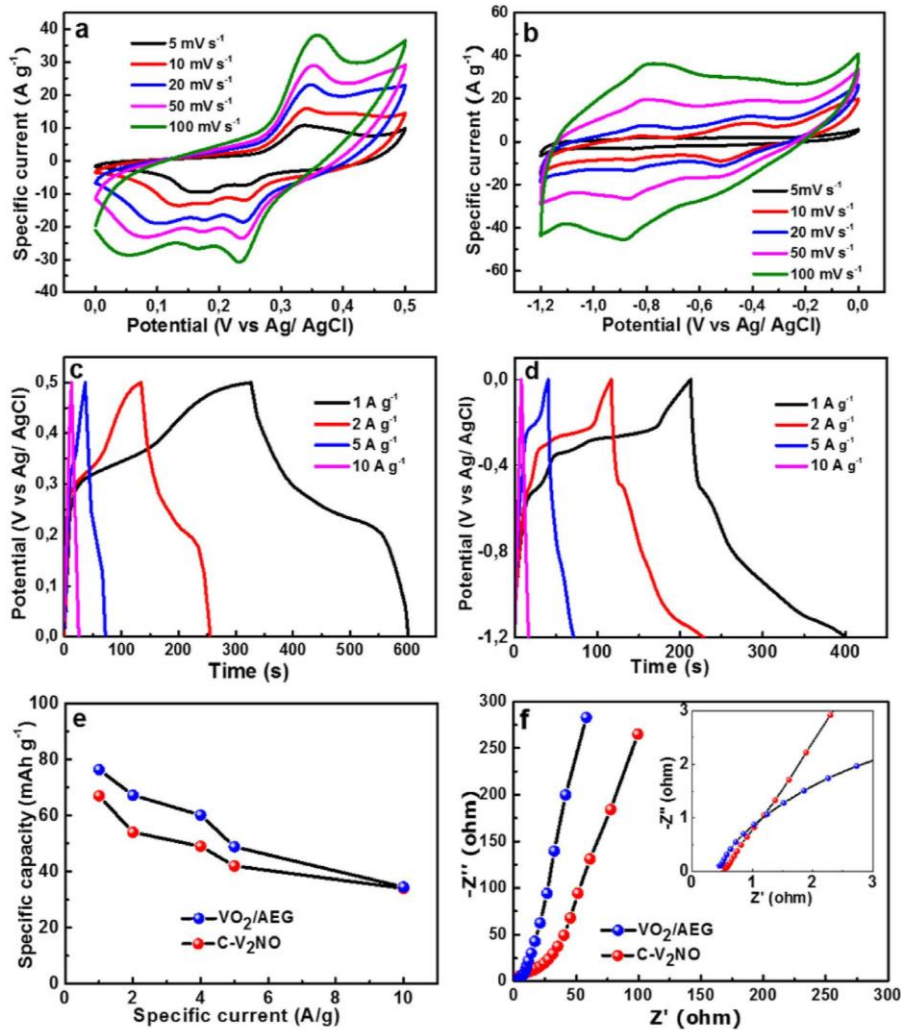Fig. 8. CV curves of the (a) VO_2/AEG composite and (b) C-V_2NO materials at different scan rates respectively. GCD profile of the (c) VO_2/AEG composite and (d) C-V_2NO at different specific currents respectively. (e) specific capacities for VO_2/AEG composite and C-V_2NO as a function of the specific current and (f) Nyquist plots of VO_2/AEG composite and C-V_2NO electrode materials.

the pseudo-capacitive behavior. The high electrochemical property of the C-V$_2$NO web-like nanostructure can be ascribed to the unique porous morphology architecture and the conductivity of the materials.

In Fig. 7(c), the corresponding galvanostatic charge discharge (GCD) curves of the electrode at different specific currents in the potential window of 0.0–0.5 V is displayed for VO$_2$/AEG composite. Each GCD curve showed a non-linear profile confirming the faradic behavior of the VO$_2$/AEG composite electrode.

The GCD curves of the C-V$_2$NO electrode shown in Fig. 7(d) present the existence of a faradaic behavior as seen in the CV plots for different specific currents.

Based on the GCD curves of VO$_2$/AEG and C-V$_2$NO electrodes, the specific capacity Q (mA h g^{-1}) was calculated using equation (2);

$$Q = \frac{I_d \times t_D}{3.6} \tag{2}$$

where I_d is the gravimetric specific current in A g^{-1}, t_D is the discharge time (s), and Q is the specific capacity (mA h g^{-1}).

Fig. 7(e) displays the calculated specific capacities of both electrodes at different specific currents. The specific capacities of the VO$_2$/AEG composite and C-V$_2$NO electrodes reach 76 and 67 mA h g^{-1}, respectively at a specific current of 1 A g^{-1}.

These high specific capacity values of the VO$_2$/AEG and C-V$_2$NO electrodes are linked to the presence of carbon in both oxides materials, which improves the electrical conductivity of both VO$_2$/AEG composite and C-V$_2$NO materials.

Fig. 7(f) displayed the Nyquist plot of the VO$_2$/AEG composite and C-V$_2$NO samples at a frequency ranging from 100 kHz to 10 mHz. As seen, the Nyquist plot of the VO$_2$/AEG composite presents a slight deviation from the vertical line. The equivalent series resistance (ESR) values for the VO$_2$/AEG and the C-V$_2$NO electrodes were 0.42 Ω and of 0.54 Ω, respectively. These low ESR values indicate a good electrolyte/electrode interface interaction and a low contact resistance between the current collector and the electrodes materials [85].

2.3.4. Two (2)-electrode configuration of the asymmetric device

To evaluate entirely the electrochemical performance of the VO$_2$/AEG composite and C-V$_2$NO electrodes, an asymmetric device was assembled using VO$_2$/AEG composite as a positive and C-V$_2$NO as a negative electrodes respectively in 6 M KOH.

Based on the difference in specific capacities of VO$_2$/AEG composite and C-V$_2$NO electrodes in Fig. 6(e), a charge balance $(Q_{vo_2/AEG} = Q_{v_2NO-C})$ is necessary for the asymmetric cell. The masses of both electrodes were calculated by using the following equations (3) and (4) with Q being the specific capacity as per equation (2):

$$\frac{Qvo_2}{AEG} = Qc - v_2NO \tag{3}$$

$$\frac{m_{\frac{vo}{AEG}}}{mc - v_2NO} = \frac{(I \cdot t_D)_{c-v_2NO}}{(I \cdot t_D)_{\frac{vo_2}{AEG}}} \tag{4}$$

where $m_{\frac{vo_2}{AEG}}$ and m_{v_2NO-c} are the mass loading of the positive and negative electrodes and $Q_{\frac{vo_2}{AEG}}$ and Q_{v_2NO-C} are the specific capacities of VO$_2$/AEG and C-V$_2$NO electrodes respectively and I is the current
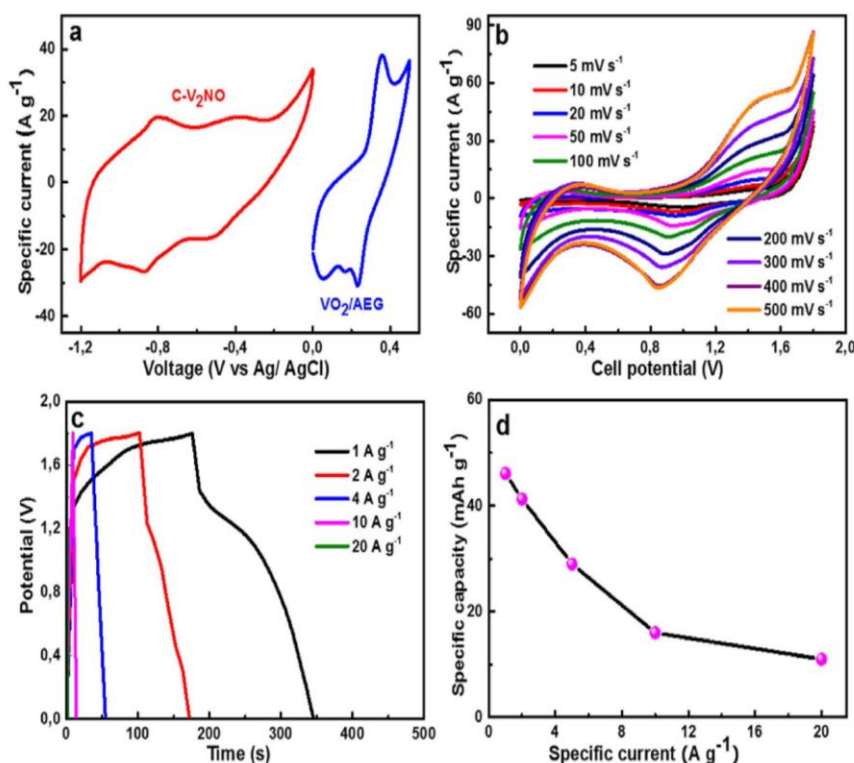

Fig. 9. (a) CV of VO$_2$/AEG and C-V$_2$NO in the positive and negative potential windows respectively, at 50 mV s^{-1} for half-cell configuration, (b) CV curves at different scan rates, (c) GCD profile at different specific currents and (d) specific capacity at different specific current of the AsyCs in the full-cell configuration.

and t_D is the discharge time.

The ratio of discharge time of the VO$_2$/AEG and C-V$_2$NO composite at the same specific current is:

$$\frac{m_{VO_2/AEG}}{m_{C-V_2NO}} = 0.68 \qquad (5)$$

From equation (4), the masses loading of VO$_2$/AEG and C-V$_2$NO electrodes were calculated to be approximatively 2.2 and 3.3 mg respectively, which indicates a total mass of the asymmetric device to be 5.5 mg.

Fig. 8(a) shows the CV curves of the VO$_2$/AEG and C-V$_2$NO electrodes as evaluated in half-cell configuration with working potential windows of 0.0−0.5 V and −1.2 to 0.0 V, respectively at a scan rate of 50 mV s^{-1}. Fig. 8(b) shows the CV curves of the

asymmetric device at different scan rates from 5 to 500 mV s^{-1}. For instance, at a scan rate of 50 mV s^{-1}, the CV curve of the device showed a pair of redox peaks corresponding to the anodic peak at ~0.94 V and cathodic peak at ~1.45 V. The CV curves obtained of the device show faradaic type behavior at different scan rates in the potential range of 0.0 V−1.8 V. As observed, the CV curves response have a similar shape with increasing scan rate from 5 to 500 mV s^{-1}, showing good efficient electron transfer in the electrodes and a superb rate capability.

Fig. 8(b) also exhibits a low positive shift of the anodic peaks (oxidation) and a low negative shift of the cathodic peaks (reduction) which indicated a quasi-reversible nature of the redox reactions [86].

Fig. 8(c) shows the GCD curves of VO$_2$/AEG//C-V$_2$NO at different
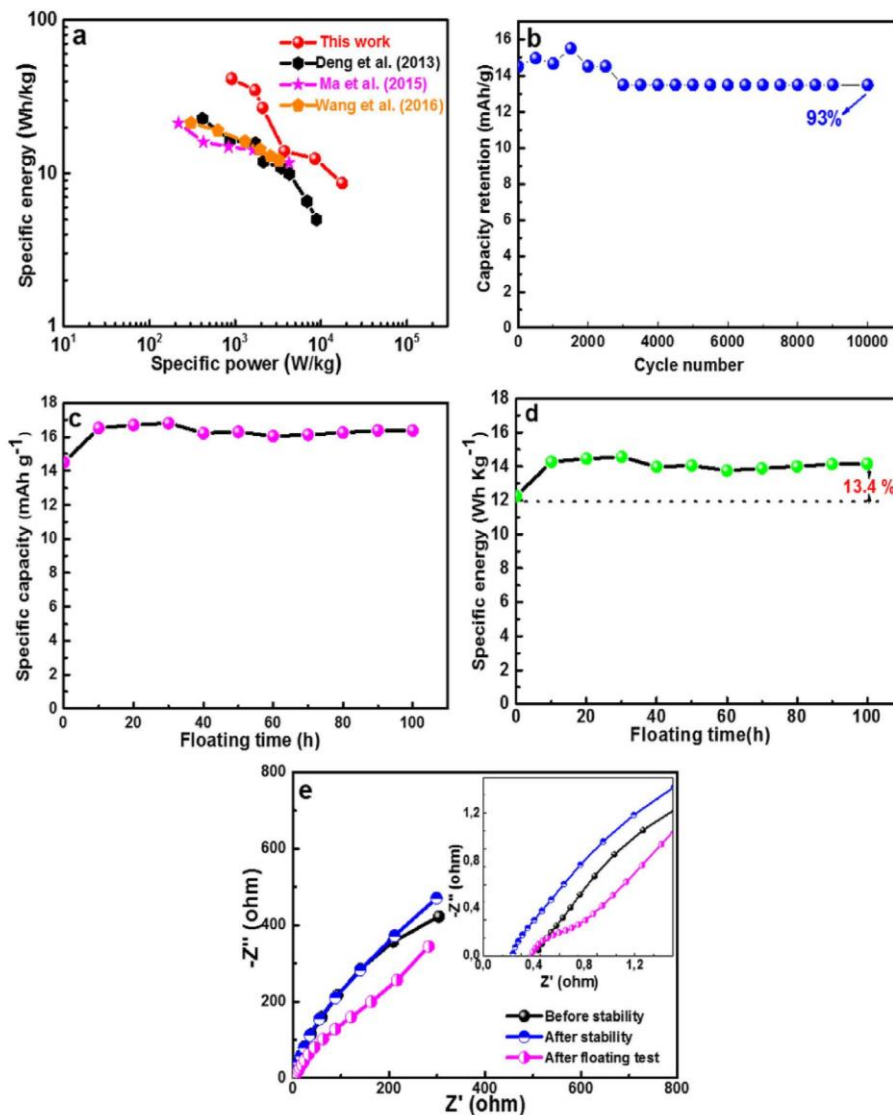

Fig. 10. (a) Ragone plot of the specific power as a function of specific energy, (b) stability test showing capacity retention for up to 10,000 cycles, (c) plot of specific capacity, (d) plot of specific energy versus floating time to 100 h at 10 A g^{-1} and (e) Nyquist plot (the inset is the ESR) of the asymmetric device before, after the stability and after floating test.

190

gravimetric current values of 1–20 A g^{-1} in a 0.0–1.8 V cell potential. The GCD curves are clearly non-linear which confirms the faradic behavior of the asymmetric device.

From the GCD curves, the specific capacity Q (mA h g^{-1}) of the VO$_2$/AEG//C-V$_2$NO was calculated using equation (2). The plot of the specific capacity as a function of the specific current is shown in Fig. 8(d). The device specific capacity reached a value of 46 mA h g^{-1} at a current density of 1 A g^{-1} and is maintained at 11 mA h g^{-1} at a 20 A g^{-1} gravimetric current.

The specific energy E$_d$ (W h kg^{-1}) and specific power, P$_d$ (W kg^{-1}) of the VO$_2$/AEG//C-V$_2$NO were also evaluated at different specific current values using equations (6) and (7) below:

$$E_d\left(W\,h\,kg^{-1}\right) = \frac{I_d}{3.6}\int V(t)dt \qquad (6)$$

$$P_d\left(W\,kg^{-1}\right) = 3600\frac{E_D}{t_D} \qquad (7)$$

where Id is the specific current in A g-1, t_D is the discharge time (s), and V is the potential window (V) of the asymmetric device.

The Ragone plot for the asymmetric device at different specific currents is shown in Fig. 9(a). A specific energy of 41.6 Wh kg^{-1} was recorded for the VO$_2$/AEG//C-V$_2$NO device with a corresponding specific power value of 904 W kg^{-1} at a specific current of 1 A g^{-1}.

At a high specific current of 20 A g^{-1}, an 18 kW kg^{-1} specific power was measured for the device with a correspond 9 W h kg^{-1} of specific energy. In addition, the specific energy and specific power values are higher than those reported for most reports on VO$_2$ and other VO$_2$/carbon-based composite materials as shown in the figure [39,42,87].

For example, Deng et al. [42] synthesized a graphene/VO$_2$ (RG/VO$_2$) composite by using a hydrothermal method with ammonium metavanadate (NH$_4$VO$_3$), formic acid and graphite oxide (GO) nanosheets as precursors. Asymmetric device assembled using the RG/VO$_2$ as a positive and RG as a negative electrodes respectively in 0.5 M K$_2$SO$_4$ electrolyte. The specific energy of the RG/VO$_2$//RG was 22.8 Wh kg^{-1} with a specific power of 425 W kg^{-1} at a specific current of 0.5 A g^{-1} [42]. Wang and co-authors [39] prepared a 3D graphene/VO$_2$ nanobelt composite hydrogel using a commercial vanadium pentoxide (V$_2$O$_5$) and graphene oxide as precursors. The symmetric capacitors delivered a specific energy of 21.3 W h kg^{-1} with a specific power ~304 W kg^{-1} at a specific current of 1 A g^{-1} in 0.5 M K$_2$SO$_4$ [39]. Ma and co-workers [87] reported a 3D VO$_2$ irregular ellipsoidal material using a simple CVD method with ammonium metavanadate (NH$_4$VO$_3$) as a precursor. The electrochemical performance of the symmetric device (VO$_2$//VO$_2$) exhibited specific energy of 21.3 W h kg^{-1} with a specific power of 207.2 W kg^{-1} at a specific current of 0.25 A g^{-1} in 1 M Na$_2$SO$_4$ [87]. The high specific energy and specific power of the VO$_2$/AEG//C-V$_2$NO asymmetric device which are superior to similar devices, reported in this work are associated with the good electrochemical performances of both electrodes and the large working potential. It can also be related to the fast kinetics of charge/discharge process and the high ionic conductivity of the electrolyte ions [88].

In order to evaluate the stability of the VO$_2$/AEG//C-V$_2$NO, the asymmetric device was exposed to 10,000 constant charge-discharge cycles at a specific current of 10 A g^{-1}.

Such a test is an essential parameter if the device is to be considered for practical application in a supercapacitor. The plot of capacity retention as a function of cycle number at 10 A g^{-1} is shown in Fig. 9(b) in a wide operating voltage of 1.8 V. An unstable capacity retention is initially observed for the first 2500 cycles due to mechanical stress [89] before stabilizing. However, above 2500 cycles, an excellent capacity retention of 93% is obtained up to

10,000th charge-discharge cycle. This indicates an excellent electrochemical stability of the electrode material. The good stability test is linked to the incorporation of VO$_2$ rods within the AEG sheet-like material (positive electrode) as well as the use of a porous web-like C-V$_2$NO nanostructure (negative electrode).

Actually, high specific energy, high specific power, and good stability are critical for a good electrochemical capacitor. The additional stability test was also studied using the floating test (also called voltage holding) after cycling. The floating test was designed to analyse the device specific capacity at each 10 h period of the potential holding step for up to 100 h. Fig. 9(c) shows a slow improvement in the device performance in terms of the specific capacity value after 30 h of floating before stabilizing at a constant value of 10 A g^{-1}. The good stability profile can be confirmed after evaluating the specific energy for each floating test as shown in Fig. 9(d) which presents the plot of specific energy as a function of floating time of 10 h interval. It shows an increase in the specific energy after 30 h which is in agreement with Fig. 9(c). The specific energy increased by 13.4% from the original value of 12.2 W h kg^{-1} which stabilizes to the same value up to 100 h (Fig. 9(d)). These increase in specific capacity and specific energy could be due to the increase in accessible redox sites during the aging time [59]. It also confirms that the VO$_2$/AEG//C-V$_2$NO device is stable with the cell voltage of 1.8 V by using 6 M KOH.

Fig. 9(e) shows the Nyquist plots of the asymmetric device before, after 10,000 cycling and after voltage holding carried out in the frequency range of 100 kHz to 10 mHz. The ESR value of the device improved from 0.43 Ω before stability tests to 0.23 Ω after cycling test and 0.37 Ω after voltage holding respectively. The Nyquist plot after 10,000 cycling test shows a smaller deviation from the vertical line and shorter diffusion length as compared to others. This continuous decrease of the ESR values after stability and after the maintenance of the voltage confirms the good accessible redox sites during the stability test.

3. Conclusion

In this work, the VO$_2$/AEG rod-like composite and porous C-V$_2$NO with a spider web-like structure were successfully synthesized by CVD method. The powder X-ray diffraction analysis of the VO$_2$/AEG composite showed the diffraction peaks of the VO$_2$ and AEG while for C-V$_2$NO, it shows a cubic crystal structure. The electrochemical performance of the electrode materials (VO$_2$/AEG//C-V$_2$NO) was evaluated in a two-electrode asymmetric device with VO$_2$/AEG composite as a positive and C-V$_2$NO as a negative electrodes respectively in a 6 M KOH. The VO$_2$/AEG//C-V$_2$NO exhibited a specific energy of 41.6 Wh kg^{-1} associated with a specific power of 904 W kg^{-1} at a specific current of 1 A g^{-1} in a large operating voltage of 1.8 V. These values supersede the recorded values reported in for VO$_2$ based devices.

The asymmetric supercapacitor showed an excellent capacity retention of 93% for up to 10,000 cycling test at a specific current of 10 A g^{-1}. It also showed good stability through floating test up to 100 h exhibiting a high specific energy which revealed that the electrode materials showed better-performance after voltage holding measurements. The results confirmed that the VO$_2$/AEG composite and C-V$_2$NO materials are suitable for high performance asymmetric capacitor applications.

recommendation expressed in this material is that of the author(s). The NRF does not accept any liability in this regard. N. M. Ndiaye thanks Dr. Bridget K. Mutuma for discussions on the morphological properties and the fitting of XPS. N. M. Ndiaye thanks Organization for Women in Science for the Developing World (OWSD) and Swedish International Development Cooperation Agency (Sida), NRF through SARChI in Carbon Technology and Materials and the University of Pretoria for financial support.

Appendix A. Supplementary data

Supplementary data to this article can be found online at https://doi.org/10.1016/j.electacta.2019.05.103

References

[1] Y. Zhang, J. Zheng, T. Hu, F. Tian, C. Meng, Synthesis and supercapacitor electrode of $VO_2(B)/C$ core–shell composites with a pseudocapacitance in aqueous solution, Appl. Surf. Sci. 371 (2016) 189–195, https://doi.org/10.1016/J.APSUSC.2016.02.199.

[2] M. Vangari, T. Pryor, L. Jiang, Supercapacitors: review of materials and fabrication methods, J. Energy Eng. 139 (2013) 72–79, https://doi.org/10.1061/(ASCE)EY.1943-7897.0000102.

[3] M. Gidwani, A. Bhagwani, N. Rohra, Supercapacitors: the near future of batteries, Int. J. Eng. Invent. 4 (2014) 22–27, accessed, www.ijeijournal.com. (Accessed 1 October 2018).

[4] R.B. Rakhi, D.H. Nagaraju, P. Beaujuge, H.N. Alshareef, Supercapacitors based on two dimensional VO_2 nanosheet electrodes in organic gel electrolyte, Electrochim. Acta 220 (2016) 601–608, https://doi.org/10.1016/J.ELECTACTA.2016.10.109.

[5] K.H. An, W.S. Kim, Y.S. Park, Y.C. Choi, S.M. Lee, D.C. Chung, D.J. Bae, S.C. Lim, Y.H. Lee, Supercapacitors using single-walled carbon nanotube electrodes, Adv. Mater. 13 (2001) 497–500, https://doi.org/10.1002/1521-4095(200104)13:7<497::AID-ADMA497>3.0.CO;2-H.

[6] J.R. Miller, R.A. Outlaw, B.C. Holloway, K.J. Ganesh, W. Cai, P.J. Ferreira, A. Pirkle, R.M. Wallace, K.A. Cychosz, M. Thommes, D. Su, E.A. Stach, R.S. Ruoff, Graphene double-layer capacitor with ac line-filtering performance, Science 329 (2010) 1637–1639, https://doi.org/10.1126/science.1194372.

[7] Z. Yu, L. Tetard, L. Zhai, J. Thomas, Supercapacitor electrode materials: nanostructures from 0 to 3 dimensions, Energy Environ. Sci. 8 (2015) 702–730, https://doi.org/10.1039/C4EE03229B.

[8] X. Pan, Y. Zhao, G. Ren, Z. Fan, Highly conductive VO2 treated with hydrogen for supercapacitors, Chem. Commun. 49 (2013) 3943, https://doi.org/10.1039/c3cc00044c.

[9] M. Winter, R.J. Brodd, What are batteries, fuel cells, and supercapacitors? Chem. Rev. 104 (2004) 4245–4269, https://doi.org/10.1021/CR020730K.

[10] M. Zhi, C. Xiang, J. Li, M. Li, N. Wu, Nanostructured carbon–metal oxide composite electrodes for supercapacitors: a review, Nanoscale 5 (2013) 72–88, https://doi.org/10.1039/C2NR32040A.

[11] J.-W. Lang, L.-B. Kong, W.-J. Wu, Y.-C. Luo, L. Kang, Facile approach to prepare loose-packed NiO nano-flakes materials for supercapacitors, Chem. Commun. 104 (2008) 4213, https://doi.org/10.1039/b800264a.

[12] H. Li, Y. Gao, C. Wang, G. Yang, A simple electrochemical route to access amorphous mixed-metal hydroxides for supercapacitor electrode materials, Adv. Energy Mater. 5 (2015) 1401767, https://doi.org/10.1002/aenm.201401767.

[13] H. Xu, X. Hu, H. Yang, Y. Sun, C. Hu, Y. Huang, Flexible asymmetric microsupercapacitors based on Bi_2O_3 and MnO2 nanoflowers: larger areal mass promises higher energy density, Adv. Energy Mater. 5 (2015) 1401882, https://doi.org/10.1002/aenm.201401882.

[14] H. Ma, J. He, D.-B. Xiong, J. Wu, Q. Li, V. Dravid, Y. Zhao, Nickel cobalt hydroxide @reduced graphene oxide hybrid nanolayers for high performance asymmetric supercapacitors with remarkable cycling stability, ACS Appl. Mater. Interfaces 8 (2016) 1992–2000, https://doi.org/10.1021/acsami.5b10280.

[15] G.A. Snook, P. Kao, A.S. Best, Conducting-polymer-based supercapacitor devices and electrodes, J. Power Sources 196 (2011) 1–12, https://doi.org/10.1016/J.JPOWSOUR.2010.06.084.

[16] A. Rudge, J. Davey, I. Raistrick, S. Gottesfeld, J.P. Ferraris, Conducting polymers as active materials in electrochemical capacitors, J. Power Sources 47 (1994) 89–107, https://doi.org/10.1016/0378-7753(94)80053-7.

[17] X. Wang, A. Sumboja, M. Lin, J. Yan, P.S. Lee, Enhancing electrochemical reaction sites in nickel–cobalt layered double hydroxides on zinc tin oxide nanowires: a hybrid material for an asymmetric supercapacitor device, Nanoscale 4 (2012) 7266, https://doi.org/10.1039/c2nr31590d.

[18] L.-B. Kong, M. Liu, J.-W. Lang, Y.-C. Luo, L. Kang, Asymmetric supercapacitor based on loose-packed cobalt hydroxide nanoflake materials and activated carbon, J. Electrochem. Soc. 156 (2009) A1000, https://doi.org/10.1149/1.3236500.

[19] H. Wang, H. Yi, X. Chen, X. Wang, Asymmetric supercapacitors based on nano-

[20] architectured nickel oxide/graphene foam and hierarchical porous nitrogen-doped carbon nanotubes with ultrahigh-rate performance, J. Mater. Chem. A. 2 (2014) 3223–3230, https://doi.org/10.1039/C3TA15046A.

[20] J. Yan, Z. Fan, W. Sun, G. Ning, T. Wei, Q. Zhang, R. Zhang, L. Zhi, F. Wei, Advanced asymmetric supercapacitors based on Ni(OH)2/Graphene and porous graphene electrodes with high energy density, Adv. Funct. Mater. 22 (2012) 2632–2641, https://doi.org/10.1002/adfm.201102839.

[21] Z.-S. Wu, W. Ren, D.-W. Wang, F. Li, B. Liu, H.-M. Cheng, High-energy MnO2 nanowire/graphene and graphene asymmetric electrochemical capacitors, ACS Nano 4 (2010) 5835–5842, https://doi.org/10.1021/nn101754k.

[22] C.M. Ghimbeu, E. Raymundo-Piñero, P. Fioux, F.F. Béguin, C. Vix-Guterl, Vanadium nitride/carbon nanotube nanocomposites as electrodes for supercapacitors, J. Mater. Chem. 21 (2011) 13268, https://doi.org/10.1039/c1jm11014d.

[23] R.L. Porto, R. Frappier, J.B.B. Ducros, C. Aucher, H. Mosqueda, S. Chenu, B. Chavillon, F. Tessier, F. Cheviré, T. Brousse, Titanium and vanadium oxynitride powders as pseudo-capacitive materials for electrochemical capacitors, in: Electrochimica Acta, Pergamon, vol. 82, 2012, pp. 257–262, https://doi.org/10.1016/J.ELECTACTA.2012.05.032.

[24] E. Eustache, R. Frappier, R.L. Porto, S. Bouhtiyya, J.-F. Pierson, T. Brousse, Asymmetric electrochemical capacitor microdevice designed with vanadium nitride and nickel oxide thin film electrodes, Electrochem. Commun. 28 (2013) 104–106, https://doi.org/10.1016/J.ELECOM.2012.12.015.

[25] L. Zhang, F. Zhang, X. Yang, G. Long, Y. Wu, T. Zhang, K. Leng, Y. Huang, Y. Ma, A. Yu, Y. Chen, Porous 3D graphene-based bulk materials with exceptional high surface area and excellent conductivity for supercapacitors, Sci. Rep. 3 (2013) 1408, https://doi.org/10.1038/srep01408.

[26] L.L. Zhang, X.S. Zhao, Carbon-based materials as supercapacitor electrodes, Chem. Soc. Rev. 38 (2009) 2520, https://doi.org/10.1039/b813846j.

[27] C. Peng, S. Zhang, D. Jewell, G.Z. Chen, Carbon nanotube and conducting polymer composites for supercapacitors, Prog. Nat. Sci. 18 (2008) 777–788, https://doi.org/10.1016/J.PNSC.2008.03.002.

[28] Z. Fan, J. Yan, T. Wei, L. Zhi, G. Ning, T. Li, F. Wei, Asymmetric supercapacitors based on graphene/MnO2 and activated carbon nanofiber electrodes with high power and energy density, Adv. Funct. Mater. 21 (2011) 2366–2375, https://doi.org/10.1002/adfm.201100058.

[29] H. Zhao, L. Pan, S. Xing, J. Luo, J. Xu, Vanadium oxides–reduced graphene oxide composite for lithium-ion batteries and supercapacitors with improved electrochemical performance, J. Power Sources 222 (2013) 21–31, https://doi.org/10.1016/j.jpowsour.2012.08.036.

[30] X. Pan, G. Ren, M.N.F. Hoque, S. Bayne, K. Zhu, Z. Fan, Fast supercapacitors based on graphene-bridged V_2O_3/VO_x core-shell nanostructure electrodes with a power density of 1 MW kg^{-1}, Adv. Mater. Interfaces 1 (2014) 1400398, https://doi.org/10.1002/admi.201400398.

[31] W.F. Mak, G. Wee, V. Aravindan, N. Gupta, S.G. Mhaisalkar, S. Madhavi, High-energy density asymmetric supercapacitor based on electrospun vanadium pentoxide and polyaniline nanofibers in aqueous electrolyte, J. Electrochem. Soc. 159 (2012) A1481–A1488, https://doi.org/10.1149/2.040209jes.

[32] E. Umeshbabu, G. Ranga Rao, Vanadium pentoxide nanochains for high-performance electrochemical supercapacitors, J. Colloid Interface Sci. 472 (2016) 210–219, https://doi.org/10.1016/j.jcis.2016.03.050.

[33] M.H. Bai, L.J. Bian, Y. Song, X.X. Liu, Electrochemical codeposition of vanadium oxide and polypyrrole for high-performance supercapacitor with high working voltage, ACS Appl. Mater. Interfaces 6 (2014) 12656–12664, https://doi.org/10.1021/am502630g.

[34] X. Pan, G. Ren, M.N.F. Hoque, S. Bayne, K. Zhu, Z. Fan, Fast supercapacitors based on graphene-bridged V_2O_3/VO_x core-shell nanostructure electrodes with a power density of 1 MW kg^{-1}, Adv. Mater. Interfaces 1 (2014) 1400398, https://doi.org/10.1002/admi.201400398.

[35] H. Li, K. Jiao, L. Wang, C. Wei, B. Xie, Micelle anchored in situ synthesis of V_2O_3 nanoflakes@C composites for supercapacitors, J. Mater. Chem.: Mater. Energy and Sustain. 2 (2014) 18806–18815, https://doi.org/10.1039/C4TA04062G.

[36] G.P. Nagabhushana, G.T. Chandrappa, Facile solution combustion synthesis of monoclinic VO2: a unique and versatile approach, J. Mater. Chem. 1 (2013) 11539, https://doi.org/10.1039/c3ta11692a.

[37] I. Derkaoui, M. Khenfouch, I. Elmokri, S.J. Moloi, B.M. Mothudi, M.S. Dhlamini, M. Maaza, I. Zorkani, A. Jorio, Experimental investigation of the effect of graphene nanosheets on the optical-electrical properties of vanadium oxide nanocomposites, Graphene 5 (2016) 14–24, https://doi.org/10.4236/graphene.2016.51002.

[38] S. Kachi, T. Takada, K. Kosuge, Electrical conductivity of vanadium oxides, J. Phys. Soc. Jpn. 18 (1963) 1839–1840, https://doi.org/10.1143/JPSJ.18.1839.

[39] H. Wang, H. Yi, X. Chen, X. Wang, D.W. Liu, J. Liu, G.Z. Cao, P.M. Ajayan, F. Wei, One-step strategy to three-dimensional graphene/VO2 nanobelt composite hydrogels for high performance supercapacitors, J. Mater. Chem. 2 (2014) 1165–1173, https://doi.org/10.1039/c3ta13932h.

[40] L. Liang, H. Liu, W. Yang, Fabrication of VO2(B) hybrid with multiwalled carbon nanotubes to form a coaxial structure and its electrochemical capacitance performance, J. Alloy. Comp. 559 (2013) 167–173, https://doi.org/10.1016/J.JALLCOM.2013.01.111.

[41] X. Xia, D. Chao, C.F. Ng, J. Lin, Z. Fan, H. Zhang, Z.X. Shen, H.J. Fan, VO2 nanoflake arrays for supercapacitor and Li-ion battery electrodes: performance enhancement by hydrogen molybdenum bronze as an efficient shell material, Mater. Horiz. 2 (2015) 237–244, https://doi.org/10.1039/C4MH00212A.

[42] L. Deng, G. Zhang, L. Kang, Z. Lei, C. Liu, Z.-H.H. Liu, Graphene/VO₂ hybrid material for high performance electrochemical capacitor, Electrochim. Acta 112 (2013) 448–457, https://doi.org/10.1016/j.electacta.2013.08.158.

[43] G. Nie, X. Lu, Y. Zhu, M. Chi, M. Gao, S. Chen, C. Wang, Reactive template synthesis of inorganic/organic VO₂@Polyaniline coaxial nanobelts for high-performance supercapacitors, ChemElectroChem 4 (2017) 1095–1100, https://doi.org/10.1002/celc.201600830.

[44] Z. Chen, V. Augustyn, J. Wen, Y. Zhang, M. Shen, B. Dunn, Y. Lu, High-performance supercapacitors based on intertwined CNT/V₂O₅ nanowire nano-composites, Adv. Mater. 23 (2011) 791–795, https://doi.org/10.1002/adma.201003658.

[45] X. Zhou, Q. Chen, A. Wang, J. Xu, S. Wu, J. Shen, Bamboo-like composites of V₂O₅/polyindole and activated carbon cloth as electrodes for all-solid-state flexible asymmetric supercapacitors, ACS Appl. Mater. Interfaces 8 (2016) 3776–3783, https://doi.org/10.1021/acsami.5b10196.

[46] S. Fleischmann, M. Zeiger, N.J. Ackel, B. Krüner, K. Krüner, V. Lemkova, M. Widmaier, V. Presser, Tuning Pseudocapacitive and Battery-like Lithium Intercalation in Vanadium Dioxide/carbon Onion Hybrids for Asymmetric Supercapacitor Anodes, 2017, https://doi.org/10.1039/c7ta02564e.

[47] H. Hosseini, S. Shahrokhian, Vanadium dioxide-anchored porous carbon nanofibers as a Na⁺ intercalation pseudocapacitance material for development of flexible and super light electrochemical energy storage systems, Appl. Mater. Today 10 (2018) 72–85, https://doi.org/10.1016/j.apmt.2017.11.011.

[48] F. Barzegar, A. Bello, D. Momodu, M.J. Madito, J. Dangbegnon, N. Manyala, Preparation and characterization of porous carbon from expanded graphite for high energy density supercapacitor in aqueous electrolyte, J. Power Sources 309 (2016) 245–253, https://doi.org/10.1016/j.jpowsour.2016.01.097.

[49] X.-J.J. Ma, W.-B. Bin Zhang, L.-B. Bin Kong, Y.-C.C. Luo, L. Kang, VO₂: from negative electrode material to symmetric electrochemical capacitor, RSC Adv. 5 (2015) 97239–97247, https://doi.org/10.1039/C5RA18758C.

[50] S. Lee, I.N. Ivanov, J.K. Keum, H.N. Lee, Epitaxial stabilization and phase instability of VO₂ polymorphs, Sci. Rep. 6 (2016) 19621, https://doi.org/10.1038/srep19621.

[51] N.M.M. Ndiaye, T.M.M. Masikhwa, B.D.D. Ngom, M.J.J. Madito, K.O.O. Oyedotun, J.K.K. Dangbegnon, N. Manyala, Effect of growth time on solvothermal synthesis of vanadium dioxide for electrochemical super-capacitor application, Mater. Chem. Phys. 214 (2018) 192–200, https://doi.org/10.1016/j.matchemphys.2018.04.087.

[52] M. Pan, J. Liu, H. Zhong, S. Wang, Z.F. Li, X. Chen, W. Lu, Raman study of the phase transition in VO₂ thin films, J. Cryst. Growth 268 (2004) 178–183, https://doi.org/10.1016/j.jcrysgro.2004.05.005.

[53] G.I. Petrov, V.V. Yakovlev, J. Squier, Raman microscopy analysis of phase transformation mechanisms in vanadium dioxide, Appl. Phys. Lett. 81 (2002) 1023–1025, https://doi.org/10.1063/1.1496506.

[54] M. Lee, S.K. Balasingam, H.Y. Jeong, W.G. Hong, H.-B.-R. Lee, B.H. Kim, Y. Jun, One-step hydrothermal synthesis of graphene decorated V₂O₅ nanobelts for enhanced electrochemical energy storage, Sci. Rep. 5 (2015) 8151, https://doi.org/10.1038/srep08151.

[55] M. Chhowalla, A.C. Ferrari, J. Robertson, G.A.J. Amaratunga, Evolution of sp² bonding with deposition temperature in tetrahedral amorphous carbon studied by Raman spectroscopy, Appl. Phys. Lett. 76 (2000) 1419, https://doi.org/10.1063/1.126050.

[56] D. Roy, M. Chhowalla, H. Wang, N. Sano, I. Alexandrou, T.W. Clyne, G.A.J. Amaratunga, Characterisation of carbon nano-onions using Raman spectroscopy, Chem. Phys. Lett. 373 (2003) 52–56, https://doi.org/10.1016/S0009-2614(03)00523-2.

[57] T.M.G. Mohiuddin, A. Lombardo, R.R. Nair, A. Bonetti, G. Savini, R. Jalil, N. Bonini, D.M. Basko, C. Galiotis, N. Marzari, K.S. Novoselov, A.K. Geim, A.C. Ferrari, Uniaxial strain in graphene by Raman spectroscopy: G peak splitting, Grüneisen parameters, and sample orientation, Phys. Rev. B Condens. Matter 79 (2009) 205433, https://doi.org/10.1103/PhysRevB.79.205433.

[58] S.-H. Lee, H.M. Cheong, M.J. Seong, P. Liu, C.E. Tracy, A. Mascarenhas, J.R. Pitts, S.K. Deb, Raman spectroscopic studies of amorphous vanadium oxide thin films, Solid State Ionics 165 (2003) 111–116, https://doi.org/10.1016/j.ssi.2003.08.022.

[59] N.M. Ndiaye, B.D. Ngom, N.F. Sylla, T.M. Masikhwa, M.J. Madito, D. Momodu, T. Ntsoane, N. Manyala, Three dimensional vanadium pentoxide/graphene foam composite as positive electrode for high performance asymmetric electrochemical supercapacitor, J. Colloid Interface Sci. 532 (2018) 395–406, https://doi.org/10.1016/j.jcis.2018.08.010.

[60] T.D. Manning, I.P. Parkin, C. Blackman, U. Qureshi, APCVD of thermochromic vanadium dioxide thin films—solid solutions V₂₋ₓMₓO₂ (M = Mo, Nb) or composites VO₂: SnO₂, J. Mater. Chem. 15 (2005) 4560, https://doi.org/10.1039/b510552h.

[61] P. Schilbe, Raman scattering in VO₂, Phys. B Condens. Matter 316–317 (2002) 600–602, https://doi.org/10.1016/S0921-4526(02)00584-7.

[62] A. Kafizas, G. Hyett, I.P. Parkin, Combinatorial atmospheric pressure chemical vapour deposition (cAPCVD) of a mixed vanadium oxide and vanadium oxynitride thin film, J. Mater. Chem. 19 (2009) 1399, https://doi.org/10.1039/b817429f.

[63] M. Fabiane, M.J. Madito, A. Bello, N. Manyala, Raman spectroscopy and im-aging of Bernal-stacked bilayer graphene synthesized on copper foil by chemical vapour deposition: growth dependence on temperature, J. Raman Spectrosc. 48 (2017) 639–646, https://doi.org/10.1002/jrs.5094.

[64] J. Yu, G. Wang, B. Cheng, M. Zhou, Effects of hydrothermal temperature and time on the photocatalytic activity and microstructures of bimodal meso-porous TiO2 powders, Appl. Catal. B Environ. 69 (2007) 171–180, https://doi.org/10.1016/J.APCATB.2006.06.022.

[65] R.L. Porto, R. Frappier, J.B.B. Ducros, C. Aucher, H. Mosqueda, S. Chenu, B. Chavillon, F. Tessier, F. Cheviré, T. Brousse, Titanium and vanadium oxy-nitride powders as pseudo-capacitive materials for electrochemical capaci-tors, Electrochim. Acta 82 (2012) 257–262, https://doi.org/10.1016/J.ELECTACTA.2012.05.032.

[66] D. Shu, H. Cheng, C. Lv, M.A. Asi, L. Long, C. He, X. Zou, Z. Kang, Soft-template synthesis of vanadium oxynitride-carbon nanomaterials for supercapacitors, Int. J. Hydrogen Energy 39 (2014) 16139–16150, https://doi.org/10.1016/J.IJHYDENE.2014.05.119.

[67] F.O. Ochai-Ejeh, D.Y. Momodu, M.J. Madito, A.A. Khaleed, K.O. Oyedotun, S.C. Ray, N. Manyala, Nanostructured porous carbons with high rate cycling and floating performance for supercapacitor application, AIP Adv. 8 (2018) 055208, https://doi.org/10.1063/1.5023046.

[68] D. Verma, D. Singh, P. Kumar, P. Avasthi, V. Balakrishnan, Gram scale synthesis of monoclinic VO₂ microcrystals by hydrothermal and argon annealing treatment, Ceram. Int. 45 (2019) 3554–3562, https://doi.org/10.1016/J.CERAMINT.2018.11.014.

[69] C. Cao, Y. Gao, H. Luo, Pure single-crystal rutile vanadium dioxide powders: synthesis, mechanism and phase-transformation property, J. Phys. Chem. C 112 (2008) 18810–18814, https://doi.org/10.1021/jp8073688.

[70] Z. Huang, H. Zeng, L. Xue, X. Zhou, Y. Zhao, Q. Lai, Synthesis of vanadium oxide, V6O13 hollow-flowers materials and their application in electrochemical supercapacitors, J. Alloy. Comp. 509 (2011) 10080–10085, https://doi.org/10.1016/J.JALLCOM.2011.08.042.

[71] M. Demeter, M. Neumann, W. Reichelt, Mixed-valence vanadium oxides studied by XPS, Surf. Sci. 454–456 (2000) 41–44, https://doi.org/10.1016/S0039-6028(00)00111-4.

[72] E. Hryha, E. Rutqvist, L. Nyborg, Stoichiometric vanadium oxides studied by XPS, Surf. Interface Anal. 44 (2012) 1022–1025, https://doi.org/10.1002/sia.3844.

[73] G. Silversmit, D. Depla, H. Poelman, G.B. Marin, R. De Gryse, Determination of the V2p XPS binding energies for different vanadium oxidation states (V⁵⁺ to V⁰⁺), J. Electron. Spectrosc. Relat. Phenom. 135 (2004) 167–175, https://doi.org/10.1016/J.ELSPEC.2004.03.004.

[74] D. Marton, K.J. Boyd, A.H. Al-Bayati, S.S. Todorov, J.W. Rabalais, Carbon nitride deposited using energetic species: a two-phase system, Phys. Rev. Lett. 73 (1994) 118–121, https://doi.org/10.1103/PhysRevLett.73.118.

[75] M. Sevilla, A.B. Fuertes, The production of carbon materials by hydrothermal carbonization of cellulose, Carbon 47 (2009) 2281–2289, https://doi.org/10.1016/j.carbon.2009.04.026.

[76] J.G.G. Chen, C.M.M. Kirn, B. Frühberger, B.D.D. DeVries, M.S.S. Touvelle, A NEXAFS determination of the oxidation state of vanadium carbide on V(110): observation of charge transfer from vanadium to carbon, Surf. Sci. 321 (1994) 145–155, https://doi.org/10.1016/0039-6028(94)90035-3.

[77] X. Song, D. Gopireddy, C.G. Takoudis, Characterization of titanium oxynitride films deposited by low pressure chemical vapor deposition using amide Ti precursor, Thin Solid Films 516 (2008) 6330–6335, https://doi.org/10.1016/J.TSF.2007.12.148.

[78] P. Mérel, M. Tabbal, M. Chaker, S. Moisa, J. Margot, Direct evaluation of the sp³ content in diamond-like-carbon films by XPS, Appl. Surf. Sci. 136 (1998) 105–110, https://doi.org/10.1016/S0169-4332(98)00319-5.

[79] A. Dementjev, A. de Graaf, M.C. van de Sanden, K. Maslakov, A. Naumkin, A. Serov, X-Ray photoelectron spectroscopy reference data for identification of the C₃N₄ phase in carbon–nitrogen films, Diam. Relat. Mater. 9 (2000) 1904–1907, https://doi.org/10.1016/S0925-9635(00)00345-9.

[80] M. Fredriksson, C. Langhammer, Electrochemical Hydride Formation in Thin Pd Films Analyzed with a Combined Optical and Electrochem-Ical Technique, Chalmers University of Technology, 2014. http://publications.lib.chalmers.se/records/fulltext/209369/209369.pdf. (Accessed 25 April 2019).

[81] C.H. Hamann, A. Hamnett, W. Vielstich, Electrochemistry, Wiley-VCH, 2007, 2nd, Completely Revised and Updated Edition-p-9783527310692, https://www.wiley.com/en-za/Electrochemistry. (Accessed 25 April 2019).

[82] S. Leijonmarck, Preparation and Characterization of Electrochemical Devices for Energy Storage and Debonding, School of Chemical Science and Engi-neering Kungliga Tekniska Högskolan, 2013. https://www.diva-portal.org/smash/get/diva2:613847/FULLTEXT01.pdf. (Accessed 25 April 2019).

[83] Y.-G. Wang, L. Cheng, Y.-Y. Xia, Electrochemical profile of nano-particle CoAl double hydroxide/active carbon supercapacitor using KOH electrolyte solu-tion, J. Power Sources 153 (2006) 191–196, https://doi.org/10.1016/j.jpowsour.2005.04.009.

[84] H. Bin Wu, H. Pang, X.W.(David) Lou, Facile synthesis of mesoporous Ni₀.₃Co₂.₇O₄ hierarchical structures for high-performance supercapacitors, Energy Environ. Sci. 6 (2013) 3619, https://doi.org/10.1039/c3ee42101e.

[85] M.M. Shaijumon, F.S. Ou, L. Ci, P.M. Ajayan, Synthesis of hybrid nanowire arrays and their application as high power supercapacitor electrodes, Chem. Commun. 0 (2008) 2373, https://doi.org/10.1039/b800866c.

[86] Y.-K. Hsu, Y.-C. Chen, Y.-G. Lin, Synthesis of copper sulfide nanowire arrays for high-performance supercapacitors, Electrochim. Acta 139 (2014) 401–407, https://doi.org/10.1016/J.ELECTACTA.2014.06.138.

[87] X.-J. Ma, W.-B. Zhang, L.-B. Kong, Y.-C. Luo, L. Kang, VO₂: from negative electrode material to symmetric electrochemical capacitor, RSC Adv. 5 (2015)

193

97239–97247, https://doi.org/10.1039/C5RA18758C.

[88] A. Leela Mohana Reddy, F. Estaline Amitha, I. Jafri, S. Ramaprabhu, Asymmetric flexible supercapacitor stack, Nanoscale Res. Lett. 3 (2008) 145–151, https://doi.org/10.1007/s11671-008-9127-3.

[89] B. Saravanakumar, K.K. Purushothaman, G. Muralidharan, Interconnected V₂O₅ nanoporous network for high-performance supercapacitors, ACS Appl. Mater. Interfaces 4 (2012) 4484–4490, https://doi.org/10.1021/am301162p.

4.5.3. Conclusion Remarks

In this work, the VO_2/AEG rod-like composite and porous $C-V_2NO$ with a spider web-like structure were successfully synthesized by CVD method. The powder X-ray diffraction analysis of the VO_2/AEG composite exhibited the diffraction peaks of the VO_2 and AEG while a cubic crystal structure was depicted for the $C-V_2NO$.

The electrochemical performance of the electrode materials (VO_2/AEG// $C-V_2NO$) was evaluated in a two-electrode asymmetric device with the VO_2/AEG composite adopted as a positive electrode and the $C-V_2NO$ as a negative electrode in a 6 M KOH.

The VO_2/AEG//$C-V_2NO$ exhibited a specific energy of 41.6 Wh kg^{-1} associated with a specific power of 904 W kg^{-1} at a specific current of 1 A g^{-1} in an operating voltage of 1.8 V. These values supersede the recorded values reported in the literature to the best of our knowledge for VO_2-based devices. The asymmetric supercapacitor showed an excellent capacity retention of 93% for up to 10,000 cycling test at a specific current of 10 A g^{-1}.

The device also demonstrated a good stability through floating test for a period of 100 h retaining a high specific energy which improved during the voltage holding process revealing that the electrode material-performance appreciated after voltage holding measurements.

The results confirmed that the VO_2/AEG composite and $C-V_2NO$ materials are suitable for high performance asymmetric capacitor applications.

Bibliography

[1] M. Zhi, C. Xiang, J. Li, M. Li, N. Wu, Nanostructured carbon–metal oxide composite electrodes for supercapacitors: a review, Nanoscale. 5 (2013) 72–88.

[2] E. Umeshbabu, G. Ranga Rao, Vanadium pentoxide nanochains for high-performance electrochemical supercapacitors, Journal of Colloid and Interface Science. 472 (2016) 210–219.

[3] L.-M.M. Chen, Q.-Y.Y. Lai, Y.-J.J. Hao, Y. Zhao, X.-Y.Y. Ji, Y.Z. Lian-Mei Chen, Qiong-Yu Lai, Yan-Jing Hao, Xiao-YangJi, Investigations on capacitive properties of the AC/V_2O_5 hybrid supercapacitor in various aqueous electrolytes, Journal of Alloys and Compounds. 467 (2009) 465–471.

[4] B. Saravanakumar, K.K. Purushothaman, G. Muralidharan, Interconnected V_2O_5 Nanoporous Network for High-Performance Supercapacitors, ACS Appl. Mater. Interfaces. 4 (2012) 4484−4490.

[5] M. Li, G. Sun, P. Yin, C. Ruan, K. Ai, Controlling the Formation of Rodlike V_2O_5 Nanocrystals on Reduced Graphene Oxide for High-Performance Supercapacitors, Nano Lett. 5 (2013) 11462–11470.

[6] X. Zhou, Q. Chen, A. Wang, J. Xu, S. Wu, J. Shen, Bamboo-like Composites of V_2O_5/Polyindole and Activated Carbon Cloth as Electrodes for All-Solid-State Flexible Asymmetric Supercapacitors, ACS Appl. Mater. Interfaces. 8 (2016) 3776–3783.

[7] B. Saravanakumar, K.K. Purushothaman, G. Muralidharan, High performance supercapacitor based on carbon coated V_2O_5 nanorods, Journal of Electroanalytical Chemistry. 758 (2015) 111–116.

[8] K.K. T Kudo, Y Ikeda, T Watanabe, M Hibino, M Miyayama, H Abe, Amorphous

V$_2$O$_5$/carbon composites as electrochemical supercapacitor electrodes, Solid State Ionics. 152–153 (2002) 833–841.

[9]   D. Imamura, Masaru Miyayama, Characterization of magnesium-intercalated V$_2$O$_5$/carbon composites, Solid State Ionics. 161 (2003) 173–180.

[10]   A. Kuwahara, S. Suzuki, M. Miyayama, Estimation of high-rate discharge capacities in V$_2$O$_5$/carbon composite electrodes, Solid State Ionics. 179 (2008) 1890–1896.

[11]   H. Zhang, A. Xie, C. Wang, H. Wang, Y. Shen, X. Tian, Bifunctional Reduced Graphene Oxide/V$_2$O$_5$ Composite Hydrogel: Fabrication, High Performance as Electromagnetic Wave Absorbent and Supercapacitor, ChemPhysChem. 15 (2014) 366–373.

[12]   H. Zhao, A. Yuan, B. Liu, S. Xing, X. Wu, J. Xu, High cyclic performance of V$_2$O$_5$@PPy composite as cathode of recharged lithium batteries, Journal of Applied Electrochemistry. 42 (2012) 139–144.

[13]   D. Chao, X. Xia, J. Liu, Z. Fan, C.F. Ng, J. Lin, H. Zhang, Z.X. Shen, H.J. Fan, A V$_2$O$_5$/Conductive-Polymer Core/Shell Nanobelt Array on Three-Dimensional Graphite Foam: A High-Rate, Ultrastable, and Freestanding Cathode for Lithium-Ion Batteries, Advanced Materials. 26 (2014) 5794–5800.

[14]   R.B. Rakhi, W. Chen, D. Cha, H.N. Alshareef, High performance supercapacitors using metal oxide anchored graphene nanosheet electrodes, Journal of Materials Chemistry. 21 (2011) 16197.

[15]   Q. Qu, Y. Zhu, X. Gao, Y. Wu, Core-Shell Structure of Polypyrrole Grown on V$_2$O$_5$ Nanoribbon as High Performance Anode Material for Supercapacitors, Advanced Energy Materials. 2 (2012) 950–955.

[16] S.D. Perera, B. Patel, N. Nijem, K. Roodenko, O. Seitz, J.P. Ferraris, Y.J. Chabal, K.J. Balkus, Vanadium Oxide Nanowire-Carbon Nanotube Binder-Free Flexible Electrodes for Supercapacitors, Advanced Energy Materials. 1 (2011) 936–945.

[17] J.-J.S. Nguyen Van Hoa, Tran Thi Hoang Quyen, Nguyen Huu Nghia, Nguyen Van Hieu, In situ growth of flower-like V_2O_5 arrays on graphene@nickel foam as high-performance electrode for supercapacitors, Journal of Alloys and Compounds. 702 (2017) 693–699.

[18] M. Afzal, Adeel, Faraj A. Abuilaiwi, Amir Habib, Awais, M.A. Waje, Samaila B. Atieh, Polypyrrole/carbon nanotube supercapacitors: Technological advances and challenges, Journal of Power Sources. 352 (2017) 174–186.

[19] R.B. Rakhi, D.H. Nagaraju, P. Beaujuge, H.N. Alshareef, Supercapacitors based on two dimensional VO_2 nanosheet electrodes in organic gel electrolyte, Electrochimica Acta. 220 (2016) 601–608.

[20] Y. Zhang, C. Huang, C. Meng, T. Hu, A novel route for synthesis and growth formation of metal oxides microspheres: Insights from V_2O_3 microspheres, Materials Chemistry and Physics. 177 (2016) 543–553.

[21] G. Silversmit, D. Depla, H. Poelman, G.B. Marin, R. De Gryse, Determination of the V2p XPS binding energies for different vanadium oxidation states (V^{5+} to V^{0+}), Journal of Electron Spectroscopy and Related Phenomena. 135 (2004) 167–175.

[22] N.M. Ndiaye, T.M. Masikhwa, B.D. Ngom, M.J. Madito, K.O. Oyedotun, J.K. Dangbegnon, N. Manyala, Effect of growth time on solvothermal synthesis of vanadium dioxide for electrochemical supercapacitor application, Materials Chemistry and Physics. 214 (2018) 192–200.

_____

5.0 Conclusions and future work

In this PhD project, diverse approaches have been studied to synthesize different vanadium-based materials for supercapacitor applications. In particular, vanadium pentoxide (V_2O_5), vanadium pentoxide/graphene foam (V_2O_5/GF) composites, Vanadium dioxide (VO_2), carbon-vanadium oxynitride (C-V_2NO) and vanadium dioxide/activated expanded graphite (VO_2/AEG) composite materials have been reported and elucidated in details.

The structural, morphological, porosity and compositional properties of the as-synthesized materials were carried out by using X-ray powder diffraction (XRD), Raman spectroscopy, field-emission scanning electron microscopy (FE-SEM), transmission electron microscopy (TEM), Brunauer-Emmett-Teller (BET) analysis and X-ray photoelectron spectroscopy (XPS). For all the materials, electrochemical tests such as cyclic voltammetry (CV), galvanostatic charge-discharge (GCD), electrochemical impedance spectroscopy (EIS) and stability (floating and cycling) test were evaluated using an aqueous electrolyte.

Vanadium oxide materials have the potential to improve the reduction-oxidation reactions of faradaic nature due to their several oxidation states and their layered structures. As all transition metal oxides, VO_2 and V_2O_5 also display low specific surface area and poor electrical conductivity as compared to graphene foam and activated expanded graphite.
These two carbon-based materials were used to prepare V_2O_5/GF (at different mass loading of GF) and VO_2/AEG composite materials for supercapacitor application.
Furthermore, detailed studies with the pristine vanadium oxide-based materials involved introducing carbon and nitrogen precursors to form carbon-vanadium oxynitride materials.

This incorporation enhanced the SSA and the electrical conductivity of the materials, which led to a corresponding improvement in the electrochemical performance.
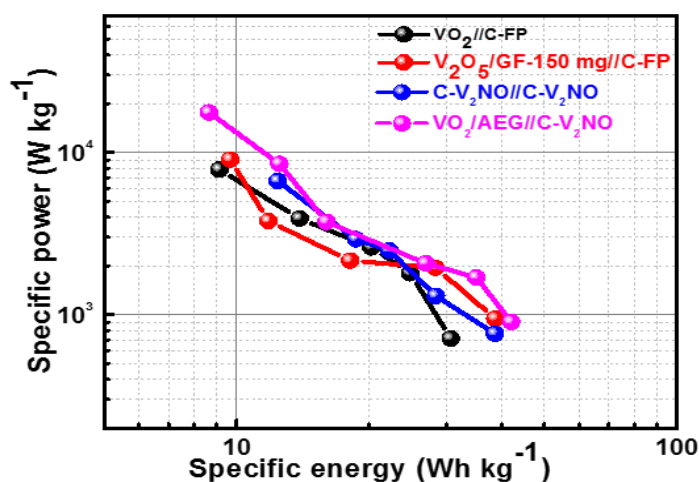

Figure 5.1: Ragone plot of vanadium-based devices for a symmetric and asymmetric devices.

Remarkably, a web-like C-V$_2$NO nanostructure was obtained via the variance of the growth temperature ranging from 700 °C to 900 °C. The C-V$_2$NO@800 °C material was adopted as the optimal temperature to synthesize the most electrochemically active electrode material due to the novel web-like morphology, high SSA and the high carbon (66.98 at%) and nitrogen (9.38 at%) contents. It also displayed variable oxidation states from V^{2+} to V^{5+} which could potentially increase the specific capacity of the material.

The ability to incorporate carbon into this web-like pristine materials and its adoption as an electrode material for supercapacitor application has also been proven to be an efficient and reliable means of boosting the overall energy storage capability.

Based on all the vanadium-based device assembled and tested in this study, a Ragone plot is presented in Figure 5.1 at different specific currents operated in the same aqueous electrolyte (6 M KOH) to compare their individual device performance. From the figure, all vanadium-based devices exhibited a remarkable specific energy as a function of specific power, which make them ideal candidates for supercapacitor applications. These results confirm the importance of incorporating carbon nanostructured material in a bid to improve the specific

surface area and electrical conductivity of the vanadium based materials, which led to improved electrochemical performance.

Specifically, the symmetric device with C-V$_2$NO electrodes materials had a comparable specific energy and specific power metrics as compared to some of the asymmetric devices studied. This is linked to the appropriate pore size distribution which is beneficial for enhanced electrochemical performance through electrolyte ion dynamics. This inspired the adoption of the C-V$_2$NO nanostructure as suitable electrode material in an asymmetric supercapacitor. When used as a negative electrode material with a vanadium/carbon–based composite materials (VO$_2$/AEG) as the positive electrode, the overall hybrid supercapacitor demonstrated the best charge storage properties as observed on the Ragone plot.

These results therefore demonstrate the potential of the web-like C-V$_2$NO nanostructured composite as an ideal energy storage electrode material for high-performance supercapacitors. It also opens a new insight into the electrochemical properties of these carbon-vanadium oxynitride materials as suitable negative electrode materials in asymmetric devices.

Further studies in the future will involve studying the electrochemical performance of these mesoporous web-like carbon-vanadium oxynitride nanostructures in ionic liquid electrolytes to design extended operating voltage devices with higher specific energy without compromising on its specific power. The electrochemical performance could be investigated and compared in different electrolytes to conclude the best suitable electrolyte for hybrid supercapacitor applications.

Another design consideration worth exploring will involve investigating the synergistic effect of introducing faradaic (battery-type) materials for testing in batteries. The incorporation of another metal-based material into the mesoporous web-like vanadium oxynitride to form bi-

metallic oxynitride nanostructures could also be an interesting aspect to study in future research projects.